

A computational biophysical model of thalamic and reticular nucleus microcircuitry: from neurons to emergent network dynamics

Présentée le 2 octobre 2020

à la Faculté des sciences de la vie
Groupe Hill
Programme doctoral en neurosciences

pour l'obtention du grade de Docteur ès Sciences

par

Elisabetta IAVARONE

Acceptée sur proposition du jury

Prof. K. Hess Bellwald, présidente du jury
Prof. S. L. Hill, directeur de thèse
Prof. D. Pinault, rapporteur
Prof. A. Destexhe, rapporteur
Prof. C. Petersen, rapporteur

Acknowledgments

I would like to thank everyone who made this thesis possible and accompanied me along this journey. First of all, I'd like to thank my thesis advisor, Sean Hill, for giving me the opportunity to work on this interesting topic; for the great time talking about the thalamus and computational modelling. For giving me the occasion to present tutorials in different schools and conferences. For giving freedom in my research, but also support and advice whenever I needed it. From you I have learned many aspects that will make me a better scientist. I would also like to thank Henry Markram and Felix Schürmann for being always supportive on this project.

I would like to thank Jane Yi, my "partner in crime", for your enthusiasm and scientific insights; without your experimental contributions little of this work would have been possible. I am also thankful to Ying Shi, Marine Bertschy and Rodrigo Perin for your constant support in the lab. Francisco Clascà and María Amado-Sancho, thank you for welcoming me in Madrid and showing me your great experimental work. I am also grateful to Christian O'Reilly and Oren Amsalem for your interest and contributions to this project, and to Polina Litvak for joining this project and help with my thesis.

There are many people who provided precious technical and scientific support and whom I'd like to thank: Benoît Coste, Michael Gevaert, Genrich Ivaska, Jean-Denis Courcol for your constant and prompt support on all software and workflows; Matthias Wolf, James King, Pramod Kumbhar for your help with s2f, Neurodamus and CoreNEURON; Cyrille Favreau, Fabien Petitjean, Nadir Román Guerrero for your great visualizations and support with Brayns; Anna-Kristin Kaufmann, Mohameth François Sy, Samuel Kerrien for your efforts on the data integration side. I would also like to thank Werner Van Geit for your constant support on single cell modelling, for giving me the opportunity to teach BluePyOpt and NEURON around the world and for being a great and fun office mate. I'd also like to thank Akiko Sato for being always so kind and for all your small and attentive gestures.

I consider myself so lucky for having met so many great minds and for the small and big scientific exchanges I had with you: Christian Rössert, András Ecker, Taylor Newton, Michael Reimann, Hugo Dictus, Vishal Sood, Srikanth Ramaswamy, Jay Coggan, Francesco Cremonesi, Daniel Keller, Lida Kanari, Eleftherios Zisis, Polina Shichkova, Yann Roussel, Stéphanie Battini, Armando Romani, Cristina Colangelo, Sirio Bolaños Puchet, Natalí Barros Zulaica, Tanguy Damart, Maria Reva, Anil Tuncel, Darshan Madge.

I would also like to thank many colleagues who are always so kind and manage logistics, organization and make our everyday life at the Blue Brain Project much easier and cheerful: Riccardo Sinisi, Adriana Salvatore, Raquel Freitas Pezzetti, Dace Stiebrina, Alina Busuioc Jiménez, Karin Holm.

I'd also like to mention one thing that helped me keeping a good research-life balance and believing in my abilities: running regularly helped me keep the focus towards my objectives, both in sports and science. In the end, preparing for a marathon is not so different from pursuing scientific objectives: it's all about finding things that motivate us, being constant in our efforts, and do a little step forward every day (and don't forget resting days!). I'd like to thank all the colleagues that followed my running adventures.

To my family: for your love and for giving me the ability to achieve my goals in this Swiss adventure.

To Giulio, for countless things: being the best teleworking mate I could have ever desired during the COVID-19 lockdown; for bearing with me every single day while I was writing this thesis; for reassuring me, for your thoughtful advice on any matter and for taking care of me in any way possible, starting with your amazing cooking skills. Looking forward to your thesis defense to give all of this and more back!

Summary

The thalamus, once believed to be a simple relay station between the body periphery and the neocortex, has started to be recognized as a key player in higher-order functions, such as attention. It participates in the transition between brain states, such as sleep and wakefulness, and thalamocortical oscillations. Many of these functions involve the reticular nucleus (Rt), an inhibitory brain structure that surrounds the thalamus and where thalamocortical and corticothalamic axons establish synaptic contacts. Recent technical advances have made possible the study of thalamic activity *in vivo* and its contributions to cortical processing and behavior. However, a unified understanding of how network dynamics in the thalamus and the thalamocortical system is shaped by its neurons and synapses is still lacking.

To address these challenges, we developed biophysically-detailed computational models of thalamic and reticular neurons. We then incorporated them in a large-scale model of thalamo-reticular microcircuitry, whose connectivity was directly constrained by three-dimensional reconstructions of neuronal morphologies. We included intrathalamic connections through chemical synapses, gap junctions and synapses from the sensory periphery and the neocortex. A large part of the data used to build and validate the model was extracted from the literature and leveraged a framework for its systematic and collaborative curation. This framework allowed us to keep track of parameter values used in the model, along with metadata describing the species, brain regions and experimental conditions.

As a first validation of the model at the network level, we studied the generation of spindle-like oscillations. We found that external inputs are necessary to initiate this rhythm, while its termination can be sustained by the synaptic interplay alone, with a key role of mutual inhibition between reticular neurons. We found that waxing-and-waning oscillations have a clear spatial component, that reflected the connectivity through chemical synapses as well as gap junctions. Finally, we investigated how differential depolarization in reticular and thalamocortical neurons influence the properties of spindle-like oscillations and predicted conditions where they are less easy to evoke.

Taken together this thesis demonstrates how a bottom-up modelling approach can be successfully applied to reconstruct and simulate thalamic microcircuitry, which shows emergent network behavior compatible with experimental findings, and paves the way for understanding the role of the thalamus in thalamocortical functions.

Keywords: thalamus, reticular nucleus of the thalamus, computational model, simulation, neurons, synapses, gap junctions, sleep spindles

Sommario (Italian abstract)

Il talamo, una volta ritenuto una semplice struttura di trasmissione d'informazione tra la periferia del corpo e la neocorteccia, si riconosce ora il suo ruolo in funzioni di ordine superiore, quali l'attenzione. Partecipa alla transizione tra stati cerebrali, come il sonno e la veglia, e nelle oscillazioni talamocorticali. Molte di queste funzioni coinvolgono il nucleo reticolare, un nucleo inibitorio che avvolge il talamo e in cui gli assoni talamocorticali e corticotalamici stabiliscono contatti sinaptici. Recenti progressi in ambito sperimentale hanno reso possibile lo studio dell'attività talamica *in vivo* e come questa contribuisca all'elaborazione corticale e al comportamento. Tuttavia, non è ancora disponibile una visione d'insieme di come i neuroni e le sinapsi a livello talamico e talamocorticale influenzino le dinamiche di rete.

Per rispondere a queste domande, abbiamo sviluppato modelli matematici biofisicamente dettagliati dei neuroni talamici e reticolari. Li abbiamo poi incorporati in un modello esteso del circuito talamo-reticolare, la cui connettività è stata derivata direttamente dalle morfologie dei neuroni ricostruite in 3D. Abbiamo incluso le connessioni intratalamiche mediate da sinapsi chimiche, giunzioni comunicanti e sinapsi dalle afferenze sensoriali e neocorticali. Gran parte dei dati usati per costruire e validare il modello sono stati estratti dalle pubblicazioni scientifiche e hanno sfruttato un *framework* per l'annotazione sistematica e collaborativa della letteratura. Questo *framework* ci ha permesso di tenere traccia dei valori assegnati ai parametri, insieme ai metadati che descrivono specie, area del cervello e condizioni sperimentali.

Come prima validazione del modello a livello di rete, abbiamo studiato la generazione di oscillazioni simili ai fusi del sonno. È risultato che *inputs* esterni sono necessari per dare inizio a questo ritmo, mentre la sua cessazione può essere sostenuta anche solo dall'attività sinaptica, con un ruolo importante rivestito dall'inibizione reciproca tra i neuroni reticolari. La forma delle oscillazioni è risultata chiara anche a livello spaziale e riflette la direzione delle connessioni attraverso sinapsi chimiche e giunzioni comunicanti (*gap junctions*). Infine, abbiamo investigato come differenti livelli di depolarizzazione nei neuroni reticolari e talamocorticali influenzino le proprietà dell'oscillazione e predetto condizioni in cui essa è più difficile da evocare.

Nell'insieme, questa tesi dimostra come un modello *bottom-up* possa essere applicato con successo nel ricostruire e simulare un microcircuito talamico e come questo modello generi attività emergente compatibile con i risultati sperimentali. Inoltre, apre la strada alla comprensione del ruolo del talamo nelle funzioni talamocorticali.

Parole chiave: talamo, nucleo reticolare del talamo, modello matematico, simulazione, neuroni, sinapsi, giunzioni comunicanti, fusi del sonno.

Contents

1	Introduction	1
1.1	Motivation	1
1.2	Experimental and computational background	2
1.2.1	The reticular nucleus and thalamo-reticular connectivity	2
1.2.2	Historical perspective of spindle generation in the thalamus and reticular nucleus	4
1.2.3	The classical model of spindle generation (thalamus and reticular nucleus interactions)	5
1.2.4	Computational models of thalamic and reticular circuits generating spindles...7	
1.2.5	Computational models of spindles in the isolated reticular nucleus	8
1.2.6	Detailed computational modelling of neural microcircuits	9
1.3	Thesis outline	10
2	A framework for literature curation	12
2.1	Introduction	13
2.1.1	Terminology	13
2.1.2	Requirements	14
2.1.3	Existing solutions	15
2.2	Design	16
2.2.1	Collaborative structure	16
2.2.2	Ontologies	16
2.2.3	Annotation format	18
2.2.4	Unique identifiers	19
2.2.5	Tags	20
2.2.6	Parameters	20
2.2.7	Experimental properties	22
2.2.8	Localizer	23
2.2.9	Zotero library	24
2.2.10	Global software infrastructure	24
2.2.11	User interface	25
2.3	Case study: corpus of annotation for the modeling of the thalamo-cortical loop26	
2.3.1	The corpus	26
2.3.2	First example: ion channel conductance in neuron models.....26	
2.3.3	Second example: neuron densities from stereological studies	30
2.4	Availability	33
2.5	Discussion	34

2.5.1	A better literature curation for a more integrated knowledge in neuroscience	34
2.5.2	Limitations	34
2.5.3	Future directions	35
3	Experimentally-constrained models of thalamic neurons	36
3.1	Introduction	37
3.2	Results	38
3.2.1	Physiological and morphological characterization	38
3.2.2	Constraining the models with experimental data	40
3.2.3	Model and experimental diversity	44
3.2.4	Assessment of model generalization	46
3.2.5	Sensitivity of electrical features to small parameter perturbations	47
3.2.6	Preservation of model firing properties with different morphologies	49
3.3	Discussion	50
3.4	Methods	53
3.4.1	Experimental procedures	53
3.4.2	Electrical features extraction	54
3.4.3	Morphology analysis	55
3.4.4	Ionic currents models	55
3.4.5	Simulation and parameters optimization	57
3.4.6	Sensitivity analysis	57
3.4.7	Data and code availability	58
4	Reconstruction and simulation of thalamic microcircuitry	59
4.1	Introduction	59
4.2	Methods	61
4.2.1	Constraining and validating the model with experimental data	61
4.2.2	Experimental data used to constrain the model	61
4.2.3	Experimental data used for model validation	62
4.2.4	Validations at the network level	62
4.2.5	Reconstructing the morphological diversity of neurons	63
4.2.6	Reconstructing the electrical diversity of neurons	66
4.2.7	Reconstructing neurons density	68
4.2.8	Microcircuit geometry	68
4.2.9	Soma positions and models assignment	69
4.2.10	Morphology placement	70
4.2.11	Connectivity based on morphological appositions	70
4.2.12	Converting morphological appositions into functional synapses	71
4.2.13	Connections from lemniscal and corticothalamic afferents	71

4.2.14	Synapse physiology and short-term plasticity	72
4.2.15	Constraining synapse conductance values	74
4.2.16	Gap junctions.....	77
4.2.17	Simulation software and high-performance computing resources	77
4.2.18	Simulating <i>in vivo</i> -like conditions.....	77
4.2.19	Simulating <i>in vitro</i> -like conditions.....	78
4.2.20	Simulating depolarization levels	78
4.2.21	Simulation analysis	78
4.3	Results	79
4.3.1	Morphological properties of thalamic and reticular neurons	79
4.3.2	Neurons electrical properties and models	81
4.3.3	Microcircuit dimension and composition.....	82
4.3.4	Reconstructing and validating the connectivity	85
4.3.5	Reconstructing and validating synapse physiology	89
4.3.6	Reconstructing and validating gap junction connectivity	92
4.3.7	Simulating <i>in vivo</i> -like spontaneous activity and sensory responses	95
4.3.8	Validation of network responses to corticothalamic inputs (<i>in vitro</i> -like).....	97
4.3.9	Evoked spindle-like oscillations in <i>in vitro</i> -like conditions	99
4.3.10	The role of different synaptic pathways in the maintenance and termination of spindle-like oscillations.....	101
4.3.11	Differential depolarization of the Rt and VPL influence oscillation properties	102
4.3.12	The effects of VPL depolarization and initial Rt_RCs recruitment	105
4.3.13	Gap junctions increase the duration of spindle-like oscillations.....	107
4.4	Discussion	110
5	Conclusion and outlook	113
5.1	Summary of main conclusions.....	113
5.2	Implications.....	115
5.2.1	Thalamic activities in wakefulness, sleep and attention	115
5.2.2	Thalamic neurons and microcircuits in neurological and mental disorders...	117
5.3	Limitations and future directions	119
5.3.1	Thalamic microcircuitry in sensory processing	119
5.3.2	Corticothalamic influences onto thalamic and reticular activities	120
5.3.3	Whole thalamus and whole thalamocortical integration	120
	Bibliography	122
	Curriculum Vitae	144

List of figures

Figure 2.1. High-level schema of the annotation format.	19
Figure 2.2. Schema of the hierarchy of data type encapsulation.	22
Figure 2.3. Software infrastructure proposed for literature curation.	25
Figure 2.4. Histogram showing the number of annotated parameters for the 30 most annotated parameter types.	26
Figure 2.5. Example of ion channel conductances annotation.....	30
Figure 2.6. Example of cell densities annotation.....	33
Figure 3.1. Simultaneous physiological and morphological characterization.	38
Figure 3.2. Morphological properties.	39
Figure 3.3. Histograms of electrical features.	41
Figure 3.4. Models of different TC e-types and their fitting errors.	43
Figure 3.5. Diversity of model parameters and experimental variability.	44
Figure 3.6. Model generalization.	46
Figure 3.7. Local sensitivity analysis.....	48
Figure 3.8. Model generalization to different experimental morphologies.	50
Figure 4.1. Single cell data and models	80
Figure 4.2. Reconstructing neuron densities, composition, microcircuit dimensions and neuron placement	83
Figure 4.3. Reconstructing and validating intrathalamic and afferents connectivity	86
Figure 4.4. Reconstructing and validating synaptic short-term plasticity and postsynaptic potentials (PSPs) amplitude	90
Figure 4.5. Reconstructing and validating gap junction connectivity between Rt_RC neurons	94
Figure 4.6 Simulated spontaneous and sensory-evoked activity (<i>in vivo</i> -like)	96
Figure 4.7 Threshold analysis of sensory-evoked responses (<i>in vivo</i> -like)	97
Figure 4.8. Reproducing <i>in vitro</i> findings in the model: corticothalamic (CT) modulation of TC cells activity (Crandall et al., 2015).	98
Figure 4.9. Spindle-like oscillations in <i>in vitro</i> -like conditions and the role of different connections	100
Figure 4.10. Depolarization levels in Rt and VPL influence oscillation properties	103
Figure 4.11. Oscillation properties with VPL depolarization and the effect of increasing initial Rt recruitment	106
Figure 4.12. The contribution of gap junctions to spindle-like oscillations	108
Figure 5.1 Draft models of the thalamus and the neocortex.	121

List of tables

Table 2.1. List of key open-access resources constituting the annotation framework.	34
Table 4.1. Synapse kinetics and short-term plasticity parameters.	75
Table 4.2. Postsynaptic potential (PSP) amplitudes.	76
Table 4.3. Coefficient of variation (CV) of first PSP amplitudes.....	76

1 Introduction

1.1 Motivation

The thalamocortical system constitutes a large portion of the mammalian brain, consisting of different thalamic nuclei and their reciprocal interactions with the neocortex. The thalamus, once believed to be a passive relay station of sensory information to the neocortex, is now recognized as a key player in some cognitive functions and more complex computations (Rikhye et al., 2018; Saalman and Kastner, 2015).

Several experimental studies supported this change of view. First, although the main role of first-order sensory nuclei is to transmit information from the body periphery to the neocortex, their main input does not come from sensory afferents. Indeed, the corticothalamic fibers projecting to the thalamus greatly outnumber thalamocortical ones (Deschênes et al., 1998; Sherman and Koch, 1986). Moreover, corticothalamic synapses are the most numerous on many, if not all, neurons of the thalamus and associated reticular nucleus (Bickford et al., 2010; Morgan and Lichtman, 2020; Sherman and Koch, 1986; Van Horn et al., 2000). Second, there is growing evidence showing that behavioral context, such as attention, modulates the information transmitted at the level of the thalamus, likely involving corticothalamic feedback to the thalamus and the reticular nucleus (McAlonan et al., 2008; Wimmer et al., 2015). Third, the thalamus and Rt participate in thalamocortical and corticothalamic rhythms associated with different states of vigilance (e.g. wakefulness and sleep), such as slow waves and sleep spindles (Adamantidis et al., 2019; Destexhe et al., 2007; Llinás and Steriade, 2006; Steriade, 2006; Steriade et al., 1993).

Several experimental and theoretical studies have explored aspects of the structure and function of thalamic circuitry, yet a comprehensive view of which cellular, synaptic and circuit components generate diverse network dynamics is still missing. Computational modelling can help the understanding of complex neuronal systems, bridging spatial and temporal scales of experimental investigation and generate experimentally-testable predictions (Einevoll et al., 2019). In this thesis, we aim to integrate diverse sources of experimental data from the rodent thalamus in a detailed computational model of thalamic microcircuitry. Differently from other models, we do not have a specific application in mind (top-down design), but start from the neuronal and synaptic components of the system and study how they interact to produce emergent network behavior (bottom-up approach).

In the following paragraphs we review known aspects of cellular and circuit properties of the thalamo-reticular loop, with a focus on network oscillations generated in the thalamus and highlight open questions that can be addressed in a detailed computational model of thalamic microcircuitry. Additional details on cellular and synaptic anatomy and physiology, gathered from the literature and from in-house experimental data, used to constrain and validate the neurons and microcircuit model, will be presented in Chapter 4.

1.2 Experimental and computational background

1.2.1 The reticular nucleus and thalamo-reticular connectivity

An important and often neglected structure, which is part of the thalamocortical system, is the reticular nucleus of the thalamus (Rt). It is a shell-shaped nucleus, critically located at the interface between ascending fibers from the thalamus to the cortex and descending corticothalamic projections (Pinault, 2004), containing mainly GABAergic inhibitory cells (de Biasi et al., 1986; Cavdar et al., 2013; Houser et al., 1980). Thalamocortical and corticothalamic neurons give off axonal collaterals in the Rt and excite reticular neurons, while the latter innervate thalamocortical neurons (Ohara and Lieberman, 1985; Scheibel and Scheibel, 1966a).

Early studies showed its role in the generation of network oscillations, in the 7-16 Hz frequency range (Steriade et al., 1987). Similar rhythms, called sleep spindles, are observed in the electroencephalogram of mammals during periods of light non-REM sleep (Fernandez and Luthi, 2019; Loomis et al., 1935). Recent technical advances, such as targeted manipulation of neuronal populations through optogenetics, have confirmed that cortical spindles can be evoked by stimulating the Rt (Bartho et al., 2014; Halassa et al., 2011; Thankachan et al., 2019), confirming its involvement in their generation. Although the Rt is involved in other functions, such as attentional-mediated sensory filtering (McAlonan et al., 2008; Nakajima et al., 2019; Wimmer et al., 2015), here we will focus on its role in the generation of spindle-like rhythms and how the same circuitry can serve pathological brain oscillations (Beenhakker and Huguenard, 2009).

Similarly to thalamocortical projection (TC) neurons, Rt neurons fire action potentials in different firing modes, tonic firing and low-threshold bursting, depending on their resting potential *in vitro* (Avanzini et al., 1989; Connelly et al., 2017; Spreafico et al., 1988). The proportion of low-threshold bursting neurons vary between different sectors of the Rt (Lee et al., 2007), with those associated with somatosensory thalamic nuclei showing a higher tendency to burst (Clemente-Perez et al., 2017; Fernandez et al., 2018). This heterogeneity among sensory modalities in the Rt is reflected by the incidence of bursting in different thalamic nuclei *in vivo* (Ramcharan et al., 2000) and the correlation of activity in sensory-projecting Rt sectors with sleep spindles (Halassa et al., 2014). Although the general physiological properties of Rt and TC neurons *in vitro* are quite similar, when considering their

ability to fire in distinct modes, there are differences in the ion channel subtypes they express. For instance, $\text{Ca}_v3.1$ low-threshold calcium channels are the major type in TC neurons, while Rt neurons express predominantly $\text{Ca}_v3.2$ and $\text{Ca}_v3.3$ types (Talley et al., 1999). Although we know that low-threshold calcium channels in Rt are necessary for spindle rhythmogenesis, as shown in knock-out mice (Pellegrini et al., 2016), while those expressed in TC neurons are not (Lee et al., 2013), no experimental study has shown that the specific types expressed in Rt neurons are necessary for rhythm generation.

Some interesting open questions remain concerning intra-reticular connectivity. While electrical coupling through gap junctions between reticular neurons has been extensively demonstrated through *in vitro* paired recordings and dye-coupling experiments (Landisman et al., 2002; Lee et al., 2014; Long et al., 2004; Parker et al., 2009), some recent findings suggested the absence of inhibitory connections between reticular neurons in adult mice (Hou et al., 2016), while other physiological studies have shown mutual inhibition between Rt neurons, at least in rodents younger than 2 weeks (Deleuze and Huguenard, 2006; Lam et al., 2006). A stimulating hypothesis has been proposed regarding the opposite functional roles of these two types of connections: while gap junctions would promote synchronized activity in Rt neuron assemblies, inhibitory synapses would mediate desynchronization via inhibition of bursting in the Rt (Beenhakker and Huguenard, 2009; Fogerson and Huguenard, 2016; Sohal and Huguenard, 2003). An indirect result supporting this hypothesis is that mutations of voltage-gated sodium channels, which are risk factors for absence epilepsy, cause a failure in inhibition between Rt neurons and spike-wave discharges (Makinson et al., 2017). Direct suppression of this inhibitory pathways is not feasible experimentally, but can be explored in computational models along with the role of electrical synapses in the Rt.

Another interesting feature of thalamo-reticular connectivity is the existence of closed-loop and open-loop circuits. In the closed-loop configuration, a TC neuron receives inhibition from the same Rt neurons that it excites (feedback inhibition); in the open-loop configuration the TC neuron receives inputs from other Rt neurons (lateral inhibition). The open-loop configuration is the most prominent (80-90%), as shown in anatomical (Pinault and Deschênes, 1998) and physiological studies (Pinault and Deschênes, 1998; Shosaku, 1986). Since the identification of closed-loops and open-loops at the single neuron level is experimentally challenging, a computational model with connectivity reconstructed from the 3D shape of neurons would give access to all the connections between TC and Rt neurons. Regarding the functions of these configurations, some open questions still remain. Computational models suggested that open-loop connectivity increases cortical output by acting as a tunable filter (Willis et al., 2015) and that heterogeneous networks, involving both open and closed-loops, support oscillation and propagation better than their homogeneous counterparts (Brown et al., 2020).

1.2.2 Historical perspective of spindle generation in the thalamus and reticular nucleus

Sleep spindles are discrete burstlike events of 10-15 Hz cycles recorded in the electroencephalogram (EEG) during sleep in different animals. Sleep spindles have been first discovered in EEG, studied through anatomical lesions studies and their research continues today, regarding their mechanisms and functions (Fernandez and Luthi, 2019). They were identified around 80 years ago in EEG recordings of naturally sleeping humans (Loomis et al., 1935) and after 50 years the thalamus was identified as pacemaker and that thalamocortical loops are necessary for recording sleep spindles in the cortical surface.

The observation of spindle rhythms in the cut ends of thalamocortical fibers in cats paved the way for the study of their origin (Adrian, 1941); it was found later found that they were present in the thalamus after removal of the cortex (Morison and Bassett, 1945). This finding triggered a lot of following studies and led to the “thalamic pacemaker” hypothesis (Andersen and Andersson, 1968; Steriade and Deschenes, 1984). According to this hypothesis, the characteristic patterns recorded at the EEG originates from rhythmic activity in the thalamus, which is then transmitted to the neocortex. A mechanism for spindle generation based on thalamo-reticular “loops” had already been suggested by Scheibel and Scheibel (Scheibel and Scheibel, 1966b, 1966a, 1967); they also predicted that the reticular nucleus is inhibitory and that the inhibition of TC cells from Rt cells was important for thalamic rhythmicity (Destexhe and Sejnowski, 2003). The role of inhibitory activity in thalamic neurons was also suggested by intracellular recordings of thalamic neurons in cats, revealing rhythmic inhibitory events in phase with cortex (Purpura, 1968).

Another hypothesis suggested that the reticular nucleus alone was capable of generating spindles. Steriade and colleagues first showed in *in vivo* recordings in anesthetized cats that spindle oscillations in thalamic neurons were abolished after disconnection from the Rt (Steriade and Deschenes, 1984). A subsequent study found spindles in the anterior portion of the Rt, isolated from other thalamic nuclei, demonstrating that the Rt nucleus is the major thalamic spindle pacemaker (Steriade et al., 1987). Experiments in thalamic slices in ferrets supported the hypothesis that spindles are generated through interactions between TC and Rt neurons (Bal et al., 1995a, 1995b; Kim et al., 1995; von Krosigk et al., 1993).

Computational models helped unveiling the cellular, synaptic and network mechanisms underlying spindle generation in networks of reticular and thalamocortical neurons (Section 1.2.4), as well as the isolated reticular nucleus (Section 1.2.5). For example, the contribution of intrinsic neuron mechanisms to spindle termination (or “waning”) spindle refractory periods (Section 1.2.3) through Ca^{2+} -mediated upregulation of the I_h current, and the non-linear activation properties of GABA_B currents were first predicted by computational models and then confirmed experimentally (see 1.2.4).

1.2.3 The classical model of spindle generation (thalamus and reticular nucleus interactions)

Different neurophysiological mechanisms have been proposed to participate in spindle initiation, synchronization and termination. Since many of these aspects can be easily dissected in computational models, they will be summarized and discussed here.

Traditionally, the intrinsic oscillatory properties of Rt neurons and their anatomical connectivity with TC neurons would sustain the generation of network oscillations, as shown in pioneering *in vitro* studies in ferret (Bal et al., 1995a, 1995b; Kim et al., 1995; von Krosigk et al., 1993), which have been associated with “spindle-like rhythms” in rats and mice slice (Huguenard and Prince, 1994; Jacobsen et al., 2001; Kleiman-Weiner et al., 2009; Warren et al., 1994). *In vivo*, cortical inputs would act as trigger of oscillatory activity in the TC-Rt-TC loop which is then relayed to the cortex through thalamocortical projections (Pratt and Morris, 2015; Steriade, 2005).

The low-threshold burst firing mode is the predominant type of discharge during sleep spindles and promotes their initiation. During non-REM sleep, burst discharge in Rt neurons often coincides with the beginning of a spindle in the EEG (Fernandez and Luthi, 2019), then increases and is phase-locked with oscillatory cycles within a spindle, as shown *in vivo* in rats (Buzsáki, 1991; Gardner et al., 2013). What is the minimal number of Rt neurons required to generate a cortical or thalamic spindle? Although *in vitro* experiments in ferrets suggested that even a single Rt neuron can initiate spindle-like rhythms in a slice (Kim et al., 1995), it is still experimentally challenging quantifying the minimum population size required to generate spindles in the thalamus and the cortex.

Burst firing in Rt neurons conveys strong inhibition to TC neurons due to the structural and functional properties of Rt synapses (Kim et al., 1995), although weaker connections from Rt to ventrobasal TC neurons have been shown as well (Cox et al., 1997). GABA released from Rt neurons terminals activate GABA_A receptors onto TC neurons, which show large inhibitory postsynaptic potential (IPSPs). The large amplitude of IPSPs is explained at least in part by the low Cl⁻ reversal potential in rat TC neurons (Ulrich and Huguenard, 1997). The contribution of GABA_B currents could be species-dependent, for instance it has not been initially shown in mice (Warren et al., 1994), probably because it was masked by the larger GABA_A component (Warren et al., 1997), or because of extrasynaptic location of GABA_B receptors. Two different computational models predicted the necessity of a nonlinear activation of GABA_B responses, which was then confirmed experimentally (see Section 1.2.4).

TC neurons can fire post-inhibitory low-threshold spikes or bursts and in turn excite Rt neurons. The predominant open-loop network configuration allows for a propagation of the oscillation and recruitment of other Rt neurons as shown in slice in ferrets to generate more synchronous bursting in Rt neurons and more robust rebound in TC neurons (Kim and McCormick, 1998a; Kim et al., 1995). Gap junctions connectivity may contribute further synchronization between bursting Rt neurons (Fernandez and Luthi, 2019), although this aspect

has not been investigated at the network level so far. At the level of electrically-coupled Rt neuron pairs, it has been shown that low-threshold Ca^{2+} spikes, due to their slower dynamics, are transmitted through gap junctions more easily than single Na^+ spikes (Long et al., 2004).

Recent *in vivo* recordings in the mouse (Bartho et al., 2014; Rovó et al., 2014; Urbain et al., 2019), showed that TC neurons do not fire on all cycles of the oscillation, confirming earlier findings in ferret (Kim et al., 1995). This suggests that network synchrony in intrathalamic circuits is relatively modest and efficient desynchronizing mechanisms, such as lateral inhibition between Rt neurons, are present (Fernandez and Luthi, 2019). Such desynchronizing and inhibitory mechanisms could also contribute to spindle termination.

Sleep spindles are limited in time to 0.5-3s and exhibit refractory periods of 5-10 seconds as shown in ferret *in vitro* (Bal and McCormick, 1996; Lüthi et al., 1998). These *in vitro* studies showed that bursting in Rt and TC neurons can be autoregulated by intrinsic mechanisms. In TC neurons, repetitive burst activates HCN channels (the molecular substrate of I_h currents) through persistent calcium influx, which progressively depolarize them and prevent them from bursting (Bal and McCormick, 1996; Lüthi and McCormick, 1998). This was indeed observed in thalamic slices of ferrets with the application of extracellular cesium (Cs^+), which primarily blocks I_h (Bal and McCormick, 1996) and ZD7288, a specific I_h blocker (Lüthi et al., 1998). In this *in vitro* preparation spindle waves are visible in TC single neurons and are characterized by barrages of IPSPs at 6-10 Hz and low-threshold Ca^{2+} spikes occurring every second to fourth IPSP (Bal and McCormick, 1996). Each spindle wave is followed by a slow 1-4 mV afterdepolarization (ADP), that makes it difficult to evoke Ca^{2+} spikes during the seconds immediately following a spindle wave. The application of Cs^+ abolished the ADP, demonstrating that it is generated by persistent activation of I_h , and transformed spindle waves into sustained rhythmicity at the same frequency. The depolarization and the change in apparent input resistance induced by the upregulation of I_h would reduce the capacity of IPSPs from the reticular nucleus of evoking low-threshold Ca^{2+} spikes in TCs (Bal and McCormick, 1996). Subsequent experimental studies in ferret slices demonstrated that the kinetics and voltage dependence of activation of I_h are sensitive to intracellular Ca^{2+} (Lüthi and McCormick, 1998). In this study the authors proposed that Ca^{2+} influx through rebound Ca^{2+} spikes and IPSPs in TC cells affect the voltage-dependent properties of I_h and upregulate it. It was later shown that the upregulation of I_h by Ca^{2+} occurs through cAMP (Lüthi and McCormick, 1999). It was proposed that persistent activation of I_h is initiated by a rapid increase of intracellular Ca^{2+} , which stimulates the production of cAMP, which interacts then with open h-channels, inducing a prolonged activation of I_h . The Ca^{2+} -mediated upregulation of HCN channels in TC cells was first predicted by computational models (see 1.2.4).

The gradual hyperpolarization of Rt neurons during the oscillation, could bring the cells below the firing threshold and contribute to the “waning” of the oscillation (von Krosigk et al., 1993). This gradual hyperpolarization could depend on the activation of Ca^+ and Na^+ -dependent potassium currents as shown in ferret (Kim and McCormick, 1998b), but also on network

mechanisms. *In vivo*, however, there's evidence showing that some reticular neurons also gradually depolarize during spindles (Bal and McCormick, 1996).

In vivo, cortical and brainstem mechanisms could contribute to spindle termination, although the exact mechanisms are still debated. Cortex could contribute to spindle termination by providing desynchronizing input to the thalamus and Rt neurons as shown *in vivo* in cats and *in computo* (Bonjean et al., 2011; Timofeev et al., 2001). A recent experimental study during natural sleep in rats provided evidence supporting the Rt hyperpolarization hypothesis, showing that Rt burst firing consistently decreases from cycle to cycle during spindles and in particular towards their end (Bartho et al., 2014). The same authors pointed out that the causes of decreased activity in Rt neurons towards the end of the spindle are still unclear.

Closely related to the termination (and “waning”) of spindle oscillations is the refractory period, which has been studied *in vitro* in ferret (Kim et al., 1995) and *in vivo* in cats (Destexhe et al., 1998a). Repetitive stimulation *in vitro* of the perigeniculate (reticular) nucleus or prethalamic afferents to the dLG (visual-related thalamic nucleus), revealed a refractory period of 7-14 s and stimuli during this period resulted in shorter local spindles that did not propagate along the slice (Kim et al., 1995). Similar values of refractory periods (8-12 s) were observed *in vivo* in cats through cortical stimulation. In the associated model the refractory period was the result of the Ca^{2+} -dependent increase of I_h activity (Destexhe et al., 1998a).

1.2.4 Computational models of thalamic and reticular circuits generating spindles

The previous paragraphs highlighted some of the open questions regarding cellular properties, intrathalamic connectivity and their role in spindle and spindle-like rhythm generation. Some of these questions are more easily accessible through computational modelling.

Several models of thalamic and thalamocortical networks have been developed and addressed different questions concerning spindle initiation (and waxing), propagation, termination (waning) and the transformation of spindles into epileptic-like rhythms. According to the scope of this thesis, here we focus on models that generate spindles in isolated thalamic networks, while the contribution of cortex will be discussed in Chapter 4.

A computational model including one TC and one Rt neuron interconnected was able to generate 8-10 Hz spindles (Destexhe et al., 1993). It suggested an important role of intrinsic currents in TC cells in the waxing and waning of spindles, the role of TC neurons in spindle initiation and rhythm generation. Later models showed how certain combinations of I_h and low-threshold calcium conductance can make TC cell models autorhythmic (Amarillo et al., 2015; Wang, 1994). Furthermore, the model by Destexhe and collaborators (1993) predicted an important role of the Ca^{2+} -mediated regulation of the I_h current in spindle termination, which has been confirmed experimentally (see 1.2.3) in thalamic slices (Bal and McCormick, 1996; Lüthi and McCormick, 1998). It was found that the regulation of I_h by Ca^{2+} occurs by Ca^{2+} -induced stabilization to the open state of the channel (Lüthi and McCormick, 1998), exactly as predicted by the model.

The propagation of spindle oscillations was the focus of a ferret slice model (Golomb et al., 1996), which improved upon a previous model by introducing spatially dependent connection architecture and a GABA_B mechanism in postsynaptic TC cells that depended non-linearly on the duration of presynaptic Rt bursts. This mechanism was modelled simultaneously in two studies, using different approaches (Destexhe and Sejnowski, 1995; Wang et al., 1995). The model in Wang et al. (1995) was phenomenological, in the sense that the nonlinear activation was necessary to yield the correct network dynamics. The study in Destexhe and Sejnowski investigated a biophysical model based on G-protein activation of potassium channels associated with GABA_B receptors, more closely related to the biological mechanism underlying GABA_B receptor function. The non-linear activation of GABA_B receptors was later confirmed experimentally in the thalamus (Kim et al., 1997), hippocampus and cortex (Thomson and Destexhe, 1999). The model in (Wang et al., 1995) reproduced a number of findings in ferret slices, but lacked a mechanism for spindle termination, thus neurons recruited from the oscillatory wavefront did not stop oscillating (Golomb et al., 1996). A 1-dimensional model of 50 TC and 50 Rt neurons closely reproduced propagating waves in ferret slices and included ionic mechanisms for the termination, as in previous models (Destexhe et al., 1993, 1996).

Different models showed how hyper-synchronous bicuculline-induced oscillations (Bal et al., 1995b; Kim et al., 1995; von Krosigk et al., 1993) can be generated in conditions similar to spindle generation, when inhibition in the Rt to TC synapse is dominated by GABA_B currents (Destexhe et al., 1996; Golomb et al., 1996). A factor that would limit GABA_B activation in the Rt to TC synapse is the GABA_A-mediated inhibition between Rt neurons: in the absence of lateral inhibition Rt neurons can produce prolonged bursts that evoke a significant GABA_B current in TC neurons (Destexhe et al., 1996). Mutual inhibition between Rt neurons, in combination with a neuromodulatory drive that depolarizes the resting potential of Rt neurons, explained the generation of oscillations in the isolated Rt neurons, as shown *in vivo* in cats and computational modelling (Destexhe et al., 1994a; Steriade et al., 1987). A recent model explored the effect of altering the degree of inhibition between Rt neurons and found that an increase in Rt to Rt inhibition caused a lengthening of spindles (Bús et al., 2018), while recent experimental findings suggested that Rt to Rt inhibition limits pathological rhythms (Makinson et al., 2017). This discrepancy may be due to the artificial re-arrangements of 2-dimensional connectivity in the model (Bús et al., 2018).

1.2.5 Computational models of spindles in the isolated reticular nucleus

Modelling studies participated in the exploration of the “thalamic pacemaker” hypothesis (Section 1.2.3) and showed how TC-Rt interactions can generate spindles (see Section 1.2.4). Computational models also showed how the isolated Rt nucleus is capable of generating self-sustained oscillations (Destexhe et al., 1994a; Golomb et al., 1994), also reviewed in (Destexhe and Sejnowski, 2003), as shown in *in vivo* recordings in cats (Steriade et al., 1987). Both models, although were different in terms of connectivity and of the kinetics of intrinsic and

synaptic currents, generated oscillations at ~ 10 Hz (Destexhe and Sejnowski, 2003), consistent with recordings *in vivo* in the isolated rostral pole of the Rt (Steriade et al., 1987). Important elements for rhythm generation inside the Rt were the rebound burst properties of its neurons and synaptic interactions through GABAergic receptors (Destexhe and Sejnowski, 2003). The model in Destexhe et al. (1994) showed that waxing and waning oscillations in the Rt are more easily seen in the average membrane potential of multiple neurons, consistent with waxing and waning patterns in the field potential (Steriade et al., 1987). At the single neuron level, the oscillation consisted of synchronized subthreshold activity, with individual cells firing single spikes or bursts only occasionally. Different connectivity patterns in the model gave rise to spindle-like oscillations, provided that each Rt neuron was connected to a neighborhood sufficiently extended. On the other hand, if Rt neurons were connected to their immediate neighbors only, another type of oscillation emerged: neighboring neurons fired multiple bursts in alternation, but the average membrane potential did not show any synchrony (Destexhe et al., 1994a).

Another computational model proposed that differences in neuromodulatory states between *in vivo* and *in vitro* conditions account for the generation of spindles in the isolated Rt *in vivo*, but not *in vitro* (Destexhe et al., 1994b). This model suggested that serotonergic, noradrenergic and glutamatergic inputs from the basal forebrain and brainstem were still present in the deafferented Rt preparations (Steriade et al., 1987) and contributed to depolarized membrane potential (between -70 and -60 mV) of Rt neurons observed *in vivo*. The depolarizing effect of noradrenaline and serotonin observed experimentally in Rt neurons of cats and guinea pigs (McCormick and Wang, 1991) was modelled by blocking $\sim 20\%$ of the leak potassium currents (Destexhe et al., 1994a). Incorporating noradrenergic and serotonergic effects of leak potassium currents showed that the Rt network can switch from a silent to an oscillatory mode (Destexhe and Sejnowski, 2003). Other factors that can explain the lack of spindle-like rhythms in slice experiments is a potential less intact collection of Rt neurons, in term of neuron numbers, and decreased dendrodendritic inhibitory connectivity, at least in cat (Fuentelba and Steriade, 2005).

1.2.6 Detailed computational modelling of neural microcircuits

The examples above illustrate that network models were able to explain different aspects of network dynamics and predict the contributions of intrinsic and synaptic mechanisms. Many of these models, while including important details on neuronal and synaptic biophysics, neither used neuronal morphologies to constrain the connectivity between neurons nor distance-dependent connectivity, which are likely to alter network dynamics (Rosenbaum et al., 2017). Moreover, the choice of neuron numbers did not take into account the relative proportion of Rt and TC neuronal populations. Another recent model (Bús et al., 2018) extended the biophysics from (Destexhe et al., 1996) by including recent anatomical findings on the relative proportion of TC and Rt neurons (Lam et al., 2006), diffuse and focal axonal arborizations of Rt neurons into the thalamus (Cox et al., 1996) and higher neuron divergence (number of efferent neurons)

from Rt neurons than TC neurons (Lam et al., 2006). Most of these models were built using single-compartment neuron models which, although being computationally parsimonious and easy to parametrize, neglect the cable properties of biological neurons, synaptic integration and active membrane conductances that contribute to dendritic properties (Connelly et al., 2015, 2017; Herz et al., 2006).

In this thesis, we propose to follow a bottom-up approach which yielded a detailed computational model of neocortical microcircuitry (Markram et al., 2015) to model a rodent thalamic microcircuit constrained and validate with experimental data. These types of models are not built with a specific hypothesis in mind and can reproduce a number of *in vitro* and *in vivo* findings without the need of parameter tuning (Markram et al., 2015; Newton et al., 2019; Nolte, 2019). Since they require as many parameters as possible to be constrained with experimental data, a framework for the systematic manual curation of the neuroscientific literature is necessary, where not only experimental data are annotated, but they are stored along with metadata, such as species, age, experimental condition (O'Reilly et al., 2017). Such frameworks will be very welcome for any neuroscience research project involving large-scale data-driven modelling, since they are the basis for leveraging automated text-mining pipelines for the curation of the literature (Shardlow et al., 2019).

As a first validation, we investigate if the model is able to generate spindle-like oscillations consistent with *in vitro*, *in computo* and recent *in vivo* findings in rodents, without being explicitly built for this purpose. A morphologically and biophysically-detailed model can generate predictions regarding the detailed chemical and electrical connectivity between neurons and provide useful insights into their role in waxing-and-waning network oscillations and other network phenomena. The goal is to dissect which neuronal and circuit mechanisms matter, provide guidance for informed simplifications and highlight which experiments would deepen our understanding of thalamic structure and function. As detailed in the concluding chapter, the model can be extended and used to study other aspects, such as the modulation and interaction between thalamocortical rhythms (e.g. slow-wave oscillations and spindles), the role of different thalamic neurons in the emergence of receptive fields and the role of cortico-reticular-thalamic interactions in attentional-mediated sensory filtering, to mention just a few.

1.3 Thesis outline

In Chapter 2 (“A Framework for literature curation”), we present a framework that allowed us to systematically annotate, store and share data and metadata from the neuroscientific literature. This literature-derived data and knowledge complement experimental data in model building and validations presented in the following chapters. This chapter is a postprint of a joint publication (O'Reilly et al., 2017) (see contributions at the beginning of the Chapter).

In Chapter 3 (“Experimentally-constrained models of thalamic neurons”) we show how an automated pipeline can be used to constrain the parameters of morphologically-detailed single

neuron models with *in vitro* experimental data. This pipeline allowed us to construct a large database of unique morpho-electrical combinations of TC and Rt neuron models, which are the building-blocks of the microcircuit model presented in Chapter 4. This chapter is a postprint of (Iavarone et al., 2019).

In Chapter 4 (“Reconstruction and simulation of thalamic microcircuitry”) we leverage the findings and models from Chapter 2 and Chapter 3 to reconstruct the detailed anatomy and physiology of a large-scale thalamic microcircuit, consisting of ~5000 Rt and ~9000 TC neurons and interneurons. Although it is based on data from the somatosensory thalamic sectors in rodents *in vitro*, we think that this model can be generalized to other thalamic microcircuits. This chapter will be submitted for publication as “Reconstruction and simulation of thalamic microcircuitry”.

Finally, in Chapter 5, we summarize the main contributions of this thesis, the implication of this study for thalamus-related functions and dysfunctions, and delineate future directions.

2 A framework for literature curation

This chapter is a postprint of joint work with Christian O'Reilly and Sean Hill; it has been published as “A Framework for Collaborative Curation of Neuroscientific Literature” in *Frontiers in Neuroinformatics* (O'Reilly et al., 2017), doi:<https://doi.org/10.3389/fninf.2017.00027>.

Contribution: I participated with C.O. in the design of this framework and in the creation of the *corpus* of annotations for thalamic neurons and circuit modelling. I was one the first users of the software before its public release and provided feedback on its usability, bugs and feature requests. I revised and edited the manuscript with SH.

Abstract

Large models of complex neuronal circuits require specifying numerous parameters, with values that often need to be extracted from the literature, a tedious and error-prone process. To help establishing shareable curated corpora of annotations, we have developed a literature curation framework comprising an annotation format, a Python API (NeuroAnnotation Toolbox; NAT), and a user-friendly graphical interface (NeuroCurator). This framework allows the systematic annotation of relevant statements and model parameters. The context of the annotated content is made explicit in a standard way by associating it with ontological terms (e.g., species, cell types, brain regions). The exact position of the annotated content within a document is specified by the starting character of the annotated text, or the number of the figure, the equation, or the table, depending on the context. Alternatively, the provenance of parameters can also be specified by bounding boxes. Parameter types are linked to curated experimental values so that they can be systematically integrated into models. We demonstrate the use of this approach by releasing a corpus describing different modeling parameters associated with thalamo-cortical circuitry. The proposed framework supports a rigorous management of large sets of parameters, solving common difficulties in their traceability. Further, it allows easier classification of literature information and more efficient and systematic integration of such information into models and analyses. Collaborative curation of the literature could be a powerful force driving future modeling endeavors.

2.1 Introduction

In the context of large-scale, highly detailed, and data-driven realistic modeling of the brain, developers are faced with the daunting task of reviewing voluminous, and ever growing, body of scientific papers to extract all information useful in constraining the large number of parameters involved in the modeling process. Without a rigorous approach to support this process, the extracted information is often not reusable outside of the project for which it has been built. Curated information from the literature that has been embedded into models are also often vulnerable to issues regarding the traceability of their origin. This happens for example when the embedding does not provide a means to trace back 1) the publication from which the value has been extracted, 2) the exact place in the paper from where the information has been taken, or 3) the precise method used to transform published numbers into the values inserted into models. The last point is particularly important and applied transformations can take different forms. The most evident is unit conversion. But more subtle alterations are often applied such as changing the nature of the variable (e.g., passing from area to volume by considering hypotheses or supplementary factors, such as using cell counts per area from stereology studies to model neuronal volumetric densities) or combining different measures (e.g., taking the median of values reported by different sources).

In this paper, we present a collaborative framework for systematic curation of literature and creation of annotation corpora that aims at solving these issues. Corpora created through this system can be queried programmatically so that curated literature information can be integrated into modeling workflows in a systematic, reproducible, and traceable way. This paper is the first of a two-paper series and it reports more specifically on the development of an annotation format for scientific literature curation and on the public release of open-access tools to assist in the creation and management of annotation corpora. The presentation of the broader workflow, including the systematic integration of annotated information into modeling pipelines will be discussed in the sequel.

The proposed annotation system has been designed to allow, among other things, systematic annotation of numerical values reported in scientific publications so that experimental outcome can be efficiently synthesized and integrated into models. We demonstrate the usefulness of this approach by presenting an example of an open-access repository of annotations that has been created for modeling the thalamo-cortical loop in the context of the Blue Brain Project.

2.1.1 Terminology

The process of curating or annotating documents or datasets is defined in various ways in different contexts. To avoid confusion, we first define these concepts, as they are used in the current project.

By *literature curation*, we refer to the process in which the curator (i.e., the person performing the curation) identifies documents relevant to a specific topic and annotates (i.e., produces *annotations*) relevant information within these documents. An *annotation* is defined as a structured set of data specifying the precise localization of a subpart of a document which is of strategic interest. It would generally be supplemented with additional information (e.g., ontological terms describing in a formal way some characteristics of the annotated content). It may also contain a free-form comment to make explicit the relevance of the annotation, although such comments can be omitted if the highlighted part of the document is self-explanatory (e.g., "region X is connected to region Y with Z% probability"). Note that this process is significantly different from “annotating” as the (generally automated) process of extracting syntactic (e.g., part-of-speech) or morphological/semantic (e.g., identifying named entities) information from a text.

2.1.2 Requirements

We established a set of requirements that a methodological framework for the curation and model-integration of the literature information should consider. These are presented in subsequent sections.

Collaborative workflow: The approach should allow for collaborative curation of a body of literature, meaning that annotations on a particular document can be made by different curators in a concurrent fashion. It must therefore be possible to easily merge produced annotations and to trace the history of modifications.

Reusable: The result of the curation process should be easily reusable by other researchers. It must therefore not rely on implicit knowledge of the curator. The important information associated with the annotations must be explicitly specified.

Easily machine-readable: The output of the curation process must be easily machine-readable. Although any computer file is “machine-readable”, what makes it easily readable is the use of a consistent formatting (e.g., CSV files, text files containing a well-defined JSON data structure) with fields using a highly consistent terminology (i.e., controlled vocabulary). This terminology should ideally be linked with identifiers from externally recognized entities (e.g., terms from public lexica or ontologies) allowing cross-referencing, indexing, and searching annotations in relation with specific concepts (e.g., species, brain regions, cell types, experimental paradigms). In that sense, free-form text fields are not easily machine-readable and should constitute only a limited part of the annotations.

Localizable: Annotations must be precisely and reliably localizable in the document of origin. This requires the specification of unique identifiers for annotated documents as well as the unambiguous localization, within the document, of the position and the extent of the annotated content.

User-friendly: The process of annotating a document must be as light as possible. The curation process is expected to be performed mainly by domain-experts, which are performing this task as part of other overarching goals. Therefore, it must not be perceived as implying a supplementary workload when compared to a more informal review of the literature. Not meeting this criterion is likely to result in poor user adoption and, consequently, limited use of the proposed framework.

Integration with the existing software ecosystem: The design of the system should rest on well-established existing tools such that its design is simpler, requires less maintenance, and is more sustainable. It should also integrate with existing tools that might be used to produce annotations (e.g., text-mining tools) or to consume annotations (e.g., external user interfaces such as web-based neuroscience portals).

Support for modeling parameters: In order for this curation process to be useful in modeling projects, the proposed tool must provide the features necessary to annotate systematically and unambiguously numerical values reported from experiments.

Respect of legal environment: Annotations should be sharable without involving copyright issues. For example, they cannot be embedded in documents that are copyrighted.

2.1.3 Existing solutions

Many projects have been conducted in the past years to support the annotation process in various contexts. For example, the online annotation service *hypothes.is*, proposes to add a supplementary layer to the Internet so that web pages can be directly annotated and commented (Perkel, 2015). WebAnno (Yimam and Gurevych, 2013) and BRAT (Stenetorp et al., 2012) are other examples of relevant projects but are more targeted along providing web-based collaborative environments for typical natural language processing tasks, such as annotating part-of-speech and syntactic dependencies, identifying named entities, etc. Other research teams have worked on developing pipelines for text-mining and automatic generation of annotation from papers (e.g., WhiteText (French et al., 2015), Sherlock (R. Richardet et al.,

2015)) or on manually annotating in great details corpora of scientific papers (e.g., the CRAFT (Bada et al., 2012) and the GENIA (Kim et al., 2003) corpora) to serve as benchmark in evaluating automated annotators. However, although these initiatives provide interesting tools to support the annotation process, none constitute a complete solution meeting our objectives: to provide an annotation framework which allows the collaborative construction of corpora containing literature-curated facts that can be integrated directly in models. Thus, these projects should not be seen as competitor or alternative to the framework we are proposing. They are more complementary tools, which we aim to interface with, rather than replace.

2.2 Design

2.2.1 Collaborative structure

At the heart of this project is the idea to provide a simple, flexible, and collaborative framework for producing and reproducibly consuming literature annotations. For this reason, each publication is associated with one plain-text file containing the related annotations (i.e., it is a standoff format (Thompson and McKelvie, 1997)), as opposed, for example to a database-centric design or an in-text annotations system. These plain-text files, which structure is discussed in section 2.3, are stored, versioned, and shared through GIT, a free and open-source distributed version control system. Aside from allowing easy sharing of annotation corpora through existing GIT servers (e.g., GitHub), it allows concurrent work on annotations, resolution of merging conflicts, and bookkeeping of modifications. Interaction with the GIT system has been made as transparent as possible to the user (e.g., automatic commit when changes to annotations are saved, dialog box asking if the modifications should be pushed to the server when exiting the application) although the underlying GIT repository can always be accessed directly in case of need.

2.2.2 Ontologies

2.2.2.1 Use of standard ontologies

Annotations are tagged with terms from neuroscience ontologies to describe their context and allow the programmatic retrieval of subsets of annotations relevant to specific modeling or analysis objectives. Further, these tags constitute a direct bridge for interacting with third-party applications using the same ontologies.

However, although promising initiatives such as the Open Biomedical Ontologies (OBO) Foundry (Smith et al., 2007) have been put in place to promote good design practices, standardization, and interoperability, the world of ontologies is still a messy one. Many propositions are available with different, sometimes overlapping, coverage of the concepts

related to neuroscience. Two common problems are the overdefinition of a concept (i.e., the same concept being partly or completely defined by different ontological terms) and its underdefinition (i.e., no ontological term defining completely or specifically a given concept). The first problem arises most acutely when trying to model a large field such as neuroscience by combining different ontologies, whose coverage overlaps (Ghazvinian et al., 2011). The second problem is intrinsic in modeling of an expanding knowledge involving dynamic creation of new concepts.

The proposed curation framework integrates terms from the Knowledge-Space.org (KS) ontologies, which is the successor to the now deprecated Neurolex service (Larson and Martone, 2013) and provides a large coverage of the neuroscience field through the integration of many domain-specific ontologies. It also provides supports for integrating ontological terms from the Neuroinformatics Platform (NIP) of the Human Brain Project since it contains many terms useful for modeling neural networks (e.g., a comprehensive classification of cortical neurons). Integrating the KS and NIP ontologies is complicated by the huge size of these ontologies. This problem has been addressed by storing locally every term previously used, and fetching online new terms whenever required (see supplementary documents section S1.1 for an extended discussion of this issue). Although using both ontologies may contribute to overdefine some terms, this effect is limited since both ontology services reuse third-party ontologies (e.g., the Allen Brain Institute ontology). Interacting with both NIP and KS ontologies is made easy by the fact that they share a very similar REST API (see (O'Reilly) for an IPython Notebook example of programmatic interaction with these ontologies).

2.2.2.2 Definition of new terms

New ontological terms have been defined to complement existing ontologies only when no alternative was available. For example, the nomenclature of ionic currents was not fine-grained enough to be used to model neurons with a detailed electrophysiology like those of the Blue Brain Project (Markram et al., 2015). This use case required completing the existing hierarchy of ionic currents with new terms. In such cases, new terms have been defined in a separate CSV file (*additionsToOntologies.csv*) which is part of the *NeuroAnnotation Toolbox* (described below) source code. Providing such a mechanism for easily adding new terms is important for the flexibility of the system. However, these terms are not meant to constitute a separated ontology and will hopefully, at some point, be migrated toward more standard resources, such as the KS or NIP ontologies.

A more comprehensive effort has been undertaken in developing a controlled vocabulary for Modeling Parameter (MPCV) since no available resource was providing an adequate coverage for the framework proposed herein. Parameter types used here must be defined unambiguously and operationally with a sufficient level of granularity so that their annotated values can be directly used to instantiate model variables. Related ontologies such as the Computational Neuroscience Ontology (Le Franc et al., 2012) could be invaluable in adding a semantic level to the modeling parameters listed in the MPCV. However, they cannot be used directly in place

of the MPCV because they do not currently provide the sufficient level of granularity. The descriptive level required by the proposed framework would be closer to the list of parameters defined in a project like NeuroElectro (Tripathy et al., 2014). However, this list is yet too limited¹ to be directly reused for the use case described here. Further, from a practical point of view, the need of rapidly adding new terms to the MPCV would make the adoption of an external resource very cumbersome in the current phase of development. Thus, for reason of coverage, precision, and flexibility, MPCV terms have been specified directly in the NeuroAnnotation Toolbox source code as a separate CSV file (`modelingDictionary.csv`). Collectively, these terms are defined as a tree structure, which can be visualized online at

<https://github.com/BlueBrain/nat/blob/master/notebooks/parameterTree.png>

2.2.3 Annotation format

To provide an annotation format that is flexible enough to be adapted to future unforeseen needs of the community while remaining simple to read and write, we adopted a JSON serialization approach. Annotations for any given publication are written as a plain-text list of pretty-printed² JSON strings (see Figure 2.5.d for an example). A schema of the structure of an annotation is shown in Figure 2.1 (see (O'Reilly) for a complete definition). In short, it contains mainly unique identifiers for the annotation and the publication, a list of tags, the identity of the authors of the annotation, the version of the annotation format, a free-form comment, a list of modeling parameters, a list of experiment properties, and a localizer. More explanation is given on the nature of some of these items below.

¹ This project currently curates 47 electrophysiological properties. Correspondences between NeuroElectro and MPCV terms have been made explicit in a CSV file (`modelingDictionary_relationships.csv`) part of the NAT code base, pending the restructuration of MPCV in a more formal ontology.

² Pretty-printing and fixed JSON element ordering are not necessary for syntactic validity of the annotation files but allows for better human-readability and, most importantly, it makes the use of GIT to track modifications or resolve merging conflicts much more practical.

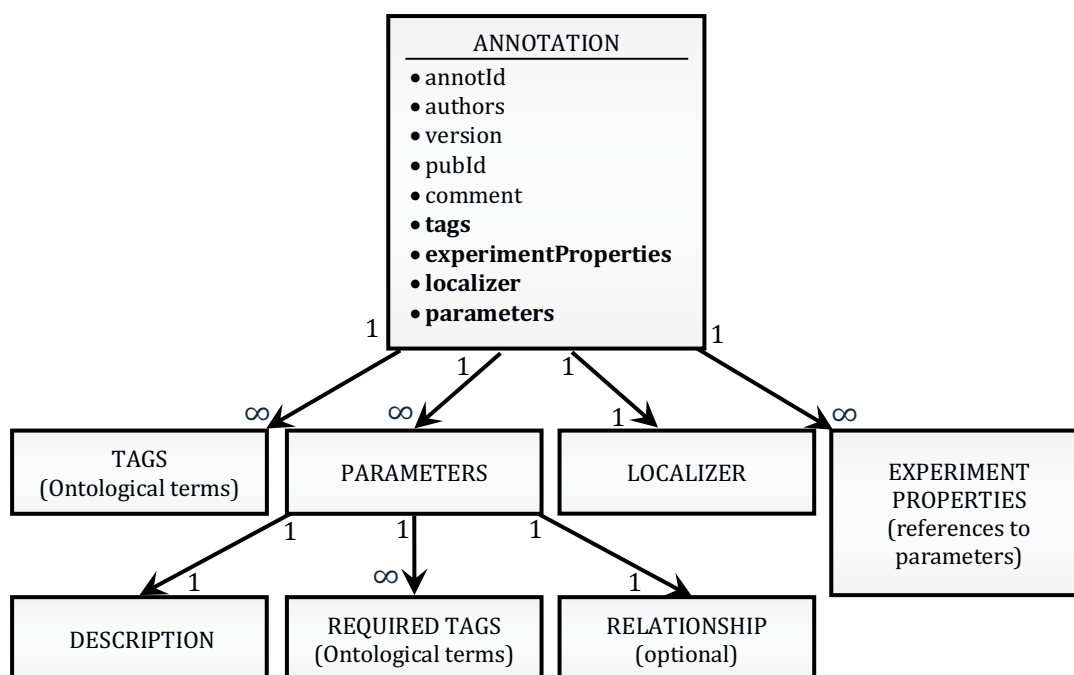


Figure 2.1. High-level schema of the annotation format.

The block at the top of the schema (ANNOTATION) lists as bullet points all the fields of an annotation record. A thin font is used for simple attributes (e.g., strings); a bold font is used for attributes which are themselves complex JSON structures. The hierarchical relationships between the top-level object and its complex attributes are shown by arrows. The internal structure of the lower-level objects (PARAMETERS, LOCALIZER, etc.) has been omitted because both the hierarchical structure and the definition of the objects are context-dependent (e.g., there are 5 different types of LOCALIZER, with different internal structures; the variability of the hierarchical structure is due to compositionality of experimental values, as exemplified in Figure 2.2).

2.2.4 Unique identifiers

Every annotated publication is associated with a unique identifier. For that purpose, we use the DOI whenever one has been attributed to the publication. Otherwise, we set it to "PMID_" followed by the PubMed (NCBI) identification number (PMID) if the paper has been attributed one. Papers that are not referenced by PubMed and that have no DOI cannot be managed by this system. This is not a serious limitation because 1) most relevant papers have a DOI and/or a PubMed ID and 2) DOI numbers can be freely generated by third-party services for research documents that have none (e.g., see (ResearchGate)).

Unique identification numbers are generated on the fly using the `uuid1()` function of Python's `uuid` package and attributed to every annotation and parameter instances.

2.2.5 Tags

Tags are provided using ontological terms, as discussed in section 2.2.

2.2.6 Parameters

Modeling parameters are specified as a list of **PARAMETER** objects (see (O'Reilly) for the format definition) which contains the following elements (described below): a *description*, a list of *required tags*, a *relationship*, and a boolean flag stating whether this parameter is an experimental property (e.g., liquid gap junction potential, temperature, age of the animals) or not. In the description of these different attributes, we will refer to corresponding examples provided in Table S1, provided in supplementary documents. These references will have the following format (Table S1; 1/27-39) to specify the line 27 to 39 of the example of the first row.

Required tags associated with particular types of parameters are defined in the MPCV. They are specified to ensure that a minimal set of information is gathered about annotated parameters, making these annotations more useful for modeling and analyses. For example, the modeling parameter *conductance_ion_curr_max* (i.e., the conductance of the transmembrane ionic flow when all ionic channels related to a particular ionic current are open simultaneously) has the following required tag specification: {"nifext_8054": "Transmembrane ionic current", "sao1813327414": "Cell"}. This means that when the users are annotating values for this type of parameter, they should specify ontological terms for the kind of ionic current and the cell type involved. Both selected terms should be defined in the ontology as children of the "Transmembrane ionic current" and "Cell" terms, respectively (Table S1; 1/27-39). This task is made simple using the NeuroCurator, which automatically populates combo boxes with the available choices.

The *relationship* object is used to specify the entities to which the parameter is related. It can be left undefined, or be specifying a single entity (e.g., an ion current type for a maximal conductance parameter; Table S1; 1/19-23), two entities linked by a directed relationship (e.g., the strength of connectivity from one type of cell to another type of cell; Table S1; 3/26-36) or an undirected relationship (e.g., the correlation of the activity of two brain regions; Table S1; 2/41-51).

Parameter *descriptions* are associated with a specific type of modeling parameter (e.g., the conductance of the leak sodium channels), taken from the list of MPCV terms. They can be defining three types of data: *numerical traces*, *functions*, and *point values*.

Numerical traces are used to specify a set of values for an independent variable (e.g., inactivation time constant) which are associated with values of a dependent variable (e.g., membrane potential) (Table S1; 5/2-37).

The *function* data type is needed to save parameter values when they are obtained by fitting some analytical function to experimental recordings. For example, two parameters ($V_{1/2}$ and k) are needed to model the steady-state inactivation of a class of ion channels by fitting experimental values to a simple Boltzmann function

$$f = 1 / \{1 + \exp((V - V_{1/2}) / k)\}$$

where V is the membrane potential, $V_{1/2}$ is the membrane potential at $f = 0.5$, and k is a slope factor (Martina and Jonas, 1997). In such a case, reporting values for $V_{1/2}$ and k makes sense only if they are associated with the expression of the modeling function f . These relationships are preserved by the *function* data type (Table S1; 4/2-28).

Point values are used for parameters that are not part of a functional relationship or of a numerical trace (e.g., resting membrane potential; Table S1; 1/3-15).

Further, any value encapsulated in these data types (i.e., *numerical trace*, *function*, and *point value*) can be either specified as a simple value or a compound value. Compound values are aggregates of simple values which are logically related such as X , Y , and Z in “ $X \pm Y$ ($N=Z$)”, where X is typically a sample mean value, Y its standard error, and Z the size of the sample (e.g., “[...] input resistance (**55 ± 19MΩ; n = 94**), resting membrane potential (**-60 ± 4 mV; n = 67**), and spike amplitude (**64 ± 7mV; n = 80**) are similar to those of LGN relay neurons [...]” in (Li et al., 2003); also see Table S1; 2/5-34 for another example of compound values). These X , Y , and Z values must be saved together since they form an interdependent set of statistics such that, for example, Y (a standard error around the mean) is meaningless if reported alone, without X (the mean) and Z (the sample size used to compute the standard error). Finally, simple values can be either “raw” values (i.e., the default category; e.g., the value 5 in “the peak conductance density for the non-inactivating K^+ current was chosen to be 5 pS/μm².” (Haeusler and Maass, 2006) is a “raw” value in the sense that it is not a statistical computed from a sample) or some statistics (e.g., mean, median, standard deviation, maximum, etc.; see also Table S1; 2/8-12 for an example of a annotation of a mean value) and they are always specified as lists of floating point values with one or more items depending on the availability of single or repeated measures. This complex hierarchical encapsulation of value types is illustrated in Figure 2.2.

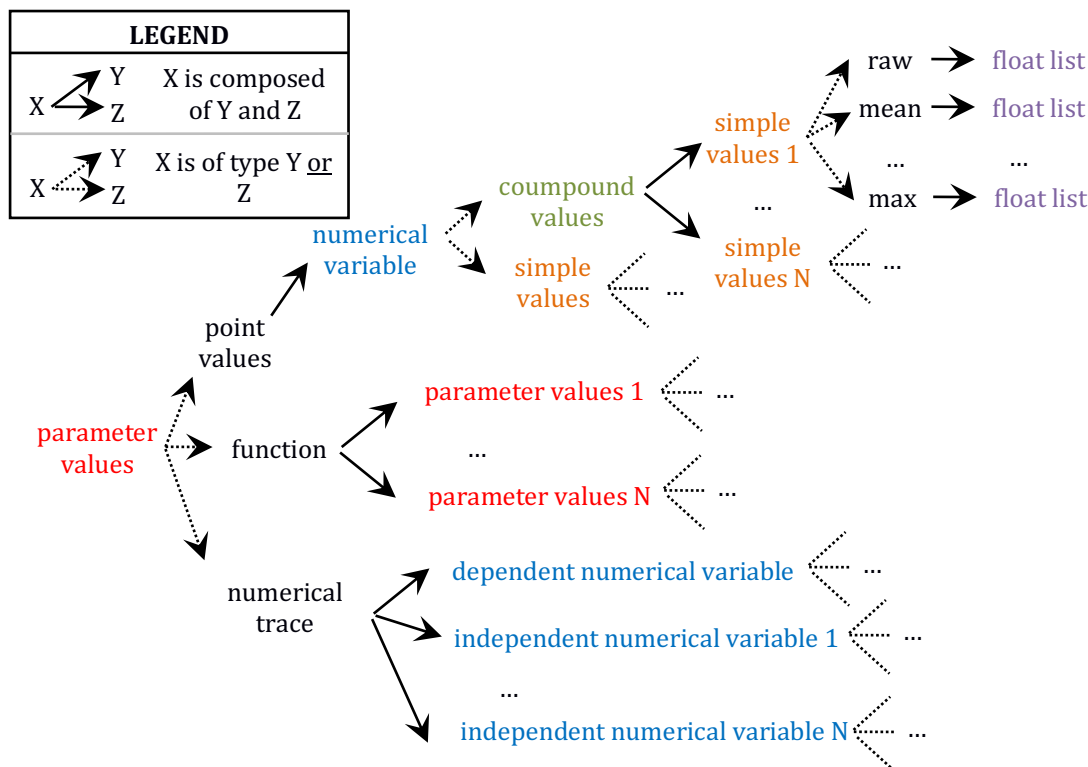


Figure 2.2. Schema of the hierarchy of data type encapsulation.

Different types of data are color coded. Only the upper branch of this recursive tree is completely defined. For example, the whole tree starting at “parameter values” would need to be reproduced at “parameter values 1”, the whole tree of “numerical variable” would need to be reproduced at “dependent numerical variable”, etc.

Annotated values should be identical to published numbers and should not be transformed in any ways. Values are saved alongside with their unit (as specified in the paper) and are checked for consistency using Python’s *quantities* package.

2.2.7 Experimental properties

Annotated parameters can be marked as experimental properties so that they can be associated with other annotations to specify the experimental context. For example, an annotation defining a “slice_thickness” parameter can be associated as an experimental property of a second annotation specifying a “neuron_density” parameter in mm^{-2} (e.g., evaluated with the dissector method). Such an association allows, before integrating this density to a model, to convert its value from a surface density (published value) to a volume density (value needed for modeling) by dividing the annotated “neuron_density” per the “slice_thickness” used for the counting procedure.

Note that two different types of information define the complete experimental context: categorical (through tagging; e.g., “Wister rat”) and numerical (through annotated parameters marked as experimental properties; e.g., age = 14 days).

2.2.8 Localizer

Various ways to localize annotations are provided to account for the different use cases. A *text* type of annotation is defined by a segment of text and the exact position (specified as the character number) where it starts in the curated document. To provide an unambiguous localization, the publication PDF is first parsed to generate a corresponding plain-text file, which is kept as a reference (see supplementary documents section S1.3 for details). To preserve the reliability of annotation localization, once created, this file should never be changed or replaced. For that reason, this localization key is saved centrally on a server (see supplementary documents section S1.2 for copyright issues related with sharing this key with clients).

In general, if the information to annotate is contained in a figure, a table, or an equation, these can be entered using the respective annotation type and specifying the respective number. These numbers are encoded as strings rather than integers to allow more flexibility for the different use cases (e.g., “1”, “1.c”, “III”, “from 4 to 10”, “1, upper-left panel”). For tables, the user can also specify a row and a column number, if those are not ambiguous (i.e., row and column numbers are not ambiguous when the shape of the table is such that it could be represented as a matrix). Finally, the *position* type is provided for situations where all other types are not appropriate. This can be the case, e.g., if the curator wants to annotate a very specific portion of a figure. These annotations are specified by the number of the page and the coordinate of a bounding box encompassing the content to be annotated. These are specified on the reference PDF file³. These are freely accessible for open access publications. For copyrighted material, access is granted only to users who have demonstrated that they already own a copy of the paper (see supplement document sections S1.2 and S1.3 for more information).

³ Although PDF versions of publications are fairly consistent, some sources add for example front pages. Alternative versions may also include supplementary documents or not. Different scanning of a same paper may have different alignments due, for example, to different page format at scanning time. For all these reasons, it is important to provide a consistent reference version of publication PDFs.

2.2.9 Zotero library

The proposed architecture integrates a citation database synchronized with a Zotero library (www.zotero.org). This citation management software has been chosen because it is free, cross-platform, and open-source. It is maintained by a University center (Roy Rosenzweig Center for History and New Media from George Mason University) and it offers a convenient Python API. Using Zotero allows integrating this framework more naturally with the existing software environment and avoid creating custom solutions for features already well covered by existing software. For the creation of our corpus described in section 3, collaborative curation work was promoted by synching with a group library.

2.2.10 Global software infrastructure

The complete system is composed of a few components: a front-end (NeuroCurator), a back-end (NeuroAnnotation Toolbox; NAT), a RESTful service for managing localization keys, RESTful ontology services (KS and NIP), the Zotero server for centralizing the citation library, and a GIT server for versioning the annotation corpus. This architecture is depicted in Figure 2.3.

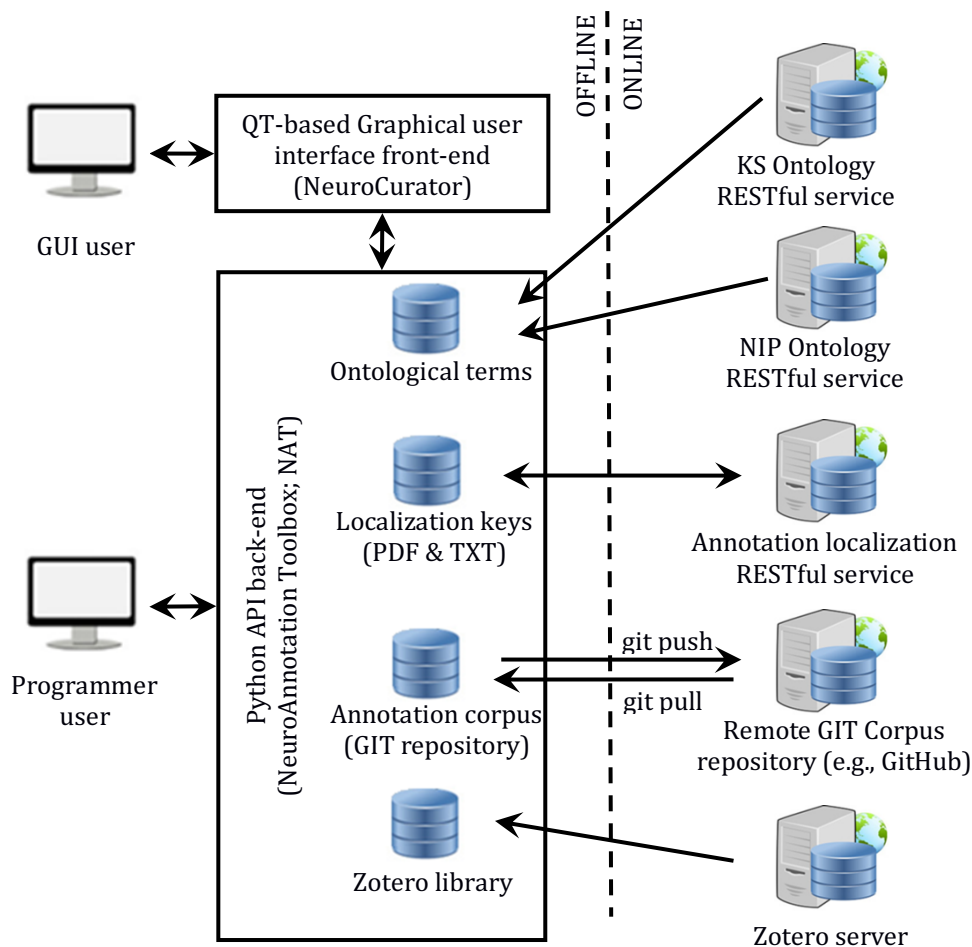


Figure 2.3 Software infrastructure proposed for literature curation.

Constitution and consultation of annotation corpora can be made either through a user-friendly graphical interface (NeuroCurator) or programmatically in Python using the NAT package. Both the NeuroCurator and the NAT package can be used offline. They require connectivity only when new resources (i.e., not already stored locally) are needed or for synching the local GIT version of the corpus with a remote one.

2.2.11 User interface

A graphical user interface (GUI) named NeuroCurator has been created as a front-end to provide all the functionalities required for a flexible and efficient curation process. It is coded using *PySide* (Python bindings for *QT*, a cross-platform C++ toolbox for creating GUIs). It allows displaying the publications contained in the Zotero library (Figure S1), to create new annotations, visualize or modify existing ones, associate tags to annotations by selecting ontological terms from those stored locally or by searching the ontologies online (Figure S2), to annotate new modeling parameters (Figure S3), and to search for annotations in the corpus according to flexible user-defined queries (Figure S4). The development of the NeuroCurator is an ongoing project and the main objective is to provide an efficient and enjoyable user experience to stimulate the adoption of this framework by the community.

The code of the NeuroCurator has been separated from the back-end, which constitute a Python package named NeuroAnnotation Toolbox (NAT). This separation allows interacting with annotation corpora programmatically (e.g., from an IPython Notebook) without having to install the NeuroCurator and its dependencies.

The front-end supports creating annotations using the full expressiveness of the annotation format described previously. Specifically, concerning the localization of the annotations, a citation can be localized by pasting a snippet of text and clicking on the “Localize” button. This searches for corresponding text and proposes options to the user if more than one similar text is found in the document. For localization according to position in the PDF, the interface allows the user to specify the region of interest by drawing a bounding box over any page of the PDF. For the other types of annotations, the user has to specify it as plain text (i.e., number of the figure, table or equation). The graphical interface does not allow yet to visualized annotated information overlaid on the PDF. Implementation of such a functionality using a third-party PDF viewer is planned.

2.3 Case study: corpus of annotation for the modeling of the thalamo-cortical loop

2.3.1 The corpus

An example of annotation corpus is already available on GitHub (see Table 1). At the moment of writing, this corpus was containing 435 manually made annotations and 257 annotated parameters from 80 different publications. This corpus is centered on the biologically detailed modeling of the thalamo-cortical loop for the somatosensory cortex of the rat. It is an ongoing curation task in the context of the Blue Brain Project. A histogram showing the number of annotated parameters for the 30 most annotated parameter types is shown on Figure 2.4. A Jupyter notebook has been included to the code base the NAT project, which allows to compute and show an up-to-date version of these information

(https://github.com/BlueBrain/nat/blob/master/notebooks/Status_thalamus_corpus.ipynb).

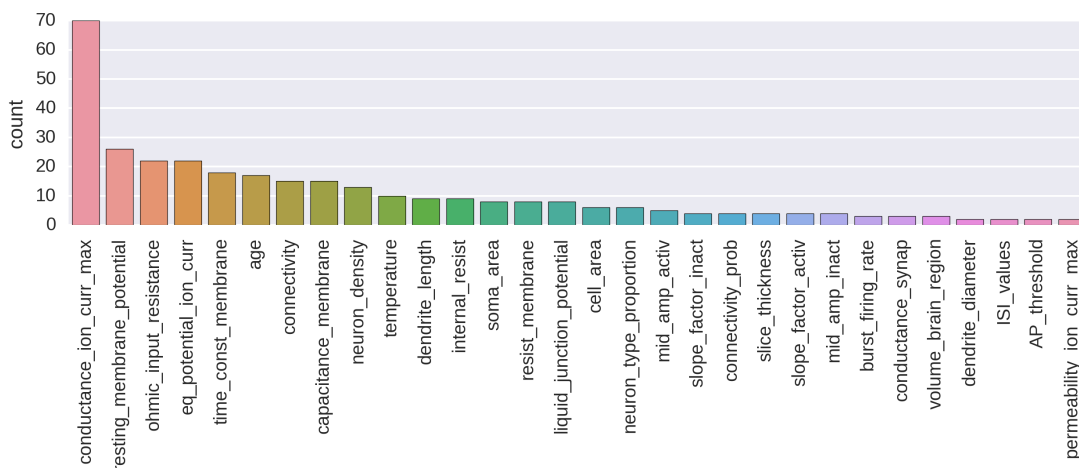


Figure 2.4. Histogram showing the number of annotated parameters for the 30 most annotated parameter types.

2.3.2 First example: ion channel conductance in neuron models

Figure 2.5 gives an example of how NAT can be used to interact programmatically with a corpus. Figure 2.5.a first shows how to get a local copy of the corpus described in section 3.1 by performing a “git clone” operation through Python. Then, it describes how to search for values of a specific parameter and visualize the corresponding data. In this particular example, we are querying for all annotated values of maximal ionic conductance and plot those that are defined as specific conductance only (i.e. conductance normalized by area of cell membrane). The Figure 2.5.b illustrates the resulting violin plot, separating annotated values per type of

ionic currents. The code in Figure 2.5.c shows how to get a specific annotation and print its JSON representation (see Figure 2.5.d for the output). Finally, the code in Figure 2.5.e demonstrates how to display this annotated content in its context. In this case, it is a *text* annotation so its context is defined by the surrounding text. Figure 2.5.f shows the output: the annotated text displayed in bold, surrounded by the 400 preceding and following characters. The complete Jupyter notebook reproducing this example can be consulted online (O'Reilly).

```
# Standard imports
import sys, os
import matplotlib.pyplot as plt
import seaborn as sns
import quantities as pq
import numpy as np
from git import Repo

# NAT imports
from nat.annotationSearch import ParameterSearch, ConditionAtom

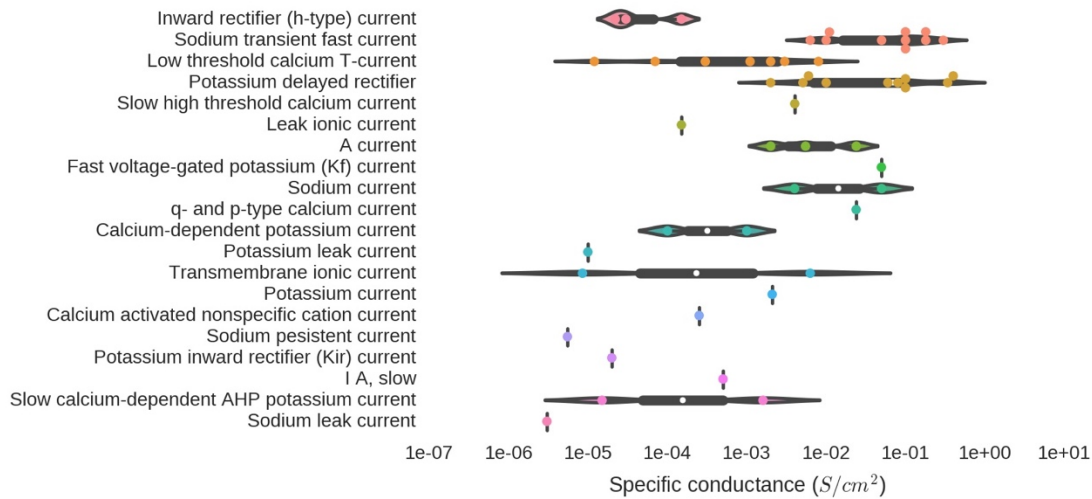
# Downloading the corpus
git_url = "https://github.com/BlueBrain/corpus-thalamus.git"
repo_dir = os.path.join(os.getcwd(), "neurocuratorDB")
Repo.clone_from(git_url, repo_dir)

# Searching for annotated maximal ionic current conductances
searcher = ParameterSearch(repo_dir)
searcher.setSearchConditions(ConditionAtom("Parameter name", "conductance_ion_curr_max"))
searcher.expandRequiredTags = True
searcher.onlyCentralTendency = True
resultDF = searcher.search()

# Checking which conductances have been specified as "specific conductances" (i.e.,
# conductance densities) and normalizing the units.
isSpecific = []
allConductances = []
for v, u in zip(resultDF["Values"], resultDF["Unit"]):
    try:
        allConductances.append(float(pq.Quantity(v, u).rescale('S/cm**2')))
        isSpecific.append(True)
    except:
        isSpecific.append(False)
resultDF = resultDF[isSpecific]
resultDF["Values"] = np.log10(allConductances)

# Plotting a violin plot for annotated values for specific conductances
# of the various kind of ionic currents
g = sns.violinplot(y="Transmembrane ionic current", x="Values", data=resultDF, bw=0.25)
g = sns.swarmplot(y="Transmembrane ionic current", x="Values", data=resultDF)
g.set_ylabel("")
g.set_xlabel("Specific conductance ($S/cm^2$)")
g.set_xticklabels(['%.0e' % 10**nb for nb in g.get_xticks()])
plt.plot()
plt.savefig('example_currents.png', bbox_inches='tight', transparent=True, dpi=200)
```

(a)



(b)

```
import json
record = resultDF[resultDF["Transmembrane ionic current"] ==
                    "Fast voltage-gated potassium (Kf) current"]
print(json.dumps(record["obj_annotation"].values[0].toJSON(),
                  sort_keys=True, indent=4, separators=(',', ': ')))
```

(c)

```
{
  "annotId": "8e3edae6-ef34-11e5-ba5d-c869cd917532",
  "authors": [
    "iavarone",
    "oreilly"
  ],
  "comment": "Fast potassium current parameters",
  "experimentProperties": [],
  "localizer": {
    "location": 26404,
    "text": "The gKIR and the\nfast voltage-gated potassium channel ( gKf) had\nconductances of 20 \u0002s/\ncm2 and 50 mS/cm2, respectively. Both\npotassium channels had reversal\npotentials of 100 mV.",
    "type": "text"
  },
  "parameters": [
    {
      "description": {
        "depVar": {
          "typeId": "BBP-030003",
          "values": {
            "statistic": "raw",
            "type": "simple",
            "unit": "mS/cm^2",
            "values": [
              50.0
            ]
          }
        }
      },
      "type": "pointValue"
    },
    {
      "id": "e47c93ba-ffdc-11e5-8b78-64006a4c56ef",
      "isExperimentProperty": false,
      "requiredTags": [
        {
          "id": "BBP_nlx_0020",
```

```

        "name": "Fast voltage-gated potassium (Kf) current",
        "rootId": "nifext_8054"
    },
    {
        "id": "NIFCELL:nifext_41",
        "name": "Thalamocortical cell",
        "rootId": "sao1813327414"
    }
]
},
{
    "description": {
        "depVar": {
            "typeId": "BBP-011001",
            "values": {
                "statistic": "raw",
                "type": "simple",
                "unit": "mV",
                "values": [
                    -100.0
                ]
            }
        },
        "type": "pointValue"
    },
    "id": "e47c95c2-ffdc-11e5-8b78-64006a4c56ef",
    "isExperimentProperty": false,
    "requiredTags": [
        {
            "id": "BBP_nlx_0020",
            "name": "Fast voltage-gated potassium (Kf) current",
            "rootId": "nifext_8054"
        },
        {
            "id": "NIFCELL:nifext_41",
            "name": "Thalamocortical cell",
            "rootId": "sao1813327414"
        }
    ]
}
],
"pubId": "10.1523/JNEUROSCI.2740-15.2015",
"tags": [
    {
        "id": "NIFINV:birnlex_2300",
        "name": "Computational model"
    },
    {
        "id": "NIFCELL:nifext_46",
        "name": "Thalamus interneuron small"
    },
    {
        "id": "NIFORG:birnlex_160",
        "name": "Rat"
    }
],
"version": "1"
}

```

(d)

```

nbContextChar = 400
context = record["obj_annotation"].values[0].getContext(nbContextChar)
from IPython.display import HTML
HTML(context[:nbContextChar] + '<b>' + context[nbContextChar:-nbContextChar]
      + '</b>' + context[-nbContextChar:])

```

(e)

st. Thus, our final model comprised the following: gLEAK was modeled with a reversal potential of X79 mV and conductance of 150 μ S/cm², and gH had a reversal potential of X45 mV and peak conductance of 150 μ S/cm². T-type Ca²⁺ channels (gT) were modeled with a reversal potential of 120 mV and a permeability of 0.7 μ m/s. The gCAN had a conductance of 250 μ S/cm² and reversal potential of X20 mV. **The gKIR and the fast voltage-gated potassium channel (gKf) had conductances of 20 μ S/cm² and 50 mS/cm², respectively. Both potassium channels had reversal potentials of X100 mV.** The gNa had conductance of 50 mS/cm² and reversal potential of 50 mV. Throughout this manuscript, when referring to the ability of gT to provide current, we use the term "conductance" rather than "permeability." Whereas the model is in actuality based on permeability rather than conductance, we use this naming convention to simplify the text. Simulations were solved with a fixed time step of

(f)

Figure 2.5. Example of ion channel conductances annotation

(a) Python code to query the corpus and plotting maximal conductances for various ionic currents. (b) Resulting set of violin plots showing the distribution of maximal conductances of ionic currents annotated in the corpus. (c) Querying for the annotation of a specific point in the plot. (d) JSON representation of the corresponding annotation. (e) Query to get the annotated text within its context. (f) Localized text in its context (in this case, 400 characters before and after the annotated text).

2.3.3 Second example: neuron densities from stereological studies

In this second example, we are interested in collecting all the information about neuron densities annotated from stereological studies and express them in a homogeneous format so that they can be integrated in a modeling processes. Skipping corpus download and package imports (see (O'Reilly) for the complete and executable notebook related to this example), Figure 2.6.a shows how to query the corpus to obtain the values for the "neuron_density" parameter and Figure 2.6.b shows an extract of the *resultDF* table. As can be seen in this tables, units are not homogeneous (mm^{-2} and μm^{-3}). Figure 2.6.c shows how these units can be normalized, using when necessary the annotated slice thickness to transform from area to volume. In the same table, we can see that the values are also specified in a heterogeneous way. The first and fourth rows of the extract show two annotations that are actually numerical traces. In total, in the current corpus, there are three such annotations of cell densities. Corresponding numerical traces can be plotted as shown in Figure 2.6.d (code) and 2.6.e (resulting plots). Also, other parameters specify compound values (row 2 and 3 in Figure 2.6.b) as mean \pm standard error (N=sample size). To homogenize these different value formats, we interpolate numerical traces to obtain densities at 14 days old (supposing that this is the age of the rat brain we want to model) and take only the mean of compound values (see code in Figure 2.6.f). The resulting table (see Figure 2.6.g for an extract) now contains parameters that are

homogeneous in units and values, making them appropriate for integration into a model of a rat⁴ thalamus with different cell types and brain regions.

```
searcher = ParameterSearch(pathDB="neurocuratorDB")
searcher.setSearchConditions(ConditionAtom("Parameter name", "neuron_density"))
searcher.expandRequiredTags = True
searcher.onlyCentralTendency = True
resultDF = searcher.search()
resultDF["Species"] = [tag[0].name for tag in resultDF["Species"]]
resultDF["Values"] = [param.valuesText() for param in resultDF["obj_parameter"]]
```

(a)

Cell	Regional part of brain	Values	Unit
Thalamic reticular nucleus	Thalamic reticular nucleus	[142.9, 178.5, 185.1, 215.8] +/- [17.3, 26.4, ...	mm ⁻²
cell - GABAergic			
Thalamus relay cell	Lateral geniculate body	246.8 +/- 38.9 (n=5)	mm ⁻²
Thalamus interneuron small	Ventral posteromedial nucleus	13.3 +/- 0.6 (n=5)	mm ⁻²
Thalamus relay cell	Ventral posterior nucleus	[0.0002782, 0.0001703, 8.88744e-05, 5.1258...	um ⁻³
...

(b)

```
paramGetter = ParameterGetter(pathDB="neurocuratorDB")
values = []
units = []

def rescale2DStereo(paramID, thicknessValue=1.0, thicknessUnit="um", desiredUnit="mm^-3"):
    density = paramGetter.getParam(paramID)
    thickness = pq.Quantity(thicknessValue, thicknessUnit)
    return (density/thickness).rescale(desiredUnit)

for param, annot, (index, row) in zip(resultDF["obj_parameter"],
                                     resultDF["obj_annotation"],
                                     resultDF.iterrows()):
    try:
        param = param.rescale("mm^-3")
    except ValueError:
        thicknessInstanceId = [param.instanceId for param in annot.experimentProperties
                              if getParameterTypeNameFromID(param.paramTypeId) ==
                              "slice_thickness"]

        if len(thicknessInstanceId) == 1:
            thicknessParameter = paramGetter.getParam(thicknessInstanceId[0])
            if len(thicknessParameter.values) == 1:
                param = rescale2DStereo(param.id, thicknessValue=thicknessParameter.values[0],
                                         thicknessUnit=thicknessParameter.unit,
                                         desiredUnit="mm^-3")

        units.append(param.unit)
        values.append(param.valuesText())
        resultDF.loc[index, "obj_parameter"] = param

resultDF["Values"] = values
resultDF["Unit"] = units
resultDF = resultDF[resultDF["Unit"] == "1/mm**3"]
```

(c)

⁴ Not shown here is the fact that all these annotations are associated with “rat” ontological terms.

```

def getFigTrace(param, title="", xlim=None, context=None, index=0):
    if context is None:
        fig, axes = plt.subplots()
    else:
        fig, axarr = context
        if isinstance(axarr, collections.Iterable):
            axes = axarr[index]
        else:
            axes = axarr

    axes.plot(param.indepValues[0], param.means, "-o")
    if not xlim is None:
        axes.set_xlim(xlim)
    else:
        axes.set_xlim([min(param.indepValues[0]) -2.5, max(param.indepValues[0])+2.5])

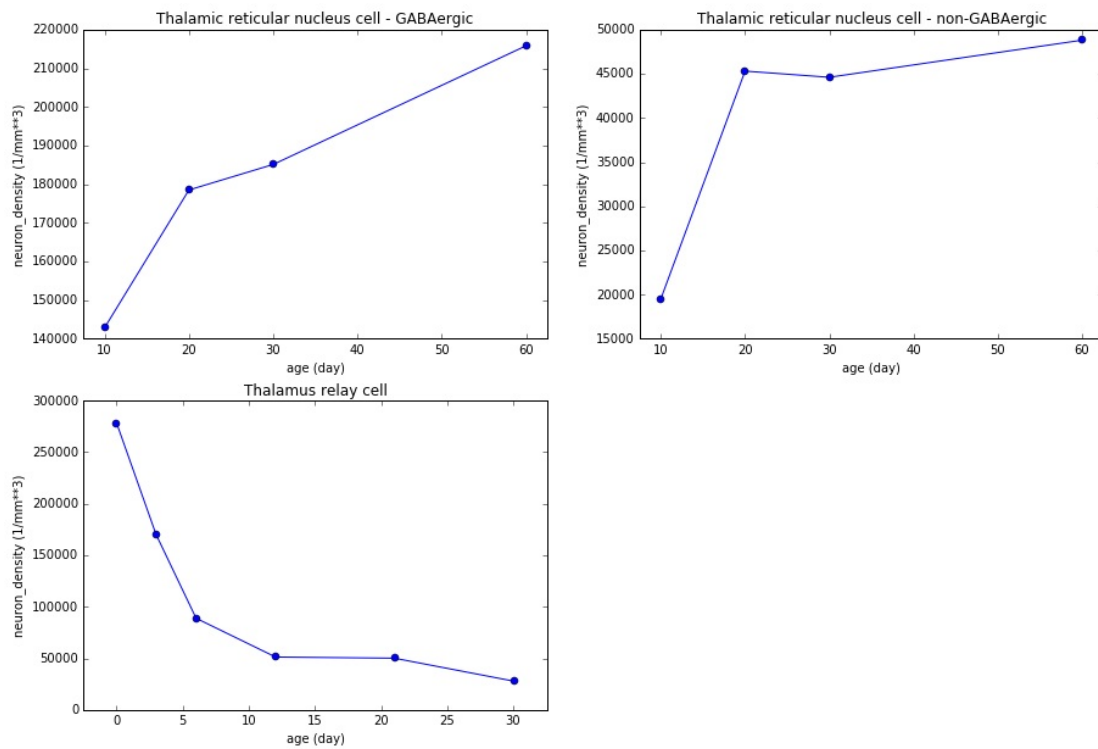
    axes.set_ylabel(param.name + " (" + param.unit + ")")
    axes.set_xlabel(param.indepNames[0] + " (" + param.indepUnits[0] + ")")
    axes.set_title(title)
    return fig

paramTraces = resultDF[resultDF["Result type"] == "numericalTrace"]["obj_parameter"].values
cellTypes = resultDF[resultDF["Result type"] == "numericalTrace"]["Cell"].values

context = plt.subplots(2, 2, figsize=(15, 10))
for no, (paramTrace, cellType) in enumerate(zip(paramTraces, cellTypes)):
    fig = getFigTrace(paramTrace, title=cellType, context=context,
                      index=(int(no/2), no%2))
context[1][1, 1].axis("off")

```

(d)



(e)

```

finalValues = np.zeros((len(resultDF["Result type"])))
for ind, (paramTrace, resType) in enumerate(zip(resultDF["obj_parameter"],
                                                resultDF["Result type"])):
    if resType == "numericalTrace":
        val = paramTrace.getInterpldValues(14, statsToReturn=["mean"])
        if isinstance(val, list):
            val = val[0]
        finalValues[ind] = float(val)

```

```

for ind, (param, resType) in enumerate(zip(resultDF["obj_parameter"], resultDF["Result
type"])):
    if resType != "numericalTrace":
        finalValues[ind] = np.mean(param.means)

resultDF["Values"] = finalValues

```

(f)

Cell	Regional part of brain	Values	Unit
Thalamic reticular nucleus cell - GABAergic	Thalamic reticular nucleus	157140	1/mm**3
Thalamus relay cell	Lateral geniculate body	246800	1/mm**3
Thalamus interneuron small	Ventral posteromedial nucleus	13300	1/mm**3
Thalamus relay cell	Ventral posterior nucleus	51011.02	1/mm**3
...

(g)

Figure 2.6. Example of cell densities annotation.

(a) Code to list annotated neuronal densities. (b) Extract of the resulting table from (a). (c) Code to rescale to mm^{-3} unit (applying 2D to 3D transformation using slice thickness whenever appropriate) and to keep only the annotations that could successfully be rescaled. (d) Code to display the three annotations that are specified as numerical traces. (e) Resulting plots from (d). (f) Code for keeping only the values interpolated at 14 days old for numerical traces and only the mean for compound values. (g) Resulting table from (f), which displays homogeneous values and units.

2.4 Availability

This project aims at promoting collaborative literature curation and reproducible integration of literature information into neuronal modeling pipelines and analyses. Accordingly, the resources described in this paper are all open-access. Table 2.1 list location of the different resources.

	Resource	Location
1	NeuroAnnotation Toolbox	https://github.com/BlueBrain/nat
2	NeuroCurator application	https://github.com/BlueBrain/neurocurator
3	Thalamo-cortical loop annotation corpus	https://github.com/BlueBrain/corpus-thalamus
4	REST end-point for annotation localization	http://bbpca063.epfl.ch:5000/neurocurator/api/v1.0/
5	Documentation of the REST API for the NIP ontology*	https://collab.humanbrainproject.eu/#/collab/47/nav/7267
6	REST end-point for the NIP ontology*	https://nip.humanbrainproject.eu/api/scigraph/

7	Documentation of the REST API for the KS ontology*	http://matrix.neuinfo.org:9000/scigraph/docs/
8	REST end-point for the KS ontology*	http://matrix.neuinfo.org:9000/scigraph/

Table 2.1. List of key open-access resources constituting the annotation framework.

* These resources are not under the responsibility of the authors, but are used as external services by the infrastructure.

2.5 Discussion

2.5.1 A better literature curation for a more integrated knowledge in neuroscience

The study of neuroscience is challenged by the extreme complexity of the brain functioning, the broad spectrum of expertise required to pull together all the evidences from different fields, and the wide range of scales involved in understanding the mechanisms at play. This often results in different research threads being performed *in silo* (i.e., in parallel, without synergy), with too little cross-scale and cross-discipline integration of the knowledge. At the same time, all the efforts invested in understanding how the brain works have resulted in an explosion of both the amount of experimental data produced and the size of the published literature. This can be seen as a curse if no infrastructure is put in place to manage this big data, or it can be turned into a blessing if *a contrario* tools and methodologies are adopted to integrate this knowledge synergistically. To contribute into this direction, we have developed a framework that supports collaborative curation of literature so that corpora of relevant facts and experimental values can be built and shared across brain modeling projects. All the tools developed in this project are open-access. They are and will continue to be in heavy development as they are part of the large-scale modeling endeavor being conducted within the Blue Brain Project. Contributions from the community in the form of feedback, constructive criticism, code patches or extensions are most welcome.

2.5.2 Limitations

There is a real challenge in developing a literature annotation framework that captures the different kind of data published in the literature (e.g., see section 2.3.3), and yet to provide some means to homogenize them in a format that is usable in modeling (e.g., see the example of section 3.2.2), without losing traceability. In the development of this annotation framework, the focus has been placed on capturing faithfully the variability. There is still a need for developing a more comprehensive set of routines for homogenizing the annotated data into a consumable form for the different modeling requirements.

The current framework also misses a systematic support for cross-referencing between publications, for example to capture in a formal way (as opposed to a free-form comment) the normalization of a parameter annotated in one paper by a factor annotated in a second paper.

Finally, ontologies have been embedded in this annotation framework mainly as controlled vocabularies used for systematic tagging. Semantically richer possibilities (e.g., adding more complex ontological constructs involving relationships between entities of an annotated text) was out of our scope. On a related topic, the MPCV created for this work could arguably be improved and made into a stand-alone ontology development project following OBO Foundry's principles.

2.5.3 Future directions

This paper is the first of a two-paper series. In the second paper we will discuss how created corpora can be integrated into modeling workflows to support a reproducible and traceable use of literature information. It is also in our future goals to better connect this framework with existing tools, either by interfacing them as producers (i.e., integrating annotations made by other software such text-mining applications or with different annotation interfaces such as *hypothes.is*) or as consumer (i.e., publishing curated information in third-party portals such as *knowledge-space.org*). The resources necessary to address the limitations described previously will be invested depending on the evolution of the needs expressed by the neuroscientific community.

Supplementary material

The Supplementary Material for this article can be found online at:

<http://journal.frontiersin.org/article/10.3389/fninf.2017.00027/full#supplementary-material>

3 Experimentally-constrained models of thalamic neurons

This chapter is a postprint of joint work with Jane Yi, Ying Shi, Bas-Jan Zandt, Christian O'Reilly, Werner Van Geit, Christian Rössert, Henry Markram, Sean L Hill; it has been published as “Experimentally-constrained biophysical models of tonic and burst firing modes in thalamocortical neurons in *PLOS Computational Biology* (Iavarone et al., 2019), doi: <https://doi.org/10.1371/journal.pcbi.1006753>.

Contribution: I integrated the experimental data provided by JY and YS for building and validating the neuron models. I built a pipeline going from the experimental data to model validation for thalamic neurons and sensitivity analysis, building on previous work from WVG, CR, BZ. I ran all the neuron parameter optimizations, analysis and generate the figures, wrote the first draft of the manuscript and integrated feedback from all the other authors. HM and SLH supervised the study.

Abstract

Somatosensory thalamocortical (TC) neurons from the ventrobasal (VB) thalamus are central components in the flow of sensory information between the periphery and the cerebral cortex, and participate in the dynamic regulation of thalamocortical states including wakefulness and sleep. This property is reflected at the cellular level by the ability to generate action potentials in two distinct firing modes, called tonic firing and low-threshold bursting. Although the general properties of TC neurons are known, we still lack a detailed characterization of their morphological and electrical properties in the VB thalamus. The aim of this study was to build biophysically-detailed models of VB TC neurons explicitly constrained with experimental data from rats. We recorded the electrical activity of VB neurons ($N = 49$) and reconstructed morphologies in 3D ($N = 50$) by applying standardized protocols. After identifying distinct electrical types, we used a multi-objective optimization to fit single neuron electrical models (e-models), which yielded multiple solutions consistent with the experimental data. The models were tested for generalization using electrical stimuli and neuron morphologies not used during fitting. A local sensitivity analysis revealed that the e-models are robust to small parameter changes and that all the parameters were constrained by one or more features. The e-models, when tested in combination with different morphologies, showed that the electrical behavior is substantially preserved when changing dendritic structure and that the e-models were not overfit to a specific morphology. The models and their analysis show that automatic parameter search can be applied to capture complex firing behavior, such as co-existence of tonic firing and low-threshold bursting over a wide range of parameter sets and in combination with different neuron morphologies.

3.1 Introduction

Thalamocortical (TC) neurons are one of the main components of the thalamus and have been extensively studied *in vitro* and *in computo*, especially in first order thalamic nuclei in different species (Sherman, 2007). One of these nuclei, namely the ventral posterolateral nucleus (VPL), relays somatosensory, proprioceptive, and nociceptive information from the whole body to the somatosensory (non-barrel) cortex (Francis et al., 2008). The VPL is located close to ventral posteromedial nucleus (VPM), which transmits information from the face to the barrel cortex. The VPL and VPM nuclei constitute the ventrobasal (VB) complex of the thalamus (Jones, 2007).

Despite its key role in sensory functions, a systematic characterization of the cellular properties of the VB complex is still missing. The morphologies of VPL neurons in adult rats were described in early anatomical studies but were limited to two-dimensional drawings of Golgi-impregnated cells (McAlliser and Wells, 1981). The general electrical properties of TC neurons maintained *in vitro* are known and similar in different thalamic nuclei and species with respect to the generation of two distinct firing modes, called tonic firing and low-threshold bursting (Llinás and Jahnsen, 1982; Jahnsen and Llinás, 1984; Turner et al., 1997; Connelly et al., 2017). However, a systematic description on the electrical types in the VB thalamus in the rodents is still missing.

Collecting morphological and electrophysiological data, by following standardized experimental procedures, is essential for the definition of cells types and it is the first step to constraining computational models of single neurons (Druckmann et al., 2007; Gouwens et al., 2018). Although models of TC neurons have already been previously published, they typically were aimed at studying specific firing properties and their parameters were hand tuned to achieve the desired result (Amarillo et al., 2014; Connelly et al., 2015; Destexhe et al., 1998b; Huguenard and McCormick, 1992; Rhodes and Llinás, 2005).

The purpose of our study is to systematically define the morphological and electrical types by collecting *in vitro* experimental data and to constrain biophysically detailed models of VB TC neurons of the juvenile rat. To the best of our knowledge, automatic parameter search has not been applied, thus far, to capture complex firing behavior in thalamic neurons, in particular low-threshold bursting and tonic firing. We defined the electrical and morphological types of TC neurons through *in vitro* patch-clamp recordings and 3D morphological reconstructions. We then extended an existing method (Markram et al., 2015) to account for their distinctive firing properties. These electrical models (e-models) were constrained by the electrical features extracted from experimental data (Druckmann et al., 2007; Hay et al., 2011; Van Geit et al., 2016). Other experimental data were used to assess the generalization of the models to different stimuli and morphologies. We further performed a sensitivity analysis by varying each parameter at a time by a small amount and recording the resulting electrical features. This analysis provides an assessment of the robustness of the models and a verification that the selected features provide sufficient constraints for the parameters.

3.2 Results

3.2.1 Physiological and morphological characterization

We characterized TC neurons in slices of the rat VB thalamus, by combining whole-cell patch-clamp recordings, biocytin filling and 3D Neurolucida (MicroBrightField) reconstruction, along with anatomical localization in a reference atlas (Paxinos and Watson, 1998) (Fig 3.1).

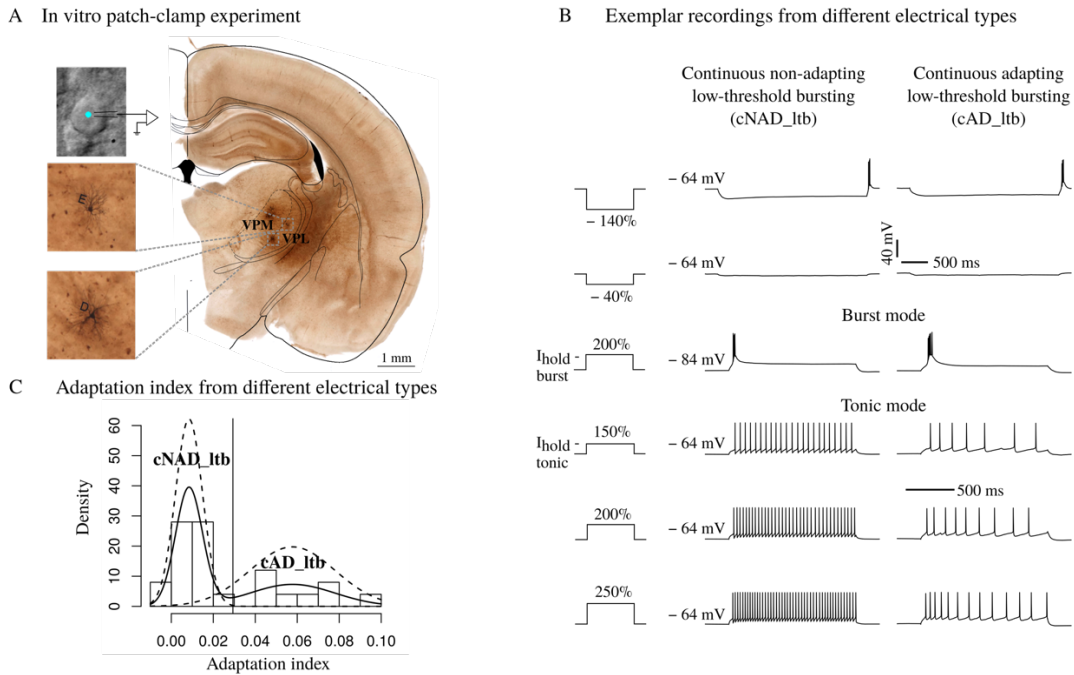
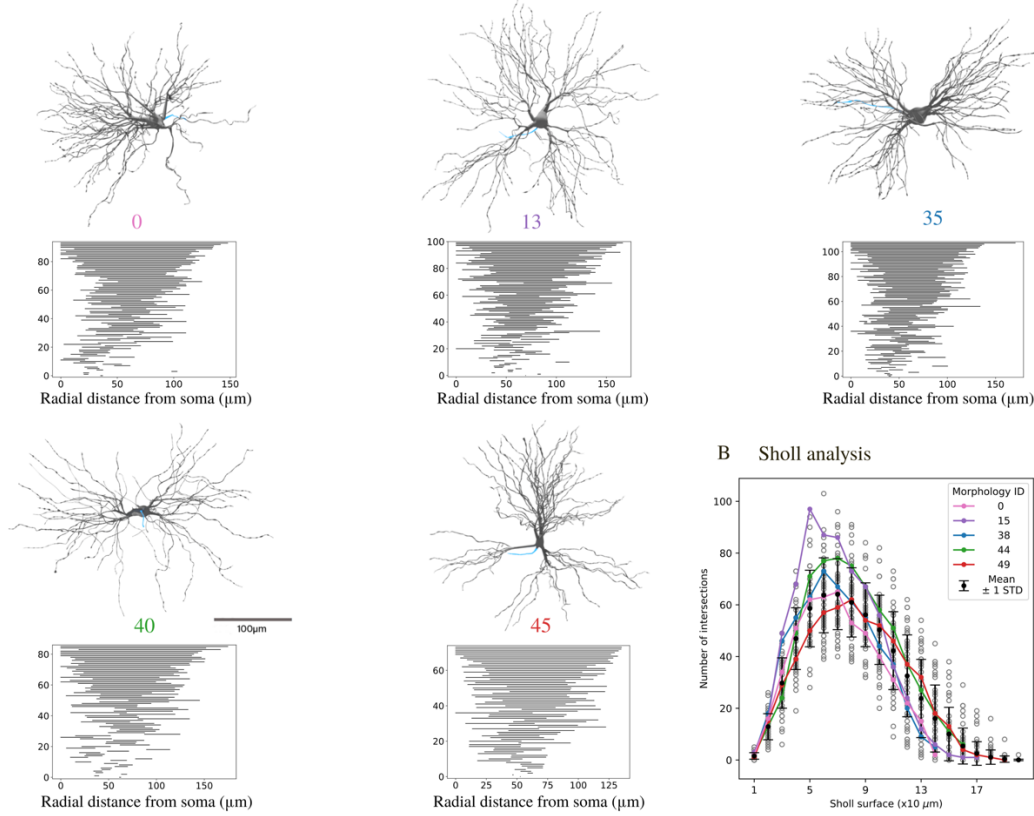


Figure 3.1. Simultaneous physiological and morphological characterization.

(A) View of a patched cell under optic microscope and anatomical localization of biocytin-filled neurons (insets) in the rat Paxinos and Watson atlas (Paxinos and Watson, 1998). Letters D and E identify morphologies in a slice. (B) Voltage responses of two different thalamocortical (TC) neurons to a standardized battery of current stimuli. Each current amplitude was normalized by the threshold current of each neuron (e.g. 150 % threshold, see Methods). Third row is a low-threshold burst response from a hyperpolarized holding potential, $V_{\text{hold}} = -84$ mV (burst mode), the other responses are elicited from a depolarized holding potential, $V_{\text{hold}} = -64$ mV (tonic mode). Two different holding currents (I_{hold} - tonic, I_{hold} - burst) are injected to obtain the desired V_{hold} . The vertical scale bar applies to all the traces, the first horizontal scale bar from the top refers to the first two rows, the second applies to the last four rows. (C) Analysis of adaptation index (AI) from recordings in tonic mode. Solid line is a non-parametric estimation of the distribution, dashed lines are two Gaussian distributions fitted to the data (see Methods). The vertical line indicates the cut-off value.

Visual inspection of 50 reconstructed morphologies (24 from the VPL, 26 from the VPM nuclei) revealed variability in the number of principal dendritic trunks and their orientation, in agreement with previous anatomical studies (McAlliser and Wells, 1981).

A Thalamo-cortical morphological type (TC) and topological description



B Sholl analysis

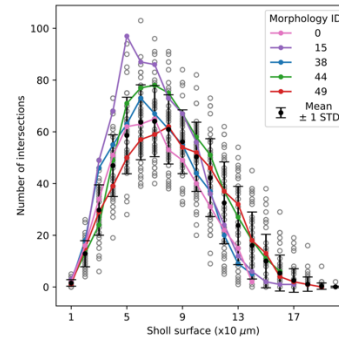


Figure 3.2. Morphological properties.

(A) Renderings of 3D reconstructed TC neurons along with their persistence barcode according to (Kanari et al., 2018). Grey: soma and dendrites, blue: axon only small sections available). The persistence barcode is a topological description of the branching pattern of the neurons' dendrites. (B) Sholl analysis of TC neuron dendrites. For each Sholl ring, the number of intersections is shown (mean \pm standard deviation, $N = 50$). Each grey circle represents one morphology, colored lines correspond to the morphologies in A. See Fig S1 for further analysis.

The maximum radial extent of the dendrites ranged between 120 and 200 μm and they started to branch between 20 and 50 μm from the soma (Fig S1). We then analyzed the morphologies with two methods in order to quantitatively classify different morphological types. We used algebraic topology to extract the persistent homology of each morphology and to visualize the persistence barcode (Kanari et al., 2018) (Fig 3.2A, see Methods). Each horizontal bar in the persistence barcode represents the start and end point of each dendritic component in terms of its radial distance from the soma. The barcodes of all the morphologies followed a semi-continuous distribution of decreasing length. To quantify the differences between the barcodes, we computed the pairwise distances of the persistence images (see Methods and Fig S1). We found that they were in general small (<0.4 , values expected to vary between 0 and 1). These findings indicate that the morphologies cannot be grouped in different classes based on the topology of their dendrites. Furthermore, we performed Sholl Analysis (Sholl, 1953) to compare the complexity of the dendritic trees (Fig 3.2B). We observed that all the

morphologies had dense dendritic branches, with a maximum number of 50-100 intersections between 50-80 μm from the soma. When comparing the Sholl profiles for each pair of neurons we could not find any statistically significant difference (Fig S1C). Considering the results of topological and Sholl analyses, we grouped all the morphologies in one morphological type (m-type) called thalamocortical (TC) m-type.

We used an adaptive stimulation protocol, called e-code, consisting of a battery of current stimuli (e- code, see Methods for details), where the stimulation amplitude was adapted to the excitability of different neurons. This standardized protocol has previously been used to build biophysically-accurate models of cortical electrical types (e-types) (Markram et al., 2015). However, TC neurons from different thalamic nuclei and species fire action potentials in two distinct firing modes, namely tonic firing, when stimulated from a relatively depolarized membrane potential or low-threshold bursting, from a hyperpolarized membrane potential (Llinás and Jahnsen, 1982). We thus extended the e-code to include two different holding currents. All the neurons recorded in this study displayed tonic and burst firing, when stimulated with the appropriate holding current (Fig 3.1). Moreover, we were able to classify different e-types by considering the voltage traces recorded in tonic mode in response to step current injections (Fig 3.1). The majority of the cells (59.3 %) showed a non- adapting tonic discharge (continuous non-adapting low-threshold bursting, cNAD_ltb e-type) while others (40.7 %) had higher adaptation rates (continuous adapting low-threshold bursting, cAD_ltb e-type), as reflected by the adaptation index (Fig 3.1C). We followed the Petilla convention (Ascoli et al., 2008) for naming the tonic firing discharge (cNAD or cAD), extending it to include “_ltb” for the low-threshold bursting property. In some rare examples, we noticed acceleration in the firing rate with decreasing inter-spike intervals (ISIs) towards the end of the stimulus. Similar adapting and accelerating responses have already been described in the VB thalamus of the cat (Turner et al., 1997). We also observed stereotypical burst firing responses within the same cell, with variation of the number of spikes per burst in different cells, but the burst firing responses alone were insufficient to classify distinct e-types.

3.2.2 Constraining the models with experimental data

Multi-compartmental models comes with the need of tuning a large number of parameters (Almog and Korngreen, 2016), therefore we constrained the models as much as possible from experimental data. We first combined the morphology and the ionic currents models in the different morphological compartments (soma, dendrites and axon). Given that the reconstruction of the axon was limited, we replaced it with a stub representing the initial segment (Markram et al., 2015). We used previously published ionic current models and selected those that best matched properties measured in rat TC neurons (see Methods). The kinetics parameters were not part of the free parameters of the models. The distribution of the different ionic currents and their conductances in the dendrites of TC neurons is largely unknown. The current amplitudes of the fast sodium, persistent and transient (A-type)

potassium currents were measured, but only up to 40-50 μm from the soma (Williams and Stuart, 2000). Indirect measures of burst properties (Connelly et al., 2015) or Ca^{2+} imaging studies (Errington et al., 2010) suggest that the low-threshold calcium (T-type) channels are uniformly distributed in the somatodendritic compartments. We thus assumed different peak conductance in the soma, dendrites and axon for all the ionic currents, except for I_{CaT} , which had the same conductance value in the soma and dendrites. We then extracted the mean and standard deviation (STD) of different electrical features in order to capture the variability of firing responses from different cells of the same e-type (Druckmann et al., 2007) (Fig 3.3). We observed that some features extracted from tonic firing responses had distinct distributions between the cAD_ltb and cNAD_ltb e-types (Fig 3.3A).

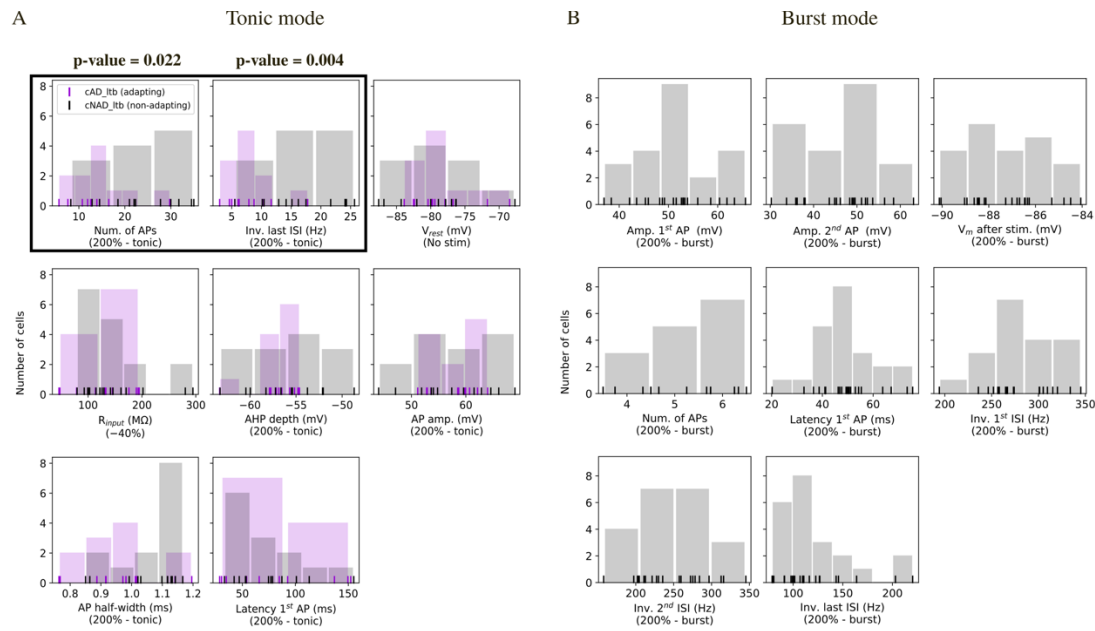


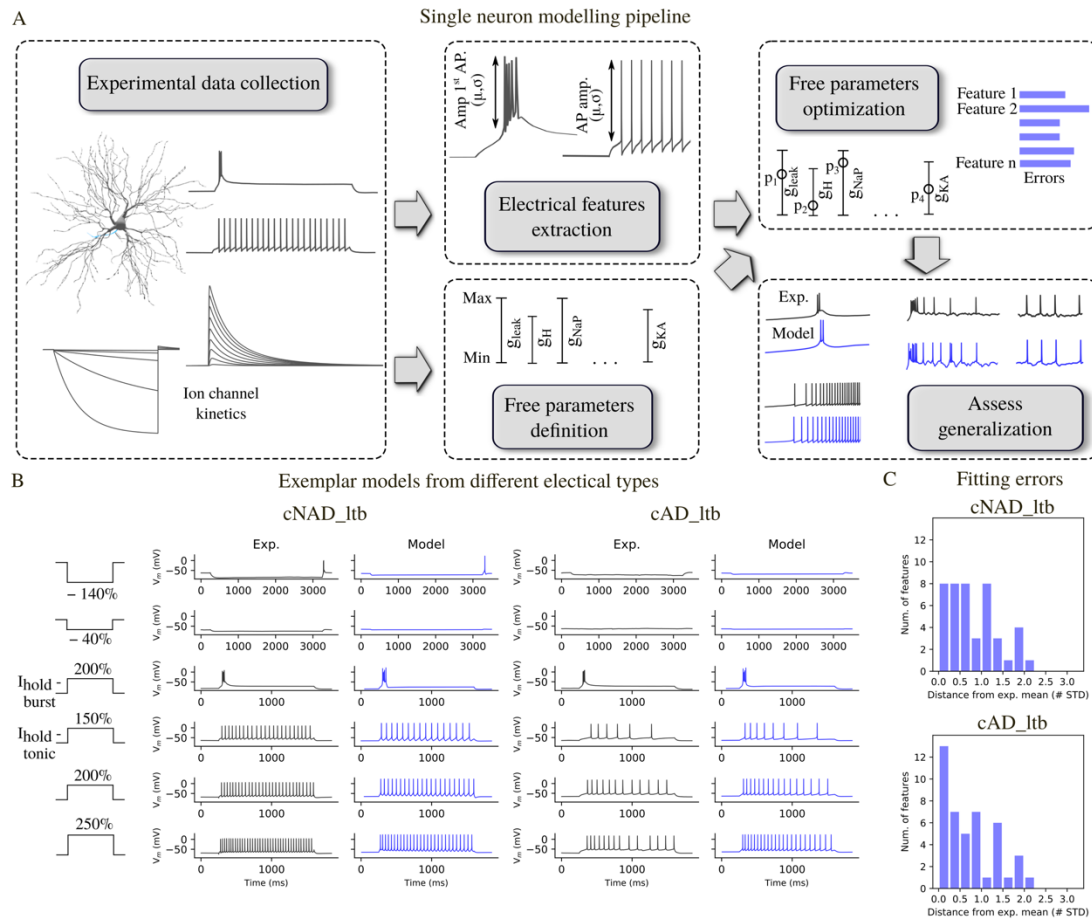
Figure 3.3 Histograms of electrical features.

Each vertical line represents the mean feature value for a cell. Tonic and burst refer to the holding voltage as in Fig 3.1. (A) Feature values extracted from recordings in tonic mode ($N = 11$ cAD_ltb cells, $N = 16$ cNAD_ltb cells). The features highlighted by a black box show different distributions for the cNAD_ltb and cAD_ltb electrical types (e-types) ($p\text{-value} < 0.05$, two-sided Mann-Whitney U test with Bonferroni correction for multiple comparisons). Passive properties (V_{rest} , R_{input}) and spike shape features (AHP depth, AP amp., etc.) did not show clear differences between the two e-types. (B) Features measuring burst firing properties ($N = 22$ cells).

For optimizing the models' parameters, we chose features that quantified passive (input resistance, resting membrane potential), burst and tonic firing properties (number of spikes, inverse of inter-spike intervals, latency to first spike, adaptation index), action potentials shape (amplitude, half-width, depth of the fast after-hyperpolarization). We aimed at finding the minimal set of features that capture the most important properties in the two firing modes. This set was a trade-off between comprehensively describing the experimental data (i.e. extracting all possible features), which can lead to over-fitting and loss of generalizability, and a too small

set that would miss some important characteristics. For the tonic firing responses, we used three stimulation amplitudes (150 %, 200 %, 250 % of firing threshold) which have been shown to reproduce the complete input-output function of the neurons (Hay et al., 2011; Markram et al., 2015). Responses to two hyperpolarizing steps of different amplitudes (−40 % and −140 % threshold) constrained the input resistance (conductance of the leak current) and the conductance of currents activated in hyperpolarization, for example the h-current, I_h (*sag_amplitude* feature). We included baseline voltage values in the optimization objectives to ensure that the models were in the right firing regime and spike count to penalize models that were firing in response to the holding currents. To constrain the low-threshold burst we used features (such as number of spikes) which are influenced by specific ionic currents, for example the low-threshold calcium current, I_{CaT} .

The average value and STD of each feature were used to calculate the feature errors. Each error measured how much the features of the models deviated from the experimental mean, in units of the experimental STD (Druckmann et al., 2008). We used a multiobjective optimization approach (MOO), where each error was considered in parallel. To rank the resulting models after optimization, we considered model A better than model B if the maximum error of all the features of A was smaller than the maximum error of all the features of B. Twenty-five parameters were allowed to vary between the upper and lower bounds shown in Fig 3.5.



3.2.3 Model and experimental diversity

We found that different sets of parameter values reproduced the target firing behavior (Fig 3.5B). We further analyzed models that had all the feature errors below 3 STD. Models' voltage responses reflected the characteristic firing properties of TC neurons (Fig S3), indicating that the selected set of features and ion channels were sufficient to capture the two firing modes, in both the adapting and non-adapting e-types. The voltage traces from different models showed small differences in spike amplitude, firing frequency, and depth of the after-hyperpolarization, as reflected by the variability of features values (Fig 3.5C), arising from differences in ion channel densities between models.

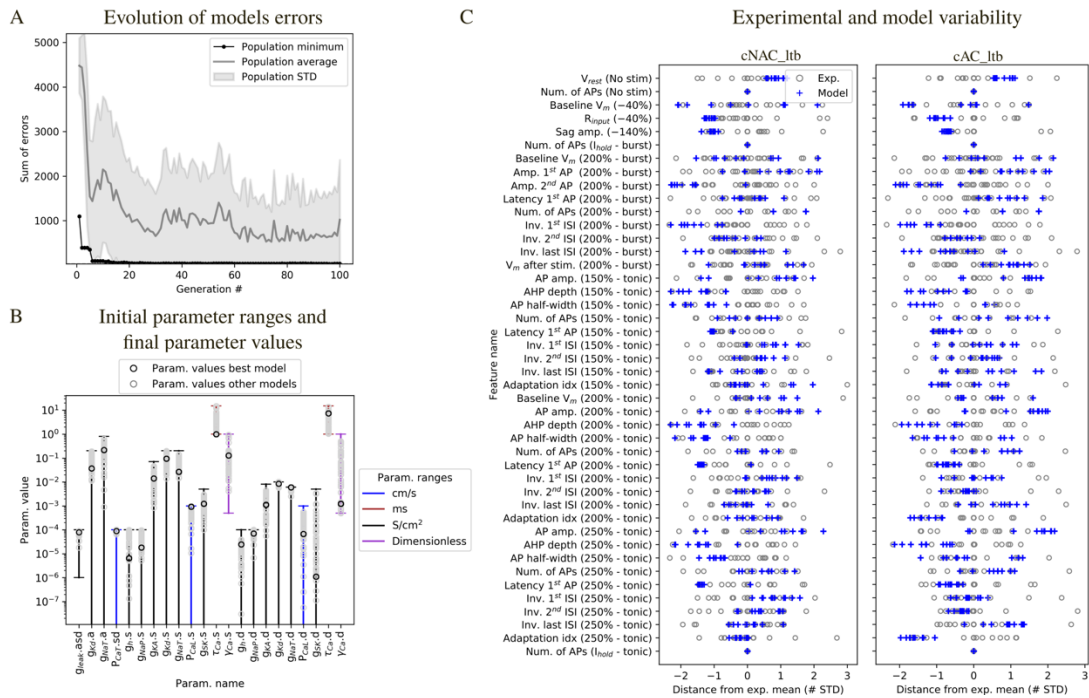


Figure 3.5. Diversity of model parameters and experimental variability.

(A) Example of model fitting errors (sum of all feature errors) during optimization. (B) Initial parameter ranges and diversity of solutions. Each vertical line represents the range for the parameters, when the horizontal lower bar is missing the bound is 0. The characters following "." in the parameter name specifies the morphological compartment for the parameter ("s": soma, "d": dendrites, "a": axon). Black circles: parameter values for one of the models in Fig 3.4, grey circles: parameter values of the models with all feature errors below 3 STD. (C) Features variability in the models and experiments. Blue crosses: feature errors of a sample of 10 models. Each grey circle is the z-scored feature value of one experimental cell, obtained from the feature values shown in Fig 3.3. The protocol names are shown in parenthesis and corresponds to the stimuli shown in Fig 3.1 and Fig 3.4, tonic and burst refer to the holding current as in Fig 3.1.

Spike-shape related features (e.g. AP. amplitude) in the different models covered the space of the experimental variability, while for some features (e.g. input resistance, R_{input}), all models tended to cluster on one of the tails of the experimental distribution. R_{input} relates to the neuron

passive properties and depends both on the number of channels open at rest (inverse of the leak conductance in the model) and the size of the cell. Given that all the models for a given e-type were constrained on a single morphology, this result is not surprising. Other features, such as sag amplitude were less variable in the models compared to experiments. We hypothesized that this depended on the variable stimulation amplitudes applied to different experimental cells, while all the models were stimulated with the same current amplitudes.

Some other features were systematically above or below the experimental values in both e-types. We suggest that this depend on the exact dynamics of some specific ion channels. For example, the amplitudes of the first and second spikes in the burst tended to be similar or above and below the experimental values, respectively. This can depend on the specific activation/inactivation properties of some ionic currents, for example the transient sodium current (I_{NaT}) and delayed potassium current (I_{Kd}). During the rising phase of the low-threshold spike, I_{NaT} in the model is readily activated and generated a first spike with higher amplitude, but is repolarized enough by the activation of I_{Kd} . At higher potentials, reached towards the peak of the low-threshold spike, the availability of I_{NaT} and other depolarizing currents seem reduced and generated a spike with smaller amplitude. Sensitivity analysis (Fig. 3.7) confirmed that I_{NaT} and I_{Kd} had an impact on the amplitude of the first and second spike in the burst. Furthermore, these two currents operate together with currents that generate the burst, such as the low-threshold calcium current (I_{CaT}) and the I_h in shaping the amplitude of the second spike in the burst (Fig. 3.7). Interestingly, the models also tended to have lower instantaneous frequency of the first two spikes in the burst (Inv. 1st ISI) and this feature had similar sensitivity (but of opposite signs) to the amplitude of the second spike in the burst (Fig 3.7B).

Another possible explanation is the lack of some ionic currents in the model, for example some specific subtype of potassium channels that promote higher firing rates (Kv3.1 and Kv3.3). While neurons of the thalamic reticular nucleus are known to express this channel subunit (Espinosa et al., 2008), the expression in TC neurons has not been confirmed yet. The dynamics of I_{Kd} could also explain why the after-hyperpolarization (AHP depth) tended to be smaller in the models compared to the experimental values. AHP depth is also influenced by other ionic currents, such as high-threshold calcium current (I_{CaL}), calcium-activated potassium current (I_{SK}) and the intracellular calcium dynamics (Fig. 3.7). The number of action potentials (Num. of APs) in different conditions (No stim, I_{hold}) ensured that the models did not spike in the absence of a stimulus or in response to the holding current. For this reason, all the experimental and model feature values in Fig. 3.5C are equal to 0.

We examined the diversity of the parameter values with respect to the initial parameter range (Fig 3.5B). Most of the optimized parameter values spanned intervals larger than one order of magnitude. On the other hand, some parameter values were restricted to one order of magnitude, for example the permeability of the low-threshold calcium current P_{CaT} . This result is in agreement with experiments showing a minimum value of I_{CaT} is critical to generate burst activity and this critical value is reached only at a certain postnatal age (Velazquez and Carlen,

1996). The value of P_{CaT} was constrained by features measuring burst activity (such as number of spikes, frequency, etc.).

3.2.4 Assessment of model generalization

We used different stimuli for model fitting (current steps) and for generalization assessment (current ramps and noise). We simulated the experimental ramp currents in-silico, by stimulating the models with the appropriate holding currents for the two firing modes and a linearly increasing current. We first compared visually the model responses with the experimental recordings (Fig 3.6A).

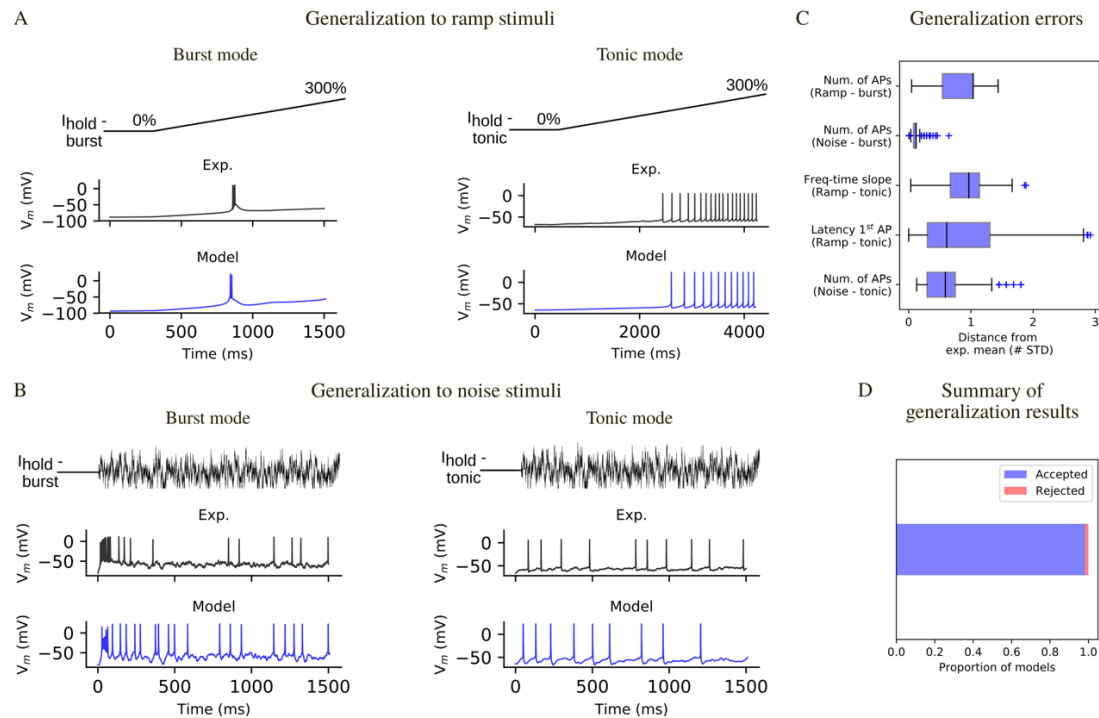


Figure 3.6. Model generalization.

(A) Responses to a ramp current injection in burst mode (left) and tonic mode (center). (B) Responses to a noise current generated according to an Ornstein-Uhlenbeck process and scaled based on the excitability of the different experimental cells and models (see Methods). (C) Generalization errors for all the models that passed the generalization test (all generalization errors < 3 STD). (D) Proportion of models that passed the generalization test (see Fig S4 for examples of models that failed this test).

In burst mode, the models reproduced the different behaviors observed experimentally: absence of a burst, small low-threshold spike, burst, burst followed by tonic firing (Fig S4). Moreover, the latency of burst generation substantially overlapped with the experimental one. However, a small fraction of models (1.2 %) generate repetitive burst that we have never observed in the experimental recordings (Fig S4). These models were quantitatively rejected by considering the number of spikes and the inter-spike intervals. In tonic mode, the latency to first spike, the voltage threshold, the shape of the subsequent action potentials and the increase in firing

frequency were comparable with the experimental recordings (Fig 3.6A). In addition, we quantified the generalization error to ramp stimuli (Fig 3.6C), by considering the latency to first spike, firing frequency increase over time (tonic mode) or number of spikes (burst mode).

Although conductance-based models can be fit by using step and ramp currents, these stimuli are different from synaptic inputs, which can be simulated by injecting noisy currents. To test the response to such network-like input, we used a noisy current varying accordingly to an Ornstein-Uhlenbeck (OU) process (Pozzorini et al., 2015) to compare models' responses with the experimental data. Each experimentally recorded cell was stimulated with the same OU input, scaled by a factor w . Experimentally, w was calculated during by evaluating the responses to previous stimuli. We developed a similar approach to generate the noise stimuli *in silico* (see Methods). The noise current was injected on top of the holding currents used during the optimization. We found that the models reproduced well the subthreshold potential, spike times and the distribution of single spikes and bursts (Fig 3.6B). Moreover, we quantitatively evaluated the generalization to the noise stimulus by extracting features (e.g. number of spikes) and comparing them with the experimental mean.

We computed generalization errors for each model, which were calculated similarly to the optimization errors (Fig 3.6C). We considered a model acceptable after generalization if it had all generalization errors < 3 STD and we found that the majority of the models ($> 90\%$) passed the generalization test.

3.2.5 Sensitivity of electrical features to small parameter perturbations

We assessed the robustness of the models to small changes in their parameter values. To that end, we varied each parameter at a time by a small amount ($\pm 2.5\%$ of the optimized value) and computed the values of the features. A sensitivity value of 2 between parameter p and feature y means that a 3% change in p caused a 6% change in f . We ranked the parameters from the most to the least influential and the features from the most sensitive to the least sensitive.

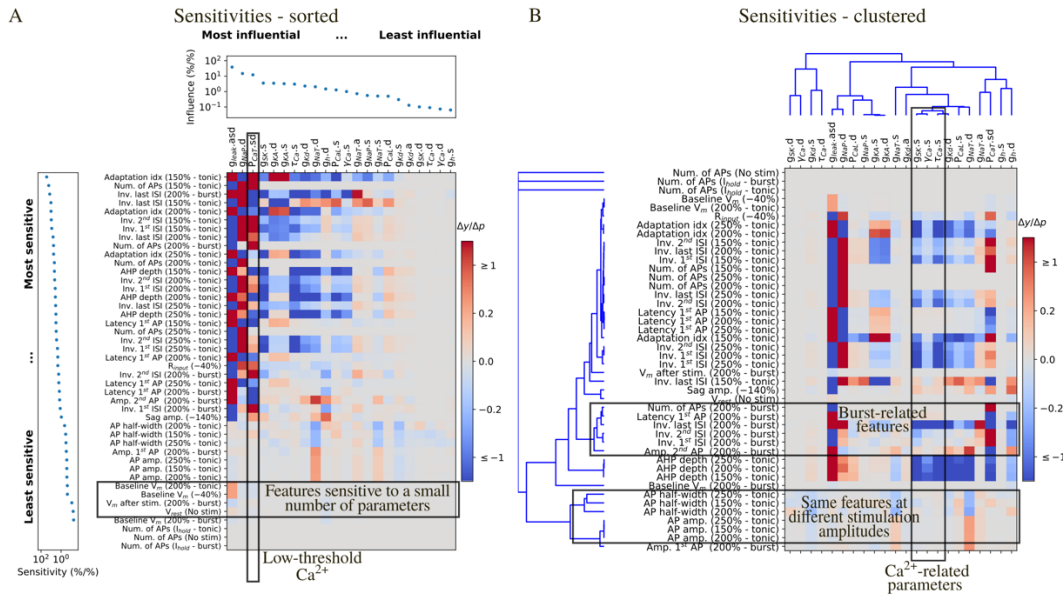


Figure 3.7. Local sensitivity analysis.

(A) Sensitivity of the feature values to small changes to the parameter values for the cAD_ltb model in Fig 3.4. Sensitivities ($\Delta y / \Delta p$) are color coded as a heat map. Features are ranked from the most to the least sensitive and parameters are ranked from the most to the least influential. The last three rows are features that ensure that the models were not firing without input or in the response to the holding current. Small changes to the parameter values are not expected to make the model firing and thus the sensitivity of these features is 0. (B) Same sensitivity values as in (a), with features and parameters clustered by similar sensitivity and influences.

Some features resulted to be more sensitive to parameter changes, both in term of magnitude of the sensitivity and number of parameters (e.g. adaptation index, inverse of inter-spike intervals, ISIs, AHP depth). Most of these features describe the model firing pattern, which depend more on the interplay between the different ionic currents than on the specific activation/inactivation dynamics. Conversely, spike shape-related features were less sensitive to parameter changes (e.g. AP half-width, AP amp.) and because they depend more on specific ionic current dynamics (e.g. I_{Kd} , I_L , I_{NaT}). Some features were very weakly influenced by small parameter changes, e.g. baseline voltage, which depend more on the holding current amplitude, than on the model parameters.

The conductance of the leak current g_{leak} emerged as the most influential parameter (Fig 3.7A). An increase in g_{leak} caused a decrease in firing frequency (inverse of ISIs) in both the tonic and burst firing modes. These results are easy to interpret when considering Ohm's law: increasing g_{leak} means decreasing the input resistance of the model, so that for the same input current the voltage response becomes smaller. The second most influential parameter was the conductance of the persistent sodium current g_{NaP} in the dendrites, which increased the tonic firing rate as expected from a depolarizing current. Interestingly, g_{NaP} had an effect on the late phase of the low-threshold burst (inverse last ISI - burst), suggesting that the low-threshold burst is initiated by the activation of I_T and modulated by I_{NaP} . An increase in the permeability of the low-

threshold calcium current P_{CaT} , known to be one the main currents underlying low threshold bursting, enhanced burst firing responses (it decreased the inverse of ISIs) and had effects on some of the tonic features. Increasing the somatic permeability of the high threshold calcium current P_{CaL} decreased the tonic firing rate, despite being a depolarizing current. Increasing P_{CaL} means higher Ca^{2+} influx and higher amplitude of the Ca^{2+} -activated potassium current (I_{SK}). The parameter g_{SK} had indeed a similar effect on the features and thus clustered together with parameters regulating the intracellular calcium dynamics γ_{Ca} and τ_{Ca} (Fig 3.7B). Sag amplitude, that is known to depend on the activity of I_h , was mainly influenced by change in g_{leak} , P_{CaT} and g_h . In summary, each parameter influenced at least one feature. These results indicate that the model ability to generate tonic and burst firing is robust to small changes in parameter values and that all the parameters were constrained during the optimization by one or more features.

We then analyzed which features depended similarly on parameter changes, as they may add superfluous degrees of freedom during parameters search. Fig 3.7B shows the same sensitivities as in Fig 3.7A, clustered by their similarities (see Methods). Features clustered together if they were sensitive to similar parameter combinations and parameters clustered based on their similar influence on the features. Not surprisingly, the same tonic features measured at different level of current stimulation clustered together (e.g. AP amplitude and half-width, AHP depth, latency of the first ISI) and tonic firing features belonged to a cluster that was different from burst features. Some features measured in tonic mode (such as AP half-width and AP amp.) clustered together because they depended mainly on the dynamics of I_{NaT} and I_{Kd} : increasing the conductance of I_{NaT} increased the amplitude of the APs and decreased its duration. This was also true for the amplitude of the 1st AP in the burst. Features measured in burst mode had similar sensitivities because they depend on currents that are active at relatively hyperpolarized potential (such I_H and I_{CaT}).

3.2.6 Preservation of model firing properties with different morphologies

We optimized the parameters for the adapting and non-adapting e-models in combination with two different experimental morphologies selected at random and then tested them with the other 48 morphologies. Considering that morphologies could not be classified in different m-types based on topological analysis of their dendrites and that TC neurons have been shown to be electrically compact (Connelly et al., 2015), we expected the electrical behavior to be conserved when changing morphology. Nonetheless, different neurons vary in their input resistance R_{input} and rheobase current I_{thr} due to variation in the surface area. Variation in R_{input} and I_{thr} made the current amplitude applied during the optimization inadequate to generate the appropriate voltage trajectories. We thus devised an algorithm to search for the holding current to obtain the target holding voltage (for example -64 mV or -84 mV for tonic and burst firing, respectively) and I_{thr} from the desired holding voltage. The different e-model/morphology combinations (me-combinations) were evaluated by computing the same feature errors calculated during optimization. For each morphology, we selected the e-model that generated

the smallest maximum error. All me-combinations reproduced burst and tonic firing (Fig 3.8C). We chose the value of 3 STD as a threshold to define which me-combinations were acceptable (Hay et al., 2013), yielding 50 acceptable me-combinations out of the 50 tested (Fig 3.8A).

Given that the generalization of the electrical models to the other 48 morphologies worked well, we can conclude that the morphological properties of the modeled neurons are very similar, at least for properties that have an impact on the electrical models (e.g. surface area, diameters of the compartments).

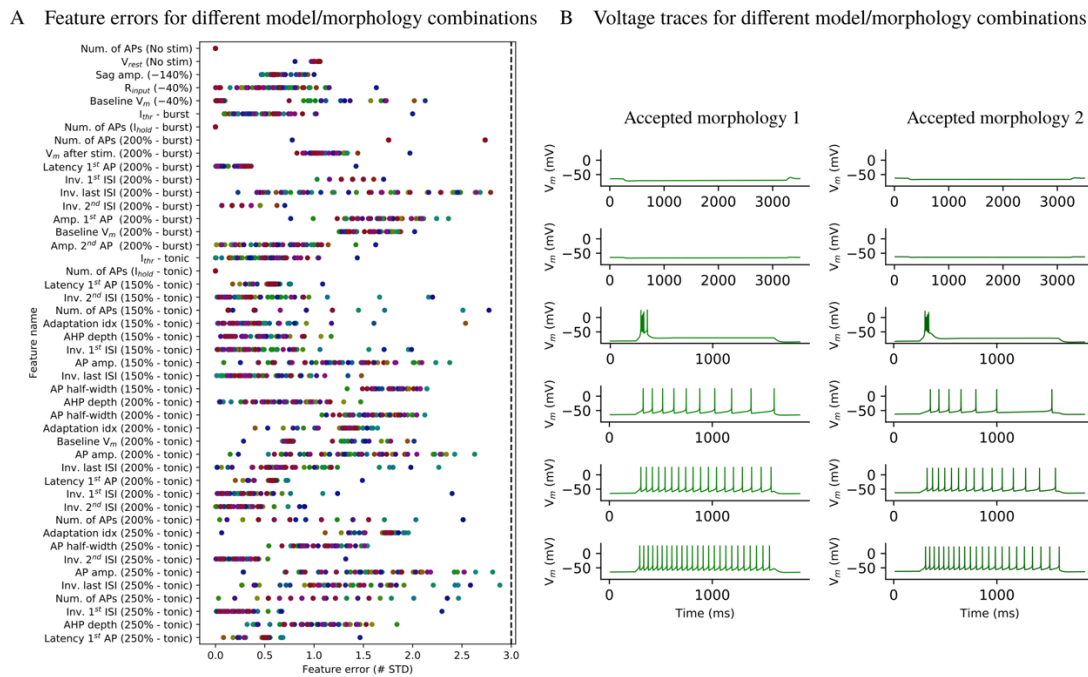


Figure 3.8. Model generalization to different experimental morphologies.

(A) Feature errors from the best electrical models (e-model) showed in Fig 3.4 applied to 50 different TC cell morphologies. Each morphology is represented with a different color. E-models/morphology combinations with at least one feature error > 3 STD (dashed line) were rejected. (B) Example of voltage responses from two accepted e-model/morphology combinations.

3.3 Discussion

Our objective was to apply and extend an existing data-driven pipeline to identify the cell types and build models of VB thalamocortical neurons that reproduce the multiple firing modes that have been experimentally observed. We successfully modelled these novel firing types, by including additional stimulation protocols and features to constrain the low-threshold burst.

Our morphological and electrical data were used to define the properties of VB TC neurons in the rat. We found two electrical types (e-types) of TC neurons, but no objectively different morphological types (m-types) were revealed either using Sholl analysis (Sholl, 1953) or

topological analysis of dendritic branching (Kanari et al., 2018). We cannot exclude that refinements to these methods will reveal different m-types similar to the ones described in the visual thalamus of the mouse (Krahe et al., 2011). We also showed that automatic parameter search can be applied to build biophysically and morphologically detailed models. This method was already applied to model canonical firing behavior in cortical (Druckmann et al., 2007; Gouwens et al., 2018; Hay et al., 2011; Markram et al., 2015), hippocampal (Migliore et al., 2018) cerebellar granule neurons (Masoli et al., 2017) and corticospinal neurons (Neymotin et al., 2016). To the best of our knowledge, such an automatic parameter search has not previously been used to capture different firing modes and complex firing behavior such as low-threshold bursting in thalamic neurons. Standardized electrophysiological protocols allowed us to identify for the first time in juvenile rat adapting and non-adapting e-types of TC VB neurons that were previously observed in other species (Turner et al., 1997). This finding suggests that the intrinsic properties of TC neurons contribute to adaptation, a key phenomenon for filtering out irrelevant stimuli, before sensory information reaches the neocortex. Further experiments are needed to elucidate the relative contribution of intrinsic mechanisms and network properties to adaptation in somatosensory systems. We named the two main e-types continuous non-adapting low-threshold bursting (cNAD_ltb) and continuous adapting low-threshold bursting (cAD_ltb) by following and extending existing conventions (Ascoli et al., 2008; Markram et al., 2015; Migliore et al., 2018).

In this study, we improved upon previous morphologically and biophysically detailed models of tonic and burst firing in TC neurons (Connelly et al., 2015; Destexhe et al., 1998b; Rhodes and Llinás, 2005) by explicitly constraining the parameters with experimental data, without hand-tuning of parameter values. Unlike previous models, we chose a multi-objective optimization for a methodological and a scientific reason: it is more time-efficient, reproducible, and it approximates the variability in ionic channel expression of biological neurons (Migliore et al., 2018; O’Leary et al., 2013; Schulz et al., 2006; Taylor et al., 2009), as shown by the family of acceptable solutions we found. However, experiments aimed at quantifying ion channel conductances are essential to assess if these solutions fall between biological ranges. Furthermore, we tested the generalization capability of the models and found that more than 90% of the models were comparable with the experimental data.

Nonetheless, we noticed some inaccuracies when comparing the voltage traces with the experimental data when assessing the generalization of some models. For instance, some models tended to generate small transient oscillations in response to ramp stimuli in burst mode. This result is not surprising, considering that the exact kinetics for all the ionic currents are not available and that there are known limitations in models of ionic channels derived from the literature or from other models (Podlaski et al., 2017; Ranjan et al., 2011). In particular, modifications of the kinetics of the low-threshold calcium current was shown to explain the propensity to generate oscillatory bursts in TC neurons of other nuclei and species (Wei et al., 2011). More generally, we included ion channels that were used in previous models and that were validated with experimental data whenever possible. We undertook an extensive literature review to use channel kinetics derived from recordings in rat TC neurons from the ventrobasal

(VB) thalamus or other first-order thalamic nuclei, whenever the data was available (see Methods). Moreover, we cannot exclude that some ionic currents were missing from our models and that they could have improved their fitness.

TC neurons have been shown to be electrically compact (Connelly et al., 2015) and could, in principle, be modeled as a single compartment. However, active mechanisms need to be located in the dendrites in order to ensure synaptic integration and amplification (Connelly et al., 2016). Information regarding specific conductances or firing properties in the dendrites of TC neurons is limited. For this reason, dendritic parameters in our models may be underconstrained. However, the sensitivity analysis (see below) revealed that dendritic parameters did not appear to be the least constrained because they influenced different tonic and burst-related features.

We included in the model fitting and validation pipeline a sensitivity analysis, which is often neglected in computational neuroscience (Tennøe et al., 2018). Although we cannot use our simple univariate approach to explore multidimensional parameter correlations and principles of co-regulation of ion channels expression, it is useful to find better constraints for parameters optimization. The selection of the features is indeed a step that still requires care and experience by modelers. Furthermore, this type of sensitivity analysis allows to identify parameters that can be traded-off during the optimization and that can be removed in order to reduce the dimensionality of the problem. In our study, parameters related to the calcium dynamics were shown to influence the features in a very similar fashion. This type of analysis is of particular importance in future work aimed at using the full diversity of ion channels that can be inferred from gene expression data. Gene expression data could also provide additional constraints on the choice of ion channels and indicate the ones that are missing in our models. More in detail, we propose that sensitivity analysis should be a fundamental tool in selecting which conductances are successfully optimized by the available experimental constraints. The example we showed is a local approach, applied to a specific solution to the optimization problem, which showed that our models are robust to small parameter changes. This analysis can be extended to study how the sensitivities vary in the neighborhood of different solutions.

In conclusion, we systematically studied the morphological and electrical properties of VB TC neurons and used these experimental data to constrain single neuron models, test their generalization capability and assess their robustness. Further work will validate these models in response to synaptic activity, in order to include them in a large-scale model of thalamocortical microcircuitry (Markram et al., 2015).

3.4 Methods

3.4.1 Experimental procedures

Experimental data were collected in conformity with the Swiss Welfare Act and the Swiss National Institutional Guidelines on Animal Experimentation for the ethical use of animals. The Swiss Cantonal Veterinary Office approved the project following an ethical review by the State Committee for Animal Experimentation.

All the experiments were conducted on coronal or horizontal brain slices (300 μm thickness) from the right hemisphere of male and female juvenile (P14-18) Wistar Han rats. The region of interest was identified using the Paxinos and Watson rat brain atlas (Paxinos and Watson, 1998). After decapitation, brains were quickly dissected and sliced (HR2 vibratome, Sigmund Elektronik, Germany) in ice-cold standard ACSF (in mM: NaCl 125.0, KCl 2.50, MgCl_2 1.00, NaH_2PO_4 1.25, CaCl_2 2.00, D-(+)-Glucose 50.00, NaHCO_3 50.00; pH 7.40, aerated with 95% O_2 / 5% CO_2). Recordings of thalamocortical neurons in the VB complex were performed at 34 °C in standard ACSF with an Axon Instruments Axopatch 200B Amplifier (Molecular Devices, USA) using 5–7 M Ω borosilicate pipettes, containing (in mM): K^+ -gluconate 110.00, KCl 10.00, ATP- Mg^{2+} 4.00, Na_2 -phosphocreatine 10.00, GTP- Na^+ 0.30, HEPES 10.00, biocytin 13.00; pH adjusted to 7.20 with KOH, osmolarity 270-300 mOsm. Cells were visualized using infrared differential interference contrast video microscopy (VX55 camera, Till Photonics, Germany and BX51WI microscope, Olympus, Japan).

Membrane potentials were sampled at 10 kHz using an ITC-18 digitizing board (InstruTECH, USA) controlled by custom-written software operating within IGOR Pro (Wavemetrics, USA). Voltage signals were low-pass filtered (Bessel, 10 kHz) and corrected after acquisition for the liquid junction potential (LJP) of -14 mV. Only cells with a series resistance <25 M Ω were used.

After reaching the whole-cell configuration, a battery of current stimuli was injected into the cells and repeated 2-4 times (e-code). During the entire protocol, we defined offset currents in order to keep the cell at -50 mV (tonic firing) or -70 mV (burst firing) before LJP correction and applied them during the entire protocol. The step and ramp currents were injected with a delay of 250 ms in the experiment. In the models, the stimuli were injected with a delay of 800 ms, to allow for the decay of transients due to initialization. Each stimulus was normalized to the rheobase current of each cell, calculated on-line as the current that elicited one spike (stimulus TestAmp, duration 1350 ms). The stimuli used for in the experiments, for fitting and testing the models were:

- IDRest: current step of 1350 ms, injected at different amplitude levels in 25 % increments (range 50-300 % threshold). IDRest was renamed to Step in the model.
- IDThresh: current step with duration of 270 ms, 4 % increments (range 50 - 130 %).

- IV: hyperpolarizing and depolarizing steps of 3000 ms injected in 20 % increments (range -140 - 60%).
- SponNoHold: the first 10 seconds of this stimulus was used to calculate the resting membrane potential. No holding or stimulation currents were applied.
- SponHold: the first 10 seconds of this stimulus was used to calculate the holding current applied to keep the cells at the target potential.
- PosCheops: ramps of current from 0 to 300 % and from 300 to 0 % having progressively shorter durations (4000 ms, 2000 ms, 1250 ms). To test the models in tonic mode we used the first increasing ramp in the stimulus, while we used the last one in the bursting firing mode. We chose the last one because the biological cells were more likely to generate a burst.
- NOISEOU3: the original wave was scaled and offset for each cell based on the spike frequency responses to IDRest responses. The scaling factor w was extracted from the frequency-current curve and corresponded to the current value that made the cell fire at 7.5 Hz.

Neurons that were completely stained and those with high contrast were reconstructed in 3D and corrected for shrinkage as previously described (Markram et al., 2015). Reconstruction used the Neurolucida system (MicroBrightField). The location of the stained cells was defined by overlaying the stained slice and applying manually an affine transformation to the Paxinos and Watson's rat atlas (Paxinos and Watson, 1998).

3.4.2 Electrical features extraction

Electrical features were extracted using the Electrophys Feature Extraction Library (eFEL) (BlueBrain, 2018a). We calculated the adaptation index (AI) from recordings in tonic mode (Step 200 % threshold) and classified TC VB neurons into adapting ($AI \geq 0.029$) and non-adapting ($AI < 0.029$) electrical types. AI was calculated using the eFEL feature *adaptation_index2* and corresponded to the average of the difference between two consecutive inter-spike intervals (ISI) normalized by their sum. The cut-off value was calculated after fitting a Gaussian mixture model to the bimodal data, using available routines for R (Choisy, 2018; RStudio Team, 2016). In order to group data from different cells and generate population features, we normalized all the stimuli by the rheobase current I_{thr} of each cell. To calculate I_{thr} , we used IDRest and IDThresh and selected the minimal amplitude that evoked a single spike. Along with the voltage features, we extracted mean holding and threshold current values for all the experimental stimuli. Description of the features and the details on their calculation are available on-line (BlueBrain, 2018a) (BlueBrain, 2018a). Current stimuli applied during the optimization and generalization were directly obtained from the experimental values or automatically calculated by following the experimental procedures (e.g. noise stimulus).

3.4.3 Morphology analysis

Reconstructed morphologies were analyzed to objectively identify different morphological types. The Sholl profiles of each pair of cells was statistically tested by using k-samples Anderson-Darling statistics. This test was preferred to the most common Kolmogorov-Smirnov test, because it does not assume that the samples are drawn from a continuous distribution. The different Sholl profiles are indeed an analysis of the intersections with discrete spheres.

To compare the topological description of each morphology we transformed the persistence barcodes into persistence images and calculated their distances as in (Kanari et al., 2018). Briefly, we converted the persistence barcode, which encodes the start and end radial distances of a branch in the neuronal tree, into a persistence diagram. In the persistence diagram, each bar of the barcode is converted into a point in a 2D space, where the X and Y coordinates are the start and end radial distances of each bar. The persistence diagram was then converted in a persistence image by applying a Gaussian kernel. We used the library NeuroM (NeuroM) to perform Sholl and morphometrics analyses. The reconstructed morphologies will be made publicly available on neuromorpho.org.

3.4.4 Ionic currents models

We used Hodgkin-Huxley types of ionic current models, starting from kinetics equations already available in the neuroscientific literature. Along with kinetics of the ionic currents, we stored information on the experimental conditions, such as temperature and LJP, by using the software NeuroCurator (O'Reilly et al., 2017). Whenever the data was available, we compared simulated voltage-clamp experiments to experimental data from juvenile rats. Ionic currents I_i were defined as functions of the membrane potential v , its maximal conductance density g_i and the constant value of the reversal potential E_i :

$$I_i = g_i m_i^x h_i^y (v - E_i)$$

m_{ion} and h_{ion} represent activation and inactivation probability (varying between 0 and 1), with integer exponents x and y . Each probability varied according to:

$$n'(v) = (n_{\infty}(v) - n)/\tau_n(v)$$

where $n_{\infty}(v)$ is a function of voltage that represents the steady-state activation/inactivation function (normally fitted with a Boltzmann curve) and $\tau_n(v)$ is a voltage-dependent time constant. Exceptions to this formalism are ionic currents that do not inactivate ($y = 0$) and ionic currents with (in)activation processes mediated by two or more time constants. Calcium currents (I_{CaT} and I_{CaL}) were modeled according to the Goldman-Hodgkin-Katz constant field equation and had permeability values instead of conductance (Hille, 1978).

Fast transient sodium current I_{NaT} and delayed potassium current I_{Kd} . I_{NaT} and I_{Kd} were taken from a previous models of rat TC neurons from the VB nucleus (Destexhe et al., 1998b),

available on SenseLab ModelDB (accession no. 279). I_{NaT} was compared with recordings of transient sodium currents in P7-11 rat neurons from the dorsolateral geniculate (dLGN) nucleus (Parri and Crunelli, 1998).

Low-threshold activated (T-type) calcium current I_{CaT} . I_{CaT} model was taken from (Destexhe et al., 1998b) and available on-line (ModelDB, accession no. 279). This model was based on data recorded from VB neurons of Sprague-Dawley rats (P7-12) at room temperature and corrected for -9 mV LJP (Huguenard and McCormick, 1992).

Hyperpolarization-activated cationic current I_h . The steady-state activation for I_h was derived from VB thalamic neurons in P10-20 Long-Evans rats and was already corrected for -10 mV LJP in the original publication (Budde et al., 1997). The equation used was:

$$m_{\infty} = 1/(1 + \exp[(v + 86.4)/11.2])$$

The time constant of activation was modeled as in (McCormick and Huguenard, 1992), which derived a mathematical description of I_h based on data from the dLGN in adult guinea pigs (McCormick and Pape, 1990). The equation describing the time dependence of activation was not corrected for simulations at different temperatures and was:

$$\tau_m = 1/[\exp(-14.59 - 0.086v) + \exp(-1.87 + 0.0701v)]$$

The equilibrium potential of the channel E_H was -43 mV.

Persistent sodium current I_{NaP} . We modeled I_{NaP} as in (Hay et al., 2011) which based their model on recordings from entorhinal neurons of Long-Evans rats (P25-P35) (Magistretti and Alonso, 1999). The model is available in ModelDB, accession no. 139653. The steady-state activation was modified according to (Parri and Crunelli, 1998) and the steady-state inactivation according to (Amarillo et al., 2014). The original steady-state activation data were recorded at room temperature ($22-24^{\circ}$) and corrected for $-6/-7$ mV LJP.

Fast transient (A-type) potassium current I_{KA} . The mathematical formulation of I_{KA} was based on data recorded from VB neurons in Sprague-Dawley rats (P7-15), recorded at room temperature ($22-24^{\circ}\text{C}$) (Huguenard and McCormick, 1992). A $Q_{10} = 2.8$ was experimentally determined and used for simulations at different temperatures. In the original experiments a small LJP (<-4 mV) was measured and not corrected. The current had a rapid and a slow component, represented by two activation and two inactivation variables. The model of this current was provided by the authors of (Amarillo et al., 2014).

High-threshold (L-type) calcium current I_{CaL} . I_{CaL} model is the same as TC neurons model previously published (Amarillo et al., 2014). The model was based on data from isolated guinea-pig hippocampal neurons, recorded at room temperature ($20-22^{\circ}\text{C}$) with modifications to the Boltzmann curve parameters of activation contained in the correction to the original models. A small LJP (<3 mV) was not corrected (McCormick and Huguenard, 1992). A Q_{10} of 3 was used for simulations at different temperatures.

Calcium-activated potassium currents. TC neuron express genes for BK-type (Ehling et al., 2013) and SK-type calcium-activated potassium channels (Gymnopoulos et al., 2014). Models of BK-type currents, similar to the I_C current, have already been used to model TC neurons (Amarillo et al., 2014; Ehling et al., 2013; McCormick and Huguenard, 1992). However, data characterizing this current in mammalian neurons are not available. We thus included only a model of I_{SK} (available on ModelDB, accession no. 139653) based on rat mRNA expression data in *Xenopus* oocytes (Köhler et al., 1996).

Intracellular calcium dynamics. A simple exponential decay mechanism was used to model the intracellular calcium dynamics (ModelDB, accession no. 139653). Both I_{CaT} and I_{CaL} contributed to the intracellular calcium concentration.

In addition, we included a voltage-insensitive membrane current I_{leak} . The equilibrium potential was -79 mV and corresponded to the average resting potential from our experimental recordings.

3.4.5 Simulation and parameters optimization

NEURON 7.5 software was used for simulation (Hines and Carnevale, 1997). We used NEURON variable time step method for all simulations. For the sake of spatial discretization, each section was divided into segments of $40\text{ }\mu\text{m}$ length. The following global parameters were set: initial simulation voltage (-79 mV), simulation temperature ($34\text{ }^{\circ}\text{C}$), specific membrane capacitance ($1\text{ }\mu\text{F}/\text{cm}^2$), specific intracellular resistivity $100\text{ }\Omega\text{cm}$ for all the sections, equilibrium potentials for sodium and potassium were 50 mV and -90 mV, respectively.

BluePyOpt (Van Geit et al., 2016) with Indicator Based Evolutionary Algorithm (IBEA) were used to fit the models to the experimental data. Each optimization run was repeated with three different random seeds and evaluated 100 individuals for 100 generations. The evaluation of these 300 individuals for 100 generations was parallelized using the *iPython ipyparallel* package and took between 21 and 52 h on 48 CPU cores (Intel Xeon 2.60 GHz) on a computing cluster. Each optimization run typically resulted in tens or hundreds of unique acceptable solutions, defined as models having all feature errors below 3 STD from the experimental mean.

3.4.6 Sensitivity analysis

We performed a sensitivity analysis of an optimization solution by varying one parameter value (p_m) at a time and calculating the electrical features from the voltage traces (y^+ and y^-). We defined the sensitivity as the ratio between the normalized feature change and the parameter change, which for smooth functions approximates a partial derivative (Olifer, 2013; Weaver and Wearne, 2008). The features changes were normalized by the optimized feature value. For small changes of parameter values, we assumed that the features depend linearly on its parameters. We could thus linearize the relationship between the features and the parameters

around an optimized parameter set and calculate the derivatives. The derivatives were calculated with a central difference scheme (Weaver and Wearne, 2008).

$$\frac{\partial y_n}{\partial p_m} \approx \frac{y_n^+ - y_n^-}{2\Delta p_m}$$

We collected the derivatives (sensitivities) in the $N \times M$ Jacobian matrix, with N representing the number of features and M the number of parameters.

To rank parameters and features we computed their relative importance by calculating their norms (the square root of the summed squared values) from the Jacobian columns and rows, respectively. To cluster parameters based on similar influences on the features and to cluster features that were similarly dependent on the parameters, we used angles between columns (or rows) to compute distances D between parameters (or features):

$$D = 1 - |\cos \theta|$$

Features were thus considered similar if they depended in a similar manner on the parameters, independent of sign or magnitude.

3.4.7 Data and code availability

The models are publicly available on ModelDB (McDougal et al., 2017), accession number 251881. The setup and configuration files (experimental features and protocols) for the optimization are publicly available on GitHub, under the examples of the BluePyOpt library (BlueBrain, 2018b). The channels densities of the acceptable models are available at the same page. The 50 3D morphological reconstructions are available on Neuromorpho.org (Ascoli et al., 2007) (DOI: 10.13021/xpbb-6y59).

4 Reconstruction and simulation of thalamic microcircuitry

This chapter is the result of a joint work with: Jane Yi, Ying Shi, Maria Garcia-Amado, Christian O'Reilly, Oren Amsalem, Francisco Clascà, Henry Markram and Sean L. Hill, to be submitted for publication.

Contribution: I performed the integration of the experimental data provided by J.Y., Y.S., M. G.-A. and F.C. C.OR. computed the microcircuit dimensions and built an initial version of the circuit model. Subsequently, I took responsibility for building and validating the neuron models, circuit and connectivity. I collaborated with O.A. for the inclusion of gap junctions into the circuit. I ran all the simulations, analyzed the results, and created all the figures. H.M. and S.L.H. supervised the study.

Abstract

The thalamus is centrally located between the periphery and the neocortex, it is involved in numerous functions and in the generation of thalamocortical rhythms. Despite significant advances in understanding its role in cognitive behavior, the bases of its structural and functional properties are still largely unknown. To address these challenges, we developed a detailed large-scale model of one of the simplest thalamic microcircuits. Although constrained and validated with extremely sparse experimental data, it reproduced fundamental cellular and network properties, without being explicitly built for generating for that purpose. As a first step, we used the model to study spindle-like oscillations, a thalamic-generated rhythm, and how neurons and connectivity through chemical and electrical synapses shape it. We dissected thalamic contributions to rhythm generation and predicted which aspects critically depend on cortical inputs. This first-draft model of thalamic microcircuit will be extended in the future with biologically-detailed models of neocortical circuits to broaden our understanding of thalamocortical computations.

4.1 Introduction

The thalamocortical system consists of different thalamic nuclei, including the inhibitory reticular nucleus of the thalamus, and their reciprocal interactions with the neocortex. The thalamus, along with the reticular nucleus, is involved in numerous functions, for instance transmission of sensory information and transition between brain states, such as sleep and

wakefulness (Jones, 2002; Rikhye et al., 2018; Steriade, 2003). The thalamus and reticular nucleus alone are able to generate and sustain rhythmic activity, such as spindle oscillations, as a result of their cellular and synaptic properties, which are transmitted to the neocortex and shaped by cortical feedback (Bal et al., 1995b; Contreras et al., 1997; Fernandez and Luthi, 2019; von Krosigk et al., 1993; Steriade et al., 1987). Subtle alterations to thalamic neurons firing and their interconnectivity have been associated with pathological brain rhythms, such as those appearing in absence epilepsy (Beenhakker and Huguenard, 2009; Huguenard and McCormick, 2007; Makinson et al., 2017; Sohal and Huguenard, 2003; Steriade, 2005) (Beenhakker and Huguenard, 2009; Huguenard and McCormick, 2007; Makinson et al., 2017; Sohal and Huguenard, 2003; Steriade, 2005).

Although the properties of thalamic and reticular neurons have been extensively studied *in vitro* (Connelly et al., 2017; Cox et al., 1996; Jahnsen and Llinás, 1984; Lee et al., 2007; Pinault and Deschênes, 1998b; Pinault et al., 1995; Spreafico et al., 1991) a detailed characterization of the anatomy and physiology of neuron pairs in the thalamus has been challenging (Cox et al., 1997; Gentet and Ulrich, 2003). Understanding these fundamental properties is the basis to broaden our knowledge of thalamic computations. Computer simulations facilitate the integration and standardization of different sources of experimental data, highlight key missing experiments, and help us understand the structural and functional complexity of neural circuits (Billeh et al., 2020; Einevoll et al., 2019; Markram et al., 2015). Previous models of small thalamic networks or thalamic slices have studied various physiological and pathological aspects of thalamic microcircuits, but the level of detail and the choice of parameters reflected the specific hypothesis that were investigated (Bazhenov et al., 1998; Bús et al., 2018; Destexhe et al., 1996; Golomb et al., 1996; Li et al., 2017; Wang et al., 1995).

In this work, we followed and extended the pipeline presented in (Markram et al., 2015) to develop a digital reconstruction of a thalamic microcircuit in the mouse, including a portion of first-order somatosensory thalamus (ventroposterolateral nucleus, VPL) and the corresponding region of the reticular nucleus. We performed targeted *in vitro* experiments to capture electrophysiological, morphological and synaptic data from the mouse. We then used these measurements, combined with systematic curation of data from the literature and open access datasets, to build biophysically and morphologically-detailed neuron models. We defined the microcircuit geometry and populated it with experimentally-measured neuron densities. 3D morphological reconstructions constituted the basis to constrain the detailed connectivity between neurons of the thalamus and the reticular nucleus. Synaptic connections comprised chemical synapses with short-term depression and facilitation and electrical synapses (gap junctions). As extra-thalamic source of inputs, we included synapses from sensory afferents (medial lemniscus) and corticothalamic feedback.

This approach yielded the first morphologically and biophysically-detailed model of a thalamic microcircuit, showing that the modelling strategy developed for cortical microcircuitry (Markram et al., 2015) can be applied to other brain regions. Although this first-draft model was constrained with extremely sparse experimental data, it reproduced a number of *in vitro*

and *in vivo* findings. While building this detailed model, we learned that the structural properties of thalamic connectivity are still largely uncharacterized experimentally, as well as synapse densities of intrinsic and extrinsic synapses. We predicted that most connections are constituted by single contacts and that electrical connections in the reticular nucleus can exist between neurons that are hundreds of micrometers apart from each other, reflecting the extent of reticular neurons dendrites.

Network simulations showed that evoked spindle-like oscillations are mainly generated by synaptic interactions and that the balance between the activity of different connections can account for oscillation termination. Reciprocal inhibition between reticular neurons and gap junctions affected the duration of the oscillation in a reciprocal way: while removing the former increased the duration of spindle-like oscillations, removing the latter shortened it. This finding is in agreement with the desynchronizing and synchronizing roles proposed from intra-reticular inhibition and gap junctions (Beenhakker and Huguenard, 2009; Fernandez and Luthi, 2019; Kohmann et al., 2016). We found that differential depolarization in the Rt and VPL influence both oscillation frequency and duration, suggesting a dynamic modulation of membrane potentials and spindle properties as shown in naturally sleeping rodents (Bartho et al., 2014; Urbain et al., 2019). We also showed that evoking network oscillation with characteristics similar to sleep spindles is easier in a limited range of Rt and VPL depolarization levels, approximating Rt and VPL activities during light NREM sleep.

4.2 Methods

4.2.1 Constraining and validating the model with experimental data

We built the microcircuit model by constraining and validating it at multiple levels, with the available experimental data. For validation we mean the direct comparison of the model properties with experimental measurements that were not used during the model building steps. Before describing the details of the reconstruction, validation and simulations, we provide a list of data used for constraining the model, the validation data and further validations at the network level.

4.2.2 Experimental data used to constrain the model

We provide below a list of experimental data used to constrain the model at each level of the reconstruction process:

- Three-dimensional reconstructions of neuron morphologies.
- Electrophysiological data from *in vitro* patch-clamp recordings (current step stimuli)
- Ion channel kinetic parameters

- Neuron densities
- Fraction of inhibitory and excitatory neurons
- Fraction of electrical types for each morphological type
- Axonal bouton densities (i.e. number of boutons per axonal unit length)
- Volumetric densities of lemniscal synapses
- Ratio of corticothalamic to lemniscal bouton densities and ratio of corticothalamic to thalamocortical bouton densities.
- Postsynaptic potential amplitudes and their change in response to trains of presynaptic inputs from *in vitro* paired-recordings (short-term plasticity protocols). Initial release probabilities are estimated from these data as well.
- Number of neurons connected through gap junctions.

4.2.3 Experimental data used for model validation

The following experimental measurements not used for constraining the model during the building process and were used for validation:

- Electrophysiological data from *in vitro* patch-clamp recordings (current ramps and noise).
- Dendritic attenuation of synaptic potentials
- Neuron convergence onto reticular neurons
- Number of synapses per connection between interneurons and thalamocortical neurons (*i.e.* number of synapses between each pair of neurons)
- Coefficient of variation of first postsynaptic potential amplitudes
- Postsynaptic potential amplitudes
- Distance-dependent gap junction connectivity between reticular neurons
- Gap junctions coupling coefficients

4.2.4 Validations at the network level

We identified the following network responses during simulated activity as a general validation of the reconstruction process:

- Spontaneous *in vivo*-like activity. In *in vivo*-like states the network should display uncorrelated firing at the population level. Single neurons can fire or be silent.

- Evoked activity with simulated sensory input. The network should respond to spiking inputs from medial lemniscal fibers. The population response should increase, and the latencies should decrease with increasing stimulus amplitude (number of fibers).
- Spontaneous *in vitro*-like activity. The network should generate low firing activity dominated by miniature potentials.
- Modulation of thalamic activity in response to simulated activation of corticothalamic fibers (Crandall et al., 2015).
- Evoked spindle-like activity.

4.2.5 Reconstructing the morphological diversity of neurons

4.2.5.1 Reconstruction of morphologies

3D reconstructions of biocytin-stained thalamocortical (TC), reticular thalamic (Rt) neurons and thalamic interneurons (IN) were obtained from *in vitro* patch-clamp experiments from 300 μm slices of P14-35 mice (GAD67-eGFP or C57Bl/6J strains) as previously described (Iavarone et al., 2019; Markram et al., 2015). During the electrophysiological recordings neurons were stained intracellularly with biocytin. *In vitro*-stained neurons were mainly located in primary somatosensory nuclei (VPL and VPM) and the somatosensory sector of the reticular nucleus (Clemente-Perez et al., 2017; Lam and Sherman, 2011; Pinault and Deschênes, 1998b). Reconstructions used the Neurolucida system (MicroBrightField) and were corrected for shrinkage along the thickness of the slice. Shrinkage along other dimensions was taken into account during the unravelling step (see below). Dendrites were reconstructed with a 100x magnification (oil immersion objective) and axons at 60x (water immersion objective).

In vivo-stained TC and Rt morphologies were obtained from different experimental techniques. In some cases, neurons were labelled by injection of replication-defective Sindbis virus particles in the thalamus or Rt nucleus in C57Bl/6J adult mice (Furuta et al., 2001) or electroporation of RNA of the same virus (Porrero et al., 2016). The virus labelled the membrane of the neurons thanks to a palmitoylation signal linked to a green fluorescent protein (GFP). Brains were cut in 50 μm serial sections and immunostained against GFP and enhanced with glucose oxidase-nickel staining (Shu et al., 1988). Neurons were reconstructed from sequentially-ordered slices under bright-field optics using the Neurolucida system (MicroBrightField). The complete method is described in (Rodriguez-Moreno et al., 2020).

TC neuron morphologies from the Janelia Mouselight project were obtained from adult C57/BL6 mice and sparsely labelled; the method is described in detail elsewhere (Winnubst et al., 2019) and summarized here. Brains were then delipidated, fluorescence was enhanced by immunolabeling and imaged with a 40x oil-immersion objective. This procedure generated large datasets of high-resolution image stacks. 3D reconstructions were conducted combining semi-automated segmentation of neurites and human annotation and quality control. Janelia

Mouselight reconstructions lacked diameter variations in their neurites, which is important for accurate electrical modelling of neurons (Jaeger, 2000). For this reason, we only used their axons in order to increase the variability of our axonal reconstructions.

Virus injections for sparse labelling of whole brain neuron morphologies were employed for *in vivo* labelling of reticular neurons in SSt-Cre;Ai139 adult mice. Brains were imaged using fluorescence micro-optical sectioning tomography (fMOST) (Gong et al., 2016). Neurons were manually reconstructed from high resolution image stacks obtained after slicing. Further details of the method are available in (Wang et al., 2019).

4.2.5.2 Morphology analysis and alignment

We analyzed the axons of TC morphologies using an open-source library (NeuroM) and identified axonal collaterals in the reticular nucleus as the morphological sections which had branch order ≥ 1 and path distance from the soma $< 2500 \mu\text{m}$ and visually validated the results. For some morphologies we considered sections with branch order ≥ 2 . For others we selected those having path distance $\leq 2000 \mu\text{m}$, because some TC neurons have collaterals projecting to other subcortical regions (e.g striatum), see (Clascá et al., 2012).

Raw morphological data did not have a common orientation along a principal axis. We thus computed a rotation matrix so that their principal axis was parallel to the vertical axis of the microcircuit. The principal axis of TC morphologies was the one connecting the center of the soma and the center of mass of the axon collaterals in the Rt nucleus. For Rt neurons, the principal axis connected the soma and the center of mass of the axonal arborization in the thalamus. An alternative approach would have been to align Rt neurons dendrites along the horizontal dimension of the microcircuit (and the Rt region). We found that in most cases the two methods gave comparable results. After rotating the morphologies, we visually validated the results. We did not perform any rotation for the INs, since information about their orientation with respect to thalamic landmarks and other nuclei was missing.

Raw morphological data were algorithmically corrected for slicing artifacts and processed to generate a large pool of unique morphologies for building the microcircuit and connectivity (morphology release). Spurious sections, which were accidentally introduced during manual reconstruction, were identified as those having $0 \mu\text{m}$ diameter and removed. The details are described in Supplemental Experimental Procedure of the neocortical microcircuit model (Markram et al., 2015), and summarized below.

4.2.5.3 Unraveling morphologies

Since we found that 3D reconstructions from *in vitro*-stained neurons had increased tortuosity in their dendrites as a result of tissue shrinkage, we unravelled them using an existing algorithm. This process resulted in an increase of the reach of the morphologies, while preserving the original length of the branches. Briefly, unravelling was performed by sections and for each section a sliding window composed of a given number of successive points was created. The number of points in the sliding window (N) was the only parameter of the algorithm and we found that $N=5$ previously used performed well on thalamic morphologies.

The general direction of the points in the window was computed using principal component analysis (PCA). The segment at the middle of the window was then aligned along this direction. It meant that its direction was set to the one of the sliding window but it retained its original length. The sliding window was moved over all points of the section and the algorithm was applied to all sections.

4.2.5.4 Repairing morphologies

Not surprisingly, most of the *in vitro*-stained morphologies were truncated at slice edges and in the case of some TC morphologies, which have very dense dendritic arborization, this resulted in a significant decrease in dendritic mass. We applied an existing algorithm (Anwar et al., 2009; Markram et al., 2015) to repair missing dendritic branches and with the inclusion of small improvements. First, the algorithm detects cut points on the XY plane, i.e. the plane parallel the slice, along the Z direction (parallel to the slice thickness). The 3D coordinate system was centered on the morphology soma. Although the algorithm was designed to detect cut points on two planes, we found that our morphologies were truncated on the top plane. We improved the algorithm by searching the cut points before unravelling the morphologies and updated their position during the unravelling step. Cut detection required a tolerance parameter to detect terminal points within a certain distance from maximum Z extents. We empirically found the 15 μm gave the most accurate results. Some terminal points were then tagged cut points and dendrites were repaired.

The dendrite repair process created new dendritic sections starting at the identified cut points. Dendrite repair did not aim at recovering the initial morphology, but rather recreated it in a statistical manner, under the assumption of statistical symmetry of the morphology. This method analyzed the behavior of intact branches as a function of branch order and euclidean distance from the soma. For each branch order, probability density clouds of branch continuation, bifurcation or termination was calculated in a series of concentric spheres (Sholl, 1953). At each cut point, the behavior of the branch was sampled according to the calculated probabilities. The factor governing the direction of the re-grown branches was empirically adjusted to achieve final branches tortuosity comparable with our experimental data. To alleviate problems created by swellings at some of the cut points, diameters of re-grown branches was the average of diameters of all the points in the section and not only the diameter at the cut point.

4.2.5.5 Morphology diversification

We increased the variability of our sample of reconstructed and repaired morphologies to ensure robust and invariant connectivity patterns (Ramaswamy et al., 2012). We followed procedures similar to (Markram et al., 2015) with the aim of generating a unique space-filling pattern for each morphology, while maintaining the general morphological and electrical structure for each m-type.

We applied a mix-and-match procedure to maximize the utilization of good morphological reconstruction data. This procedure divided dendrites from axons and allowed us to combine good dendritic reconstructions of TC and Rt cells dendrites from *in vitro* and *in vivo*-stained

neurons. *In vitro*-stained neurons typically lacked reconstruction of the full axon due to the slicing procedure and/or poor labelling. For each morphology, we manually annotated which dendrites and axons were to be kept. The decision in most cases depended on the labelling method (*in vitro* vs. *in vivo*).

To increase the probability that *in vivo*-stained morphologies and in particular the axons of TC and Rt morphologies were compatible with the microcircuit dimensions (see below) we duplicated and scaled the morphologies along their principal axis (Y-axis) by $\pm 2.5\%$ and $\pm 5.0\%$.

We used an existing algorithm to further increase morphological variability, as detailed in (Markram et al., 2015). In summary, branch lengths and rotations at each bifurcation point were varied according to random numbers drawn from Gaussian distributions with mean 0% and standard deviation 20 % for branch lengths and mean 0° and standard deviation 20° for branch rotations. A sample of the resulting morphologies was visually validated, and we did not find significant alterations of their structure for any of the m-types.

4.2.6 Reconstructing the electrical diversity of neurons

4.2.6.1 Electrophysiological data

The firing patterns of TC, Rt neurons and interneurons (INs) were characterized *in vitro* from brain slices of P14-35 GAD67-eGFP or C57Bl/6J mice and expert-classified into 5 electrical types (see Results). The detailed electrophysiological protocol has been published elsewhere (Iavarone et al., 2019). Neurons were sampled from the ventrobasal complex of the thalamus (VPL and VPM nuclei) and the somatosensory sector of the reticular nucleus (Clemente-Perez et al., 2017; Lam and Sherman, 2011).

We used responses to step-like currents to build electrical models, ramp and noise currents to validate them (Iavarone et al., 2019), along with EPSC-like currents injected into the dendrites. All the recordings were corrected for liquid junction potential by subtracting 14 mV from the recorded voltage.

4.2.6.2 Neuron models

Multicompartmental conductance-based models were obtained by using reconstructed morphologies. Active ion currents and a simple intracellular calcium dynamics model were distributed in the somatic, dendritic and axonal compartments. The complete axon was not modelled (Markram et al., 2015), but only the axonal initial segment (AIS). The axons were substituted by 60 μm stub constituted by 2 sections, 5 segments each. For each segment, the diameter was extracted from the original axon in order to preserve its tapering. Morphologies were divided into compartments of 40 μm maximal length. Specific membrane capacitance was set to 1 $\mu\text{F}/\text{cm}^2$ and specific intracellular resistivity to 100 Ωcm .

4.2.6.3 Ion channel models

We included ion current models whose kinetics was obtained from previously published ion current models or derived from experimental data. All ion channel models were corrected for liquid junction potential and for simulation at different temperatures whenever possible. Simulation temperature was always set to 34° C. The types of ionic currents represented in the neuron models were: transient sodium, persistent sodium, A-type transient potassium, delayed potassium, low-threshold calcium, high-threshold calcium, calcium-activated potassium (SK-type), h-current. The details of the ion channel kinetics and calcium dynamics used for low-threshold bursting neurons (thalamocortical, TC, and reticular neurons, Rt) has been detailed elsewhere (Iavarone et al., 2019). Since interneurons had firing patterns similar to cortical ones, we used the same ion channel models of (Markram et al., 2015). The reversal potential of sodium, potassium and h-current were set to 50 mV, -90 mV and -43 mV, respectively.

Ion channel models were distributed uniformly and with different peak conductance values for somatic, dendritic and axonal compartments.

4.2.6.4 Optimization of neuron models

Five electrical models (e-models), corresponding to each electrical-type (e-type), were fitted using a multiobjective optimization algorithm using the Python library BluePyOpt (Iavarone et al., 2019; Van Geit et al., 2016). The free parameters of the model were the peak conductances of the different mechanisms and parameters of the intracellular calcium dynamics. Each e-model was fitted with an exemplar morphology. The optimization objectives were the electrical features extracted from the electrophysiological recordings.

For all the e-types, 3 levels of positive steps and 2 negative steps were used to fit passive properties, firing patterns and spike shape related features (see for a detailed list of features in Iavarone et al., 2019). The negative step with the smaller amplitude was used to constrain passive properties (e.g. input resistance), while higher amplitudes were used to constrain the conductance of currents activated in hyperpolarization (with features such as *sag_amplitude*). For low-threshold bursting cells, one step on top a hyperpolarizing current was used to constrain the bursting response. For reticular neurons, a new feature (*initburst_sahp*) was added for the AHP after the burst. Additional protocols without any current injection or only holding currents were used to ensure that the e-models were not firing without stimulus or with the holding current only.

We considered a model a good fit to the experimental data if all the feature errors (i.e. the Z-scored) were below 3.

4.2.6.5 Quality assurance of morpho-electrical models

After fitting the 5 e-models they were combined with the 92970 morphologies generated as output of morphology diversification step. An automated pipeline tested the e-models in combination with the different morphologies (me-models) and filtered out those that deviated significantly from the experimental electrical features. To decide which me-model was to be

accepted, we used the repaired exemplar morphology (*i.e.* the morphology used during the optimization, after being repaired) as a benchmark: a me-model passed if it had all the feature errors below 5 standard deviations of the repaired exemplar, as in (Markram et al., 2015).

In addition, we first run this pipeline on a small subset of the morphologies generated after morphology repair. In this way, we could visually inspect if the accepted me-models were generating biologically-plausible firing behavior and the reasons why other me-models had high feature errors. In some cases, after inspecting the me-model voltage responses, we set less stringent criteria on some features, to ensure that we had enough different me-models for building the microcircuit. At the same time, we set more stringent criteria to reject me-models that were active without any input, since we did not find neurons that were spontaneously active in our experimental recordings.

4.2.7 Reconstructing neurons density

4.2.7.1 Immunohistochemistry of Rt and VPL for cell counting

We complemented the neuron densities values from the Blue Brain Cell Atlas (Erö et al., 2018) by counting neurons in adult brain slices of the mouse brain. We used adult mice brains cryosliced at 50 μm on the sagittal plane and stained with standard immunohistological procedures with antibodies anti-GABA (for inhibitory neurons), anti-NeuN (for neurons) and DAPI (for all cells), using an existing protocol (Markram et al., 2015). The slices were imaged with a confocal microscope (Zeiss, 710). The immunohistology and imaging of the entire was completed for one P21 C57B1/6J mouse.

4.2.7.2 Semi-automated cell counting and cell densities

The images were aligned to the Allen Reference Atlas to create proper boundaries for the Rt and VPL. We used Imaris® software (Bitmap) to create the Region of Interest (ROI), for counting the neurons and to estimate the volume for density calculation. For a chosen ROI, the software detected the difference of signal intensity, created a 3D shape around the detected cells and extracted statistics (count, positions...) following given parameters. These parameters were defined by running multiple trials so that the results from semi-automated cell counting were as close as possible to those from manual cell counting. The semi-automated counting method have very little error (2,25%) and is less time consuming compared to manual counting. A 3D shape of the entire ROI was created in order to extract the volume for density calculation. Neuron densities were calculated as the ratio between neuron counts in a ROI and the volume as calculated in Imaris for each slice. For modelling we used the average cell densities for Rt and VPL neurons.

4.2.8 Microcircuit geometry

Since the thalamus doesn't have a clear laminar structure, we approximated a thalamic microcircuit to a cylindrical volume having its base parallel a portion of the reticular nucleus

of the thalamus (Rt) and its vertical dimension (y-axis) running through the VPL and Rt. To calculate Rt and VPL thicknesses along the y-axis, we started from the thalamus parcellation from the Allen Brain Atlas version 3 (25 μm resolution) (Allen Institute For Brain Science, 2017; Goldowitz, 2010). A spherical coordinate system was fitted to the bilateral 3D volume of the Rt, which can be approximated to a spheroidal surface. We chose a region of interest (ROI) located approximately in the middle of the VPL nucleus and computed the distribution of widths in the ROI for the VPL and corresponding region of the Rt (aligned along the radius of the sphere). The thickness corresponded to the middle value of the distributions, which was 550 μm for the Rt and 250 μm for the VPL.

The horizontal dimensions of the microcircuit were calculated from the density of the dendritic fibers at the center of the circuit (Markram et al., 2015). For each m-type, we began by considering all the morphologies (after repairing them) that had their somata located within 25 μm from the circuit center on the horizontal (XZ) plane. We then increased the maximal distance in steps of 25 μm which resulted in an increase of dendritic densities at the center. The microcircuit horizontal dimension (radius) resulting from this process was 294 μm , corresponding to the distance where 95% of the asymptotical maximal density of reticular neuron dendrites was reached. As a comparison, considering only thalamocortical cell morphologies, would have resulted in a circuit with radius 125 μm , while with only interneurons the radius would have been 279 μm .

We used a hexagon with the same area as the resulting circle to facilitate tiling of multiple microcircuits, while keeping asymmetrical edge effects minimal. The resulting side of the hexagon was 323 μm and the longest diagonal (vertex-to-vertex) measured 646 μm . When the 7 hexagons were stacked, with a central one surrounded by the 6 others (e.g. Fig. 4.5), the widest dimensions were 1292 x 1680 μm .

4.2.9 Soma positions and models assignment

The horizontal and vertical extents resulted in a microcircuit having the shape of a hexagonal prism, that was 646 μm wide (at the widest point) and 800 μm high; 69 % of the volume was occupied by the VPL and 31 % by the Rt. This volume was then populated by defining somata positions according to the experimentally-measured neuron densities in the Rt and VPL. The positions were distributed according to an algorithm based on Poisson disc sampling (Bridson, 2007; Tulleken, 2009). This algorithm avoids clustering normally obtained with sampling according to uniform distributions, by using a parameter for the minimum distance between points. To calculate the minimum distance, we used the cell densities to calculate the expected number of cell positions per voxel. Each soma position was assigned an m-type according to the excitatory/inhibitory fractions and an electrical model in agreement with the me-types composition (Fig. 2). Moreover, each position was associated with a random rotation around the y-axis to be applied to each morphology.

4.2.10 Morphology placement

Our pool of experimental morphologies and the ones derived from the morphology diversification contained morphologies with different sizes and shapes. Moreover, it contained TC morphologies whose somata was not located in the VPL nucleus and Rt morphologies whose axons were not arborizing in the VPL nucleus. We adapted a placement scoring algorithm (Markram et al., 2015) to ensure that each position was assigned a suitable morphology considering its geometrical properties and the microcircuit vertical dimension. We thus defined placement rules that took into account the known properties of Rt and TC neurons arborizations relative to the anatomical boundaries of thalamic nuclei (Harris, 1986; Pinault et al., 1995).

Each reconstruction of TC and Rt neuron morphologies was manually annotated, in order to identify the putative axonal arborization in Rt for TC cells and the Rt densest axonal arborization, which should be located in the thalamus. Each annotation was carried over during the unravelling, repairing and diversification steps. Moreover, we included a stricter rule to avoid that Rt morphologies were located outside the top of the circuit boundary, with a 30 μm tolerance. Scores were then computed for each rule separately and combined by using a harmonic mean.

4.2.11 Connectivity based on morphological appositions

After placing the morphologies in the 3D microcircuit volume we generate the first version of the connectivity by detecting zones of geometrical overlap (“touches”) using the an existing algorithm (Kozloski et al., 2008; Markram et al., 2015). Briefly, this algorithm sub-divided the circuit 3D space in sub-volumes ensuring that each sub-volume contained the same amount of data, i.e. the same number of morphological segments. Each sub-volume was processed in parallel on different cores and written in parallel to disk. All geometrical overlaps were considered as touches if their distance was smaller or equal to 1 μm (“touch distance”).

Touches were then filtered according to biological rules: touches were allowed between all m-types, except between VPL_IN (interneurons) and Rt_RC (reticular neurons), because interneurons are only located in the thalamus and are not expected to have neurites extending into the reticular nucleus. Touches between VPL_TC and VPL_TC, VPL_TC and VPL_IN were removed, in agreement with experimental findings (see Results section). Interneurons also formed synapses from presynaptic dendrites. For all other m-type combinations, touches formed between presynaptic axons and postsynaptic dendrites and somata. The same algorithm was used to detect touches between Rt_RC dendrites, i.e. the locations of putative gap junctions. Since gap junctions are established with close appositions of cell membranes, we used touch distance of 0 μm in this case. At the end of this process the resulting contacts (or “appositions”) are normally higher compare to experimental findings and are pruned further (Reimann et al., 2015).

4.2.12 Converting morphological appositions into functional synapses

We employed an existing algorithm to decide which appositions were to be converted into functional synapses according to biological constraints (Reimann et al., 2015). The main constraints were the experimental bouton densities (number of boutons / axonal length) from 3D neuron reconstructions (n=9 TC axons and n=2 Rt axons) and the coefficient of variation of number of synapses per connections (i.e. the number of functional synapses, between a pair of neurons) from presynaptic INs and post-synaptic INs and TCs (Morgan and Lichtman, 2020).

In the first two steps, the algorithm tried to match the predicted distribution of synapses per connection, using the coefficient distribution of appositions per connections and the coefficient of variation of synapses per connection. Then, in step 3, it compared the current bouton density to the target value and removed connections until the target value was matched. The number of synapses per connections, N_{func} , was predicted from the number of appositions per connections (N_{app}) resulting from the previous steps, similarly to uncharacterized pathways in cortical microcircuitry (Reimann et al., 2015). N_{func} was predicted from N_{app} according to a simple formula ($N_{func} = 1 \cdot N_{app}$) for each m-type to m-type connection. We used a generalized coefficient of variation for N_{func} of 0.9 for all connections (as extracted from Morgan and Lichtman, 2020, Fig. 3B). Coefficient of variations were combined with the predicted N_{func} to calculate its standard deviation, as detailed in (Reimann et al., 2015). At the end of this pruning process, we verified that the bouton densities in the model matched the experimental ones (see Fig. 4.3A). The shape of a geometric distribution for N_{func} was a prediction from our touch detection process.

4.2.13 Connections from lemniscal and corticothalamic afferents

We followed an approach similar to the generation of thalamic input to the cortical microcircuit model (Markram et al., 2015) to model afferent synapses in the thalamus from the sensory periphery (medial lemniscus) and from cortex. The algorithm uses volumetric bouton densities and the morphologies already placed in a circuit to map afferent synapses from afferent “virtual” fibers to postsynaptic morphologies.

We built medial lemniscus and corticothalamic afferents separately for one microcircuit. Since data for lemniscal innervation in the mouse VPL was not available we calculated volumetric bouton density from data of mouse VPM (Takeuchi et al., 2017). Volumetric bouton densities for the corticothalamic pathway were derived from known proportions between corticothalamic synapses and other synapses onto TC and Rt neurons, as found in electron microscope investigations (see Results for details). Once the algorithm matched the prescribed volumetric bouton densities, we did not perform further pruning of the resulting synapses.

Each synapse was assigned a virtual lemniscal or corticothalamic fiber. A rough estimation of the number of lemniscal fibers is presented in the Results section and took into account the

ratio between the putative number of neurons from the dorsal column nuclei projecting to the thalamus (Shishido and Toda, 2017) and the number of neurons in the VPL (see (Jones, 2007) for a similar calculation). The number of corticothalamic fibers was about ten times the number of thalamocortical fibers in a microcircuit (Crandall et al., 2015; Monconduit et al., 2006; Sherman and Koch, 1986).

To take into account the correlation between synaptic inputs onto postsynaptic neurons innervated from the same afferent fiber, the mapping between postsynaptic synapses and fibers took into account their reciprocal positions, i.e. synapses that were closer together were more likely to be innervated by the same presynaptic fiber. As in the neocortical microcircuit model (Markram et al., 2015), the probability that a synapse was assigned to a fiber depended on the distance between the synapse and the fiber:

$$P(S_{pre} = i) \propto e^{-\frac{|f_i - T_{pre}|}{2\sigma^2}}$$

where S_{pre} represents the mapping of a synapse S to the presynaptic fiber i , T_{pre} is its spatial location, f_i the spatial location of fiber i and σ denoted the degree of spatial mapping, that was set to 25 μm .

4.2.14 Synapse physiology and short-term plasticity

4.2.14.1 Stochastic synaptic transmission and short-term plasticity

We used existing models of stochastic transmission at excitatory and inhibitory synapses (Markram et al., 2015). They consisted of a two state Markov model, where the ensemble average response is equivalent to the phenomenological Tsodyks-Markram model (Fuhrmann et al., 2002; Tsodyks and Markram, 1997). The underlying assumptions were derived from the classical model of quantal synaptic release, in which each synapse is assumed to have N independent release sites, each have a probability p of releasing a single quantum q (del Castillo and Katz, 1954; Korn and Faber, 1991). The number of release sites was assumed to be equivalent to the number of synapses per connections as in (Markram et al., 2015). The detailed implementation of the synapse models can be downloaded from the neuron model packages in the Neocortical Microcircuit Portal (Ramaswamy et al., 2015). In this first version of the model, we did not implement multi-vesicular release (Barros-Zulaica et al., 2019).

We modelled short term synapse plasticity with depressing (E2 and I2) and facilitating synapses (E1). In our experimental recordings, in agreement with experimental findings, all intrathalamic and lemniscal connections were depressing (Cox et al., 1997; Gentet and Ulrich, 2003; Miyata and Imoto, 2006; Mo et al., 2017), while corticothalamic ones were facilitating (Golshani et al., 2001; Miyata, 2007; Mo et al., 2017; Reichova and Sherman, 2004). When sufficient experimental paired recordings data was available, the short-term synaptic parameters (U, D and F) were directly extracted from the EPSPs/IPSPs peaks amplitudes (or

EPSCs/IPSCs in the case of voltage-clamp recordings), evoked by stimulating the presynaptic cell with a train of 8 pulses followed by a recovery pulse (see Fig. 4.4). To find the values for U, D, F, the post-synaptic responses were filtered and deconvolved for easier automatic identification of the peaks (Barros-Zulaica et al., 2019). A multi-objective optimization algorithm was used to find the values for U, D and F (Van Geit et al., 2016). This process was possible for Rt to TC, IN to TC and IN to IN connections; for all the other pathways we followed these generalization rules:

- TC to Rt synapses were shown to be strong, reliable and depressing (Gentet and Ulrich, 2003). We used parameters from L4Exc to L4Exc connections from (Markram et al., 2015) as they had the highest release probability (analogous to the U value in the case of depressing synapses (Ecker et al., 2019)).
- All uncharacterized inhibitory to inhibitory synapses (i.e. Rt to Rt and Rt to IN) had the same dynamics of an inhibitory-inhibitory characterized pathway (i.e. IN to IN).
- Corticothalamic synapses onto first order thalamic nuclei (e.g. VPL, VPM, dLG) have been consistently reported to be facilitating. As we did not have paired recordings to estimate synapse parameters for CT to TC, CT to IN and CT to Rt pathways we took parameters from an excitatory facilitating synapse (E1: L5TTPC-L5MC, Markram et al., 2015).
- Lemniscal inputs to first order sensory thalamic nuclei (e.g. VPM) were shown to be depressing (e.g. see Mo et al., 2017; Reichova and Sherman) and we used parameters from excitatory depressing synapses from (Markram et al., 2015), i.e. E2 synapses for all other excitatory to excitatory connections.

Synapse dynamic parameters in the model were different for each synapse and drawn for truncated gaussian distributions.

Spontaneous miniature potentials (minis) were modelled as independent Poisson processes at each synapse that triggered release at low rates. The spontaneous rate was set to 0.025 Hz for intrathalamic connections and 0.01 for afferent ML and CT synapses.

4.2.14.2 Synapse models

Excitatory synaptic transmission was modelled with AMPA and NMDA receptor kinetics, and GABA_A receptors were used for inhibitory connections. The rise and decay phases of the currents were described by using mono-exponential functions. We used the same values as the cortical synapse models, unless synaptic currents were characterized in thalamic rodent neurons at 34-35 degree C. The rise time and decay time constants for AMPA receptors were 0.2 ms and 1.74 ms, respectively (Häusser and Roth, 1997). For TC to Rt connections the AMPA decay time constant was 1.58 ms and CT afferents to Rt was 2.74 ms (Deleuze and Huguenard, 2016). The rise and decay time constants of the NMDA component were 0.29 and 43 ms (Sarid et al., 2007). The magnesium concentration was set to 1 mM (Jahr and Stevens, 1990) and the reversal potential of the AMPA and NMDA currents was 0 mV. Experimentally

measured ratios of NMDA and AMPA conductances were gathered from the literature and are summarized in Table 4.1 (Arsenault and Zhang, 2006; Deleuze and Huguenard, 2016; Miyata and Imoto, 2006). For pathways where values were lacking we extrapolated them from similar pathways (e.g. the values for CT afferents to VPL_IN was extrapolated from CT afferents to Rt_RC).

Inhibitory synaptic transmission was modelled with GABA_A receptor kinetics. The rise and decay time constants were 0.2 ms and 8.3 ms, respectively. The reversal potential of GABA_A current was set to -82 mV for all inhibitory pathways, except for connections onto postsynaptic TC neurons, where it was -94 mV, consistent with lower chloride reversal potentials in TC compared to Rt neurons (Huguenard and Prince, 1994; Ulrich and Huguenard, 1997).

4.2.15 Constraining synapse conductance values

Synaptic conductance values were optimized by performing *in silico* paired recordings to match the postsynaptic potential (PSP) amplitudes measure experimentally whenever data was available, similarly to other morphologically detailed models (Ecker et al., 2019; Markram et al., 2015). For each pathway, 50 neuron pairs were simulated, and each pair was recorded for 30 trials. Experimentally characterized values in rodents are summarized in Table 4.2. For all other pathways, we extrapolated the quantal synapse conductances from similar pathways, according to the same generalization principles applied for short-term plasticity parameters (see above).

Pathway	Synapse type	g_{syn} (nS)	τ_d (ms)	NMDA/AMPA ratio	U_{SE}	D	F
Rt_RC to Rt_RC	Inh. Dep.	0.9 ± 0.23	8.3 ± 2.2	NA	0.41 ± 0.14	464 ± 339	54 ± 71
Rt_RC to VPL_TC	Inh. Dep.	1.1 ± 0.4	8.3 ± 2.2	NA	0.32 ± 0.18	352 ± 46	2 ± 209
Rt_RC to VPL_IN	Inh. Dep.	0.9 ± 0.23	8.3 ± 2.2	NA	0.41 ± 0.14	464 ± 339	54 ± 71
VPL_TC to Rt_RC	Exc. Dep.	2.8 ± 0.1	1.58 ± 0.26	0.57	0.86 ± 0.09	671 ± 17	17 ± 5
VPL_IN to VPL_TC	Inh. Dep.	0.4 ± 0.4	8.3 ± 2.2	NA	0.47 ± 0.18	137 ± 46	239 ± 209
VPL_IN to VPL_IN	Inh. Dep.	2.7 ± 0.4	8.3 ± 2.2	NA	0.41 ± 0.14	464 ± 339	54 ± 71
ML to VPL_TC	Exc. Dep.	3.4 ± 0.34	1.74 ± 0.18	0.41	0.86 ± 0.09	671 ± 17	17 ± 5
ML to VPL_IN	Exc. Dep.	3.4 ± 0.34	1.74 ± 0.18	0.41	0.86 ± 0.09	671 ± 17	17 ± 5
CT to Rt_RC	Exc. Fac.	0.16 ± 0.016	2.74 ± 0.25	0.99	0.09 ± 0.12	138 ± 211	670 ± 830
CT to VPL_TC	Exc. Fac.	0.16 ± 0.016	1.74 ± 0.18	1.91	0.09 ± 0.12	138 ± 211	670 ± 830
CT to VPL_IN	Exc. Fac.	0.16 ± 0.016	1.74 ± 0.18	0.99	0.09 ± 0.12	138 ± 211	670 ± 830

Table 4.1. Synapse kinetics and short-term plasticity parameters.

Synaptic parameters for all pathways in the model. g_{syn} is the quantal synaptic conductance, τ_d is the decay time constant of AMPA and GABA_A currents for excitatory and inhibitory connections. U_{SE} (utilisation of synaptic efficacy, analogous to release probability), D (time constant of synaptic depression), F (time constant of facilitation) are the short-term plasticity parameters. Values are expressed as mean \pm standard deviation.

Presynaptic	Postsynaptic	PSP amplitude, experiment (mV)	PSP amplitude, model (mV)	Data source
Rt_RC	VPL_TC	$1.33 \pm 0.36^*$	0.36 ± 1.31	In house
VPL_TC	Rt_RC	7.4 ± 1.5	6.79 ± 1.30	(Gentet and Ulrich, 2003)
VPL_IN	VPL_TC	0.55 ± 0.15	1.16 ± 1.56	In house
VPL_IN	VPL_IN	1.66 ± 1.44	0.82 ± 0.77	In house
ML	VPL_TC	4.58 ± 0.30	4.41 ± 1.57	(Mo et al., 2017)
CT	VPL_TC	0.085 ± 0.008	0.071 ± 0.022	(Golshani et al., 2001)

Table 4.2. Postsynaptic potential (PSP) amplitudes.

PSP amplitude values as characterized experimentally through *in vitro* paired recordings. Values are reported as mean \pm standard deviation (of multiple pairs). Values marked by * are for 1 single paired recorded.

Presynaptic	Postsynaptic	CV 1 st PSP amplitude, experiment (mV)	CV 1 st PSP amplitude, model (mV)	Data source
Rt_RC	VPL_TC	0.4600^*	0.8424 ± 0.3450	In house
VPL_TC	Rt_RC	0.1232 ± 0.0686	0.3089 ± 0.2112	(Gentet and Ulrich, 2003)
VPL_IN	VPL_TC	0.5479 ± 0.1744	0.8663 ± 0.386	In house
VPL_IN	VPL_IN	0.5028 ± 0.2783	1.0993 ± 0.4132	In house
ML	VPL_IN	0.3874^*	0.3301 ± 0.1995	In house

Table 4.3. Coefficient of variation (CV) of first PSP amplitudes.

C.V. of first PSP amplitudes values as characterized experimentally through *in vitro* paired recordings. Values are reported as mean \pm standard deviation. Values marked by * are for 1 single paired recorded.

4.2.16 Gap junctions

We used the same algorithm described above to find appositions between Rt neuron dendrites and a fraction of this appositions was converted into functional gap junctions. We iteratively removed a constant fraction of all gap junctions from each neuron, until each neuron was coupled to 5-20 other neurons through gap junctions (Lee et al., 2014), see Fig. 4.5. To analyse the number of coupled neurons and their spatial properties (Fig. 4.5), we reproduced the protocol from Lee et al., by analysing a sample of 33 Rt neurons in a 90 μm vertical slice in the microcircuit.

Once the structural properties of gap junctions-coupled neurons were validated, we performed *in silico* paired recordings and measured the coupling coefficients for each pair of neurons. We found that the mean coupling coefficients in the model compared well with the experiments for gap junction conductance values of 0.2 nS.

Not surprisingly, after adding gap junctions to the circuit, the neurons input resistance changed. To guarantee that the passive properties of the neurons did not change, thus changing the responses to synaptic inputs, we devised an algorithm to compensate for the change in input resistance (Amsalem et al., 2016). The algorithm changed the conductance of the leak current (g_{pas}) to restore the input resistance of the neuron before adding gap junctions. This compensation resulted in a different g_{pas} value for each neuron.

4.2.17 Simulation software and high-performance computing resources

The reconstructed microcircuit was simulated using software based on the NEURON simulation package (Hines and Carnevale, 1997). A collection of tools and templates were written in order to handle simulation configuration, *in silico* network experiments and to save the results. Moreover, NEURON compute engine has been extracted and in a software called CoreNEURON (Kumbhar et al., 2019). A typical simulation run of a microcircuit for 3500 ms of simulation time took around 45 minutes on Intel Xeon 6140 CPUs (288 cores, with HyperThreading enabled).

4.2.18 Simulating *in vivo*-like conditions

To simulate spontaneous activity *in vivo*-like states we depolarized all the neurons from their resting potential to around -65 mV, a level at which thalamocortical and reticular neurons fire single spikes rather than bursts, and activated lemniscal and corticothalamic fibers with Poisson spike trains at 2.5 and 1 Hz, respectively. We lowered the extracellular calcium concentration from 2 mM (*in vitro*-like conditions) to 1.2 mM, with the effect of reducing synapse release probabilities and postsynaptic potential amplitudes (PSPs). PSPs depended on calcium concentration as uncharacterized pathways in (Markram et al., 2015, Fig. S11 – Intermediated $[\text{Ca}^{2+}]_o$ dependence).

4.2.19 Simulating *in vitro*-like conditions

In these conditions all the neurons were left at their resting potentials (which ranged between -75 and -70 mV) and the only source of input was the spontaneous release from intrathalamic (at a rate of 0.025 Hz), medial lemniscus and corticothalamic synapses (at a rate of 0.01 Hz). The extracellular calcium concentration was set to 2 mM.

4.2.20 Simulating depolarization levels

As a first approximation of the action of neuromodulators in the VPL and Rt, we applied constant current injections to the soma of each neuron. All the neurons in the VPL or Rt regions were depolarized to the same target baseline membrane potential. The amplitude of the current was different for each neuron, to take into account the different input resistance of each morpho-electrical model.

4.2.21 Simulation analysis

For calculating oscillation duration (number of cycles) we used firing rate histograms of TC neurons and extract their peaks, using the `scipy.signal.find_peaks` function (see example in Fig. 4.10). We used TC, rather than Rt neurons, because oscillations occurring in the former are more directly linked to signals that would be transmitted to the neocortex. Peaks were counted only if they were significantly higher than baseline firing rates.

Oscillation frequency was calculated from the first non-zero peak of the firing rate histogram autocorrelation of TC neurons.

For the cycle by cycle analysis of the percentage of neurons firing (Fig. 4.9 and 4.10), we calculated oscillation peaks from the firing rate histograms of TC neurons, in the same way as we calculated peaks for the oscillation duration. We then added a peak corresponding to the time of the stimulus injected into Rt neurons (cycle 0). Spikes for each m-type were then assigned to the different cycles if they occurred within 30 ms of the oscillation peak.

4.3 Results

4.3.1 Morphological properties of thalamic and reticular neurons

To build a detailed model of thalamic microcircuitry, we started by collecting >90 three-dimensional reconstructions of neuronal morphologies of thalamocortical neurons (TCs), thalamic interneurons (INs) and neurons of the reticular nucleus of the thalamus (Rt). Neurons were reconstructed from *in vitro* and *in vivo* labelling experiments in the mouse (see Methods). We classified the reconstructed morphologies into 3 broad classes, or morphological types (m-types).

4.3.1.1 Experimental data

Reconstructions of thalamocortical neurons included *in vitro* and *in vivo*-labelled neurons and axons from the open-access MouseLight Project at Janelia (Winnubst et al., 2019). We obtained 96 morphologies whose soma was located in the thalamus and we visually inspected their shape along with 3D meshes of the reticular nucleus of the thalamus. Since most thalamocortical neurons project to the Rt on their path to the cortex (Clascá et al., 2012; Lam and Sherman, 2011) we selected the 41 morphologies which gave off collaterals in the reticular nucleus. We assumed that neurons without collaterals in the Rt were partially labelled and/or reconstructed, since those collaterals are often very thin (Harris, 1987). To increase the biological variability of the reconstructions and the robustness of the derived connectivity (Hill et al., 2012; Ramaswamy et al., 2012), we included axons from different thalamic nuclei and asked whether the geometrical properties of the Rt axonal collaterals were different. After analyzing the length of the arborizations in the Rt (see Methods), we found that the difference within the same nucleus was as high as the difference between nuclei. We concluded that using axons from different thalamic nuclei would have not altered the geometrical properties of the model.

3D morphologies of reticular neurons were obtained from whole brain neuron reconstructions from a SSt-Cre;Ai139 mouse line and *in vitro*-labelled neurons, while interneurons were reconstructed from *in vitro* experiments on GAD67-eGFP mice (see Methods).

4.3.1.2 Morphological types

We then attempted to classify TC, Rt and IN morphologies into different classes. Although we could subjectively distinguish different types of TC morphologies, considering the number and angles of dendritic branches, as reported in the dorsal lateral geniculate nucleus (Krahe et al., 2001; Ling et al., 2012; McAllister and Wells, 1981), we could not objectively identify these classes using recent quantitative methods (Kanari et al., 2018). We obtained similar results for reticular morphologies, when considering differences in soma shape and dimension, dendritic extent and branching patterns reported previously (Deleuze and Huguenard, 2016; Spreafico et al., 1991). We found that reticular neurons had axonal arborizations similar to what reported previously in the rat, with a main arborization that was more or less dense (Cox et al., 1997) and, occasionally, distinct axonal branches that putatively projected to different nuclei (Pinault and Deschênes, 1998).

For the purpose of this work, we classified the morphologies into three main types (Fig. 4.1A). To assign a name to each m-type we followed a scheme similar to (Markram et al., 2015): *BrainRegion_MorphologicalType*. We grouped all thalamocortical (TC) morphologies in one morphological type (m-type), called VPL_TC. Similarly, the m-type corresponding to the interneurons was called VPL_IN. One m-type, reticular cell of the reticular nucleus of the thalamus Rt_RC, grouped all morphologies in the reticular nucleus.

We extended an existing algorithm to statistically recover dendrites from slicing artifacts (Anwar et al., 2009; Markram et al., 2015) of *in vitro* labelled neurons and validated the results against *in vivo* labelled reconstructions. We then used a validated pipeline to generate a large dataset of thalamic and reticular morphologies (n=92970) that respected the biological variability (Markram et al., 2015), in a process called morphology diversification (see Methods).

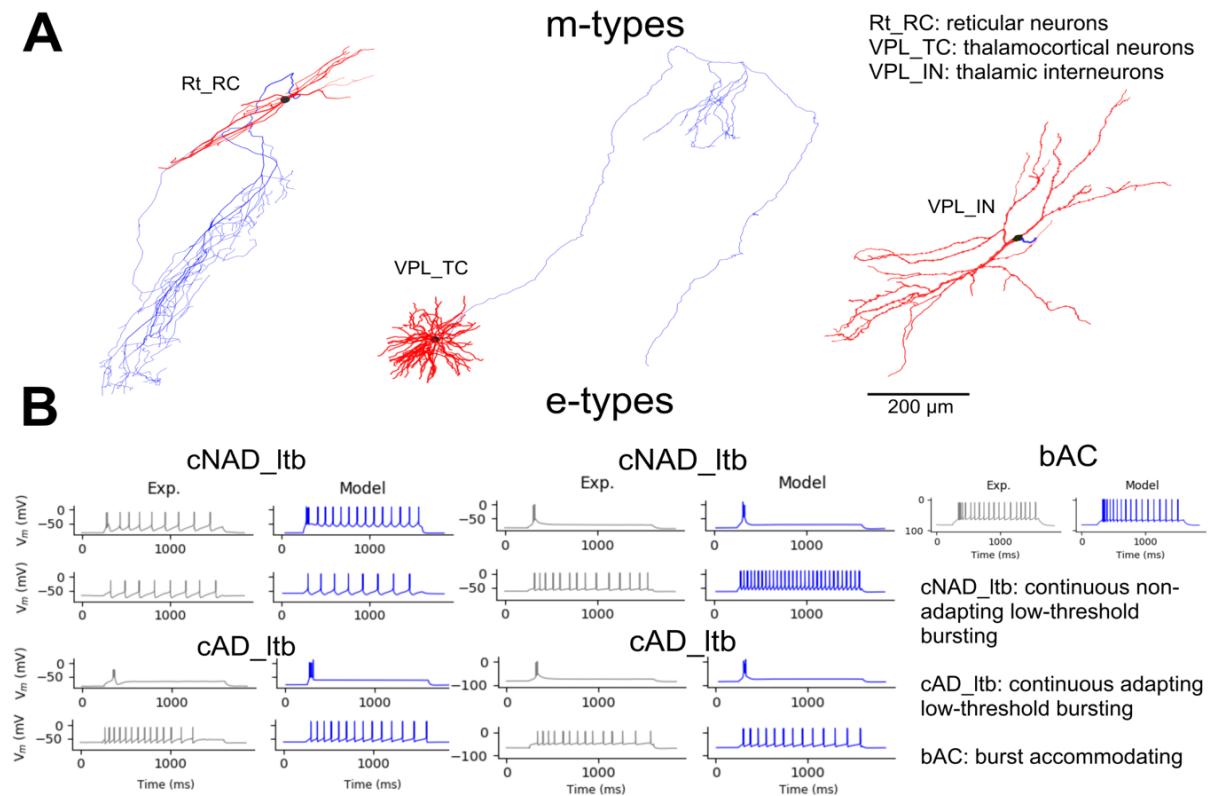


Figure 4.1. Single cell data and models

(A) Exemplar 3D reconstructions of 3 thalamic morphological types (m-types) from the mouse. Axon in blue, dendrites in red, soma in black. For the VPL_TC m-type, the part of axon projecting to the neocortex is omitted. All the reconstructions are shown on the same scale (scale bar corresponds to 200 μ m). (B) Electrical types (e-types) and corresponding electrical models. From left to right: exemplar recordings (grey) and models (blue) corresponding to Rt_RC, VPL_TC and VPL_IN m-types. For cNAD_ltb and cAD_ltb e-types two distinct firing modes are shown: low threshold-bursting (first row) and tonic firing (second row).

4.3.2 Neurons electrical properties and models

We characterized 5 electrical types of thalamic neurons and built morphologically-detailed multicompartmental neuron models for each of them. Ion channel models were derived from literature findings and their peak conductances were constrained by using a multi-objective optimization algorithm (Druckmann et al., 2007; Hay et al., 2011; Iavarone et al., 2019). This algorithm used electrical features (such as spike amplitude, firing frequency,...) extracted from *in vitro* patch-clamp recordings. To validate the neuron models we used features from current stimuli not used during the optimization phase and dendritic attenuation properties from the literature (Connelly et al., 2016).

4.3.2.1 Experimental data and electrical types

We characterized the firing behavior of more than 100 thalamocortical neurons, interneurons and reticular neurons through patch-clamp recordings in brain slices of the mouse. TC and IN neurons were located mainly in the VPL and VPM nuclei of the thalamus and Rt neurons in the somatosensory sector of the Rt (Lam and Sherman, 2011; Pinault and Deschênes, 1998). VPL_TC and Rt_RC neurons were recorded with the injection of two different holding currents, to characterize their two firing modes: low-threshold bursting and tonic firing at hyperpolarized and depolarized membrane potentials, respectively (see Methods and Fig. 1B).

For classifying the electrical types (e-types) we took into account the voltage responses to current steps and we assigned name to the e-types by following the Petilla convention for the tonic firing responses (Ascoli et al., 2008; Markram et al., 2015). We added a suffix (*_ltb*) for the low-threshold bursting properties of TC and Rt neurons. We classified TC neurons in adapting (cAD_ltb) and non-adapting types (cNAD_ltb) by considering their tonic firing responses (Fig. 4.1B). These e-types were similar to the ones we identified for rat TC cells (Iavarone et al., 2019). We found similar adapting and non-adapting responses in Rt_RCs.

Other firing patterns have been described for reticular neurons, when considering low-threshold firing responses (Clemente-Perez et al., 2017; Lee et al., 2014, 2007). In our dataset, we mainly observed neurons with an intermediate burst propensity, which fired typically 1-2 bursts, followed by tonic firing for higher stimuli amplitude, similar to the “Typical Burst” type, which is more common in somatosensory sectors of the Rt (Lee et al., 2007). We found 1 Rt neuron that had a very deep after-hyperpolarization (AHP) and tended to fire in bursts for the whole duration of the stimulus and 2 Rt neurons which did not fire low-threshold bursts at any level of membrane hyperpolarization, as described previously (Lee et al., 2014, 2007). Since we did not have enough recordings of these other Rt bursting types, we did not include them in this first version of the model.

With our standard set of stimuli protocols (see Methods), interneurons did not generate low-threshold bursts. Since they tended to initially fire action potentials with short interspike intervals, we classified all IN recordings as one e-type, called burst accommodating (bAC). It is possible that bursting and oscillatory behaviors can only be observed in more hyperpolarized conditions (Zhu and Lo, 1999).

4.3.2.2 Constraining and validating morpho-electrical models

We have shown previously that a multi-objective optimization pipeline (Druckmann et al., 2007; Hay et al., 2011) can be applied to capture different firing modes of thalamocortical neurons (Iavarone et al., 2019). We applied a similar strategy to build electrical models (e-models) for the e-types shown in Fig. 4.1B (see Methods). In brief, we used electrical features (e.g. action potential amplitude, number of spikes per burst) extracted from the experimental recordings, in combination with one exemplar morphology, as constraints for the ion channel peak conductances. Active membrane mechanisms were present in all cellular compartments (i.e. soma, dendrites and axonal initial segment). To build e-models for Rt_RC cells, we started from the same ion current kinetics of VPL_TC cells and added electrical features to quantify the deeper AHP after the burst of Rt_RCs.

The resulting e-models were tested with stimuli not used during the fitting step (Iavarone et al., 2019) and with synaptic-like inputs to assess the attenuation properties along the dendrites (data not shown), whenever experimental data was available (Connelly et al., 2016). In this way, we created five e-models, one for each e-type, and combined them with the 92970 morphologies generated during the morphology diversification step. We assessed the quality of each morphology-electrical model combination (me-model) and rejected those having electrical features and firing behavior significantly different from the experimental data (see Methods).

4.3.3 Microcircuit dimension and composition

The reconstruction began by defining a microcircuit with its dimension, the percentage of inhibitory neurons, the percentage of neurons for each m-type and e-type. For constraining the dimensions, we used the 3D reconstructed morphologies and the thickness of VPL and Rt from the Allen Brain Atlas (Goldowitz, 2010). Experimentally-measured neuron densities and fraction of inhibitory neurons were used to predict the number of neurons for each m-type. The reconstruction yielded a microcircuit with the shape of a hexagonal prism, with a base of 323 μm in length, height of 800 μm and consisting of ~14000 neurons.

4.3.3.1 Reconstructing microcircuit dimensions

We started by defining a thalamic microcircuit as a cylindrical volume spanning a portion of the ventral posterolateral nucleus of the thalamus (VPL) and the reticular nucleus of the thalamus (Rt). Its longest (vertical) dimension run through the two nuclei, with the Rt as the topmost region (Fig. 4.2). We chose the VPL nucleus because it receives information from the hindlimb (Francis et al., 2008) and relays it to the somatosensory cortex; the corresponding cortical microcircuit was reconstructed in (Markram et al., 2015). The Rt is intimately associated with the different thalamic nuclei and it is the main source of inhibition to the thalamus (de Biasi et al., 1986; Cavdar et al., 2013; Houser et al., 1980; Pinault, 2004). Since the VPL does not have a clear modular organization, we decided to follow the same approach as in (Markram et al., 2015) to define the microcircuit radius and its height (see Methods).

We placed reconstructed morphologies in a cylindrical volume and calculated the minimal radius of a cylinder where the density of the dendrites saturated at the center. We found that the largest radius was obtained when we placed reconstructed morphologies of Rt_RC neurons. This resulted in a radius of 294 μm , corresponding to 95 % of the density asymptotic value (Fig. 4.2B). Defining the circuit height consisted in calculating the thickness of the Rt and VPL nuclei along the major (vertical) axis. The thickness values were derived from the Allen Brain Atlas and the resulting values were 250 μm for Rt and 550 μm for VPL, yielding an overall microcircuit height of 800 μm (see Methods for details).

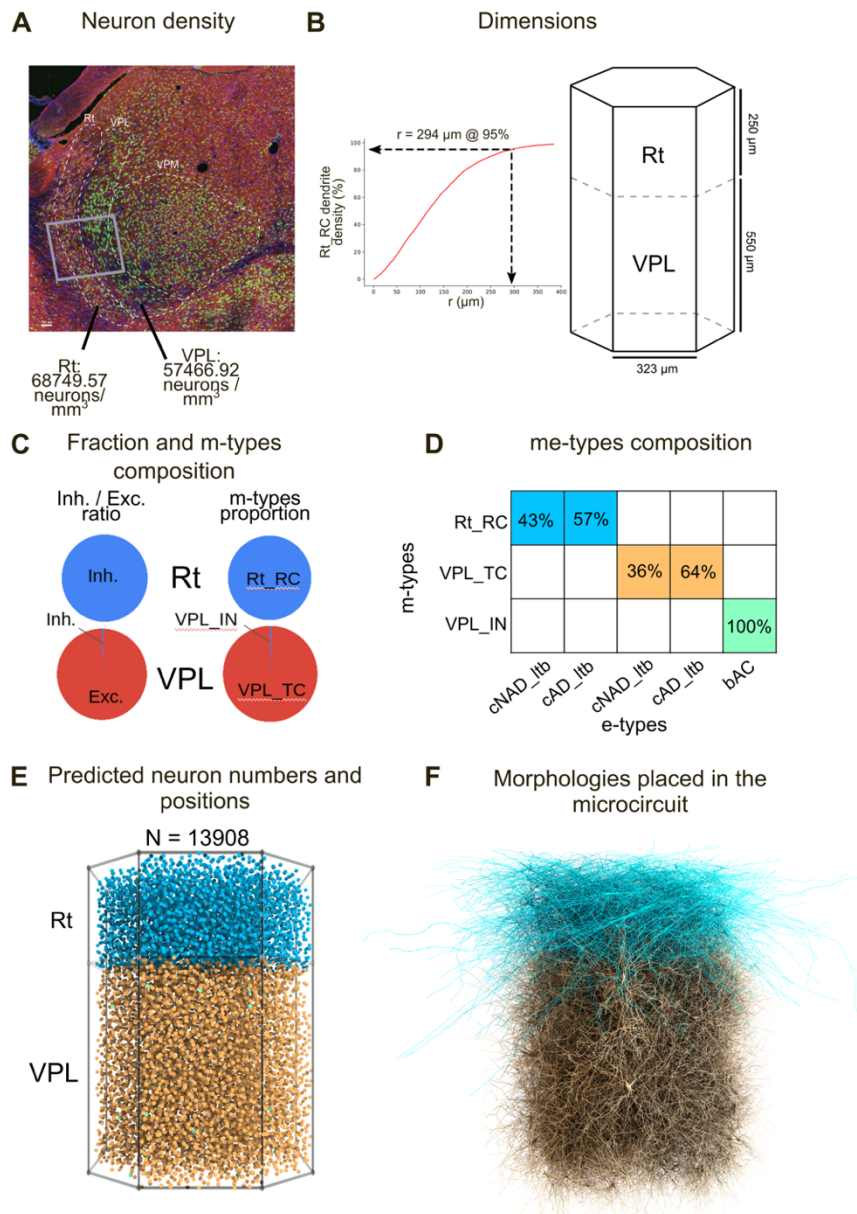


Figure 4.2. Reconstructing neuron densities, composition, microcircuit dimensions and neuron placement

(A) Mean neuron densities in the reticular nucleus (Rt) and the ventroposterolateral nucleus (VPL) nucleus of the thalamus. Confocal imaging of an exemplar slice after staining with anti-GABA (red), anti-NeuN (green) and DAPI (blue). Brain regions outlines were drawn after the

alignment of the slice with the Allen Reference Atlas. The grey box represents a thalamic microcircuit. **(B)** Microcircuit dimensions (lateral and vertical dimensions). Left: the lateral dimension was the smallest circle for obtaining saturated Rt_RC dendritic density. The cut-off radius at 95 % of the plateau density was 294 μm . Right: vertical dimensions of the Rt and VPL regions as calculated from the Allen Reference Atlas (see Methods). **(C)** Excitatory/inhibitory fractions and m-types composition. Inhibitory fractions as reported in the Mouse Cell Atlas (Erö et al., 2018). **(D)** Fraction of e-types corresponding to each m-type as found in our single cell recordings. **(E)** Predicted neuron numbers and soma positions in the microcircuit. **(F)** Morphologies placed in the microcircuit, only ~10 % of the neuron densities is shown and axons are omitted for clarity.

4.3.3.2 Reconstructing neuron numbers and composition

Once we established the microcircuit volume, we distributed the neurons according to densities and excitatory/inhibitory ratios measured experimentally (Fig. 4.2A and 4.2C). We obtained neuron counts through semi-automated cell counting in consecutive sagittal slices of the mouse brain and divided those numbers by the calculated volume (see Methods). We found an average cell density of 68750 ± 1976 cells/ mm^3 for Rt and 57467 ± 5201 cells/ mm^3 for the VPL (mean and standard deviation for multiple slices from one brain).

We next collected information on the inhibitory and excitatory neuron ratios in the microcircuit regions (Fig. 4.2C). As reported in many studies (de Biasi et al., 1986; Houser et al., 1980; Pinault, 2004), 100% of neurons in Rt were inhibitory. In this first draft, we included 0.5% of inhibitory cells in the VPL, according to an open-access cell atlas for the mouse brain (Erö et al., 2018). The cell atlas is a resource that integrates whole brain Nissl and gene expression stains to predict neuron densities and positions. The proportion of inhibitory neurons in the VPL will be re-evaluated when more data will become available, since some studies reported around 3.7% of GABAergic cells in the VPL of the rat (Cavdar et al., 2014).

As a result, the microcircuit was populated with 4909 Rt_RCs, 8952 VPL_TCes and 47 VPL_TCes (for a total of ~14000 neurons).

Once we had obtained the inhibitory and excitatory cells densities, by multiplying the overall densities by the inhibitory and excitatory ratios, the morphological and electrical types composition (me-composition) was directly determined (Fig. 4.2D): the reticular nucleus (Rt) had 100 % of inhibitory neurons of m-type Rt_RC. Each Rt_RC neuron had one of two e-types (57 % cAD_ltb and 43 % cNAD_ltb). In the VPL, all inhibitory neurons corresponded to the VPL_IN m-type and bAC e-type. The excitatory neurons in VPL, which corresponded to thalamocortical cells (m-type VPL_TC), had e-type cAD_ltb (64 %) or cNAD_ltb (36 %). The percentage of e-types for each m-type (e-type fractions) were derived from our *in vitro* electrophysiological recordings (Fig. 4.1D).

4.3.3.3 Soma positions and morphology placement

After establishing dimensions and the number of neurons for each me-type, we generated somata positions using an algorithm to fill the space, ensuring that somata were not overlapping and that neurons were uniformly spaced between each other (see Methods). Once neuron positions were defined, we used an algorithm to select the morphology that best fulfilled the anatomical constraints of the microcircuit (Markram et al., 2015). The logic followed was based on experimental findings showing that the axons of reticular neurons point towards the different thalamic nuclei of the thalamus (Pinault and Deschênes, 1998) and that thalamocortical cells have axonal collaterals projecting to the reticular nucleus (Harris, 1986; Monconduit et al., 2006). To choose the best morphology for each position, we manually annotated these patterns on each reconstructed morphology and calculated their overlap with the microcircuit subregions (see Methods).

4.3.4 Reconstructing and validating the connectivity

We applied an existing algorithm to build detailed connectivity between each individual neuron morphology in the microcircuit (Markram et al., 2015; Reimann et al., 2015). Detailed anatomical studies found a linear relation between the available dendritic surface in the thalamus and bouton numbers on reticular axons (Pinault and Deschênes, 1998). This finding suggested that connectivity in the thalamus, at least between Rt and TC neurons, could be predicted by the statistical overlap between neurites (Hill et al., 2012).

To build the connectivity, we used as experimental constraints the neuron morphologies placed in the microcircuit and the available data on axonal bouton densities on 3D reconstructed morphologies (number of boutons/axonal length). We included synapses from medial lemniscus (ML) and corticothalamic (CT) afferents by using volumetric bouton densities as constraints.

As an initial validation of the predicted connectivity, we compared the synapse convergence onto reticular neurons (Liu and Jones, 1999) and the distribution of number of synapses per connections in the model when experimental data was available (Morgan and Lichtman, 2020).

4.3.4.1 Reconstructing intrathalamic connectivity

We started by finding algorithmically all the appositions between the neuron morphologies, i.e. potential synapses, and removed them until experimental constraints were met (see Methods for details, Fig. 4.3A). Along with the space available on the morphologies, we used as constraint the bouton densities (number of boutons / axonal length) on the axons of Rt_RCs and VPL_TCs (Fig. 4.3A). In our experimental dataset, we found that TCs had on average 0.102 ± 0.021 boutons / μm ($n = 9$ axons) and Rt neurons 0.124 ± 0.002 boutons / μm ($n = 2$ axons).

Connections in the model were allowed to form between all m-types, except for VPL_TCs to VPL_TCs and from VPL_TCs to VPL_INs. Connections between VPL_TCs are likely to

disappear during development (Lee et al., 2010), while we could not find any experimental evidence of connections between TCs and INs, neither in the ventrobasal thalamus, nor in the visual thalamus, where INs are present in higher proportions (Arcelli et al., 1997; Evangelio et al., 2018; Jager et al., 2019). Connections between all m-types were formed by presynaptic axons and postsynaptic dendrites and somata, while those formed by INs were largely established by presynaptic dendrites, as shown the visual thalamus (Morgan and Lichtman, 2020; Sherman, 2004).

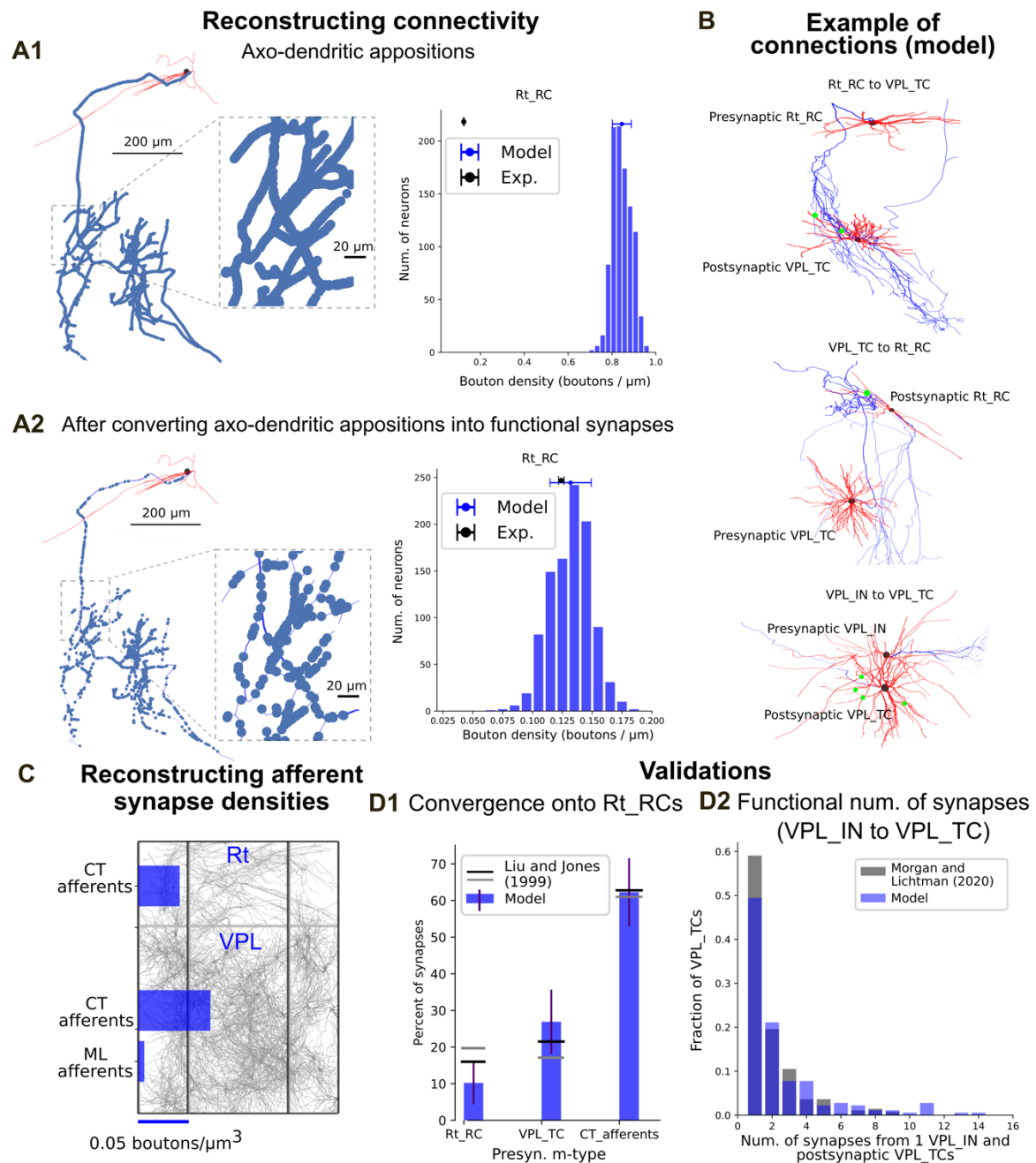


Figure 4.3. Reconstructing and validating intrathalamic and afferents connectivity

(A1-2) Constraining intrathalamic connectivity using neuron morphologies and bouton densities. **(A1)** As a first step, axodendritic appositions are used as location of putative synapses. The connectivity based on these appositions is characterized by high numbers of bouton densities (number of boutons / axonal length). Left: the location of putative synapses is shown for an exemplar Rt_RC neuron (red: dendrites, blue: axon, black: soma). Right: distribution of bouton density for 1000 Rt_RC morphologies in the model and mean and std in the experiment (n=2 Rt_RC morphologies). **(A2)** The experimental bouton densities are used as constraint to convert only a fraction of axodendritic appositions into functional synapses (see Methods for details). **(B)** Example of the resulting mono- and multi-synapse connections between pairs of neurons in the model. Green dots represent the location of functional synapses. Third row is an example of dendrodendritic inhibitory synapses between VPL_IN and VPL_TC. **(C)** Reconstructing functional connectivity from external afferents, using volumetric bouton densities as constraint. Synapses from medial lemniscus afferents (ML afferents) are included in the VPL region (onto VPL_TCs and VPL_INs). Similarly, corticothalamic synapses (from CT afferents) are added to all m-types in the model. **(D)** Validation of the resulting functional connectivity. **(D1)** Validation of synapse convergence onto Rt_RC neurons in the model (n=4909) was validated against electron microscope (EM) experiments in the rat (2 Rt neurons from Fig. 5C in Liu & Jones (1999), grey and black horizontal lines). Bars and vertical lines show mean and standard deviation in the model. **(D2)** Validation of the distribution of synapses per connection. 1 VPL_IN in the model was compared to findings from an EM reconstruction of 1 dLG interneuron in the mouse (Morgan & Lichtman, 2020).

4.3.4.2 Prevalence of mono-synaptic connections in the reconstructed connectivity

An important difference between the reconstruction of connectivity in the cortical and thalamic microcircuit models is that we did not explicitly remove connections between neurons if they shared only one contact (Reimann et al., 2015; Markram et al., 2015), because we did not have any direct anatomical data supporting that. Rather, a recent electron microscope reconstruction of a IN in the visual thalamus, showed that most connections from INs involve only one functional synapse (Morgan and Lichtman, 2020).

The resulting distributions of number of functional synapses per connections, i.e. the number of functional contacts between a pair of neurons, followed geometric distributions, similar to the one shown in Figure 4.3D2. Most of the m-type to m-type connections had 60-70% of pairs with one synapse, with the exception of Rt_RCs to VPL_TCs, where most of the connections had 2 (30%) or more synapses (70%).

4.3.4.3 Reconstructing connectivity from lemniscal and corticothalamic afferents

By following similar principles, we included synapses from extrathalamic sources (see Methods), i.e. from the sensory periphery through the medial lemniscus (ML) and cortex (corticothalamic afferents, CT). We used as experimental constraints the volumetric bouton densities of lemniscal synapses in the mouse VPM (Takeuchi et al., 2017), since data for the VPL was not available (Fig. 4.3C). For CT afferents, we used the relative proportions of corticothalamic to lemniscal synapses onto TCs in the VB (around 12) and the ratio of CT to TCs synapses in the reticular nucleus (around 2.8) (Çavdar et al., 2012; Mineff and Weinberg, 2000). Lemniscal synapses were assigned to 1814 virtual fibers (see Methods for details); this number was estimated by taking into account the number of TCs in the model, the number of

VPL neurons and number of dorsal column nuclei (DCN) projecting to the thalamus (Shishido and Toda, 2017). We used a cell mouse atlas (Erő et al., 2018) to determine the number of excitatory neurons in the VPL and DCN. The number of CT fibers was 75325, consistent with data reporting a ratio of ~ 10 between CT afferents and the corresponding TC neurons (Crandall et al., 2015; Monconduit et al., 2006; Sherman and Koch, 1986).

4.3.4.4 Validating the connectivity

Although anatomical data to constrain thalamic connectivity was extremely sparse, we were able to reproduce some experimental findings not used so far (Fig. 4.3D), such as the relative contributions of synapses from different sources onto Rt morphologies (Liu and Jones, 1999) and the shape of the distribution of synapses per connection between INs and TCs (Morgan and Lichtman, 2020). We found that the percentage of Rt synapses onto other Rt neurons was slightly lower (mean around 10% in the model, 17-20% in the experiment) than what reported for the rat, while the percentage of TC synapses were slightly higher (25% in the model compared to around 20% in the experiment). The reasons of these differences will be investigated in the future.

Clearly, the proposed anatomical connectivity is a first draft that will be challenged and refined when new experimental data become available.

4.3.4.5 Predicted synapse numbers, afferent and efferent neuron numbers

We found that each neuron in the microcircuit projected on average to 246 ± 88 other neurons (mean \pm std, sample of 1000 neurons); each Rt_RC neuron projected to 64 ± 28 Rt_RCs and 136 ± 60 VPL_TC; each VPL_TC projected to 34 ± 46 Rt_RC neurons; VPL_IN sent efferents on average to 220 VPL_TC (± 78.0). In a mesocircuit, which is constituted by a central microcircuit, surrounded by 6 others (see Fig. 4.5A), we found a total of 38.8 million synapses. Each neuron received inputs on average from 203 ± 41.0 other neurons. Each Rt_RC neurons received inputs from 28 ± 15 other Rt_RCs and 74 ± 28 VPL_TC, while VPL_TC were contacted on average by 75 ± 32.0 Rt_RCs.

In a preliminary investigation, we determined the relative proportions of closed and open-loop configurations between Rt_RCs and VPL_TC. We found that closed-loops were present in our model and that they were a minority of the connections, in qualitative agreement with experimental findings (Gentet and Ulrich, 2003; Pinault and Deschênes, 1998a; Shosaku, 1986). As a starting point for this analysis, we considered all connected VPL_TC to Rt_RC (or Rt_RC to VPL_TC) pairs and for each presynaptic neuron we counted how many among its postsynaptic neurons it received input from. In this way we found that percentage of closed-loops was always lower than 10%. It is worth noticing that this analysis is not directly comparable with experimental findings, since it explicitly considers connected neurons.

4.3.5 Reconstructing and validating synapse physiology

Once we created a first draft of the anatomical connectivity, we constrained synapse physiology with available experimental and literature data.

To model synapse kinetics, we used existing models of synaptic currents (Markram et al., 2015) and included literature findings on decay time constants, the relative contribution of AMPA, NMDA, GABA_A and GABA_B currents (Warren et al., 1994; Zhu and Lo, 1999; Deleuze and Huguenard, 2016; Miyata and Imoto, 2006; Arsenault and Zhang, 2006), summarized in Table 4.1.

To model short-term synaptic plasticity and stochastic transmission, we used existing models (Tsodyks and Markram, 1997; Fuhrmann et al., 2002; Markram et al., 2015) and constrained their parameters with available thalamic data, by integrating literature findings and in house paired recordings (Cox et al., 1997; Gentet and Ulrich, 2003; Castro-Alamancos, 2002; Miyata, 2007; Mo et al., 2017; Connelly et al., 2016; Crandall et al., 2015; Cruickshank et al., 2010; Jurgens et al., 2012).

To constrain the synaptic conductance (g_{syn}) value we collected information on postsynaptic potential (PSP) amplitude and scaled g_{syn} to reproduce the experimentally-reported PSPs.

We validated synapse physiology in the model by performing *in silico* paired recordings and comparing PSP properties (amplitude and coefficient of variation) with the experiments.

As a result, we obtained an initial map of synapse types in a thalamic microcircuit with its external afferents, consistent with the available experimental data (Fig. 4.4).

4.3.5.1 Reconstructing and validating short-term synaptic plasticity

We identified 3 synapse types: inhibitory depressing (I2), excitatory depressing (E2) and excitatory facilitating (E1), (Ecker et al., 2019; Markram et al., 2015).

Short-term plasticity parameters were directly extracted from our experimental recordings when data was available (Fig. 4.4A) or generalized from similar pathways (see Methods and Table 2). Synapse types for VPL_TC to Rt_RC and Rt_RC to VPL_TC were consistent with literature findings showing that they are depressing and that VPL_TC to Rt_RC connections are more depressing than Rt_RC to VPL_TC (Cox et al., 1997; Gentet and Ulrich, 2003). Connections from presynaptic interneurons have never been characterized in the somatosensory thalamus of the rodent and we found that they were depressing as well.

For some connections, such as extrinsic synapses from ML and CT fibers, we found information in the literature regarding their short-term plasticity types, but experiments were limited to the analysis of two consecutive EPSPs (paired-pulse ratios). In those cases, parameters were predicted from similar pathways from our recordings or from the neocortical microcircuit model (Markram et al., 2015, see Methods for details, Fig. 4.4B). Short-term plasticity types in the model were consistent with data reporting that lemniscal synapses are

depressing (Castro-Alamancos, 2002; Miyata, 2007; Mo et al., 2017) and that corticothalamic synapses are facilitating (Connelly et al., 2016; Crandall et al., 2015; Cruikshank et al., 2010; Jurgens et al., 2012; Miyata, 2007).

Stochasticity of synaptic transmission was modelled as in reported previously (Fuhrmann et al., 2002; Markram et al., 2015). As independent validation of the and short-term plasticity model we compared the coefficient of variation (c.v.) of first PSPs against experimental data (Fig. 4.4 C1 and Table 4.3).

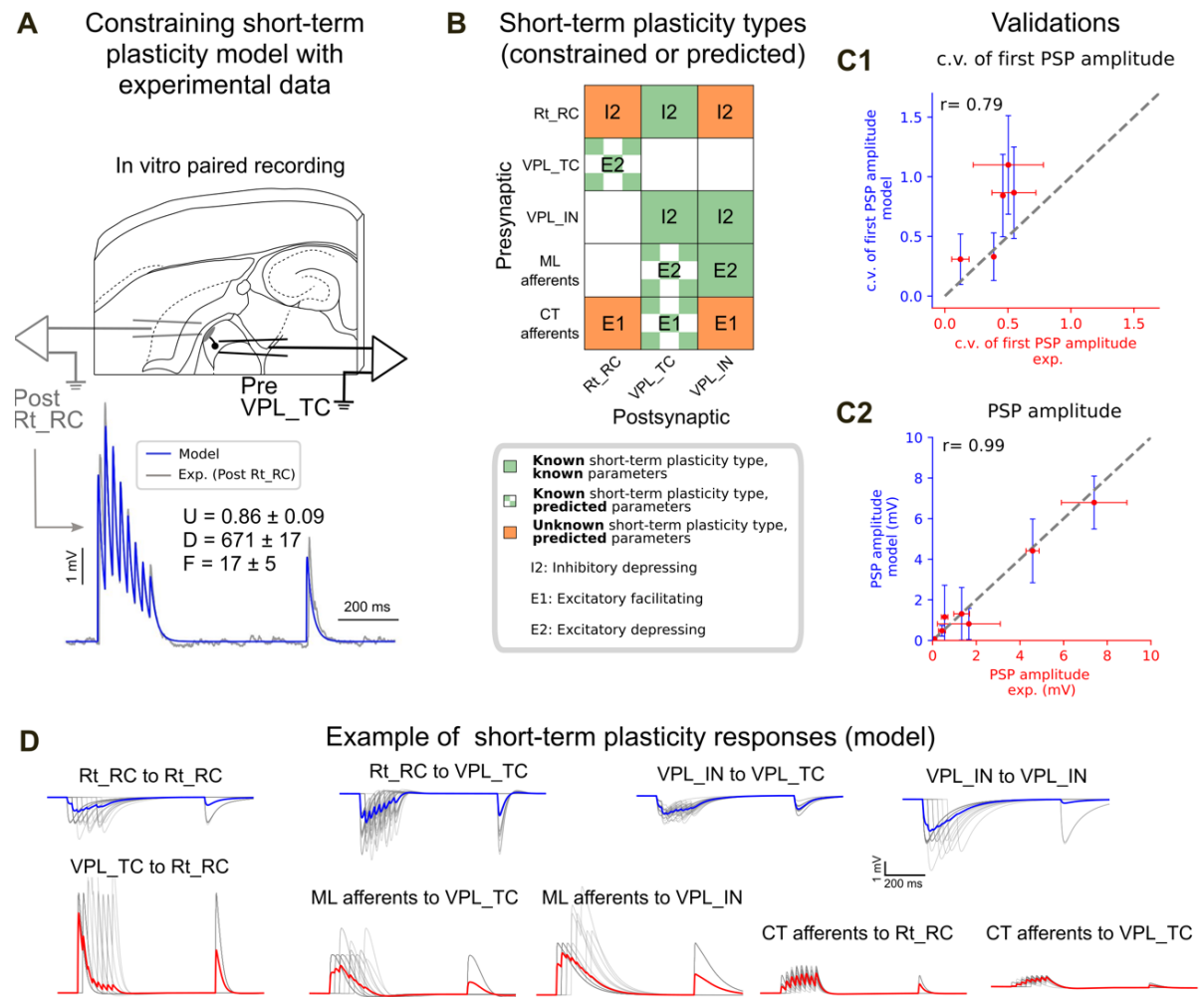


Figure 4.4. Reconstructing and validating synaptic short-term plasticity and postsynaptic potentials (PSPs) amplitude

(A) Top: illustration of *in vitro* paired recordings, used to constrain the parameters of the Tsodyks-Markram model of short-term plasticity. A presynaptic VPL_TC neuron (black pipette) was stimulated with 40 Hz pulses followed by a recovery stimulus. The response in a postsynaptic Rt_RC neuron (grey pipette) was recorded and used to constrain the model parameters (U , D , F). (B) Map of synapse types in the model. Green: in house experimentally-characterized pathways (as in A), green checked: pathways for which the synapse type was derived from literature and parameters were generalized from similar pathways (see Methods for details), orange: pathways for which paired recording data was not available. (C1) Validation of the coefficient of variation (c.v.) of first PSP amplitudes, quantifying the trial-to-

trial variability for 5 *in vitro* characterized pathways (see Table 4.3). **(C2)** Comparison of PSP amplitudes in the model for 7 characterized pathways in house or in the literature (see Table 4.2). Dots and error bars show mean and standard deviation, dashed line shows the regression fit. **(D)** Example of *in silico* paired recordings for different pathways. For each pathway, the somatic membrane potential of the postsynaptic neuron is shown (grey: trials; blue and red: mean traces for inhibitory or excitatory connections). All recordings are shown on the same scale for easy comparison of PSP amplitudes in different pathways.

4.3.5.2 *Reconstructing and validating postsynaptic potential amplitudes*

Once we had determined the short-term plasticity types for each of the 11 m-type to m-type connections, we estimated the conductance of single synapses (g_{syn}). Since no experimental estimates of g_{syn} was available, we performed *in silico* paired recordings on 50 randomly selected pairs for each pathway and scaled the values of g_{syn} , until we matched the available data on postsynaptic potentials (PSPs) amplitude. As an internal validation of the scaling process itself, we repeated the same protocol on another set of 50 randomly selected pairs and compared the resulting PSP amplitudes with the experimental measurements (Fig. 4.4 C2).

We integrated data from our experimental paired recordings and literature findings (Gentet and Ulrich, 2003; Golshani et al., 2001; Mo et al., 2017; Zhu and Lo, 1999), which are summarized in Table 4.2. For uncharacterized pathways, we predicted g_{syn} by using values from similar pathways (see Methods).

We predicted that single synapse conductances from inhibitory neurons are in general small (e.g. 0.9 ± 0.23 nS for VPL_IN to VPL_IN), while conductances from VPL_TC and lemniscal afferents were larger (>2 nS), consistent with being “driver” synapses (Mo et al., 2017; Sherman and Guillery, 1998). Corticothalamic synapses had small conductances (<0.5 nS), but were facilitating; by applying the same conductance of CT to VPL_TC connections to CT to Rt_RC connections, we found that the latter was around 2 times stronger than the former, similar to what reported in (Golshani et al., 2001).

4.3.5.3 *Reconstructing NMDA/AMPA and GABA_B/GABA_A ratios*

Each excitatory connection was modelled as a combination of a fast AMPA and slower NMDA components (see Methods and Table 4.1 for synaptic currents time constants). In the case of inhibitory synapses, we included only GABA_A currents in this first draft, based on the following findings. In some pathways (e.g. Rt to IN in the visual thalamus of the rat) GABA_B currents are not present (Zhu and Lo, 1999) or not characterized in terms of their relative contribution (e.g. Rt_RCs to Rt_RCs or VPL_INs to VPL_INs). In the case of Rt_RC to VPL_TC we found contrasting literature, showing the presence of GABA_B components in rat neurons (Huguenard and Prince, 1994) or their absence in mice neurons (Warren et al., 1994). In preliminary experimental investigations (in mouse slices), we did not find GABA_B responses in TC neurons when stimulating the Rt.

4.3.6 Reconstructing and validating gap junction connectivity

Neurons of the reticular nucleus of the thalamus are functionally connected through electrical synapses (Landisman et al., 2002; Lee et al., 2014; Long et al., 2004). Different studies in rodents estimated that gap junctions-coupled neurons represent between 30-50 % of the total neuron population in the Rt (Crabtree, 2018; Deleuze and Huguenard, 2006; Lam et al., 2006; Lee et al., 2014).

We included dendrodendritic and dendrosomatic gap junctions between Rt_RC dendrites (Fig. 4.5). To constrain the anatomical properties of gap junctions (GJs) we used the neuron morphologies and information on the number of coupled neurons from dye-coupling experiments. To validate the anatomical properties of GJs we compared the distance-dependent connectivity in the model with dye-coupling experiments, at the single neuron as well as the level of small populations.

Functionally, gap junctions were modelled as simple conductances that coupled the membrane potential of the adjacent morphological compartments. We predicted the value of gap junction conductance for all gap junctions and validated their functional properties by comparing coupling coefficient values with experiments (Haas et al., 2011; Landisman et al., 2002; Lee et al., 2014; Long et al., 2004).

We found that most of the anatomical properties of GJ coupling in the reticular nucleus can be predicted by the morphological properties of Rt_RC neurons.

4.3.6.1 Reconstructing and validating gap junction anatomy

We included gap junctions (GJs) in our model by following an approach similar to chemical synapses. We started by finding all possible appositions between Rt_RCs and Rt_RCs dendrites and somata. We found that dendrodendritic appositions resulted in neuron divergence (number of neurons connected to target neurons) that was higher compared to literature findings (Fig. 4.5A1). Moreover, the resulting mean number of GJs per neuron (~300) was higher than values reported in other species or brain regions (Amsalem et al., 2016). Since we did not have any experimental data on the number of GJs between connected neurons or the density of GJs (number of GJs per unit length of dendrite or volume), in this first draft we randomly removed a certain fraction of GJs until we matched data on neuron divergence (Fig. 4.5A2). Interestingly, the target value was reached when 30 % of the appositions were kept and converted into functional GJs.

We then validated the resulting connectivity by comparing the extent of anatomical coupling in the model with available dye-coupling data in the mouse Rt (Lee et al., 2014). We found that each neuron in a virtual slice in the model was directly coupled with 2-20 other neurons and that the majority of coupled neurons was at 50-100 μm from the primary injected neuron (Fig 4.5B). When we analyzed single injections, most of the coupled neurons were found at 40-120 μm as found experimentally. Furthermore, we predicted that the highest variability on the number of coupled neurons is in a similar distance range (80-120 μm). Rare coupled neurons

can be found at distances of 300-400 μm , consistent with the extent of some Rt_RC neuron morphologies. When we analyzed all the coupled neurons in the microcircuit, we found that the extent of coupling is even larger (range of number of neurons per cluster 7-50, with few connected neurons with somata located at more than 400 μm from each other).

4.3.6.2 Reconstructing and validating gap junction physiology

We used a gap junction conductance of 0.2 nS, as estimated in previous morphologically-detailed models of GJs (Amsalem et al., 2016). To validate that the coupling strength was within biological reported values, we analyzed the coupling coefficients (CCs) between pairs of neurons with simulated paired recordings (Fig. 4.5C). In the model, we found that electrically coupled Rt_RC neurons had CCs values of 0.23 ± 0.008 (mean \pm standard deviation, Fig. 4.5C) and that the mean value fell within the reported variability in mouse Rt neurons (Landisman et al., 2002).

Reconstructing gap junction connectivity

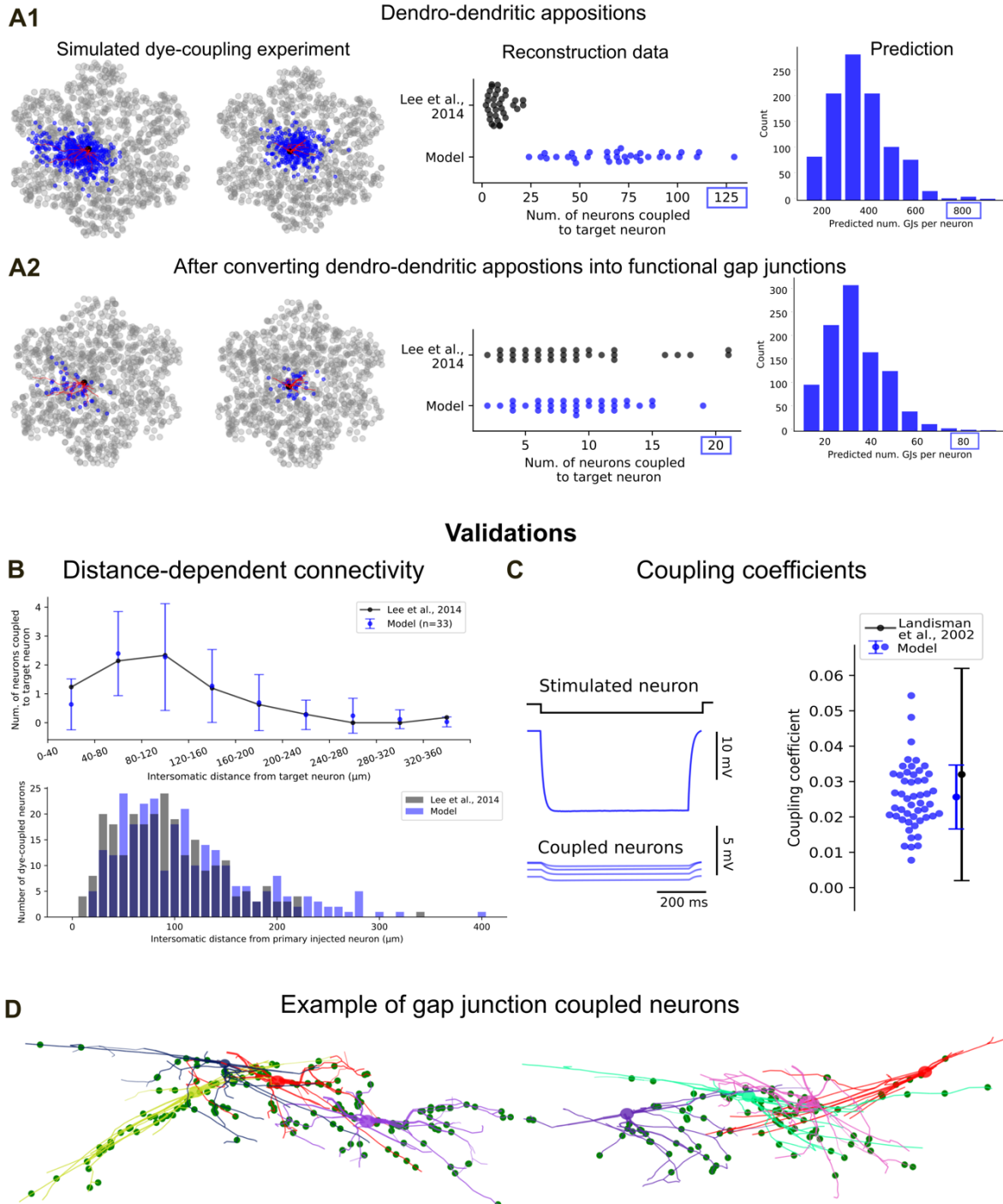


Figure 4.5. Reconstructing and validating gap junction connectivity between Rt_RC neurons

(A1) Connectivity based on dendro-dendritic appositions between Rt_RC dendrites. Left: view of a mesocircuit (7 microcircuits) from the Rt side showing the location of a sample of 1000 Rt_RC neurons (grey dots), an example “injected” Rt_RC morphology (2D projection, dendrites in red) and the location of Rt_RC neurons connected to the injected Rt_RC (blue dots). Two exemplar injections are shown. Middle: neuron divergence (number of neurons connected to the injected neurons) in the model and literature. Each dot represents one injected

neuron. Right: predicted distribution of GJs divergence (number of GJs per neuron, for a sample of 1000 Rt_RC neurons in the model). **(A2)** Connectivity after conversion of dendrodendritic appositions into functional GJs. Left: as in A1, after converting 30 % of dendrodendritic appositions into functional GJs. Middle: neuron divergence in the model matches experimental findings. Right: the resulting GJ divergence is reduced by an order of magnitude. Note different maximal values in A1 and A2 (blue rectangles). **(B)** Validations of distance dependent GJs connectivity. In silico dye-injections were performed in the model to reproduce dye-coupling experiments (n=33 neurons injected). **(C)** Validation of GJs functional properties. Left: example of *in silico* paired recordings, where a Rt_RC is stimulated with a hyperpolarizing current step, its somatic potential is recorded, along with the somatic potential of all GJ-coupled neurons (only a sample is shown). The ratio of the voltage response between a coupled neuron and the stimulated neuron is the coupling coefficient (CC). Right: comparison of CC values in the model (n = 50 pairs, each one represented by a dot) with paired recordings from the literature. Dots: mean, error bars: standard deviation. **(D)** Resulting GJ connectivity. Example of clusters of 4 Rt_RC neurons coupled by GJs and GJ locations. Each neuron morphology is represented by a different color, axons are omitted for clarity. Green dots show the detailed morphological location of GJs that each of the neurons receive from the 3 others and from other Rt_RC neurons not shown here.

4.3.7 Simulating *in vivo*-like spontaneous activity and sensory responses

In first preliminary investigations, we explored spontaneous and evoked activity in the microcircuit as a whole. We found uncorrelated population and single cell responses during spontaneous activity and clear evoked response when at least 50 medial lemniscus (ML) fibers were activated.

We simulated spontaneous and evoked medial lemniscus (ML) activity in *in vivo*-like conditions (Fig. 4.6). The *in vivo*-like condition was approximated by tonic depolarization of all m-types and activation of lemniscal and corticothalamic (CT) fibers with uncorrelated spike trains, aimed at simulating background activity from the afferents (see Methods for details). We lowered the calcium concentration from 2 mM (*in vitro*-like conditions) to 1.2 mM, with the effect of reducing synapse release probabilities (Markram et al., 2015).

The first simulation results showed uncorrelated firing activity in all m-types (Fig. 4.6A1). Under this depolarization condition, the activity of Rt_RCs was sufficient to hyperpolarize part of the VPL_TC population (see voltage raster in Fig. 4.6A1). We then compared spontaneous activity with sensory evoked responses with brief activation of ML fibers (Fig. 4.6B), simulating a whisker flick or a skin electrical stimulus to the hindlimb (Kimura, 2017). We found clear population responses in VPL_TC neurons, with a peak in firing rates in the 5 ms following the stimulus and increased firing probability in the 20-25 ms following the stimulus. Rt_RCs showed increased firing rates compared to the spontaneous activity as a result of the excitation they receive from VPL_TCs. The increase in firing rates of Rt_RCs lasted for ~25 ms after the stimulus and gradually decreased to baseline levels.

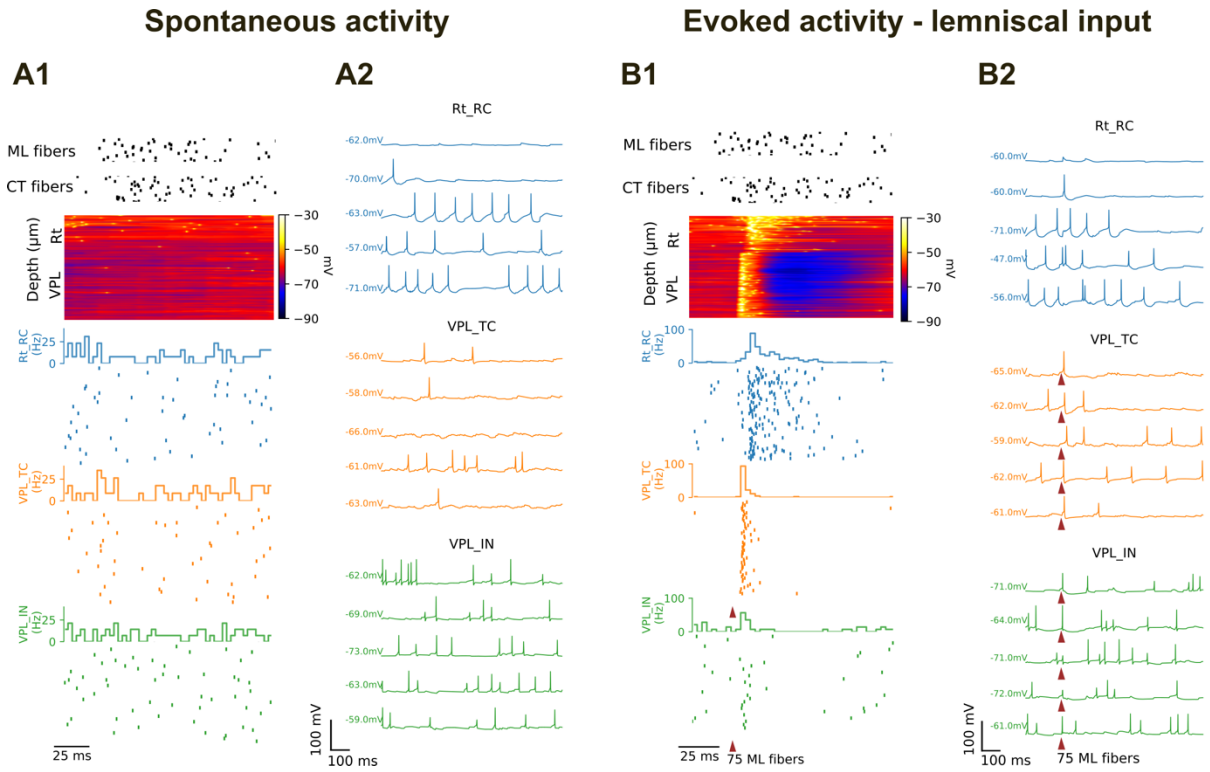


Figure 4.6 Simulated spontaneous and sensory-evoked activity (*in vivo*-like)

Simulating *in vivo*-like spontaneous activity with background firing from medial lemniscus (ML) and corticothalamic (CT) afferents, extracellular Ca^{2+} concentration $[\text{Ca}^{2+}]_o$ of 1.2 mM and depolarization of Rt and VPL. (A1) Top: population voltage raster showing the membrane potential of a sample of 500 neurons. Each row is a neuron and neurons are sorted according to microcircuit depth. Bottom: spike rasters and firing rate histograms for a sample of neurons for each m-type. (A2) Exemplar single cell recordings for each of the m-types. (B1) and (B2) as in (A1) and (A2) for simulated sensory-evoked activity with the activation of 75 ML fibers with 1 synchronous spike.

We next explored the effect on network responses by activating an increasing number of afferent ML fibers and found the activation of at least 50 ML fibers was required to observe population responses in the microcircuit (Fig. 4.7). We observed a sigmoidal dependence between stimulus amplitude and peak firing rates (Fig. 4.7 B) and an exponential decrease of response latencies in lemniscal-recipient cells (thalamic interneurons, VPL_IN and thalamocortical cells, VPL_TC). A clear effect on VPL_IN latency was visible with activation of 75 or more fibers (Fig. 4.7D).

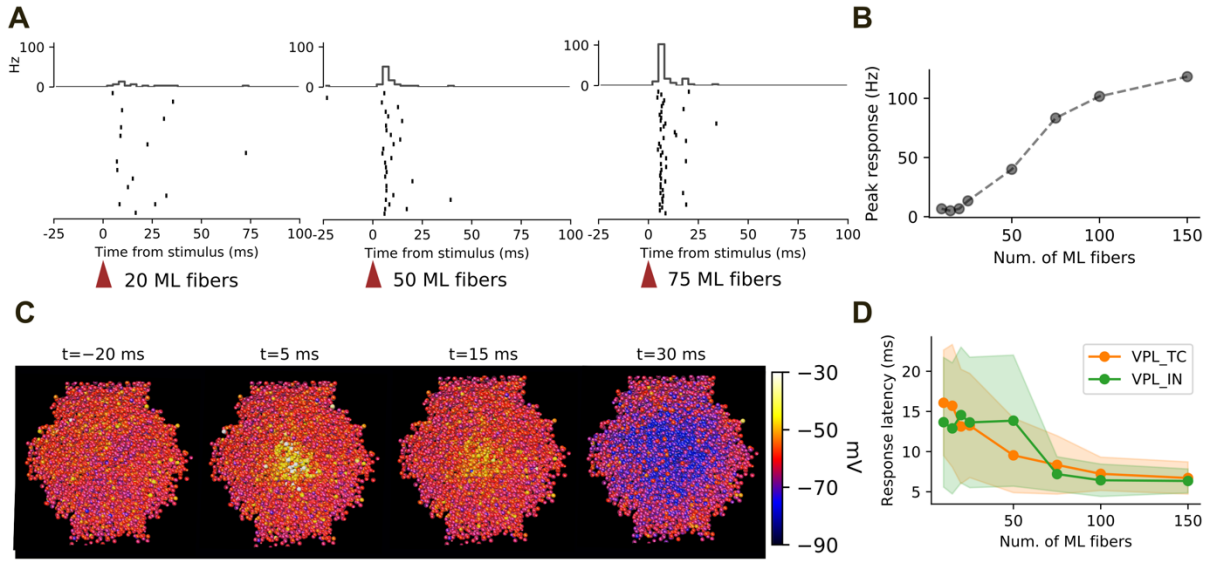


Figure 4.7 Threshold analysis of sensory-evoked responses (*in vivo*-like)

Same simulation conditions as in Fig. 4.6 (A) Simulated sensory inputs with activation of increasing numbers of lemniscal fiber (ML) with 1 synchronous spike. Spiking responses (rasters and firing rate histograms) are shown for three stimulation intensities for a sample of VPL neurons. (B) Stimulus-response curve. The response is calculated as the peak firing rate in response to the stimulus. (C) Spatial map showing a sample of neurons in the VPL at different times before, during and after the stimulus, 75 fibers are activated. Neurons are color-coded according to their membra potential. (D) Response latencies of neurons in the VPL at increasing number of stimulated ML fibers. Mean (lines) and standard deviations (shades) of all VPL neurons are shown.

4.3.8 Validation of network responses to corticothalamic inputs (*in vitro*-like)

A recent experimental study showed the effect of activating corticothalamic (CT) inputs onto thalamic activity in thalamocortical slices (Crandall et al., 2015). This experiment showed that at low firing rates CT input inhibits ongoing activity but at higher rates the initial inhibition is overcome by excitation, as a result of different patterns of short-term plasticity in CT and intrathalamic synapses. We obtained qualitatively similar results in the model.

4.3.8.1 The model reproduces the modulation of TC cells firing by single and high frequency activation of corticothalamic fibers

To reproduce *in vitro* like conditions, all the modelled neurons were left at their resting potential and the extracellular calcium concentration was set to 2 mM (see Methods). We activated a small subset of VPL_TC cells (around 10 cells), so that they fired in tonic mode at 10-12 Hz (as in Crandall et al., 2015) and observed the change in activity induced by corticothalamic stimulation (Fig. 4.8A). To approximate the optogenetics stimulus, without knowing the extent of light-induced recruitment of corticothalamic (CT) axons in the experiments, we activated an increasing number of CT fibers with 1 synchronous spike, until we could observe a response in the activated VPL_TC, which happened for 1500 fibers.

As found by Crandall and co-authors (see their Fig. 1), VPL_TC cells responded to corticothalamic activation with a brief increase in firing rates after the stimulus, which was then dominated by a longer (>100 ms) Rt-mediated inhibition (Fig. 4.7A). We then activated CT fibers at 10 Hz and we found that the initial inhibition was progressively overcome by excitation, as in the corresponding experiment (Fig. 4.8B). In these conditions, we found a less pronounced increase of firing rates in the model compared to the experiment (Crandall et al., 2015, Fig. 2), mainly due to less synchronous responses in the model compared to the experiment (see also the two peaks just after the stimulus in Fig. 4.8A2).

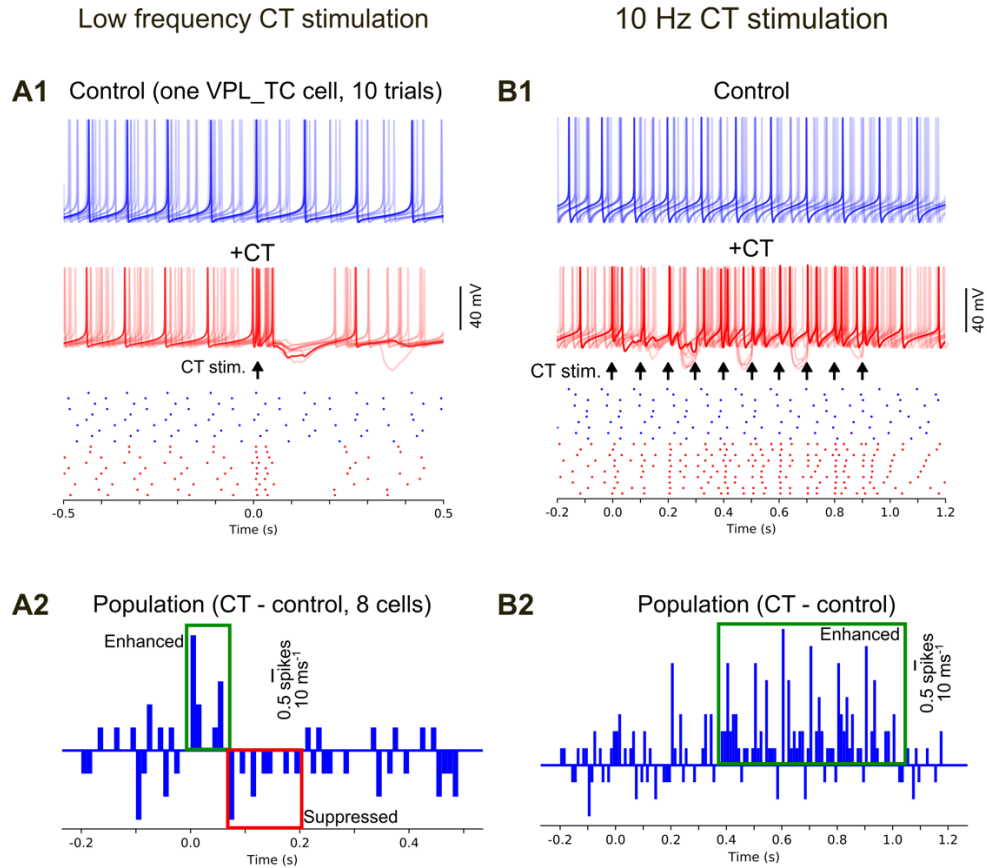


Figure 4.8. Reproducing *in vitro* findings in the model: corticothalamic (CT) modulation of TC cells activity (Crandall et al., 2015).

(A1) Top: example membrane potential responses of one VPL_TC neuron (overlay of 10 different simulation trials) in control conditions (injection of a depolarizing step, so that VPL_TC cells fired single spikes at 10-12 Hz). Middle: same neuron and conditions with the addition of a CT stimulus (1 synchronous spike in 1500 CT fibers, simulating the effect of optogenetic activation). Bottom: raster plot of the neuron's firing for the traces shown above. (A2) Population peristimulus time histograms (PSTHs) showing the difference in firing rates between control condition and with CT stimulation (8 cells). (B1) As in A1, except for repetitive stimulation of CT fibers at 10 Hz. (B2) Difference between PSTHs between control and CT as in A2. See Crandall et al., 2015, Fig. 1 for A and Fig. 2 for B.

Reproducing qualitatively these experimental findings was of particular importance, given our simple representation of corticothalamic fibers (see section 4.2.13). It confirmed that the following emergent aspects of the model were good approximations of biological findings: the time course of GABA mediated-inhibition between Rt_RC and VPL_TC neurons, which depend on the time constant of synaptic currents and the membrane time constants; the balance between direct CT excitation and indirect inhibition onto thalamic neurons through the Rt, the relative contribution of facilitating excitatory (from cortex) and depressing inhibitory inputs (from Rt_RC neurons) onto TC neurons. Although we could not directly measure synaptic parameters for all CT connections, these simulations suggest that we successfully captured some of their key properties.

It would be interesting to explore how these responses would change if CT synapses onto Rt_RC neurons were less facilitating than CT synapses onto TC neurons. Whether CT synapses onto Rt_TC neurons are facilitating or not is still not clear in experimental findings (Deleuze and Huguenard, 2016).

4.3.9 Evoked spindle-like oscillations in *in vitro*-like conditions

As a further validation of network dynamics, we tested if the model was able to reproduce spindle-like network activity, as reported previously in experimental and modelling studies in ferrets (Destexhe et al., 1993, 1996; Kim et al., 1995; von Krosigk et al., 1993, Bal et al., 1995). We found that we could evoke spindle-like oscillations in the model by briefly stimulating Rt_RC neurons, approximating the responses to extracellular electrical stimulation of the reticular nucleus (Huguenard and Prince, 1994; Li et al., 2017; Lu et al., 2020). The oscillatory activity was self-sustaining, through the synaptic interaction between Rt_RCs and VPL_TC, and network mechanisms were responsible for its termination (Fig. 4.9).

We began by simulating the network at rest with spontaneous synaptic release as the only source of input (*in vitro*-like condition, see Methods). The extracellular calcium concentration in this and all the following simulations was set to *in vitro* levels (2 mM). Under this condition, all the neurons were hyperpolarized, as expected from the *in vitro* recordings used to build the neuron models, and the network was silent. We then activated all Rt_RC neurons with a 20 ms current pulse (Fig. 4.9A), resulting in ~50% of Rt_RC neurons firing in response to the stimulus (Fig. 4.9 C2). Rt_RC neurons recruited VPL_TC through post-inhibitory rebound responses, which in turn excited Rt_RCs. This back-and-forth of activity lasted for ~800 ms and generated network oscillations at a frequency of ~6-7 Hz, visible as increased peaks of activity in the average membrane potentials and firing rate histograms (Fig. 4.9 A1 and C2, ~3.5 peaks in the first 500 ms after the stimulus). The frequency was similar to some of the barrages of IPSPs in TC cells recorded during spindle waves in ferrets (Bal et al., 1995b).

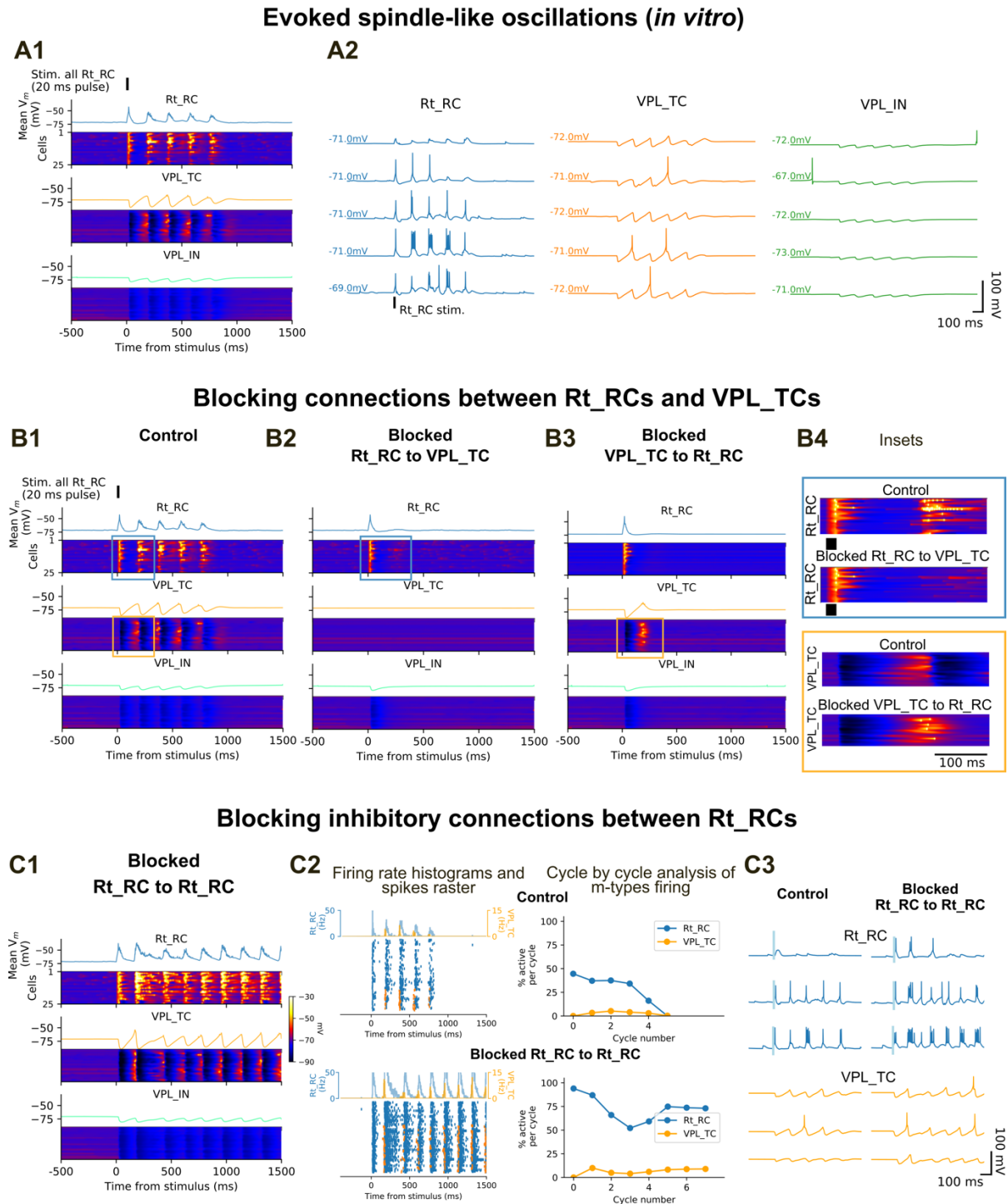


Figure 4.9. Spindle-like oscillations in *in vitro*-like conditions and the role of different connections

Evoked activity in *in vitro*-like conditions with brief stimulation of Rt_RCs. (**A1**) Voltage rasters showing spindle-like activity. A sample of 25 neurons per each m-type is shown and color-coded according to its membrane potential (see colormap in C1). (**B**) Connections that block the oscillation. (**B2**) Blocking Rt_RC to VPL_TC disrupted the oscillation and revealed a small depolarization of Rt_RC neurons following the stimulation, probably caused by partial reactivation of the low-threshold calcium current (B4). (**B3**) When VPL_TC to Rt_RC connections were blocked VPL_TC generated only one post-inhibitory rebound response with

higher firing probabilities (B3). (B4) insets from B1-3. (C1) Blocking chemical synapses between Rt_RC neurons (while gap junctions were left unchanged) generated a prolonged oscillation. (C2) Left: firing rate histograms and spike raster plots for a sample of 1000 neurons in the circuit. Note that the firing histograms are truncated at 50 Hz. Right: cycle by cycle analysis showing the percentage of Rt_RC and VPL_TC neurons firing around each oscillation peak (see Fig. 4.10 for the calculation of oscillation peaks and Methods). (C3) Single cell recordings showing the same cells in the control conditions and with Rt_RC to Rt_RC chemical synapses removed. Vertical bars indicate stimulus time in Rt_RC neurons.

4.3.10 The role of different synaptic pathways in the maintenance and termination of spindle-like oscillations

4.3.10.1 Activity “ping-pong” between Rt and TC neurons is necessary for the generation of spindle-like oscillations

To understand the cellular and connectivity substrates underlying the oscillation, we removed one by one connections between different m-types (Fig. 4.9). Not surprisingly, each synaptic pathway involving chemical synapses in Rt_RCs or VPL_TCs had a role in the generation and/or maintenance of the oscillation (Fig. 4.9B), while removing pathways involving VPL_INs did not have a remarkable effect (data not shown). When we removed the connection between Rt_RCs and VPL_TCs, the first cycle of the oscillation in Rt_RCs did not change, but no subsequent firing response was evoked either in VPL_TCs nor in Rt_RCs. This knockout experiment revealed a small depolarization of Rt_RC neurons following the stimulus, probably caused by partial reactivation of the low-threshold calcium current. This means that in these hyperpolarized conditions, the isolated Rt could not generate any self-sustained activity.

Without connectivity from VPL_TCs to Rt_RCs, VPL_TCs displayed slightly stronger post-inhibitory rebounds (Fig. 4.9B3), which were not transmitted back to Rt_RCs. This result showed that the thalamus alone cannot generate oscillatory activity and that post-inhibitory rebound bursts occurring later in some VPL_TCs can be partially suppressed by Rt_RC neurons firing.

This set of results confirmed that the oscillation is generated through the interplay between bursting in the reticular nucleus and post-inhibitory responses in thalamocortical cells. Although oscillatory burst firing in Rt neurons have been shown to be important in the generation of spindles (Astori et al., 2011), we observed that bursting of Rt_RCs neurons alone was not sufficient without the interplay with VPL_TCs.

4.3.10.2 Mutual inhibition between Rt_RC neurons plays a role in the termination of spindle-like oscillations

Interestingly, when we removed the inhibitory connections between Rt_RCs, we found a prolongation of the oscillation (Fig. 4.9C), caused by an increase in burst firing in Rt_RCs and a subsequent increase in post-inhibitory rebound responses in VPL_TCs (Fig. 4.9C1). This means that the intra-Rt inhibition controls the level of activity in Rt, by limiting the probability of synchronous burst firing in reticular neurons and subsequent excitation of the Rt_RCs from VPL_TCs (Fig. 4.9C3). Increased in burst firing in reticular neurons is in agreement with

results from rat slices, with focal application of picrotoxin, a GABA_A receptor blocker (Sohal and Huguenard, 2003). At the population level, when inhibitory connections were removed, between 50 and 90 % of Rt_RC neurons fired during each oscillatory cycle and almost all of them fired in response to the stimulus (Fig. 4.9C2).

4.3.11 Differential depolarization of the Rt and VPL influence oscillation properties

Spindle oscillations in naturally sleeping (i.e. non-anesthetized) rodents occur during non-REM (NREM) sleep and are more easily evoked when thalamic activity is mildly synchronized (Bartho et al., 2014). Their features evolve during NREM episodes as a result of brain state-dependent modulations of membrane potential dynamics in the thalamus and the reticular nucleus (Bartho et al., 2014; Urbain et al., 2019).

In the model, we found that the depolarization levels of Rt and TC neurons influence oscillation frequency and duration and predicted depolarization conditions where spindle-like oscillations are less easy to evoke.

4.3.11.1 Increasing depolarization in the Rt or VPL results in increase of oscillation frequency

We studied network dynamics over a wide range of depolarization levels in the Rt and VPL, as an approximation of neuromodulatory influences onto thalamic and reticular activity (McCormick, 1992). The baseline potentials explored, through current injection to all neurons, went from hyperpolarized, mildly depolarized (~ -65 mV) to close to firing threshold. All Rt_RC neurons were stimulated with a 20 ms current pulse, which resulted in varying spiking responses depending on the depolarization levels. For each combination of membrane potentials in Rt_RCs and VPL_TC, we calculated oscillation frequency and duration (number of cycles) (Fig. 4.10A). We found that the frequency as well as the duration were modulated when depolarization levels were changed (Fig. 4.10A). Although we cannot directly compare our results with *in vivo* findings, modulation of spindles frequency and duration in the somatosensory cortex has been shown to vary during non-REM sleep in naturally sleeping mice; more specifically the frequency decreases during NREM sleep along with TC neurons membrane potentials (Urbain et al., 2019). We found that while the frequency tended to increase with increasing depolarizations in both Rt and VPL, the dependence of oscillation duration was more complex.

4.3.11.2 Longer spindle-like oscillations are evoked when the VPL is more depolarized than the Rt

Oscillation duration map showed that clear spindle-like oscillations (having more than 5 cycles, i.e. duration around 500 ms) could only be evoked in a small region, where Rt_RC membrane potentials are below -65 mV and VPL_TC are more depolarized than Rt_RCs (Fig. 4.10A). If we assume that VPL_TC neurons are in general more depolarized during wake-like states than during sleep-like states, and that Rt_RC neurons are more hyperpolarized, this result suggests that spindle-like oscillations are easier to evoke at the transition between wake-like

and sleep-like states. When both VPL_TCs and Rt_RCs were hyperpolarized, although 5-6 oscillation cycles could be evoked, the frequency decreased below 5 Hz.

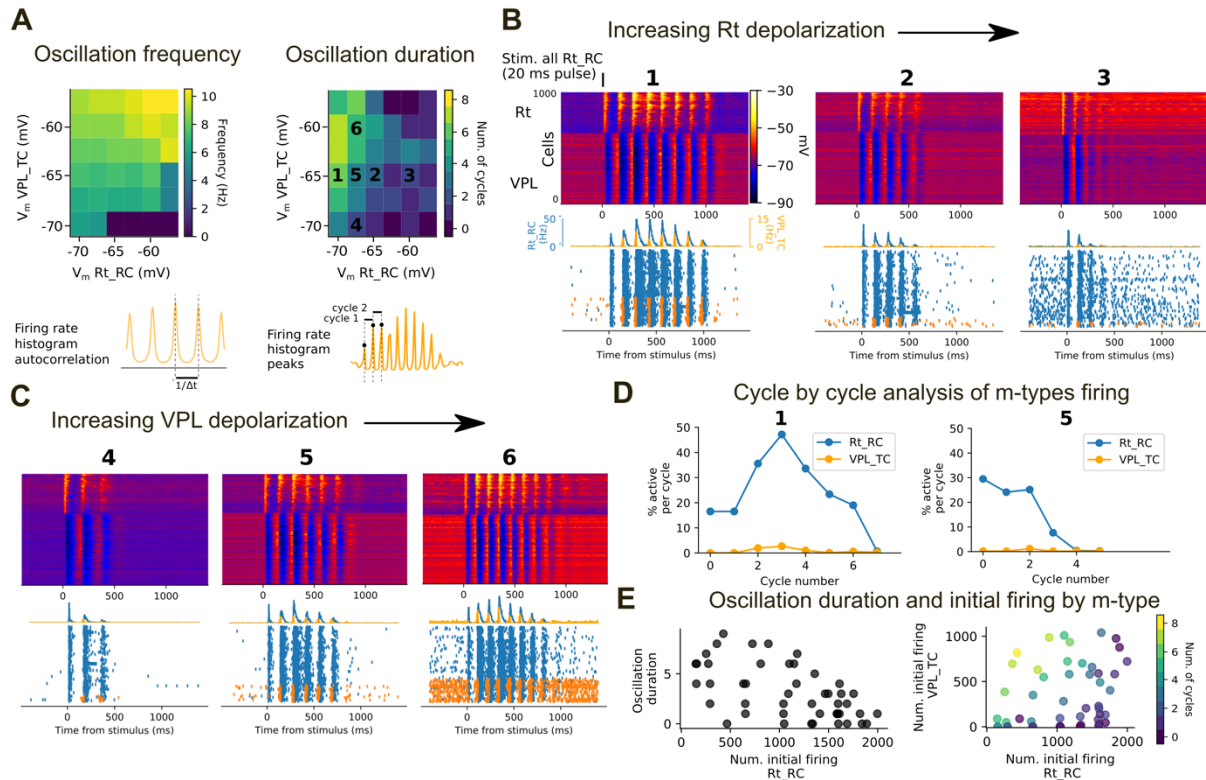


Figure 4.10. Depolarization levels in Rt and VPL influence oscillation properties

Spindle-like oscillations were evoked with a brief 20 ms current stimulus to all Rt_RC neurons and VPL_TCs and Rt_RCs membrane potential was depolarized to different levels. (A) Top: Frequency and duration maps. Oscillation frequency and duration at different depolarization levels are color-coded according to a heatmap. Bottom: illustration showing how oscillation frequency and duration were calculated (see Methods for details). (B) Population voltage rasters, spike raster and firing rate histograms showing the effect of increasing Rt depolarization, while VPL_TCs are mildly depolarized. Sample of 1000 neurons sorted by microcircuit depth. (C) Same as in (B) for increasing depolarization of VPL_TCs. (D) Cycle by cycle analysis showing the percentage of Rt_RCs and VPL_TCs firing around each oscillation peak. (E) Left: oscillation duration as a function of initial activity of Rt neurons. Right: oscillation duration as a function of initial activities in Rt_RCs (0-20 ms from stimulus onset) and VPL_TCs (90-150 ms from stimulus onset, corresponding to the first post-inhibitory rebound responses).

4.3.11.3 Depolarization conditions where spindle-like oscillations are less easy to evoke

We found a region of depolarization conditions where oscillations were less likely to occur, namely when VPL_TCs and Rt_RCs were depolarized (upper right corner of the duration map). We speculated that this state would correspond to awake like-states. *In vivo* recordings in awake mice showed that TC neurons in the VPM are more depolarized during active states than in quiet wakefulness (Urbain et al., 2015). Intracellular recordings of Rt and TC neurons comparing their membrane potentials during wakefulness and sleep are not available yet. Moreover, spindle-like oscillations were difficult to evoke when VPL_TCs were

hyperpolarized and Rt_RCs were depolarized. Under the assumption of upregulation of leak potassium currents and consequent membrane hyperpolarization in TCs (Hill and Tononi, 2005; Li et al., 2017), this network state would correspond to deep-NREM sleep. Our results also suggest that during deep-NREM sleep leak potassium currents in TCs are more upregulated than in Rt_RCs cells.

To study in more detail how oscillation duration was affected by differential depolarization of the Rt or VPL, we analyzed population responses when only one of the two populations were depolarized.

4.3.11.4 Rt depolarization alone decreases oscillation duration

We depolarized only the Rt and we kept the VPL at intermediate levels (-65 mV) of membrane depolarization. In these conditions, increasing Rt depolarization decreased oscillation duration (Fig. 4.10B). This result can be explained by increased inhibition from the Rt to the VPL and decrease firing probability in VPL_TC. Furthermore, the waxing-and-waning in firing responses (Fig. 4.10B, condition 1) tended to become a predominantly waning response when Rt was depolarized (Fig. 4.10B, condition 3).

4.3.11.5 VPL depolarization increases oscillation duration

When the membrane potential in Rt was kept constant (slightly below -65 mV) and the VPL was depolarized, the oscillation increased in length (Fig. 4.10C). With increased depolarization of the VPL, more VPL_TC were firing before as well as after the stimulus and excited more Rt_RCs. This increased excitation in the VPL, resulted in more post-inhibitory rebound responses in VPL_TC, which in turn excited more Rt_RCs causing a longer back-and-forth of activity between the two populations. With increasing VPL depolarization waning responses in the population firing (Fig. 4.10C, condition 4) tended to become waxing-and-waning (Fig. 4.10C, condition 6).

4.3.11.6 Initial firing of Rt_RCs, along with VPL_TC, can predict oscillation duration

In vivo recordings in naturally sleeping rats suggested that brain state influences spindle length by regulating the activity of reticular neurons (Bartho et al., 2014). As found by Barthó et al., spindle-like oscillations in our simulation tended to be longer when the initial activity of Rt neurons was lower (see conditions 1 and 6 in Fig. 4.10B and C). When less than 20% of Rt_RCs neurons fired in response to the stimulus, more Rt_RC neurons were recruited in the following cycles (Fig. 4.10D). On the other hand, when $\sim 30\%$ were initially recruited the activity of Rt_RCs decreased during the following cycles (Fig. 4.10D). We asked whether the initial response in the Rt could predict the duration of evoked oscillation and we found that longer oscillations tended to occur when the initial response of Rt_RC neurons was lower (Fig. 4.10E, left). However, different oscillation lengths corresponded to the very similar initial responses in Rt_RCs. We found that the combination of the initial responses in the Rt_RCs and VPL_TC was a better predictor of oscillation length (Fig. 4.10E, right). This result suggests that the membrane potential of Rt, as well TC neurons, upon spindle initiation can influence spindle duration.

4.3.12 The effects of VPL depolarization and initial Rt_RCs recruitment

We found previously that the membrane potential level changes oscillation frequency and duration (Fig. 4.10). In the following set of simulations, we analyzed the network responses to spatially organized inputs in the center of the Rt of increasing sizes and depolarization levels where longer oscillations can be evoked (VPL depolarized more depolarized than the Rt). In this condition, we found that spindle-like oscillations can be evoked by stimulating 200-250 Rt_RCs and that the oscillation duration tended to decrease with increasing initial recruitment of Rt_RC neurons (Fig. 4.11).

4.3.12.1 Waxing-and-waning oscillations at the single cell and population levels

We found that for intermediate levels of depolarization in VPL_TCs (~ -65 - 60 mV) and moderate hyperpolarization in the Rt (~ -70 mV) the activation of 250 neighboring Rt_RCs was sufficient to trigger a self-sustaining oscillation lasting ~ 1.5 s. We also found spindle-like oscillations when we stimulated 200 central Rt_RCs, but not 175 Rt_RCs (data not shown). At the population level, we observed synchronized increase of firing rates (waxing) in both Rt_RCs and VPL_TCs, sustained activity and decrease (waning) starting around 300 ms before the end of the oscillation (Fig. 4.11A-D). At the single cells level, the initial responses were dominated by subthreshold PSPs, while action potentials were more frequent during the intermediate phase of the oscillation (Fig. 4.11B). The responses in VPL_TCs were dominated by oscillatory IPSPs, recurring at the same frequency of the population responses of the Rt_RC neurons, and occasional post-inhibitory rebound spikes (Fig. 4.10B). The waxing-and-waning pattern was visible also in the spatial average of somatic membrane potentials (Fig. 4.10C).

4.3.12.2 Waxing-and-waning oscillation along the vertical and lateral dimensions of the microcircuit

Analysis of the membrane potentials along the depth and lateral extent of the microcircuit revealed waxing-and-waning responses in the Rt and VPL in time as well in space (Fig. 4.11C). Along the depth, neurons located in the upper half of the Rt started to activate before the ones in the lower half. In the VPL, neurons located in the center were more hyperpolarized, especially around the first 500 ms from the start of the oscillation. Around the middle phase of the oscillation (500-1000 ms) the hyperpolarization was visible along the whole depth.

Along the lateral extent, neurons in the center of the Rt and VPL were activated earlier; during the middle phase of the oscillation (500-1000 ms) the excitation (in the Rt) and inhibition (in the VPL) spread along the whole lateral extent of the microcircuit.

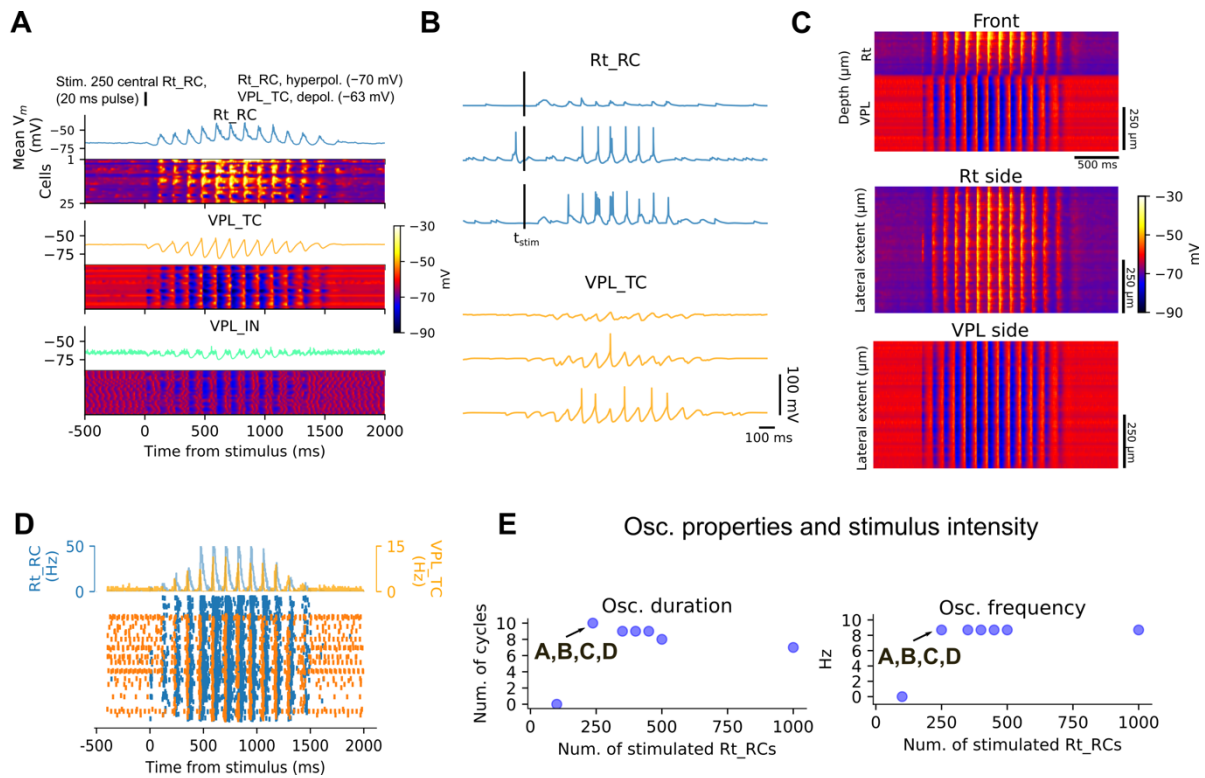


Figure 4.11. Oscillation properties with VPL depolarization and the effect of increasing initial Rt recruitment

(A) Membrane potential raster plots and mean membrane potential showing oscillatory activity in a sample of 25 cells for each m-type. Each row in the membrane potential rasters shows one cell and cells are sorted by microcircuit depth. (B) Representative single cell recordings from the neurons shown in A. (C) Activity along the spatial dimensions of the microcircuit. Top: neurons membrane potential along the depth, showing the alternating activations in the Rt and VPL and waning of the oscillation both in time and space. Neurons are sorted by depth. Bottom: propagation of the activity along the lateral extent showing how central neurons activate earlier than more lateral ones. Neurons are sorted by position on the lateral extent of the microcircuit. (D) Population spiking responses as assessed by raster plots and firing rate histograms (sample of 1000 cells). (E) Oscillation duration and frequency for different stimulus intensities (number of central Rt_RCs stimulated).

4.3.12.3 Increasing initial Rt recruitment tends to decrease oscillation duration

We found that activating more Rt_RC neurons tended to decrease oscillation duration from 10 to 7 cycles when 1000 central Rt_RCs were activated, corresponding to $\sim 1/5$ of the total number of Rt_RC neurons (Fig. 4.11E). Increasing the initial recruitment of Rt_RCs did not alter significantly the oscillation frequency, which remained constant around 8-9 Hz. The decrease in oscillation duration with increasing number of stimulated Rt_RCs neurons is in line with our previous results showing the role of mutual inhibition between reticular neurons in the termination of the oscillation (Fig. 4.9C) and decrease in oscillation duration with increasing Rt depolarization (Fig. 4.10B).

4.3.13 Gap junctions increase the duration of spindle-like oscillations

Gap junctions (GJs) between neurons in the reticular neurons can efficiently transmit low-threshold bursts between cells, promote spiking correlations when coupling between cell pairs is strong and synchronize the activity in the reticular nucleus *in vitro* (Landisman et al., 2002; Long et al., 2004). GJs have been hypothesized to contribute to the maintenance of network oscillations, through network synchronization (Beenhakker and Huguenard, 2009; Fernandez and Luthi, 2019).

We found that removing GJs from the model decreased the recruitment in the Rt, tended to shorten spindle-like oscillations and made oscillation duration depend more significantly on stimulus intensity (Fig. 4.12).

4.3.13.1 Gap junctions influence Rt_RC membrane potentials distribution

We performed GJs knockout experiments in the model and compared oscillations properties across different stimulation intensities (Fig. 4.12). To control the extent of the stimulus, we activated an increasing number of Rt_RC neurons located at the center of the microcircuit (as in Fig. 4.11). We found that without GJs, at least 400 Rt_RC neurons needed to be stimulated in order to evoke any self-sustained activity (Fig. 4.12A and 4.12D), while 250 neurons were enough with a network with GJs (Fig. 4.12D and Fig. 4.11). Although the initial population firing responses were comparable to the control condition (Fig. 4.11A), we found that without GJs the average membrane potential and the membrane potential in individual Rt_RCs were slightly lower compared to the control condition (Fig. 4.11C). This finding suggests that GJs can influence the excitability in the Rt by bringing the membrane potential of Rt neurons closer to threshold and more likely to fire synchronously in response to the stimulus and in response to post-inhibitory rebounds from VPL_TC.

This result was confirmed by comparing the spatial responses in the Rt in a time window around the stimulus (Fig. 4.11A insets). We found that the Rt_RC neurons were on average more depolarized in the 30 ms following the stimulus in the control condition than without GJs.

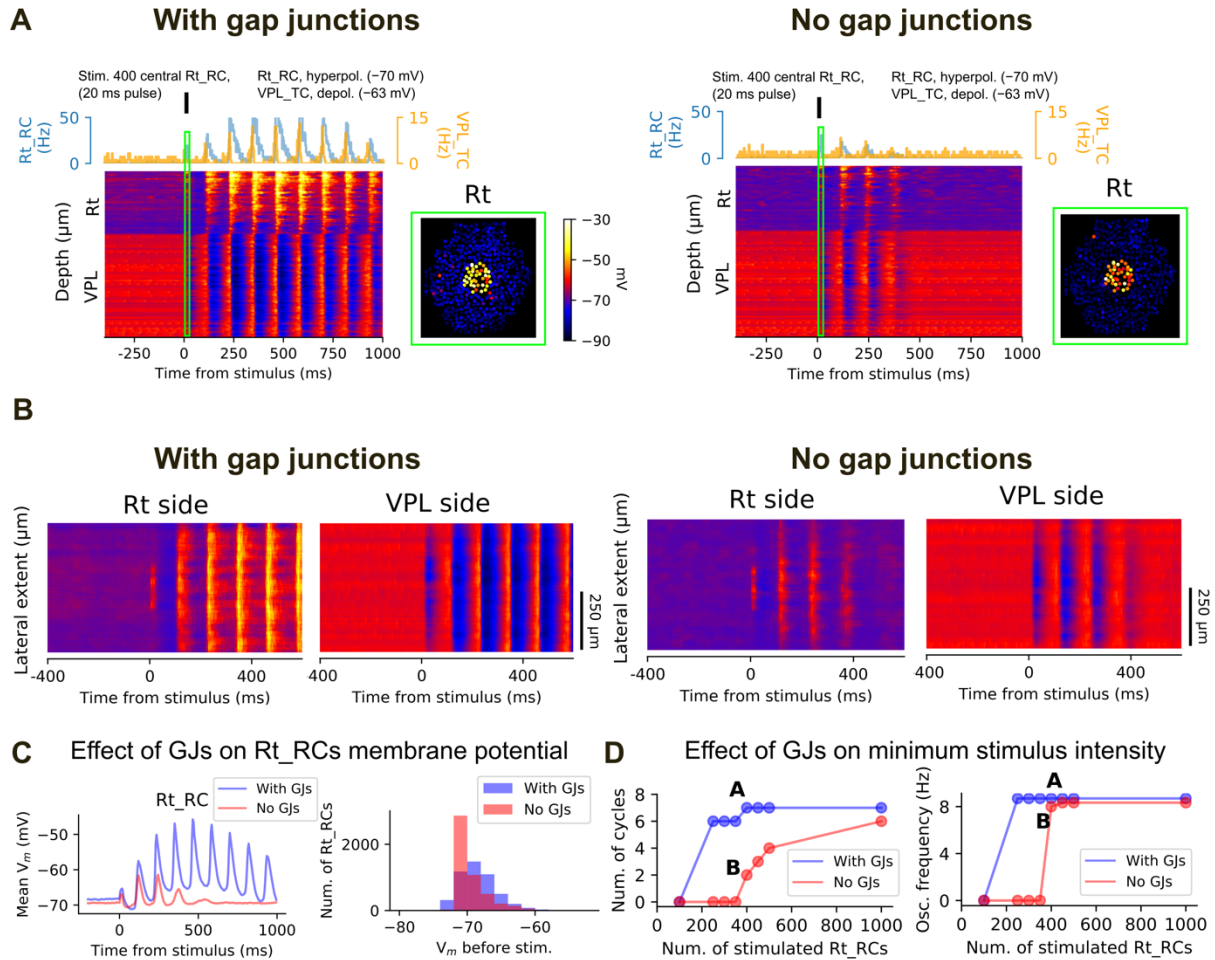


Figure 4.12. The contribution of gap junctions to spindle-like oscillations

Simulation conditions as in Fig. 4.11, with VPL more depolarized than the Rt. **(A)** Spindle-like oscillations in control conditions (left) and with gap junctions (GJs) between Rt_RCs removed (right). Population responses are shown with voltage rasters and firing rate histograms. Insets: average activity in a sample of neurons in the Rt in a time window of 30 ms after the stimulus (green boxes on the plots on the left). **(B)** Membrane potential along the lateral extent of the microcircuit for the simulations shown in A. Each row represents the membrane potentials in the Rt and VPL averaged in 25 μm bins color-coded as in A. **(C)** Left: average membrane potential of all Rt_RC neurons, right: membrane potential distribution for all Rt_RCs in the 10 ms preceding stimulus onset. **(D)** Oscillations properties as a function of the number of Rt_RCs stimulated. To control the spatial extent of the stimulus with and without GJs, the same Rt_RCs located at the centre of the circuit were stimulated.

4.3.13.2 Gap junctions increase excitation in the Rt along the lateral extent of the microcircuit

When we analyzed the membrane potential along the lateral dimension of the microcircuit in the two conditions, we found that the excitation in the Rt was extended to more lateral neurons and lasted for a longer time, with corresponding increased inhibition in the VPL (Fig. 4.11B). More central regions in the Rt were more excited for longer times when GJs were present and the overall network response involved more lateral regions in the Rt and VPL. This was clearer in the oscillation cycles after 100 ms from stimulus onset. Taken together with the anatomical

connectivity through GJs between neurons that are also 250-300 μm apart (see Fig. 4.6) this result shows that GJs have functional effect on neurons which are distributed along the whole lateral extent of the Rt (and, indirectly, of the VPL).

When we increased the stimulus intensity (number of Rt_RCs stimulated, Fig. 4.11D) we found that longer oscillations could be evoked without GJs when more Rt_RCs were initially recruited (6 cycles with 1000 out of the total 4909 Rt_RCs stimulated); the frequency of the network responses was very similar to the control condition. This result indicates that spindle-like oscillations evoked with Rt stimulation are all-or-none events: i.e. when a minimum number of Rt_RC neurons are recruited, the activity spreads to all the network, the oscillation is self-sustaining and is scarcely dependent on stimulus intensity.

4.4 Discussion

Here we present a first-draft large-scale model of thalamic microcircuitry, that integrates experimental measurements of the detailed anatomy and physiology of single neurons, the three-dimensional organization of the reticular and VPL nuclei, neuron densities, synaptic anatomy and physiology, and electrical connectivity mediated by gap junctions. It has been validated against a set of structural and physiological data that was not used during the building process. To build and validate the model, we followed and extended the workflow and principles of a detailed model of neocortical microcircuitry (Markram et al., 2015). Part of the challenge was to build a network model with extremely sparse experimental data. For instance, information on the detailed neuron to neuron connectivity between thalamocortical and reticular neurons is not available and only two studies performed paired recordings in primary somatosensory thalamic pathways in the rat (Cox et al., 1997; Gentet and Ulrich, 2003). To deal with missing data, we had to include measurements from different species (rat or mice) or sometimes different age (P15-P50 mice, juvenile rats) during model building. Our main goal was to integrate available experimental data on thalamic microcircuitry in a unified view that only a biologically-detailed model can provide.

This model should be considered a first-draft reconstruction of thalamic microcircuitry, and although it has been constrained by available experimental data, it has a number of limitations. For instance, inclusion of specific ion channel mechanisms in different neuron types would more accurately reproduce differences in bursting behavior in reticular neurons and the dendritic properties of thalamic interneurons (Acuna-Goycolea et al., 2008; Astori et al., 2011; Huguenard and Prince, 1992; Lüthi and McCormick, 1998; Pellegrini et al., 2016). Neurites and synapse densities from electron microscope reconstructions could be used to validate the neurons and connectivity reconstructions (Kubota et al., 2018; Yin et al., 2019). Neuron counts and density will be more accurately estimated by acquiring more data and by using them to create different instantiations of the microcircuit (Keller et al., 2018; Markram et al., 2015). The distinction of different morphological types and a more accurate distribution within thalamic and reticular domains (Deleuze and Huguenard, 2006; Krahe et al., 2011; Li et al., 2020; Martinez-Garcia et al., 2020; Spreafico et al., 1991), could constrain further our derived connectivity. We did not adjust model parameters to reproduce specific network phenomena, as they were constrained by experimental data. Nevertheless, we found that the model was robust to the specific parameter values, when we varied them within experimentally plausible ranges.

Although the model was built with the primary goal of integrating experimental measurements from different levels of investigation, we found that it was able to generate emergent network phenomena, such as spindle-like oscillations. Observing evoked oscillations in the model was

surprising, considering that the model was built and validated with rodents data, while the generation of network oscillations in slice was mainly demonstrated in ferrets (Bal et al., 1995b; von Krosigk et al., 1993; Steriade et al., 1987). Furthermore, although the model was mainly based on *in vitro* findings, many aspects closely resemble thalamic activities during spindle oscillations *in vivo* in rodents (Bartho et al., 2014; Rovó et al., 2014; Urbain et al., 2019).

The model presented here provided novel insights on the generation of sleep spindles in thalamic networks. It differs from previous models in several aspects, besides the different scales (in terms of number of neurons), the level of biological detail and scope (Bazhenov et al., 2000; Bonjean et al., 2011; Destexhe et al., 1994, 1996, 1998b; Golomb et al., 1996). Since the model was not explicitly constrained for the generation of sleep spindles, we gained some novel insights on the thalamic mechanisms underlying rhythm generation, maintenance and termination and on the aspects where external input may be necessary. While we found that spindles cannot initiate spontaneously in our model, the maintenance and termination of the oscillation can be sustained by thalamic mechanisms.

In agreement with previous experimental and modelling studies, spindle oscillations are generated through a combination of intrinsic mechanisms, namely low-threshold calcium bursting in reticular neurons (Astori et al., 2011; Pellegrini et al., 2016) and the synaptic interactions between reticular and thalamocortical neurons (Destexhe et al., 1993, 1996; Li et al., 2017). Neither the thalamus, nor the reticular nucleus alone sustained network oscillations. It is possible that the reticular nucleus model alone could generate spindle-like activity with stronger inhibitory connections and gap junctions, as suggested by *in vivo* recordings in cat and computational models (Destexhe and Sejnowski, 2003; Destexhe et al., 1994a, 1994b; Steriade et al., 1987). In our model, we observed that TC cells tended to fire single spikes, rather than bursts, in response to Rt-mediated inhibition. This aspect needs further investigation, since intracellular recordings in naturally sleeping mice show bursting activity (consisting of more than 1 spike) in VPM neurons (Urbain et al., 2019). Yet, the responses of TCs in the model were sufficient to activate Rt neurons and began a new oscillation cycle. We also found that the percentage of neurons activated during each oscillation cycle and the population firing rates were in general higher for Rt than TC neurons, in line with data in naturally sleeping rats (Bartho et al., 2014).

In most simulation conditions, Rt and TC neurons fire with higher probabilities around the middle part of the oscillation, indicating that the progressive recruitment of more Rt and TC neurons underlies the waxing phase of the oscillation. This “crescendo” of activity had a temporal as well as a spatial component (Destexhe et al., 1996). We found spatial recruitment from the center to the sides of the circuit in the Rt and VPL; along the vertical dimension, inhibition started and was more prominent in the central portion of the VPL. Spatial recruitment was visibly reduced when we removed gap junctions from the model, in particular along the horizontal dimension in the Rt, which is the main direction along which reticular dendrites are oriented. We also showed that gap junctions are not strictly necessary for the generation of

synchronized thalamic oscillations, but facilitate the fast recruitment of larger populations of Rt neurons and the emergence of longer oscillations with smaller pools of “initiator” cells.

The model accounted for spindle termination through synaptic mechanisms alone, and therefore did not require specific ionic mechanisms, such as Ca^{2+} -dependent upregulation of the I_h current in TC cells (Bonjean et al., 2011; Bús et al., 2018; Destexhe et al., 1996, 1998) or desynchronizing cortical input (Bonjean et al., 2011). It will be interesting to verify if the current model can account for the spindle refractory period, which have been shown to depend on the upregulation of the I_h current in TC cells (Destexhe et al., 1998a; Kim et al., 1995). Nevertheless, we found that the modelled cells and circuit had mechanisms that limit the duration of the oscillation. Although further analysis of the intrinsic and synaptic conductances and other state variables would be helpful, we already have results supporting an important role of mutual inhibition between reticular neurons (Beenhakker and Huguenard, 2009; Fogerson and Huguenard, 2016; Makinson et al., 2017; Sohal and Huguenard, 2003), since removal of this connection resulted in prolonged oscillations. We propose that contribution of Rt cells to spindle oscillations could have a self-limiting factor: on the one hand they promote synchronized IPSPs and post-inhibitory excitatory responses from the TCs, thus recruiting more and more Rt neurons, with the contribution of gap junctions; on the other hand, when a critical recruitment in the Rt is reached, the overall excitation is overcome by reciprocal inhibition between Rt neurons, and the oscillatory activity would limit itself. Other possible mechanisms are synaptic short-term depression, which is present in all our intrathalamic connections, as suggested by *in vitro* recordings in ferret and a recent computational study (Kim et al., 1995; Li et al., 2017).

In summary, we developed a first-draft large-scale model of thalamic and reticular microcircuitry. Although it is, to the best of our knowledge, the most detailed thalamic model created so far, it is just a first step. Network simulations validated its general behavior with the generation of spindle-like oscillations. The next steps would be to study in more detail the network properties in *in vivo*-like spontaneous and evoked conditions (e.g. with simulated sensory inputs), and the thalamic contributions to functionally relevant thalamocortical states.

5 Conclusion and outlook

At the beginning of this thesis, we highlighted the importance of the thalamus in the transmission of information between the periphery and the neocortex. We also reviewed how the reticular nucleus is a key structural and functional component in the modulation of this information. Recent experimental advances have made the reticular nucleus selectively accessible and paved the way for understanding its role in behavior and in shaping thalamocortical rhythms *in vivo* (Halassa et al., 2011, 2014; Wimmer et al., 2015). On the other hand, such targeted manipulations of different thalamic nuclei are not possible yet.

Although the ultimate goal of any neuroscience project is understanding the complexity of the brain *in vivo*, there are countless factors that influence its activity during behaviorally relevant states. To tackle this challenge, we proposed a complementary computational approach, which had already proven successful to reconstruct a dense model of neocortical microcircuitry from sparse experimental data (Markram et al., 2015). While building a model of thalamic neurons and microcircuitry (Chapters 3 and 4), we realized that direct measurement of its fundamental components, such as synaptic interactions between neuron pairs, can be very challenging. We thus included findings from the neuroscientific literature to constrain and validate our models. To extract this information from the literature and to guarantee the reproducibility of our results, we developed a framework for its collaborative and systematic curation (Chapter 2). Through a continue cycle of model building and validation, we developed a first-draft model of thalamic microcircuitry, which will be continuously refined as experimental data become available. This model allowed us to study the cellular and circuit contributions to rhythm generation in the thalamus, and to perform initial simulations to validate the network activity in response to external inputs from the periphery and from the neocortex.

5.1 Summary of main conclusions

In this thesis we developed the first experimentally-constrained models of thalamic and reticular neurons and integrated them in a unified model of thalamo-reticular microcircuitry, which leveraged a framework for systematic curation of the literature. Below we summarize the most important novel contributions and insights that are part of this thesis, grouped in three main topics:

- Open-access resources for the computational neuroscience community (Chapters 2 and 3):

- A software for systematic curation of the literature, implementing data standardization and reusability principles.
- An initial corpus of literature annotations for modelling thalamic neurons and microcircuitry.
- Three-dimensional reconstructions of thalamic neurons available on the main online resource for neuron morphologies (Neuromorpho.Org).
- Biophysically-detailed neuron models of thalamic neurons and resources for constraining their parameters with experimental data and multiobjective optimizations.
- Structural principles underlying thalamic connectivity (Chapter 4):
 - The detailed connectivity in thalamic microcircuits can be predicted by the morphological properties of their neurons. This extends principles already validated for neocortical circuit models (Hill et al., 2012; Reimann et al., 2015) to a subcortical brain region.
 - Gap junctions connect reticular neurons that are more than 200 μm away, and this was entirely predicted from their morphological properties. We predict that each reticular neuron in the mouse has on average 30 GJs (range 10-80).
- Cellular and synaptic contributions to thalamic rhythm generation (Chapter 4):
 - Spindle-like rhythms can be evoked at the network level in a detailed model of thalamic microcircuitry, constrained with *in vitro* data from studies in rodents.
 - External inputs are necessary for spindle initiation, while intrathalamic network mechanisms sustain the activity and promote its termination.
 - Cortical inputs are not necessary for the termination of spindle-like oscillations. We found intrathalamic mechanisms that gradually decrease population activities that do not involve intrinsic neuron properties. We showed that one of these key mechanisms is mutual inhibition between reticular neurons. Another possible mechanism is synaptic short-term depression at thalamo-reticular and reticulo-thalamic synapses, which is present in our model. Its role in spindle termination will be investigated in the future, along with the contribution of these mechanisms to spindle refractory periods characterized *in vitro* (Kim et al., 1995) and *in vivo* (Destexhe et al., 1998a).
 - Burst firing in reticular neurons, post-inhibitory rebound responses in thalamocortical neurons and their synaptic interactions are necessary for the maintenance of spindle rhythms in thalamic networks in *in vitro*-like conditions. The ability of the model to generate spindle-like oscillations in the isolated reticular nucleus will be investigated in the future.

- Reticular neurons have higher population firing rates compared to thalamocortical neurons during spindle-like oscillations.
- Spindle-like oscillations have waxing-and-waning patterns in time and space, that are organized along the directions of thalamic and reticular neurons axons (vertical dimension of the microcircuit) and reticular neurons dendrites (lateral dimension of the microcircuit).
- Gap junctions contribute to the spatial recruitment of reticular neurons along the lateral dimension of the microcircuit.
- The duration of the oscillation, as well its frequency can be varied by changing the depolarization levels in reticular and thalamocortical neurons. The dependence of spindle length on the activity of reticular neurons observed *in vivo* (Bartho et al., 2014) can be explained by their membrane potentials upon spindle initiation.

5.2 Implications

In this thesis we focused on a model of thalamic microcircuitry and studied in detail different aspects of rhythm generation (spindle-like oscillations). The activity of this circuit and its dynamical modulation across different states (e.g. wakefulness, sleep, inattentive and vigilant states) have important roles in behavior and correlations with neurological (e.g. childhood absence epilepsy) and mental diseases (e.g. schizophrenia).

5.2.1 Thalamic activities in wakefulness, sleep and attention

5.2.1.1 Thalamic firing modes in wakefulness and NREM sleep

During different states, the membrane potential of thalamic and reticular neurons are modulated by different neuromodulatory systems (Lee and Dan, 2012; McCormick, 1992). Modulation of the membrane potential has important effects on network dynamics and are associated with different firing modes, with tonic spiking associated with awake states and bursting occurring more frequently during drowsiness or NREM sleep (Bezudnaya et al., 2006; McCormick and Bal, 1997; Sherman, 2005). We showed these different firing modes at the single neuron level (Chapter 3) and in network simulations (Chapter 4). At the network level in the model, tonic firing was the main firing mode in *in vivo*-like spontaneous activities, while low-threshold bursting emerged during spindle-like oscillations.

The membrane potential of thalamic neurons dynamically changes during different awake states, for example it decreases (neurons are more hyperpolarized) from active states to quiet wakefulness (Urbain et al., 2015). It also evolves from quiet wakefulness to sleep, with thalamic neurons becoming more hyperpolarized during the transition to NREM sleep (Urbain

et al., 2019). These changes are accompanied by variations in spindle features during NREM (Urbain et al., 2019), such as a decrease in their frequency, as we have predicted in the model (Fig. 4.10). All these aspects and the relationships between spindle and other sleep-related rhythms, such as the slow oscillations, will be explored in future studies (Section 5.3.2).

5.2.1.2 The role of the reticular nucleus in attention

In behavioral tasks requiring attending to conflicting stimuli, the regulation of the activity in different sectors is correlated to the attended sensory modality (Wimmer et al., 2015). This attention-mediated sensory filtering in the Rt involves a prefrontal cortex-basal ganglia-Rt circuit (Nakajima et al., 2019). Alterations in Rt activities, that likely reflect impaired attention and poor ability to select between conflicting sensory stimuli, have been linked to genes, such as *ErbB4*, which are associated with mental disorders and schizophrenia (Ahrens et al., 2015). *ErbB4* encodes for a receptor contributes to the maturation of corticoreticular projections. In this study, mice that had deficiency of *ErbB4* in somatostatin-positive Rt neurons performed better in single-modality tasks, whereas their ability to discriminate between conflicting sensory modalities impaired. At the thalamic level, it was found that cortical drive onto Rt neurons was increased, suggesting a key role of the corticoreticular (and corticothalamic) pathways in sensory discrimination.

Gene association studies found other genes expressed in the Rt and linked to attention- and autism-related deficits (Krol et al., 2018). One of this cases is the mutation of *PTCHD1* gene (Patch domain-containing protein 1) (Wells et al., 2016). During postnatal development in mice, *PTCHD1* is selective expressed in the reticular nucleus and its mutation attenuate Rt neurons bursting activity through reduction of the SK Ca^{2+} -activated potassium channels. Furthermore, *PTCHD1* knockout mice showed an overall reduction in the number of spindles, reduced sensory-related thalamic inhibition, highly fragmented sleep and decreased performance in sensory tasks involving visual distractors. These results show how alterations of single channels and neuron activities have an impact on brain activity during sleep and behavior.

There are also intriguing relationships between sleep-related rhythms and attention. A recent study proposed that spindle waves during sleep may be the counterpart of alpha oscillations in awake states during attention (Chen et al., 2016). This hypothesis calls for a mechanistic understanding of these two rhythms that can be provided by a computational model of the full thalamocortical loop. It was found that subpopulations of sensory-related reticular neurons fired in correlation with spindles recorded at the cortical level (Halassa et al., 2014) and that Rt neurons that were active during sleep spindles were associated with alpha oscillations (9-15 Hz) during attention (Chen et al., 2016). More specifically, Rt neurons fired on opposite phases of alpha and spindle oscillations and might indicate overlapping but non-identical mechanisms (Chen et al., 2016).

5.2.2 Thalamic neurons and microcircuits in neurological and mental disorders

5.2.2.1 Thalamic “choke points” and epileptic-like rhythms

Pathological perturbations of rhythm-generating circuits can result in local and generalized hypersynchronous and epileptiform activity. These forms of activity have similar 3-4 Hz phasic EEG waveforms in human and rodents, called spike-and-wave discharges (SWDs). SWDs are typical of absence epilepsy in children, a pathological state characterized by nonconvulsive loss of consciousness that lasts for a few seconds.

Many genetic and pharmacological studies showing SWD-like activity in brain slices suggested that the same thalamic circuits that generate sleep spindles are implicated in epileptic-like activities (Beenhakker and Huguenard, 2009; Fogerson and Huguenard, 2016). However, it's important to note that SWD discharges are probably non simply “perverted” sleep spindles and may have distinct origins (Leresche et al., 2012). Different microcircuit motives, involving feedback inhibition (from Rt to TC neurons) and mutual inhibition (between Rt neurons) have been identified as potential epileptic “choke points” (Paz and Huguenard, 2015). As we have showed in the model, the mutual inhibition between reticular neurons has an important role in limiting synchronous burst firing in Rt cells and consequent strong inhibition/rebound responses in TC neurons (Fig. 4.9). In the model, we found that mutual inhibition between Rt neurons can decrease the number of spikes in the bursts of Rt neurons or suppress the burst completely, in agreement with slice experiments (Sohal and Huguenard, 2003). When the mutual inhibition was removed in the model, feedback inhibition (from Rt to TC neurons) was enhanced. This results are in agreement with *in vitro* studies in mice showing that hypersynchronous thalamic activity can be the result of loss of GABA_A receptor-mediated inhibition specific to the Rt (Huntsman et al., 1999).

Increased Rt hypersynchronous bursting results in increased GABA release and activation of not only synaptic GABA_A receptors, but also extrasynaptic GABA_A or GABA_B receptors (Cope et al., 2009; Kim et al., 1997). Increased activation of GABA_B currents, with their slower kinetics compared to GABA_A currents, could explain the lower frequency (3-4 Hz) of bicuculline-induced oscillation in slice experiments compared to spindle-like rhythms (Beenhakker and Huguenard, 2009). When we included GABA_B currents in our model, we also observed a decrease in the oscillation frequency (data not shown). It is worth mentioning that bicuculline blocks GABA_A receptors, as well as Ca²⁺-activate potassium currents (SK-type) in reticular neurons, as shown in rat slices, and enhances their low-threshold burst activity (Debarbieux et al., 1998). An interesting case for the importance of Rt-mediated inhibition has been recently made in adult *Scn8a*-knockout mice (Makinson et al., 2017). The selective suppression of this gene, coding for a widely expressed subtype of voltage-gated sodium channels, resulted in specific failure at the Rt to Rt synapses, while it left the Rt to TC synapse relatively unaffected, as shown *in vitro*. *In vivo*, the loss of this single gene was sufficient to cause SWDs.

In the model we found that mutual inhibition between Rt neurons shorten spindle-like oscillations, while gap junctions tended to make them longer, in agreement with a desynchronizing role proposed for the former and synchronizing for the latter (Beenhakker and Huguenard, 2009; Fernandez and Luthi, 2019). Furthermore, coupling through gap junctions is stronger for low-threshold calcium spikes (underlying the bursts) than single sodium spikes, due to the low-pass filter properties of the coupled membranes (Long et al., 2004). Low-threshold bursting is the predominant firing mode of reticular neurons during oscillatory activities. Since gap junctions directly join the membranes of coupled neurons and are thought to transmit rapidly depolarizing signals between dendrites and contribute to network synchronization (Kohmann et al., 2016).

5.2.2.2 *The reticular nucleus in schizophrenia*

Sleep spindle density correlates with several disorders which lead to cognitive deficits, for example they are reduced in schizophrenic patients (Castelnovo et al., 2018; Ferrarelli et al., 2007, 2010; Manoach et al., 2014, 2016). Schizophrenia arises out of combinations of genetic predispositions and environmental factors and can result in sensory misperceptions and sleep disturbances, among other symptoms (Fernandez and Luthi, 2019).

Among the many sleep alternations, the decrease of spindles is a common denominator in many patients (Fernandez and Luthi, 2019). Despite the diversity of functional deficits in schizophrenia, the reticular nucleus and thalamic neurons are frequently affected at different levels. At the cellular and network levels, a recent study showed that the decrease of spindle in animal models of psychosis-related states is associated with increased depolarization and tonic firing in thalamocortical and reticular neurons (Mahdavi et al., 2020). This increased transient depolarization would decrease spindling activity, in agreement with the difficulty of evoking spindle-like oscillations in our model when TC and Rt were depolarized (Fig. 4.10).

At the molecular and cellular levels, it was found that the number of parvalbumin-expressing (PV) neurons in the Rt nucleus are reduced in mouse models and schizophrenic patients (Steullet et al., 2018). PV Rt cells are a subpopulation of reticular neurons with higher tendency to burst and rhythmogenic activity, due to at least in part to higher amplitudes of the low-threshold calcium current (Clemente-Perez et al., 2017). Furthermore, many genetic risk factors that have been linked to schizophrenia are highly expressed in the reticular nucleus and have important roles in spindle generation, such as the *CACNA1I* gene encoding for the low-threshold calcium channel Cav3.3 (Andrade et al., 2016; Astori et al., 2011).

These findings are in agreement with a recent comprehensive study of Rt cellular heterogeneity, linking single cell gene expression at different locations of the Rt nucleus, cellular electrophysiology, morphology and system-level study of spindles *in vivo* (Li et al., 2020). Such multi-level studies, similarly to detailed computational models, are extremely powerful in bridging levels of experimental investigations and in providing frameworks for understanding the detailed contributions of genes, neurons and their connections to system-level functions.

5.3 Limitations and future directions

Although the microcircuit model we presented in this thesis is very detailed and constrained with biological data, it comes with caveats and limitations, as already detailed in Chapter 4.3. Many aspects of neuron properties, connectivity and synaptic properties can shift emergent network behavior in different directions. For instance, small differences in Ca^{2+} concentration between *in vitro* and *in vivo* conditions can generate a large spectrum of network activities, through changes in synaptic release probabilities (Markram et al., 2015). To further validate the model and gain insights on dynamics that are closer to functionally relevant states, it is important to further explore the model in *in vivo*-like states.

To address these questions, we introduce below two major simulation projects, that will be addressed in the near future. A further development of this thesis is the extension of the microcircuit model to the full thalamus and integration in a thalamo-neocortical model.

5.3.1 Thalamic microcircuitry in sensory processing

The goal of this simulation project is to study the responses of thalamic neurons to inputs from the periphery, extending the initial results shown in Chapter 4. We have already created an initial model of afferent medial lemniscus synapses (see Chapter 4.2.3). However, we did not take into account anatomical and physiological studies showing that, in adult animals, each thalamic neuron receive inputs from only one or few lemniscal fibers, at least in the VPM (Arsenault and Zhang, 2006; Takeuchi et al., 2014). We think that including this constrain will affect the network responses and will be likely reflected in the input/output relationship between activated fibers and populations responses. Another aspect that will be investigated is the expected responses at the network level, in terms of magnitude and delays, which depend on the strength and specificity of lemniscal synapses and multiple release sites (Castro-Alamancos, 2015; Spacek and Lieberman, 1974).

Moreover, to study sensory responses in *in vivo*-like conditions we will need to carefully consider spontaneous firing rates from cuneate and gracilis neurons projecting to the ventrobasal thalamus, corticothalamic neurons and the frequency of spontaneous synaptic release. For example, cuneate neurons whose axons are part of the medial lemniscus, have been reported to fire at low rates, around 5 Hz, in anesthetized rats (Alloway et al., 2003; Sánchez et al., 2006). Pyramidal neurons in layer 6, which provide the main cortical input to primary thalamic nuclei (Bourassa and Deschenes, 1995; Bourassa et al., 1995) have been reported to spontaneously fire at low frequencies *in vivo* (0.1-2 Hz) (Crandall et al., 2015; Pausin and Krieger, 2018). Spontaneous firing rates of thalamic neurons can be validated against values reported *in vivo* (Gwak et al., 2010; Monconduit et al., 2006; Urbain et al., 2015). Evoked responses can then be studied *in vivo*-like conditions, along with the influences of corticothalamic inputs onto sensory adaptation (Mease et al., 2014), for instance.

Sensory responses in the visual thalamus have been shown to be enriched by direct and rapid synaptic inhibitions from interneuron dendrites in triadic synaptic arrangements (Heiberg et al., 2016; Hirsch et al., 2015; Morgan and Lichtman, 2020; Sherman, 2004). Since interneurons are present in the somatosensory thalamus, we think that similar synaptic motives can shape sensory responses in different ways. After assessing the presence of triadic synapses in our model, their functional role will be explored.

5.3.2 Corticothalamic influences onto thalamic and reticular activities

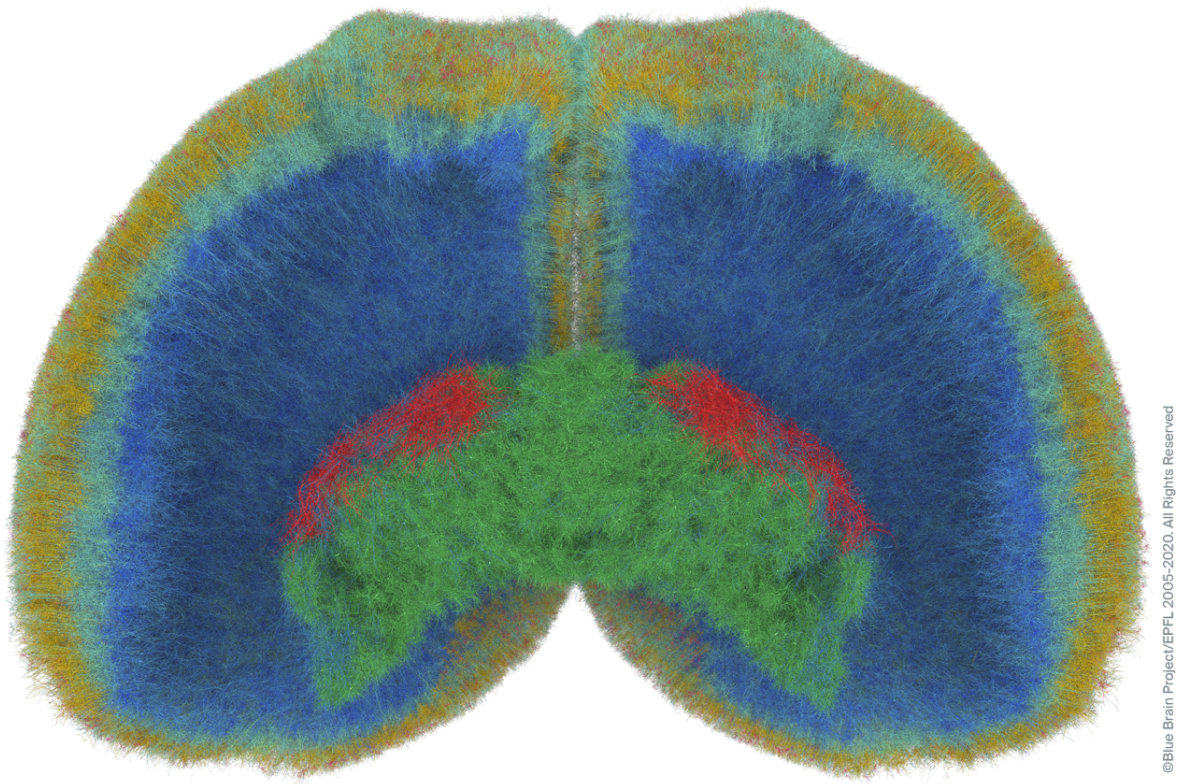
We focused our initial efforts on studying the thalamic contributions to spindle-like rhythms. While our simulations helped clarifying which aspects can be sustained by the thalamo-reticular network, they showed that external inputs are necessary to trigger the oscillation. This external input during non-REM sleep is likely to come from the neocortex (Blumenfeld and McCormick, 2000; Bonjean et al., 2011; Destexhe et al., 1998a). The relationship between cortical up-states and thalamic activity has been extensively studied in anesthetized animals, with spindles often occurring near the trough of cortical slow waves (up-states), when cortical neurons are more active (Destexhe et al., 2007; McCormick and Bal, 1997; Steriade et al., 1993). Our next step will be to study the role of corticothalamic input in the generation of thalamic spindles and comparing the model predictions with findings in naturally sleeping mice (Urbain et al., 2019).

5.3.3 Whole thalamus and whole thalamocortical integration

At the beginning of this thesis we set out to shed light on the complexity of thalamic function in thalamocortical circuitry. We started from a tiny portion of one of the simplest thalamic circuits, the one that processes primary somatosensory information. A natural development would be to integrate our thalamic model in a model of the whole thalamus and neocortex. Such a model would be an ideal benchmark to study thalamic modulation of cortical activity (Poulet et al., 2012) or the interaction between primary and higher-order thalamic nuclei in shaping sensory and sensory-motor responses (Mease et al., 2016; Mo and Sherman, 2019), among others.

Although we are still far from developing a detailed model of the thalamocortical system, which we estimated comprises ~12 million neurons, at the level of detail described here, it might be soon possible to tackle this challenge (Fig. 5.1). Indeed, computational approaches, such as morphology synthesis, could help us generate unique neuron models for millions of cells (Kanari et al., 2020), which can be placed according to biologically-plausible neuron densities thanks to a cell atlas of the mouse brain (Erö et al., 2018). Furthermore, significant steps have been taken to make large-scale detailed simulations more efficient (Kumbhar et al., 2019). Finally, findings from the neuroscientific literature, tools to systematically and automatically extract them, along with international collaboration, will be very helpful for such

large-scale modelling efforts (Huang and Luo, 2015; O'Reilly et al., 2017; Shardlow et al., 2019).



©Blue Brain Project/EPFL 2005-2020. All Rights Reserved

Figure 5.1 Draft models of the thalamus and the neocortex.

Illustration showing draft models of the thalamus (green), bilateral reticular nuclei (red) and neocortex with the anatomical constraint of the Allen Atlas of the Mouse Brain. Only 1% of the neurons are shown and each neuron is assigned a detailed morphology. *Image courtesy of Cyrille Favreau, Blue Brain Visualization Team.*

Bibliography

Acuna-Goycolea, C., Brenowitz, S.D., and Regehr, W.G. (2008). Active dendritic conductances dynamically regulate GABA release from thalamic interneurons. *Neuron* 57, 420–431.

Adamantidis, A.R., Herrera, C.G., and Gent, T.C. (2019). Oscillating circuitries in the sleeping brain. *Nat Rev Neurosci* 1–17.

Adrian, E.D. (1941). Afferent discharges to the cerebral cortex from peripheral sense organs. *J. Physiol. (Lond.)* 100, 159–191.

Ahrens, S., Jaramillo, S., Yu, K., Ghosh, S., Hwang, G.-R., Paik, R., Lai, C., He, M., Huang, Z.J., and Li, B. (2015). ErbB4 regulation of a thalamic reticular nucleus circuit for sensory selection. *Nat. Neurosci.* 18, 104–111.

Allen Institute For Brain Science (2017). Technical white paper: Allen mouse common coordinate framework and reference atlas, October 2017.

Alloway, K.D., Hoffer, Z.S., and Hoover, J.E. (2003). Quantitative comparisons of corticothalamic topography within the ventrobasal complex and the posterior nucleus of the rodent thalamus. *Brain Research* 968, 54–68.

Almog, M., and Korngreen, A. (2016). Is realistic neuronal modeling realistic? *Journal of Neurophysiology* 116, 2180–2209.

Amarillo, Y., Zagha, E., Mato, G., Rudy, B., and Nadal, M.S. (2014). The interplay of seven subthreshold conductances controls the resting membrane potential and the oscillatory behavior of thalamocortical neurons. *Journal of Neurophysiology* 112, 393–410.

Amarillo, Y., Mato, G., and Nadal, M.S. (2015). Analysis of the role of the low threshold currents I_T and I_h in intrinsic delta oscillations of thalamocortical neurons. *Front Comput Neurosci* 9.

Amsalem, O., Van Geit, W., Muller, E., Markram, H., and Segev, I. (2016). From Neuron Biophysics to Orientation Selectivity in Electrically Coupled Networks of Neocortical L2/3 Large Basket Cells. *Cereb. Cortex* 26, 3655–3668.

Andersen, P., and Andersson, S.A. (1968). *Physiological basis of the alpha rhythm* (Plenum Publishing Corporation).

Andrade, A., Hope, J., Allen, A., Yorgan, V., Lipscombe, D., and Pan, J.Q. (2016). A rare schizophrenia risk variant of CACNA1I disrupts Ca V 3.3 channel activity. *Scientific Reports* 6, 34233.

- Anwar, H., Riachi, I., Hill, S., Schürmann, F., and Markram, H. (2009). An approach to capturing neuron morphological diversity. In *Computational Neuroscience. Realistic Modeling for Experimentalists.*, E. De Schutter, ed. (Cambridge, Mass: MIT Press), pp. 211–232.
- Arcelli, P., Frassoni, C., Regondi, M.C., De Biasi, S., and Spreafico, R. (1997). GABAergic neurons in mammalian thalamus: a marker of thalamic complexity? *Brain Res Bull* 42, 27–37.
- Arsenault, D., and Zhang, Z. (2006). Developmental remodelling of the lemniscal synapse in the ventral basal thalamus of the mouse. *J Physiol* 573, 121–132.
- Ascoli, G. a, Alonso-Nanclares, L., Anderson, S. a, Barrionuevo, G., Benavides-Piccione, R., Burkhalter, A., Buzsáki, G., Cauli, B., Defelipe, J., Fairén, A., et al. (2008). Petilla terminology: nomenclature of features of GABAergic interneurons of the cerebral cortex. *Nature Reviews. Neuroscience* 9, 557–568.
- Ascoli, G.A., Donohue, D.E., and Halavi, M. (2007). NeuroMorpho.Org: A Central Resource for Neuronal Morphologies. *J. Neurosci.* 27, 9247–9251.
- Astori, S., Wimmer, R.D., Prosser, H.M., Corti, C., Corsi, M., Liaudet, N., Volterra, A., Franken, P., Adelman, J.P., and Lüthi, A. (2011). The Ca(V)3.3 calcium channel is the major sleep spindle pacemaker in thalamus. *Proc. Natl. Acad. Sci. U.S.A.* 108, 13823–13828.
- Avanzini, G., de Curtis, M., Panzica, F., and Spreafico, R. (1989). Intrinsic properties of nucleus reticularis thalami neurones of the rat studied in vitro. *J Physiol* 416, 111–122.
- Bada, M., Eckert, M., Evans, D., Garcia, K., Shipley, K., Sitnikov, D., Baumgartner, W.A., Cohen, K.B., Verspoor, K., Blake, J.A., et al. (2012). Concept annotation in the CRAFT corpus. *BMC Bioinformatics* 13, 161.
- Bal, T., and McCormick, D.A. (1996). What Stops Synchronized Thalamocortical Oscillations? *Neuron* 17, 297–308.
- Bal, T., von Krosigk, M., and McCormick, D.A. (1995a). Role of the ferret perigeniculate nucleus in the generation of synchronized oscillations in vitro. *J Physiol* 483, 665–685.
- Bal, T., von Krosigk, M., and McCormick, D.A. (1995b). Synaptic and membrane mechanisms underlying synchronized oscillations in the ferret lateral geniculate nucleus in vitro. *J. Physiol. (Lond.)* 483 (Pt 3), 641–663.
- Barros-Zulaica, N., Rahmon, J., Chindemi, G., Perin, R., Markram, H., Muller, E., and Ramaswamy, S. (2019). Estimating the Readily-Releasable Vesicle Pool Size at Synaptic Connections in the Neocortex. *Frontiers in Synaptic Neuroscience* 11, 29.
- Bartho, P., Slezia, A., Matyas, F., Faradzs-Zade, L., Ulbert, I., Harris, K.D., and Acsady, L. (2014). Ongoing network state controls the length of sleep spindles via inhibitory activity. *Neuron* 82, 1367–1379.
- Bazhenov, M., Timofeev, I., Steriade, M., and Sejnowski, T.J. (1998). Cellular and network models for intrathalamic augmenting responses during 10-Hz stimulation. *Journal of Neurophysiology* 79, 2730–2748.

Beenhakker, M.P., and Huguenard, J.R. (2009). Neurons that Fire Together Also Conspire Together: Is Normal Sleep Circuitry Hijacked to Generate Epilepsy? *Neuron* 62, 612–632.

Bezudnaya, T., Cano, M., Bereshpolova, Y., Stoelzel, C.R., Alonso, J.-M., and Swadlow, H.A. (2006). Thalamic burst mode and inattention in the awake LGNd. *Neuron* 49, 421–432.

de Biasi, S., Frassoni, C., and Spreafico, R. (1986). GABA immunoreactivity in the thalamic reticular nucleus of the rat. A light and electron microscopical study. *Brain Research* 399, 143–147.

Bickford, M.E., Slusarczyk, A., Dilger, E.K., Krahe, T.E., Kucuk, C., and Guido, W. (2010). Synaptic development of the mouse dorsal lateral geniculate nucleus. *Journal of Comparative Neurology* 518, 622–635.

Billeh, Y.N., Cai, B., Gratiy, S.L., Dai, K., Iyer, R., Gouwens, N.W., Abbasi-Asl, R., Jia, X., Siegle, J.H., Olsen, S.R., et al. (2020). Systematic Integration of Structural and Functional Data into Multi-scale Models of Mouse Primary Visual Cortex. *Neuron* 0.

BlueBrain (2018a). BlueBrain/eFEL.

BlueBrain (2018b). BlueBrain/BluePyOpt.

Blumenfeld, H., and McCormick, D.A. (2000). Corticothalamic Inputs Control the Pattern of Activity Generated in Thalamocortical Networks. *J. Neurosci.* 20, 5153–5162.

Bonjean, M., Baker, T., Lemieux, M., Timofeev, I., Sejnowski, T., and Bazhenov, M. (2011). Corticothalamic Feedback Controls Sleep Spindle Duration In Vivo. *Journal of Neuroscience* 31, 9124–9134.

Bourassa, J., and Deschenes, M. (1995). Corticothalamic projections from the primary visual cortex in rats: a single fiber study using biocytin as an anterograde tracer. *Neuroscience* 66, 253–263.

Bourassa, J., Pinault, D., and Deschênes, M. (1995). Corticothalamic projections from the cortical barrel field to the somatosensory thalamus in rats: a single-fibre study using biocytin as an anterograde tracer. *Eur. J. Neurosci.* 7, 19–30.

Bridson, R. (2007). Fast Poisson disk sampling in arbitrary dimensions. *SIGGRAPH Sketches* 10, 1278780.1278807.

Brown, J.W., Taheri, A., Kenyon, R.V., Berger-Wolf, T.Y., and Llano, D.A. (2020). Signal Propagation via Open-Loop Intrathalamic Architectures: A Computational Model. *ENeuro* 7.

Budde, T., Biella, G., Munsch, T., and Pape, H.-C. (1997). Lack of Regulation by Intracellular Ca²⁺ of the Hyper Polarization-Activated Cation Current in Rat Thalamic Neurones. *The Journal of Physiology* 503, 79–85.

Bús, B., Antal, K., and Emri, Z. (2018). Intrathalamic connections shape spindle activity - a modelling study. *Acta. Biol. Hung.* 69, 16–28.

Buzsáki, G. (1991). The thalamic clock: emergent network properties. *Neuroscience* 41, 351–364.

Castelnovo, A., Graziano, B., Ferrarelli, F., and D'Agostino, A. (2018). Sleep spindles and slow waves in schizophrenia and related disorders: main findings, challenges and future perspectives. *Eur. J. Neurosci.* 48, 2738–2758.

del Castillo, J., and Katz, B. (1954). Quantal components of the end-plate potential. *J Physiol* 124, 560–573.

Castro-Alamancos, M.A. (2002). Properties of primary sensory (lemniscal) synapses in the ventrobasal thalamus and the relay of high-frequency sensory inputs. *J. Neurophysiol.* 87, 946–953.

Castro-Alamancos, M.A. (2015). The Whisker Thalamus. In *Sensorimotor Integration in the Whisker System*, P. Krieger, and A. Groh, eds. (New York, NY: Springer), pp. 31–58.

Çavdar, S., Hacıoğlu, H., Doğukan, S.Y., and Onat, F. (2012). Do the quantitative relationships of synaptic junctions and terminals in the thalamus of genetic absence epilepsy rats from Strasbourg (GAERS) differ from those in normal control Wistar rats. *Neurol Sci* 33, 251–259.

Cavdar, S., Bay, H.H., Kirazli, O., Cakmak, Y.O., and Onat, F. (2013). Comparing GABAergic cell populations in the thalamic reticular nucleus of normal and genetic absence epilepsy rats from Strasbourg (GAERS). *Neurol Sci* 34, 1991–2000.

Cavdar, S., Bay, H.H., Yildiz, S.D., Akakin, D., Sirvanci, S., and Onat, F. (2014). Comparison of numbers of interneurons in three thalamic nuclei of normal and epileptic rats. *Neurosci Bull* 30, 451–460.

Chen, Z., Wimmer, R.D., Wilson, M.A., and Halassa, M.M. (2016). Thalamic Circuit Mechanisms Link Sensory Processing in Sleep and Attention. *Front Neural Circuits* 9.

Choisy, M. (2018). Identifying a cutoff value from bimodal data.

Clascá, F., Rubio-Garrido, P., and Jabaudon, D. (2012). Unveiling the diversity of thalamocortical neuron subtypes: Thalamocortical neuron diversity. *European Journal of Neuroscience* 35, 1524–1532.

Clemente-Perez, A., Makinson, S.R., Higashikubo, B., Brovarney, S., Cho, F.S., Urry, A., Holden, S.S., Wimer, M., Dávid, C., Fenno, L.E., et al. (2017). Distinct thalamic reticular cell types differentially modulate normal and pathological cortical rhythms. *Cell Rep* 19, 2130–2142.

Connelly, W.M., Crunelli, V., and Errington, A.C. (2015). The Global Spike: Conserved Dendritic Properties Enable Unique Ca²⁺ Spike Generation in Low-Threshold Spiking Neurons. *Journal of Neuroscience* 35, 15505–15522.

Connelly, W.M., Crunelli, V., and Errington, A.C. (2016). Passive Synaptic Normalization and Input Synchrony-Dependent Amplification of Cortical Feedback in Thalamocortical Neuron Dendrites. *J Neurosci* 36, 3735–3754.

Connelly, W.M., Crunelli, V., and Errington, A.C. (2017). Variable action potential backpropagation during tonic firing and low-threshold spike bursts in thalamocortical but not thalamic reticular nucleus neurons. *The Journal of Neuroscience* 0015–0017.

- Contreras, D., Destexhe, A., Sejnowski, T.J., and Steriade, M. (1997). Spatiotemporal patterns of spindle oscillations in cortex and thalamus. *J. Neurosci.* *17*, 1179–1196.
- Cope, D.W., Di Giovanni, G., Fyson, S.J., Orbán, G., Errington, A.C., Lorincz, M.L., Gould, T.M., Carter, D.A., and Crunelli, V. (2009). Enhanced tonic GABAA inhibition in typical absence epilepsy. *Nat. Med.* *15*, 1392–1398.
- Cox, C.L., Huguenard, J.R., and Prince, D.A. (1996). Heterogeneous axonal arborizations of rat thalamic reticular neurons in the ventrobasal nucleus. *J Comp Neurol* *366*, 416–430.
- Cox, C.L., Huguenard, J.R., and Prince, D.A. (1997). Nucleus reticularis neurons mediate diverse inhibitory effects in thalamus. *Proc Natl Acad Sci U S A* *94*, 8854–8859.
- Crabtree, J.W. (2018). Functional Diversity of Thalamic Reticular Subnetworks. *Front. Syst. Neurosci.* *12*.
- Crandall, S.R., Cruikshank, S.J., and Connors, B.W. (2015). A Corticothalamic Switch: Controlling the Thalamus with Dynamic Synapses. *Neuron* *86*, 768–782.
- Cruikshank, S.J., Urabe, H., Nurmikko, A.V., and Connors, B.W. (2010). Pathway-Specific Feedforward Circuits between Thalamus and Neocortex Revealed by Selective Optical Stimulation of Axons. *Neuron* *65*, 230–245.
- Debarbieux, F., Brunton, J., and Charpak, S. (1998). Effect of bicuculline on thalamic activity: a direct blockade of IAHP in reticularis neurons. *J. Neurophysiol.* *79*, 2911–2918.
- Deleuze, C., and Huguenard, J.R. (2006). Distinct Electrical and Chemical Connectivity Maps in the Thalamic Reticular Nucleus: Potential Roles in Synchronization and Sensation. *J. Neurosci.* *26*, 8633–8645.
- Deleuze, C., and Huguenard, J.R. (2016). Two classes of excitatory synaptic responses in rat thalamic reticular neurons. *Journal of Neurophysiology* *116*, 995–1011.
- Deschênes, M., Veinante, P., and Zhang, Z.-W. (1998). The organization of corticothalamic projections: reciprocity versus parity. *Brain Research Reviews* *28*, 286–308.
- Destexhe, A., and Sejnowski, T.J. (1995). G protein activation kinetics and spillover of gamma-aminobutyric acid may account for differences between inhibitory responses in the hippocampus and thalamus. *Proc. Natl. Acad. Sci. U.S.A.* *92*, 9515–9519.
- Destexhe, A., and Sejnowski, T.J. (2003). Interactions Between Membrane Conductances Underlying Thalamocortical Slow-Wave Oscillations. *Physiological Reviews* *83*, 1401–1453.
- Destexhe, A., McCormick, D.A., and Sejnowski, T.J. (1993). A model for 8-10 Hz spindling in interconnected thalamic relay and reticularis neurons. *Biophysical Journal* *65*, 2473–2477.
- Destexhe, A., Contreras, D., Sejnowski, T.J., and Steriade, M. (1994a). A model of spindle rhythmicity in the isolated thalamic reticular nucleus. *J. Neurophysiol.* *72*, 803–818.
- Destexhe, A., Contreras, D., Sejnowski, T.J., and Steriade, M. (1994b). Modeling the control of reticular thalamic oscillations by neuromodulators. *Neuroreport* *5*, 2217–2220.

Destexhe, A., Bal, T., McCormick, D.A., and Sejnowski, T.J. (1996). Ionic mechanisms underlying synchronized oscillations and propagating waves in a model of ferret thalamic slices. *J. Neurophysiol.* 76, 2049–2070.

Destexhe, A., Contreras, D., and Steriade, M. (1998a). Mechanisms underlying the synchronizing action of corticothalamic feedback through inhibition of thalamic relay cells. *J. Neurophysiol.* 79, 999–1016.

Destexhe, A., Neubig, M., Ulrich, D., and Huguenard, J. (1998b). Dendritic low-threshold calcium currents in thalamic relay cells. *Journal of Neuroscience* 18, 3574–3588.

Destexhe, A., Hughes, S.W., Rudolph, M., and Crunelli, V. (2007). Are corticothalamic “up” states fragments of wakefulness? *Trends Neurosci.* 30, 334–342.

Druckmann, S., Banitt, Y., Gidon, A.A., Schürmann, F., Markram, H., and Segev, I. (2007). A novel multiple objective optimization framework for constraining conductance-based neuron models by experimental data. *Frontiers in Neuroscience* 1, 1.

Druckmann, S., Berger, T.K., Hill, S., Schürmann, F., Markram, H., and Segev, I. (2008). Evaluating automated parameter constraining procedures of neuron models by experimental and surrogate data. *Biological Cybernetics* 99, 371.

Ecker, A., Romani, A., Sáray, S., Káli, S., Migliore, M., Mercer, A., Markram, H., Muller, E., and Ramaswamy, S. (2019). Data-driven integration of hippocampal CA1 synapse physiology in silico. *BioRxiv* 716480.

Ehling, P., Cerina, M., Meuth, P., Kanyshkova, T., Bista, P., Coulon, P., Meuth, S.G., Pape, H.-C., and Budde, T. (2013). Ca²⁺-dependent large conductance K⁺ currents in thalamocortical relay neurons of different rat strains. *Pflügers Archiv-European Journal of Physiology* 465, 469–480.

Einevoll, G.T., Destexhe, A., Diesmann, M., Grün, S., Jirsa, V., Kamps, M. de, Migliore, M., Ness, T.V., Plesser, H.E., and Schürmann, F. (2019). The Scientific Case for Brain Simulations. *Neuron* 102, 735–744.

Erö, C., Gewaltig, M.-O., Keller, D., and Markram, H. (2018). A Cell Atlas for the Mouse Brain. *Front. Neuroinform.* 12.

Errington, A.C., Renger, J.J., Uebele, V.N., and Crunelli, V. (2010). State-dependent firing determines intrinsic dendritic Ca²⁺ signaling in thalamocortical neurons. *Journal of Neuroscience* 30, 14843–14853.

Espinosa, F., Torres-Vega, M.A., Marks, G.A., and Joho, R.H. (2008). Ablation of Kv3.1 and Kv3.3 Potassium Channels Disrupts Thalamocortical Oscillations In Vitro and In Vivo. *J Neurosci* 28, 5570–5581.

Evangelio, M., García-Amado, M., and Clascá, F. (2018). Thalamocortical Projection Neuron and Interneuron Numbers in the Visual Thalamic Nuclei of the Adult C57BL/6 Mouse. *Front. Neuroanat.* 12.

Fernandez, L.M.J., and Luthi, A. (2019). Sleep Spindles: Mechanisms and Functions. *Physiol. Rev.*

- Fernandez, L.M., Vantomme, G., Osorio-Forero, A., Cardis, R., Béard, E., and Lüthi, A. (2018). Thalamic reticular control of local sleep in mouse sensory cortex. *ELife* 7, e39111.
- Ferrarelli, F., Huber, R., Peterson, M.J., Massimini, M., Murphy, M., Riedner, B.A., Watson, A., Bria, P., and Tononi, G. (2007). Reduced sleep spindle activity in schizophrenia patients. *Am J Psychiatry* 164, 483–492.
- Ferrarelli, F., Peterson, M.J., Sarasso, S., Riedner, B.A., Murphy, M.J., Benca, R.M., Bria, P., Kalin, N.H., and Tononi, G. (2010). Thalamic dysfunction in schizophrenia suggested by whole-night deficits in slow and fast spindles. *Am J Psychiatry* 167, 1339–1348.
- Fogerson, P.M., and Huguenard, J.R. (2016). Tapping the Brakes: Cellular and Synaptic Mechanisms that Regulate Thalamic Oscillations. *Neuron* 92, 687–704.
- Francis, J.T., Xu, S., and Chapin, J.K. (2008). Proprioceptive and cutaneous representations in the rat ventral posterolateral thalamus. *J Neurophysiol* 99, 2291–2304.
- French, L., Liu, P., Marais, O., Koreman, T., Tseng, L., Lai, A., and Pavlidis, P. (2015). Text mining for neuroanatomy using WhiteText with an updated corpus and a new web application. *Frontiers in Neuroinformatics* 9, 13.
- Fuentealba, P., and Steriade, M. (2005). The reticular nucleus revisited: Intrinsic and network properties of a thalamic pacemaker. *Progress in Neurobiology* 75, 125–141.
- Fuhrmann, G., Segev, I., Markram, H., and Tsodyks, M. (2002). Coding of temporal information by activity-dependent synapses. *J. Neurophysiol.* 87, 140–148.
- Furuta, T., Tomioka, R., Taki, K., Nakamura, K., Tamamaki, N., and Kaneko, T. (2001). In vivo transduction of central neurons using recombinant Sindbis virus: Golgi-like labeling of dendrites and axons with membrane-targeted fluorescent proteins. *J. Histochem. Cytochem.* 49, 1497–1508.
- Gardner, R.J., Hughes, S.W., and Jones, M.W. (2013). Differential spike timing and phase dynamics of reticular thalamic and prefrontal cortical neuronal populations during sleep spindles. *J Neurosci* 33, 18469–18480.
- Gentet, L.J., and Ulrich, D. (2003). Strong, reliable and precise synaptic connections between thalamic relay cells and neurones of the nucleus reticularis in juvenile rats. *J. Physiol. (Lond.)* 546, 801–811.
- Ghazvinian, A., Noy, N.F., and Musen, M.A. (2011). How orthogonal are the OBO Foundry ontologies? *J Biomed Semantics* 2, S2.
- Goldowitz, D. (2010). Allen Reference Atlas. A Digital Color Brain Atlas of the C57BL/6J Male Mouse - by H. W. Dong. *Genes, Brain and Behavior* 9, 128–128.
- Golomb, D., Wang, X.J., and Rinzel, J. (1994). Synchronization properties of spindle oscillations in a thalamic reticular nucleus model. *J. Neurophysiol.* 72, 1109–1126.
- Golomb, D., Wang, X.J., and Rinzel, J. (1996). Propagation of spindle waves in a thalamic slice model. *J. Neurophysiol.* 75, 750–769.

- Golshani, P., Liu, X.-B., and Jones, E.G. (2001). Differences in quantal amplitude reflect GluR4- subunit number at corticothalamic synapses on two populations of thalamic neurons. *Proceedings of the National Academy of Sciences* 98, 4172–4177.
- Gong, H., Xu, D., Yuan, J., Li, X., Guo, C., Peng, J., Li, Y., Schwarz, L.A., Li, A., Hu, B., et al. (2016). High-throughput dual-colour precision imaging for brain-wide connectome with cytoarchitectonic landmarks at the cellular level. *Nature Communications* 7, 1–12.
- Gouwens, N.W., Berg, J., Feng, D., Sorensen, S.A., Zeng, H., Hawrylycz, M.J., Koch, C., and Arkhipov, A. (2018). Systematic generation of biophysically detailed models for diverse cortical neuron types. *Nature Communications* 9, 710.
- Gwak, Y.S., Kim, H.K., Kim, H.Y., and Leem, J.W. (2010). Bilateral hyperexcitability of thalamic VPL neurons following unilateral spinal injury in rats. *J Physiol Sci* 60, 59–66.
- Gymnopoulos, M., Cingolani, L.A., Pedarzani, P., and Stocker, M. (2014). Developmental mapping of small-conductance calcium-activated potassium channel expression in the rat nervous system. *Journal of Comparative Neurology* 522, 1072–1101.
- Haas, J.S., Zavala, B., and Landisman, C.E. (2011). Activity-dependent long-term depression of electrical synapses. *Science* 334, 389–393.
- Haeusler, S., and Maass, W. (2006). A Statistical Analysis of Information-Processing Properties of Lamina-Specific Cortical Microcircuit Models. *Cerebral Cortex* 17, 149–162.
- Halassa, M.M., Siegle, J.H., Ritt, J.T., Ting, J.T., Feng, G., and Moore, C.I. (2011). Selective optical drive of thalamic reticular nucleus generates thalamic bursts and cortical spindles. *Nature Publishing Group* 14, 1118–1120.
- Halassa, M.M., Chen, Z., Wimmer, R.D., Brunetti, P.M., Zhao, S., Zikopoulos, B., Wang, F., Brown, E.N., and Wilson, M.A. (2014). State-dependent architecture of thalamic reticular subnetworks. *Cell* 158, 808–821.
- Harris, R.M. (1986). Morphology of physiologically identified thalamocortical relay neurons in the rat ventrobasal thalamus. *J. Comp. Neurol.* 251, 491–505.
- Harris, R.M. (1987). Axon collaterals in the thalamic reticular nucleus from thalamocortical neurons of the rat ventrobasal thalamus. *J. Comp. Neurol.* 258, 397–406.
- Häusser, M., and Roth, A. (1997). Estimating the time course of the excitatory synaptic conductance in neocortical pyramidal cells using a novel voltage jump method. *J. Neurosci.* 17, 7606–7625.
- Hay, E., Hill, S., Schürmann, F., Markram, H., and Segev, I. (2011). Models of Neocortical Layer 5b Pyramidal Cells Capturing a Wide Range of Dendritic and Perisomatic Active Properties. *PLoS Computational Biology* 7, e1002107.
- Hay, E., Schürmann, F., Markram, H., and Segev, I. (2013). Preserving axosomatic spiking features despite diverse dendritic morphology. *Journal of Neurophysiology* 109, 2972–2981.

- Heiberg, T., Hagen, E., Haldnes, G., and Einevoll, G.T. (2016). Biophysical Network Modelling of the dLGN Circuit: Different Effects of Triadic and Axonal Inhibition on Visual Responses of Relay Cells. *PLOS Computational Biology* 12, e1004929.
- Herz, A.V.M., Gollisch, T., Machens, C.K., and Jaeger, D. (2006). Modeling single-neuron dynamics and computations: a balance of detail and abstraction. *Science* 314, 80–85.
- Hill, S., and Tononi, G. (2005). Modeling sleep and wakefulness in the thalamocortical system. *J. Neurophysiol.* 93, 1671–1698.
- Hill, S.L., Wang, Y., Schürmann, F., Markram, H., and Riachi, I. (2012). Statistical connectivity provides a sufficient foundation for specific functional connectivity in neocortical neural microcircuits. *Proceedings of the National Academy of Sciences* 109, E2885–E2894.
- Hille, B. (1978). Ionic channels in excitable membranes. Current problems and biophysical approaches. *Biophysical Journal* 22, 283–294.
- Hines, M.L., and Carnevale, N.T. (1997). The NEURON simulation environment. *Neural Computation* 9, 1179–1209.
- Hirsch, J.A., Wang, X., Sommer, F.T., and Martinez, L.M. (2015). How inhibitory circuits in the thalamus serve vision. *Annu. Rev. Neurosci.* 38, 309–329.
- Hou, G., Smith, A.G., and Zhang, Z.-W. (2016). Lack of Intrinsic GABAergic Connections in the Thalamic Reticular Nucleus of the Mouse. *Journal of Neuroscience* 36, 7246–7252.
- Houser, C.R., Vaughn, J.E., Barber, R.P., and Roberts, E. (1980). GABA neurons are the major cell type of the nucleus reticularis thalami. *Brain Res.* 200, 341–354.
- Huang, Z.J., and Luo, L. (2015). It takes the world to understand the brain. *Science* 350, 42–44.
- Huguenard, J.R., and McCormick, D.A. (1992). Simulation of the currents involved in rhythmic oscillations in thalamic relay neurons. *Journal of Neurophysiology* 68, 1373–1383.
- Huguenard, J.R., and McCormick, D.A. (2007). Thalamic synchrony and dynamic regulation of global forebrain oscillations. *Trends in Neurosciences* 30, 350–356.
- Huguenard, J.R., and Prince, D.A. (1992). A novel T-type current underlies prolonged Ca(2+)-dependent burst firing in GABAergic neurons of rat thalamic reticular nucleus. *J. Neurosci.* 12, 3804–3817.
- Huguenard, J.R., and Prince, D.A. (1994). Intrathalamic rhythmicity studied in vitro: nominal T-current modulation causes robust antioscillatory effects. *J. Neurosci.* 14, 5485–5502.
- Huntsman, M.M., Porcello, D.M., Homanics, G.E., DeLorey, T.M., and Huguenard, J.R. (1999). Reciprocal inhibitory connections and network synchrony in the mammalian thalamus. *Science* 283, 541–543.
- Iavarone, E., Yi, J., Shi, Y., Zandt, B.-J., O'Reilly, C., Geit, W.V., Rössert, C., Markram, H., and Hill, S.L. (2019). Experimentally-constrained biophysical models of tonic and burst firing modes in thalamocortical neurons. *PLOS Computational Biology* 15, e1006753.

- Jacobsen, R.B., Ulrich, D., and Huguenard, J.R. (2001). GABAB and NMDA Receptors Contribute to Spindle-Like Oscillations in Rat Thalamus In Vitro. *Journal of Neurophysiology* 86, 1365–1375.
- Jaeger, D. (2000). Accurate reconstruction of neuronal morphology. In *Computational Neuroscience: Realistic Modeling for Experimentalists*, pp. 159–178.
- Jager, P., Calpin, P., Durmishi, X., Salgarella, I., Shimogori, T., and Delogu, A. (2019). Inhibitory interneurons distribute widely across the mouse thalamus and form ontogenetic spatial clusters. *BioRxiv* 651745.
- Jahnsen, H., and Llinás, R. (1984). Electrophysiological properties of guinea-pig thalamic neurones: an in vitro study. *J Physiol* 349, 205–226.
- Jahr, C.E., and Stevens, C.F. (1990). Voltage dependence of NMDA-activated macroscopic conductances predicted by single-channel kinetics. *J. Neurosci.* 10, 3178–3182.
- Jones, E.G. (2002). Thalamic organization and function after Cajal. *Prog Brain Res* 136, 333–357.
- Jones, E.G., 1939-2011 (2007). *The thalamus* (Second edition. Cambridge, UK ; New York : Cambridge University Press, 2007.).
- Jurgens, C.W.D., Bell, K.A., McQuiston, A.R., and Guido, W. (2012). Optogenetic stimulation of the corticothalamic pathway affects relay cells and GABAergic neurons differently in the mouse visual thalamus. *PLoS ONE* 7, e45717.
- Kanari, L., Dłotko, P., Scolamiero, M., Levi, R., Shillcock, J., Hess, K., and Markram, H. (2018). A topological representation of branching neuronal morphologies. *Neuroinformatics* 16, 3–13.
- Kanari, L., Dictus, H., Chalimourda, A., Geit, W.V., Coste, B., Shillcock, J., Hess, K., and Markram, H. (2020). Computational synthesis of cortical dendritic morphologies. *BioRxiv* 2020.04.15.040410.
- Keller, D., Erő, C., and Markram, H. (2018). Cell Densities in the Mouse Brain: A Systematic Review. *Front. Neuroanat.* 12, 83.
- Kim, U., and McCormick, D.A. (1998a). The functional influence of burst and tonic firing mode on synaptic interactions in the thalamus. *J. Neurosci.* 18, 9500–9516.
- Kim, U., and McCormick, D.A. (1998b). Functional and ionic properties of a slow afterhyperpolarization in ferret perigeniculate neurons in vitro. *J. Neurophysiol.* 80, 1222–1235.
- Kim, J.-D., Ohta, T., Tateisi, Y., and Tsujii, J. (2003). GENIA corpus—a semantically annotated corpus for bio-textmining. *Bioinformatics* 19, i180–i182.
- Kim, U., Bal, T., and McCormick, D.A. (1995). Spindle waves are propagating synchronized oscillations in the ferret LGNd in vitro. *Journal of Neurophysiology*.

- Kim, U., Sanchez-Vives, M.V., and McCormick, D.A. (1997). Functional dynamics of GABAergic inhibition in the thalamus. *Science* 278, 130–134.
- Kimura, A. (2017). Robust interactions between the effects of auditory and cutaneous electrical stimulations on cell activities in the thalamic reticular nucleus. *Brain Research* 1661, 49–66.
- Kleiman-Weiner, M., Beenhakker, M.P., Segal, W.A., and Huguenard, J.R. (2009). Synergistic roles of GABAA receptors and SK channels in regulating thalamocortical oscillations. *J. Neurophysiol.* 102, 203–213.
- Köhler, M., Hirschberg, B., Bond, C., Kinzie, J.M., Marrion, N., Maylie, J., and Adelman, J. (1996). Small-conductance, calcium-activated potassium channels from mammalian brain. *Science* 273, 1709–1714.
- Kohmann, D., Lüttjohann, A., Seidenbecher, T., Coulon, P., and Pape, H.-C. (2016). Short term depression of gap junctional coupling in reticular thalamic neurons of absence epileptic rats. *J. Physiol. (Lond.)*.
- Korn, H., and Faber, D.S. (1991). Quantal analysis and synaptic efficacy in the CNS. *Trends Neurosci.* 14, 439–445.
- Kozloski, J., Sfyraakis, K., Hill, S., Schurmann, F., Peck, C., and Markram, H. (2008). Identifying, tabulating, and analyzing contacts between branched neuron morphologies. *IBM Journal of Research and Development* 52, 43–55.
- Krahe, T.E., El-Danaf, R.N., Dilger, E.K., Henderson, S.C., and Guido, W. (2011). Morphologically distinct classes of relay cells exhibit regional preferences in the dorsal lateral geniculate nucleus of the mouse. *Journal of Neuroscience* 31, 17437–17448.
- Krol, A., Wimmer, R.D., Halassa, M.M., and Feng, G. (2018). Thalamic Reticular Dysfunction as a Circuit Endophenotype in Neurodevelopmental Disorders. *Neuron* 98, 282–295.
- von Krosigk, M., Bal, T., and McCormick, D.A. (1993). Cellular mechanisms of a synchronized oscillation in the thalamus. *Science* 261, 361–364.
- Kubota, Y., Sohn, J., and Kawaguchi, Y. (2018). Large Volume Electron Microscopy and Neural Microcircuit Analysis. *Front. Neural Circuits* 12.
- Kumbhar, P., Hines, M., Fouriaux, J., Ovcharenko, A., King, J., Delalondre, F., and Schürmann, F. (2019). CoreNEURON: An Optimized Compute Engine for the NEURON Simulator. *Front. Neuroinform.* 13, 63.
- Lam, Y.-W., and Sherman, S.M. (2011). Functional organization of the thalamic input to the thalamic reticular nucleus. *J. Neurosci.* 31, 6791–6799.
- Lam, Y.-W., Nelson, C.S., and Sherman, S.M. (2006). Mapping of the functional interconnections between thalamic reticular neurons using photostimulation. *J. Neurophysiol.* 96, 2593–2600.
- Landisman, C.E., Long, M.A., Beierlein, M., Deans, M.R., Paul, D.L., and Connors, B.W. (2002). Electrical synapses in the thalamic reticular nucleus. *The Journal of Neuroscience : The Official Journal of the Society for Neuroscience* 22, 1002–1009.

Larson, S.D., and Martone, M.E. (2013). NeuroLex.org: an online framework for neuroscience knowledge. *Front Neuroinform* 7, 18.

Le Franc, Y., Davison, A.P., Gleeson, P., Imam, F.T., Kriener, B., Larson, S.D., Ray, S., Schwabe, L., Hill, S., and De Schutter, E. (2012). Computational Neuroscience Ontology: a new tool to provide semantic meaning to your models. *BMC Neuroscience* 13, P149.

Lee, S.-H., and Dan, Y. (2012). Neuromodulation of Brain States. *Neuron* 76, 209–222.

Lee, J., Song, K., Lee, K., Hong, J., Lee, H., Chae, S., Cheong, E., and Shin, H.-S. (2013). Sleep spindles are generated in the absence of T-type calcium channel-mediated low-threshold burst firing of thalamocortical neurons. *Proceedings of the National Academy of Sciences of the United States of America* 1–6.

Lee, S.-C., Cruikshank, S.J., and Connors, B.W. (2010). Electrical and chemical synapses between relay neurons in developing thalamus. *J Physiol* 588, 2403–2415.

Lee, S.-C., Patrick, S.L., Richardson, K.A., and Connors, B.W. (2014). Two Functionally Distinct Networks of Gap Junction-Coupled Inhibitory Neurons in the Thalamic Reticular Nucleus. *Journal of Neuroscience* 34, 13170–13182.

Lee, S.-H., Govindaiah, G., and Cox, C.L. (2007). Heterogeneity of firing properties among rat thalamic reticular nucleus neurons: Electrophysiological heterogeneity of TRN neurons. *The Journal of Physiology* 582, 195–208.

Leresche, N., Lambert, R.C., Errington, A.C., and Crunelli, V. (2012). From sleep spindles of natural sleep to spike and wave discharges of typical absence seizures: is the hypothesis still valid? *Pflugers Arch* 463, 201–212.

Li, G., Henriquez, C.S., and Fröhlich, F. (2017). Unified thalamic model generates multiple distinct oscillations with state-dependent entrainment by stimulation. *PLOS Computational Biology* 13, e1005797.

Li, J., Bickford, M.E., and Guido, W. (2003). Distinct firing properties of higher order thalamic relay neurons. *J Neurophysiol* 90, 291–299.

Li, Y., Lopez-Huerta, V.G., Adiconis, X., Levandowski, K., Choi, S., Simmons, S.K., Arias-Garcia, M.A., Guo, B., Yao, A.Y., Blosser, T.R., et al. (2020). Distinct subnetworks of the thalamic reticular nucleus. *Nature* 1–6.

Liu, X.B., and Jones, E.G. (1999). Predominance of corticothalamic synaptic inputs to thalamic reticular nucleus neurons in the rat. *J Comp Neurol* 414, 67–79.

Llinás, R., and Jahnsen, H. (1982). Electrophysiology of mammalian thalamic neurones in vitro. *Nature* 297, 406.

Llinás, R.R., and Steriade, M. (2006). Bursting of thalamic neurons and states of vigilance. *J. Neurophysiol.* 95, 3297–3308.

Long, M.A., Landisman, C.E., and Connors, B.W. (2004). Small clusters of electrically coupled neurons generate synchronous rhythms in the thalamic reticular nucleus. *J. Neurosci.* 24, 341–349.

Loomis, A.L., Harvey, E.N., and Hobart, G. (1935). Potential Rhythms of the Cerebral Cortex During Sleep. *Science* 81, 597–598.

Lu, A.C., Lee, C.K., Kleiman-Weiner, M., Truong, B., Wang, M., Huguenard, J.R., and Beenhakker, M.P. (2020). Nonlinearities between inhibition and T-type calcium channel activity bidirectionally regulate thalamic network oscillations. *BioRxiv* 2020.06.02.129601.

Lüthi, A., and McCormick, D.A. (1998). Periodicity of thalamic synchronized oscillations: the role of Ca²⁺-mediated upregulation of I_h. *Neuron* 20, 553–563.

Lüthi, A., and McCormick, D.A. (1999). Modulation of a pacemaker current through Ca²⁺-induced stimulation of cAMP production. *Nature Neuroscience* 2, 634–641.

Lüthi, A., Bal, T., and McCormick, D.A. (1998). Periodicity of Thalamic Spindle Waves Is Abolished by ZD7288, a Blocker of I_h. *Journal of Neurophysiology* 79, 3284–3289.

Magistretti, J., and Alonso, A. (1999). Biophysical properties and slow voltage-dependent inactivation of a sustained sodium current in entorhinal cortex layer-II principal neurons: a whole-cell and single-channel study. *The Journal of General Physiology* 114, 491–509.

Mahdavi, A., Qin, Y., Aubry, A.-S., Cornec, D., Kulikova, S., and Pinault, D. (2020). A single psychotomimetic dose of ketamine decreases thalamocortical spindles and delta oscillations in the sedated rat. *Schizophrenia Research*.

Makinson, C.D., Tanaka, B.S., Sorokin, J.M., Wong, J.C., Christian, C.A., Goldin, A.L., Escayg, A., and Huguenard, J.R. (2017). Regulation of Thalamic and Cortical Network Synchrony by Scn8a. *Neuron* 93, 1165–1179.e6.

Manoach, D.S., Demanuele, C., Wamsley, E.J., Vangel, M., Montrose, D.M., Miewald, J., Kupfer, D., Buysse, D., Stickgold, R., and Keshavan, M.S. (2014). Sleep spindle deficits in antipsychotic-naïve early course schizophrenia and in non-psychotic first-degree relatives. *Front Hum Neurosci* 8, 762.

Manoach, D.S., Pan, J.Q., Purcell, S.M., and Stickgold, R. (2016). Reduced Sleep Spindles in Schizophrenia: A Treatable Endophenotype That Links Risk Genes to Impaired Cognition? *Biol. Psychiatry* 80, 599–608.

Markram, H., Muller, E., Ramaswamy, S., Reimann, M.W., Abdellah, M., Sanchez, C.A., Ailamaki, A., Alonso-Nanclares, L., Antille, N., Arsever, S., et al. (2015). Reconstruction and Simulation of Neocortical Microcircuitry. *Cell* 163, 456–492.

Martina, M., and Jonas, P. (1997). Functional differences in Na⁺ channel gating between fast-spiking interneurons and principal neurons of rat hippocampus. *J Physiol* 505, 593–603.

Martinez-Garcia, R.I., Voelcker, B., Zaltsman, J.B., Patrick, S.L., Stevens, T.R., Connors, B.W., and Cruikshank, S.J. (2020). Two dynamically distinct circuits drive inhibition in the sensory thalamus. *Nature* 583, 813–818.

Masoli, S., Rizza, M.F., Sgritta, M., Van Geit, W., Schürmann, F., and D'Angelo, E. (2017). Single neuron optimization as a basis for accurate biophysical modeling: the case of cerebellar granule cells. *Frontiers in Cellular Neuroscience* 11, 71.

- McAlliser, J., and Wells, J. (1981). The structural organization of the ventral posterolateral nucleus in the rat. *Journal of Comparative Neurology* 197, 271–301.
- McAlonan, K., Cavanaugh, J., and Wurtz, R.H. (2008). Guarding the gateway to cortex with attention in visual thalamus. *Nature* 456, 391–394.
- McCormick, D.A. (1992). Neurotransmitter actions in the thalamus and cerebral cortex and their role in neuromodulation of thalamocortical activity. *Prog. Neurobiol.* 39, 337–388.
- McCormick, D. a, and Huguenard, J.R. (1992). A model of the electrophysiological properties of thalamocortical relay neurons. *Journal of Neurophysiology* 68, 1384–1400.
- McCormick, D.A., and Bal, T. (1997). SLEEP AND AROUSAL: Thalamocortical Mechanisms. *Annual Review of Neuroscience* 20, 185–215.
- McCormick, D.A., and Pape, H.-C. (1990). Properties of a hyperpolarization-activated cation current and its role in rhythmic oscillation in thalamic relay neurones. *The Journal of Physiology* 431, 291–318.
- McCormick, D.A., and Wang, Z. (1991). Serotonin and noradrenaline excite GABAergic neurones of the guinea-pig and cat nucleus reticularis thalami. *J Physiol* 442, 235–255.
- McDougal, R.A., Morse, T.M., Carnevale, T., Marengo, L., Wang, R., Migliore, M., Miller, P.L., Shepherd, G.M., and Hines, M.L. (2017). Twenty years of ModelDB and beyond: building essential modeling tools for the future of neuroscience. *J Comput Neurosci* 42, 1–10.
- Mease, R.A., Krieger, P., and Groh, A. (2014). Cortical control of adaptation and sensory relay mode in the thalamus. *PNAS* 111, 6798–6803.
- Mease, R.A., Metz, M., and Groh, A. (2016). Cortical Sensory Responses Are Enhanced by the Higher-Order Thalamus. *Cell Rep* 14, 208–215.
- Migliore, R., Lupascu, C.A., Bologna, L.L., Romani, A., Courcol, J.-D., Antonel, S., Van Geit, W.A., Thomson, A.M., Mercer, A., Lange, S., et al. (2018). The physiological variability of channel density in hippocampal CA1 pyramidal cells and interneurons explored using a unified data-driven modeling workflow. *PLoS Computational Biology* 14, e1006423.
- Mineff, E.M., and Weinberg, R.J. (2000). Differential synaptic distribution of AMPA receptor subunits in the ventral posterior and reticular thalamic nuclei of the rat. *Neuroscience* 101, 969–982.
- Miyata, M. (2007). Distinct properties of corticothalamic and primary sensory synapses to thalamic neurons. *Neuroscience Research* 59, 377–382.
- Miyata, M., and Imoto, K. (2006). Different composition of glutamate receptors in corticothalamic and lemniscal synaptic responses and their roles in the firing responses of ventrobasal thalamic neurons in juvenile mice. *J. Physiol. (Lond.)* 575, 161–174.
- Mo, C., and Sherman, S.M. (2019). A Sensorimotor Pathway via Higher-Order Thalamus. *J. Neurosci.* 39, 692–704.

Mo, C., Petrof, I., Viaene, A.N., and Sherman, S.M. (2017). Synaptic properties of the lemniscal and paralemniscal pathways to the mouse somatosensory thalamus. *PNAS* *114*, E6212–E6221.

Monconduit, L., Lopez-Avila, A., Molat, J.-L., Chalus, M., and Villanueva, L. (2006). Corticofugal output from the primary somatosensory cortex selectively modulates innocuous and noxious inputs in the rat spinothalamic system. *J. Neurosci.* *26*, 8441–8450.

Morgan, J.L., and Lichtman, J.W. (2020). An Individual Interneuron Participates in Many Kinds of Inhibition and Innervates Much of the Mouse Visual Thalamus. *Neuron*.

Morison, R.S., and Basset, D.L. (1945). Electrical activity of the thalamus and basal ganglia in decorticate cats. *Journal of Neurophysiology*.

Nakajima, M., Schmitt, L.I., and Halassa, M.M. (2019). Prefrontal Cortex Regulates Sensory Filtering through a Basal Ganglia-to-Thalamus Pathway. *Neuron* *103*, 445–458.e10.

NCBI PubMed.

NeuroM BlueBrain/NeuroM.

Newton, T.H., Abdellah, M., Chevtchenko, G., Muller, E.B., and Markram, H. (2019). Voltage-sensitive dye imaging reveals inhibitory modulation of ongoing cortical activity. *BioRxiv* 812008.

Neymotin, S.A., Suter, B.A., Dura-Bernal, S., Shepherd, G.M.G., Migliore, M., and Lytton, W.W. (2016). Optimizing computer models of corticospinal neurons to replicate in vitro dynamics. *Journal of Neurophysiology* *117*, 148–162.

Nolte, M. (2019). Untangling emergent cortical dynamics: neurons from networks, noise from chaos. EPFL.

Ohara, P.T., and Lieberman, A.R. (1985). The thalamic reticular nucleus of the adult rat: experimental anatomical studies. *J. Neurocytol.* *14*, 365–411.

O’Leary, T., Williams, A.H., Caplan, J.S., and Marder, E. (2013). Correlations in ion channel expression emerge from homeostatic tuning rules. *Proceedings of the National Academy of Sciences* *110*, E2645–E2654.

Olifer, A.V. (2013). Neuronal Parameter Sensitivity. In *Encyclopedia of Computational Neuroscience*, D. Jaeger, and R. Jung, eds. (New York, NY: Springer New York), pp. 1–6.

O’Reilly, C. Introduction to the NeuroInformatics Platform - FENS 2016 - Part 3 - Ontology services.

O’Reilly, C. NeuroAnnotation Toolbox Wiki - Annotation format.

O’Reilly, C. Example of interaction with a corpus using the NeuroAnnotation Toolbox - ionic currents.

O’Reilly, C. Example of interaction with a corpus using the NeuroAnnotation Toolbox - stereology.

- O'Reilly, C., Iavarone, E., and Hill, S.L. (2017a). A Framework for Collaborative Curation of Neuroscientific Literature. *Front Neuroinform* *11*, 27.
- O'Reilly, C., Iavarone, E., and Hill, S.L. (2017b). A Framework for Collaborative Curation of Neuroscientific Literature. *Frontiers in Neuroinformatics* *11*, 27.
- Parker, P.R.L., Cruikshank, S.J., and Connors, B.W. (2009). Stability of electrical coupling despite massive developmental changes of intrinsic neuronal physiology. *J. Neurosci.* *29*, 9761–9770.
- Parri, H.R., and Crunelli, V. (1998). Sodium current in rat and cat thalamocortical neurons: role of a non-inactivating component in tonic and burst firing. *Journal of Neuroscience* *18*, 854–867.
- Pauzin, F.P., and Krieger, P. (2018). A Corticothalamic Circuit for Refining Tactile Encoding. *Cell Reports* *23*, 1314–1325.
- Paxinos, G., and Watson, C. (1998). The rat brain atlas in stereotaxic coordinates. San Diego: Academic.
- Paz, J.T., and Huguenard, J.R. (2015). Microcircuits and their interactions in epilepsy: is the focus out of focus? *Nature Neuroscience* *18*, 351–359.
- Pellegrini, C., Lecci, S., Lüthi, A., and Astori, S. (2016). Suppression of Sleep Spindle Rhythmogenesis in Mice with Deletion of CaV3.2 and CaV3.3 T-type Ca(2+) Channels. *Sleep* *39*, 875–885.
- Perkel, J.M. (2015). Annotating the scholarly web. *Nature* *528*, 153–154.
- Pinault, D. (2004). The thalamic reticular nucleus: structure, function and concept. *Brain Research Reviews* *46*, 1–31.
- Pinault, D., and Deschênes, M. (1998a). Anatomical evidence for a mechanism of lateral inhibition in the rat thalamus. *Eur. J. Neurosci.* *10*, 3462–3469.
- Pinault, D., and Deschênes, M. (1998b). Projection and innervation patterns of individual thalamic reticular axons in the thalamus of the adult rat: a three-dimensional, graphic, and morphometric analysis. *J. Comp. Neurol.* *391*, 180–203.
- Pinault, D., Bourassa, J., and Deschênes, M. (1995). The axonal arborization of single thalamic reticular neurons in the somatosensory thalamus of the rat. *Eur. J. Neurosci.* *7*, 31–40.
- Podlaski, W.F., Seeholzer, A., Groschner, L.N., Miesenböck, G., Ranjan, R., and Vogels, T.P. (2017). Mapping the function of neuronal ion channels in model and experiment. *Elife* *6*, e22152.
- Porrero, C., Rodríguez-Moreno, J., Quetglas, J.I., Smerdou, C., Furuta, T., and Clascá, F. (2016). A Simple and Efficient In Vivo Non-viral RNA Transfection Method for Labeling the Whole Axonal Tree of Individual Adult Long-Range Projection Neurons. *Front Neuroanat* *10*.
- Poulet, J.F.A., Fernandez, L.M.J., Crochet, S., and Petersen, C.C.H. (2012). Thalamic control of cortical states. *Nature Neuroscience* *15*, 370–372.

Pozzorini, C., Mensi, S., Hagens, O., Naud, R., Koch, C., and Gerstner, W. (2015). Automated high-throughput characterization of single neurons by means of simplified spiking models. *PLoS Computational Biology* 11, e1004275.

Pratt, J.A., and Morris, B.J. (2015). The thalamic reticular nucleus: a functional hub for thalamocortical network dysfunction in schizophrenia and a target for drug discovery. *Journal of Psychopharmacology* (Oxford, England) 29, 127–37.

Purpura, D.P. (1968). Role of synaptic inhibition in synchronization of thalamocortical activity. *Prog. Brain Res.* 22, 107–122.

R. Richardet, J. C. Chappelier, S. Tripathy, and S. Hill (2015). Agile text mining with Sherlock. In *Big Data (Big Data)*, 2015 IEEE International Conference On, pp. 1479–1484.

Ramaswamy, S., Hill, S.L., King, J.G., Schürmann, F., Wang, Y., and Markram, H. (2012). Intrinsic morphological diversity of thick-tufted layer 5 pyramidal neurons ensures robust and invariant properties of *in silico* synaptic connections: Comparison of *in vitro* and *in silico* TTL5 synaptic connections. *The Journal of Physiology* 590, 737–752.

Ramaswamy, S., Markram, H., Schürmann, F., Segev, I., Ramaswamy, S., Courcol, J.D., Courcol, J.-D., Abdellah, M., Abdellah, M., Adaszewski, S.R., et al. (2015). The neocortical microcircuit collaboration portal: a resource for rat somatosensory cortex. *Frontiers in Neural Circuits* 9, 557.

Ramcharan, E.J., Gnadt, J.W., and Sherman, S.M. (2000). Burst and tonic firing in thalamic cells of unanesthetized, behaving monkeys. *Visual Neuroscience* 17, 55–62.

Ranjan, R., Khazen, G., Gambazzi, L., Ramaswamy, S., Hill, S.L., Schürmann, F., and Markram, H. (2011). Channelpedia: an integrative and interactive database for ion channels. *Frontiers in Neuroinformatics* 5, 36.

Reichova, I., and Sherman, S.M. (2004). Somatosensory corticothalamic projections: distinguishing drivers from modulators. *J. Neurophysiol.* 92, 2185–2197.

Reimann, M.W., King, J.G., Muller, E.B., Ramaswamy, S., and Markram, H. (2015). An algorithm to predict the connectome of neural microcircuits. *Front Comput Neurosci* 9.

ResearchGate Generating a DOI.

Rhodes, P.A., and Llinás, R. (2005). A model of thalamocortical relay cells. *The Journal of Physiology* 565, 765–781.

Rikhye, R.V., Wimmer, R.D., and Halassa, M.M. (2018). Toward an Integrative Theory of Thalamic Function. *Annual Review of Neuroscience* 41, 163–183.

Rodriguez-Moreno, J., Porrero, C., Rollenhagen, A., Rubio-Teves, M., Casas-Torremocha, D., Alonso-Nanclares, L., Yakoubi, R., Santuy, A., Merchan-Pérez, A., DeFelipe, J., et al. (2020). Area-Specific Synapse Structure in Branched Posterior Nucleus Axons Reveals a New Level of Complexity in Thalamocortical Networks. *J. Neurosci.* 40, 2663–2679.

Rosenbaum, R., Smith, M.A., Kohn, A., Rubin, J.E., and Doiron, B. (2017). The spatial structure of correlated neuronal variability. *Nat. Neurosci.* 20, 107–114.

Rovó, Z., Mátyás, F., Barthó, P., Slézia, A., Lecci, S., Pellegrini, C., Astori, S., Dávid, C., Hangya, B., Lüthi, A., et al. (2014). Phasic, Nonsynaptic GABA-A Receptor-Mediated Inhibition Entrain Thalamocortical Oscillations. *J Neurosci* 34, 7137–7147.

RStudio Team (2016). RStudio: Integrated Development Environment for R (Boston, MA: RStudio, Inc.).

Saalmann, Y.B., and Kastner, S. (2015). The cognitive thalamus. *Front. Syst. Neurosci.* 9.

Sánchez, E., Reboreda, A., Romero, M., and Lamas, J.A. (2006). Spontaneous bursting and rhythmic activity in the cuneate nucleus of anaesthetized rats. *Neuroscience* 141, 487–500.

Sarid, L., Bruno, R., Sakmann, B., Segev, I., and Feldmeyer, D. (2007). Modeling a layer 4-to-layer 2/3 module of a single column in rat neocortex: Interweaving in vitro and in vivo experimental observations. *PNAS* 104, 16353–16358.

Scheibel, M.E., and Scheibel, A.B. (1966a). The organization of the nucleus reticularis thalami: a Golgi study. *Brain Res.* 1, 43–62.

Scheibel, M.E., and Scheibel, A.B. (1966b). Patterns of organization in specific and nonspecific thalamic fields. In *The Thalamus*, (New York: Columbia University Press), pp. 13–46.

Scheibel, M.E., and Scheibel, A.B. (1967). Structural organization of nonspecific thalamic nuclei and their projection toward cortex. *Brain Res.* 6, 60–94.

Schulz, D.J., Goaillard, J.-M., and Marder, E. (2006). Variable channel expression in identified single and electrically coupled neurons in different animals. *Nature Neuroscience* 9, 356.

Shardlow, M., Ju, M., Li, M., O'Reilly, C., Iavarone, E., McNaught, J., and Ananiadou, S. (2019). A Text Mining Pipeline Using Active and Deep Learning Aimed at Curating Information in Computational Neuroscience. *Neuroinformatics* 17, 391–406.

Sherman, S.M. (2004). Interneurons and triadic circuitry of the thalamus. *Trends Neurosci* 27, 670–675.

Sherman, S.M. (2005). Thalamic relays and cortical functioning. *Progress in Brain Research* 149, 107–126.

Sherman, S.M. (2007). The thalamus is more than just a relay. *Current Opinion in Neurobiology* 17, 417–422.

Sherman, S.M., and Guillery, R.W. (1998). On the actions that one nerve cell can have on another: Distinguishing “drivers” from “modulators.” *Proceedings of the National Academy of Sciences* 95, 7121–7126.

Sherman, S.M., and Koch, C. (1986). The control of retinogeniculate transmission in the mammalian lateral geniculate nucleus. *Exp Brain Res* 63, 1–20.

Shishido, S.-I., and Toda, T. (2017). Temporal Patterns of Individual Neuronal Firing in Rat Dorsal Column Nuclei Provide Information Required for Somatosensory Discrimination. *Tohoku J. Exp. Med.* 243, 115–126.

- Sholl, D.A. (1953). Dendritic organization in the neurons of the visual and motor cortices of the cat. *Journal of Anatomy* 87, 387.
- Shosaku, A. (1986). Cross-correlation analysis of a recurrent inhibitory circuit in the rat thalamus. *Journal of Neurophysiology* 55, 1030–1043.
- Shu, S., Ju, G., and Fan, L. (1988). The glucose oxidase-DAB-nickel method in peroxidase histochemistry of the nervous system. *Neuroscience Letters* 85, 169–171.
- Smith, B., Ashburner, M., Rosse, C., Bard, J., Bug, W., Ceusters, W., Goldberg, L.J., Eilbeck, K., Ireland, A., Mungall, C.J., et al. (2007). The OBO Foundry: coordinated evolution of ontologies to support biomedical data integration. *Nat Biotechnol* 25, 1251–1255.
- Sohal, V.S., and Huguenard, J.R. (2003). Inhibitory interconnections control burst pattern and emergent network synchrony in reticular thalamus. *J. Neurosci.* 23, 8978–8988.
- Spacek, J., and Lieberman, A.R. (1974). Ultrastructure and three-dimensional organization of synaptic glomeruli in rat somatosensory thalamus. *J Anat* 117, 487–516.
- Spreafico, R., de Curtis, M., Frassoni, C., and Avanzini, G. (1988). Electrophysiological characteristics of morphologically identified reticular thalamic neurons from rat slices. *Neuroscience* 27, 629–638.
- Spreafico, R., Battaglia, G., and Frassoni, C. (1991). The reticular thalamic nucleus (RTN) of the rat: Cytoarchitectural, Golgi, immunocytochemical, and horseradish peroxidase study. *J. Comp. Neurol.* 304, 478–490.
- Stenetorp, P., Pyysalo, S., Topić, G., Ohta, T., Ananiadou, S., and Tsujii, J. 'ichi (2012). BRAT: A Web-based Tool for NLP-assisted Text Annotation. In *Proceedings of the Demonstrations at the 13th Conference of the European Chapter of the Association for Computational Linguistics*, (Stroudsburg, PA, USA: Association for Computational Linguistics), pp. 102–107.
- Steriade, M. (2003). The corticothalamic system in sleep. *Front. Biosci.* 8, d878-899.
- Steriade, M. (2005). Sleep, epilepsy and thalamic reticular inhibitory neurons. *Trends in Neurosciences* 28, 317–324.
- Steriade, M. (2006). Grouping of brain rhythms in corticothalamic systems. *Neuroscience* 137, 1087–1106.
- Steriade, M., and Deschenes, M. (1984). The thalamus as a neuronal oscillator. *Brain Res.* 320, 1–63.
- Steriade, M., Domich, L., Oakson, G., and Deschenes, M. (1987). The deafferented reticular thalamic nucleus generates spindle rhythmicity. *Journal of Neurophysiology* 57, 260–273.
- Steriade, M., McCormick, D., and Sejnowski, T. (1993). Thalamocortical oscillations in the sleeping and aroused brain. *Science* 262, 679–685.
- Steuillet, P., Cabungcal, J.-H., Bukhari, S.A., Ardelt, M.I., Pantazopoulos, H., Hamati, F., Salt, T.E., Cuenod, M., Do, K.Q., and Berretta, S. (2018). The Thalamic Reticular Nucleus in

Schizophrenia and Bipolar Disorder: Role of Parvalbumin-Expressing Neuron Networks and Oxidative Stress. *Mol Psychiatry* 23, 2057–2065.

Takeuchi, Y., Asano, H., Katayama, Y., Muragaki, Y., Imoto, K., and Miyata, M. (2014). Large-Scale Somatotopic Refinement via Functional Synapse Elimination in the Sensory Thalamus of Developing Mice. *J. Neurosci.* 34, 1258–1270.

Takeuchi, Y., Osaki, H., Yagasaki, Y., Katayama, Y., and Miyata, M. (2017). Afferent Fiber Remodeling in the Somatosensory Thalamus of Mice as a Neural Basis of Somatotopic Reorganization in the Brain and Ectopic Mechanical Hypersensitivity after Peripheral Sensory Nerve Injury. *ENeuro* 4, ENEURO.0345-16.2017.

Talley, E.M., Cribbs, L.L., Lee, J.H., Daud, A., Perez-Reyes, E., and Bayliss, D.A. (1999). Differential distribution of three members of a gene family encoding low voltage-activated (T-type) calcium channels. *J. Neurosci.* 19, 1895–1911.

Taylor, A.L., Goaillard, J.-M., and Marder, E. (2009). How multiple conductances determine electrophysiological properties in a multicompartment model. *Journal of Neuroscience* 29, 5573–5586.

Tennøe, S., Halnes, G., and Einevoll, G.T. (2018). Uncertainpy: A Python toolbox for uncertainty quantification and sensitivity analysis in computational neuroscience. *BioRxiv* 274779.

Thankachan, S., Katsuki, F., McKenna, J.T., Yang, C., Shukla, C., Deisseroth, K., Uygun, D.S., Strecker, R.E., Brown, R.E., McNally, J.M., et al. (2019). Thalamic Reticular Nucleus Parvalbumin Neurons Regulate Sleep Spindles and Electrophysiological Aspects of Schizophrenia in Mice. *Scientific Reports* 9, 1–16.

Thompson, H.S., and McKelvie, D. (1997). Hyperlink semantics for standoff markup of read-only documents. In *Proceedings of SGML Europe '97: The next Decade – Pushing the Envelope*, pp. 227–229.

Thomson, A.M., and Destexhe, A. (1999). Dual intracellular recordings and computational models of slow inhibitory postsynaptic potentials in rat neocortical and hippocampal slices. *Neuroscience*.

Timofeev, I., Bazhenov, M., Sejnowski, T.J., and Steriade, M. (2001). Contribution of intrinsic and synaptic factors in the desynchronization of thalamic oscillatory activity. *Thalamus & Related Systems* 1, 53–69.

Tripathy, S.J., Savitskaya, J., Burton, S.D., Urban, N.N., and Gerkin, R.C. (2014). NeuroElectro: a window to the world's neuron electrophysiology data. *Front Neuroinform* 8, 40.

Tsodyks, M.V., and Markram, H. (1997). The neural code between neocortical pyramidal neurons depends on neurotransmitter release probability. *PNAS* 94, 719–723.

Tulleken, H. (2009). Poisson Disk Sampling.

- Turner, J.P., Anderson, C.M., Williams, S.R., and Crunelli, V. (1997). Morphology and membrane properties of neurones in the cat ventrobasal thalamus in vitro. *The Journal of Physiology* 505, 707–726.
- Ulrich, D., and Huguenard, J.R. (1997). Nucleus-Specific Chloride Homeostasis in Rat Thalamus. *J. Neurosci.* 17, 2348–2354.
- Urbain, N., Salin, P.A., Libourel, P.-A., Comte, J.-C., Gentet, L.J., and Petersen, C.C.H. (2015). Whisking-Related Changes in Neuronal Firing and Membrane Potential Dynamics in the Somatosensory Thalamus of Awake Mice. *Cell Reports* 13, 647–656.
- Urbain, N., Fourcaud-Trocmé, N., Laheux, S., Salin, P.A., and Gentet, L.J. (2019). Brain-State-Dependent Modulation of Neuronal Firing and Membrane Potential Dynamics in the Somatosensory Thalamus during Natural Sleep. *Cell Reports* 26, 1443-1457.e5.
- Van Geit, W., Gevaert, M., Chindemi, G., Rössert, C., Courcol, J.-D., Muller, E.B., Schürmann, F., Segev, I., and Markram, H. (2016). BluePyOpt: leveraging open source software and cloud infrastructure to optimise model parameters in neuroscience. *Frontiers in Neuroinformatics* 10, 17.
- Van Horn, S.C., Erişir, A., and Sherman, S.M. (2000). Relative distribution of synapses in the A-laminae of the lateral geniculate nucleus of the cat. *J. Comp. Neurol.* 416, 509–520.
- Velazquez, J.L.P., and Carlen, P.L. (1996). Development of firing patterns and electrical properties in neurons of the rat ventrobasal thalamus. *Developmental Brain Research* 91, 164–170.
- Wang, X.-J. (1994). Multiple dynamical modes of thalamic relay neurons: Rhythmic bursting and intermittent phase-locking. *Neuroscience* 59, 21–31.
- Wang, X.J., Golomb, D., and Rinzel, J. (1995). Emergent spindle oscillations and intermittent burst firing in a thalamic model: specific neuronal mechanisms. *PNAS* 92, 5577–5581.
- Warren, R.A., Agmon, A., and Jones, E.G. (1994). Oscillatory synaptic interactions between ventroposterior and reticular neurons in mouse thalamus in vitro. *Journal of Neurophysiology* 72, 1993–2003.
- Warren, R.A., Golshani, P., and Jones, E.G. (1997). GABA(B)-receptor-mediated inhibition in developing mouse ventral posterior thalamic nucleus. *J. Neurophysiol.* 78, 550–553.
- Weaver, C.M., and Wearne, S.L. (2008). Neuronal firing sensitivity to morphologic and active membrane parameters. *PLoS Computational Biology* 4, e11.
- Wei, H., Bonjean, M., Petry, H.M., Sejnowski, T.J., and Bickford, M.E. (2011). Thalamic burst firing propensity: a comparison of the dorsal lateral geniculate and pulvinar nuclei in the tree shrew. *Journal of Neuroscience* 31, 17287–17299.
- Wells, M.F., Wimmer, R.D., Schmitt, L.I., Feng, G., and Halassa, M.M. (2016). Thalamic reticular impairment underlies attention deficit in *Ptch1* Y/– mice. *Nature* 532, 58–63.

Williams, S.R., and Stuart, G.J. (2000). Action potential backpropagation and somato-dendritic distribution of ion channels in thalamocortical neurons. *Journal of Neuroscience* 20, 1307–1317.

Willis, A.M., Slater, B.J., Gribkova, E.D., and Llano, D.A. (2015). Open-loop organization of thalamic reticular nucleus and dorsal thalamus: a computational model. *J. Neurophysiol.* 114, 2353–2367.

Wimmer, R.D., Schmitt, L.I., Davidson, T.J., Nakajima, M., Deisseroth, K., and Halassa, M.M. (2015). Thalamic control of sensory selection in divided attention. *Nature* 526, 705–709.

Winnubst, J., Bas, E., Ferreira, T.A., Wu, Z., Economo, M.N., Edson, P., Arthur, B.J., Bruns, C., Rokicki, K., Schauder, D., et al. (2019). Reconstruction of 1,000 Projection Neurons Reveals New Cell Types and Organization of Long-Range Connectivity in the Mouse Brain. *Cell* 179, 268–281.e13.

Yimam, S.M., and Gurevych, I. (2013). WebAnno: A flexible, web-based and visually supported system for distributed annotations. In *Proceedings of the 51th Annual Meeting of the Association for Computational Linguistics (ACL) - System Demonstrations*, pp. 1–6.

Yin, W., Brittain, D., Borseth, J., Scott, M.E., Williams, D., Perkins, J., Own, C., Murfitt, M., Torres, R.M., Kapner, D., et al. (2019). A Petascale Automated Imaging Pipeline for Mapping Neuronal Circuits with High-throughput Transmission Electron Microscopy. *BioRxiv* 791889.

Zhu, J.J., and Lo, F.S. (1999). Three GABA receptor-mediated postsynaptic potentials in interneurons in the rat lateral geniculate nucleus. *J. Neurosci.* 19, 5721–5730.

.

Curriculum Vitae

Elisabetta Iavarone

École Polytechnique Fédérale de Lausanne
Blue Brain Project, Campus Biotech, Ch. des Mines 9, CH-1202 Genève
Tel +41 779233721
elisabetta.iavarone@epfl.ch
LinkedIn: <https://www.linkedin.com/in/elisabetta-iavarone>

EDUCATION

November 2015 – Present

**École Polytechnique Fédérale de Lausanne (EPFL),
Switzerland, Blue Brain Project**

Doctoral Student

Dissertation: *A computational biophysical model of thalamic and reticular nucleus microcircuitry: from neurons to emergent network dynamics* (Advisor: Sean Hill)

2013 – 2015

Università di Pavia, Italy

Erasmus Medical Center, Rotterdam, Netherlands

Master's degree in Neurobiology and exchange student (EU Erasmus program)

Master thesis: *Axonal conversion of somatodendritic signals into spike bursts in an extended multicompartment model of Inferior Olive neurons* (Advisor: Egidio d'Angelo)

2010 – 2013

Università di Pavia, Italy

Bachelor's degree in Biology

Bachelor thesis: *Analysis of resonance profiles of stellate cells in the medial entorhinal cortex*. (Advisor: Jacopo Magistretti)

TEACHING EXPERIENCE

Teaching assistant for the following graduate courses at EPFL:

- “In Silico Neuroscience” (Prof. Prof. Felix Shürmann and Prof. Sean Hill) – Spring 2016 and Spring 2017
- “Neuroscience II” (Prof. Carl Petersen, Prof. Ralf Schneggenburger) – Fall 2017

Tutorials and workshops in the following conferences and schools:

- “HBP Neuroinformatics and Single cell modelling tutorial”, part of Cells, Circuit and Computation FENS Workshop – FENS 2016, Copenhagen (Denmark)
- “Single cell modelling tutorial”, HBP School 2016, Obergurgl (Austria)
- “Single cell and synapses modelling tutorial”, Neuroscience School of Advance Studies, Connectomics School, 2017, Certosa di Pontignano (Italy)
- “Detailed modelling of structure and function at the cellular level tutorial”, CNS 2017, Antwerp (Belgium).
- “Data-driven Neurophysiology and Neuronal Modelling”, SfN 2017, Washington DC (US)

PUBLICATIONS

O'Reilly, C., Iavarone, E., & Hill, S. L. (2017). A framework for collaborative curation of neuroscientific literature. *Frontiers in neuroinformatics*, 11, 27.

Shardlow, M., Ju, M., Li, M., O'Reilly, C., Iavarone, E., McNaught, J., & Ananiadou, S. (2019). A Text Mining Pipeline Using Active and Deep Learning Aimed at Curating Information in Computational Neuroscience. *Neuroinformatics*, 17(3), 391-406.

Negrello, M., Warnaar, P., Romano, V., Owens, C. B., Lindeman, S., Iavarone, E., ... & De Zeeuw, C. I. (2019). Quasiperiodic rhythms of the inferior olive. *PLoS computational biology*, 15(5), e1006475.

Iavarone, E., Yi, J., Shi, Y., Zandt, B. J., O'reilly, C., Van Geit, W., ... & Hill, S. L. (2019). Experimentally-constrained biophysical models of tonic and burst firing modes in thalamocortical neurons. *PLoS computational biology*, 15(5), e1006753.

AWARDS

Best Poster: CNS, Seattle, WA, USA, 2018